New Techniques and Methods for In-Situ Orbital Debris Detectors

By

Luke Travis Cornwell

Thesis

Submitted to the University of Kent

for the degree of

Doctor of Philosophy

School of Physics and Astronomy

September 2023

University of Kent

Declaration

The content within this thesis was produced by myself, and has not been previously submitted for any other qualification or degree at any other institution. All of the data is my own, unless explicitly stated otherwise. Instances of other work that have been included are cited.

Abstract

The rapidly increasing population of orbital debris in the near-Earth environment poses a significant hazard for operational spacecraft and future space missions. This has led to an increased need for in-situ detectors capable of observing, and distinguishing between, natural space dust and anthropogenic orbital debris, to both measure their flux and help quantify the threat that they pose. Accordingly, this thesis is concerned with the development of new techniques for in-situ orbital debris detection, with a focus on the development of acoustic thin film time of flight (TOF) detectors, specifically the Debris Resistive Acoustic Grid Orbital NASA-Navy Sensor (DRAGONS) developed by NASA, and my industrial partners AstroAcoustics.

TOF detectors are valued for their impactor speed and direction measurement capabilities that allow the distinction between orbital debris and natural space dust particles. The development and successful implementation of thin film TOF detectors, which measure impactor speed via the passage of the impactor through successive thin films, requires that two key questions be answered: Firstly, what is the measurement accuracy of such a detector? Secondly, what effect does passage through the thin film have on the impactor and the resulting speed measurement, i.e. is the impactor decelerated upon passage through the first film? To address these questions prototype detectors based on the DRAGONS concept were constructed, one with two successive 12.5 µm Kapton films and the other with two successive 25 µm Kapton films. These were then impacted with stainless steel projectiles ranging from 0.2 mm to 1 mm in diameter at hypervelocity speeds of $\sim$ 2 km s^{-1} and $\sim$ 4 km s^{-1} using the University of Kent's two-stage Light Gas Gun. This range of projectile sizes provided a film thickness to projectile diameter ratio (f/d_p) of between $1/80 \leq f/d_p \leq 1/8$.

For the largest 1 mm projectiles impacting 12.5 µm Kapton films, no deceleration was observed, and the speed obtained from the detector was found to be accurate to less than 1% error. This confirms that acoustic thin film detectors can measure the speed of 1 mm-sized impactors to a high degree of accuracy and are thus suitable for use in space to measuring this size of orbital debris, which poses the greatest threat to space missions in low Earth orbit (LEO). As f/d_p increases, the penetration hole morphology becomes more complex and with-it acoustic signal onset determination decreases in accuracy, resulting in a decrease in speed measurement accuracy. Deceleration was not observed for projectiles

≥ 0.4 mm impacting 12.5 µm Kapton films (f/d_p = 1/32), however, as f/d_p increased to f/d_p = 1/16, deceleration started to occur. Broadly deceleration was found to have size dependent effects, with the absolute film thickness playing a role as well as f/d_p. Furthermore, comparison to previous results in the literature would suggest that there is also a material dependence. During the investigation, non-acoustic noise was identified in some of the traces from the polyvinylidene fluoride (PVDF) acoustic sensors. This was observed to coincide with impact light flash produced during projectile impact and is the likely source of this noise.

With the space industry moving towards using smaller spacecraft in favour of larger, more traditional spacecraft, a preliminary analysis of the feasibility of using small area detectors applied to small spacecraft (specifically CubeSats), to perform orbital debris flux measurements, was conducted. Traditionally large areas on single spacecraft are required for impact detectors to ensure they provide meaningful statistical data. Thus, the use of small area detectors that can be applied to CubeSats faces an important question: can the accumulation of data from detection areas split over multiple small detectors provide statistically meaningful results? Comparison between the accumulated flux from CubeSat-sized surfaces that have previously been exposed to space and predictions from ESA's most up to date space environment modelling software - MASTER 8.0.3 - suggests that the accumulation of detection area does provide statistically meaningful data, with accumulated fluxes within or very close to the estimated minimum uncertainties for the predicted fluxes.

Acknowledgements

Firstly, I must express my deepest gratitude to my supervisors Professor Mark Burchell, and Dr. Penelope Wozniakiewicz, for their invaluable support and guidance throughout my PhD. I would especially like to thank Mark for helping me to foster such a good work-life balance in the early days of my PhD, and for his continued supervision as he transitioned to Emeritus Professor. Similarly, I would like to thank Penny for all of her help and support, and providing a great role model.

I wish to show my appreciation to the University of Kent and the Global Network On Sustainability In Space (GNOSIS) for jointly funding my research. I also acknowledge that the GNOSIS funding came from an STFC grant. These thanks must be extended to the individuals from these organisations that helped provided me with excellent opportunities during my time as a PhD researcher. Thanks also goes to the Kent outreach team, and my peers, for helping me to develop as a professional in my enjoyable time as an Academic Mentor.

I acknowledge and thank Robert Corsaro, from my industrial partner AstroAcoustics, and Frank Giovane, both members of the DRAGONS team, for their useful discussion and the materials provided in the early days. My gratitude must also go to Dr. Luke Alesbrook the LGG lab technician, for operating the gun and showing me the ropes in the LGG lab.

Thanks to all the great people at the Equestrian, and Salsa societies for helping to keep the work-life balance in the sweet spot, and for the great times. For all those that go unmentioned, who have helped to make my PhD journey a great one, I express my thanks. I hope that you know who you are.

My heartfelt gratitude goes to my best friend and partner Nadia, the most supportive and understanding partner anyone could hope for, for all of her support and encouragement. Last and by no means least, my eternal thanks go to those that have always been there to support me, and always will be there to support me, my incredible family!

Contents

Abstract i

Acknowledgements iii

Contents iv

List of Tables vii

List of Figures ix

List of Acronyms xiv

Chapter 1 Introduction and Thesis outline 1

1.1 Introduction 1

1.2 Research Objectives 3

1.3 Thesis Outline 4

Chapter 2 Background 6

2.1 Introduction 6

2.2 Cosmic Dust 6

2.2.1 Interplanetary Dust 6

2.2.2 Origins of Interplanetary Dust 7

2.3 Orbital Debris 9

2.3.1 Orbital Debris Sources 10

2.3.2 Risks from Orbital Debris 13

2.3.3 Measurement and Quantification 17

2.4 Past Detectors 19

2.5 The Debris Resistive Acoustic Grid Orbital NASA-Navy Sensor 22

2.6 Old Space vs. New Space 23

2.7 Hypervelocity Impacts 26

2.7.1 Initial Partition of Energy: Contact and Compression 27

2.7.1.1 Shockwaves 29

2.7.1.2 Impact Pressure the Planar Impact Approximation 30

2.7.2 Cratering, Excavation and Ejecta 32

2.7.2.1 Oblique Impacts 33

2.7.3 Melting, Vaporisation, and Impact Ionisation/Light Flash 33

2.8 Development of Thin Film Detectors 34

2.8.1 Penetration of Thin Films 36
2.8.2 Deceleration of Projectiles Penetrating Thin Films 41
2.9 Conclusions 45

Chapter 3 Experimental Equipment and Method 47
3.1 The Light Gas Gun 47
3.1.1 Design and Operation of LGGs 49
3.1.2 Velocity Dependence 58
3.1.3 LGG Summary 59
3.2 Detector Materials 59
3.2.1 Introduction to PVDF 59
3.2.2 Properties of PVDF Sensors 61
3.2.3 Sensors Used in this Research 62
3.2.4 Kapton Polyimide Film 63
3.3 Experimental Method 66
3.3.1 Construction of the Prototype Thin Film Detector 66
3.3.2 Sensor Positioning 67
3.3.3 Experimental Procedure 69
3.3.4 The Time of Flight Method to Calculate Speed 72
3.3.5 Signal Onset Determination 73
3.3.6 Uncertainties 76
3.3.7 Microscopy 81
3.4 Conclusion 83

Chapter 4 Determination of Detector Performance and Results for Large Projectiles ... 84
4.1 Introduction 84
4.2 Experimental Parameters 84
4.3 Results 85
4.3.1 Determination of Signal Features 90
4.3.2 Non-acoustic Noise 97
4.3.3 Projectile Penetration 102
4.3.4 Speed Measurement Accuracy 105
4.4 Summary 108

Chapter 5 Small Projectile Results and Deceleration 110
5.1 Introduction 110
5.2 Automated Signal Detection 110
5.3 Experimental Parameters 115
5.4 Results 118
5.4.1 Penetration Hole Formation 118
5.4.2 Speed Measurement and Deceleration Results 128
5.5 Conclusions 137

Chapter 6 MASTER Model Orbital Environment Simulations 141
6.1 Introduction 141
6.2 Basic Functionality and Background of MASTER 142
6.2.1 Population Sources and Spatial Distribution 143
6.2.2 Flux Modelling 146
6.2.3 Uncertainties in MASTER 149
6.3 ESABase2/Debris 150
6.4 Validation of MASTER 151
6.4.1 Validation on the Implementation of MASTER 151
6.4.2 Validation of the Real World Applicability of MASTER 153
6.4.2.1 Validation against LDEF Data 153
6.4.2.2 Validation against HST Data 160
6.4.2.3 Summary 162
6.5 Results from MASTER 163
6.5.1 Current Particle Environment in Earth-orbit 163
6.5.2 Small-Area Detectors 165
6.5.2.1 Time Scales for Small Area Detectors and CubeSats 170
6.6 Conclusions 176

Chapter 7 Conclusions and Future Work 178
7.1 Conclusions 178
7.2 Future Work 181
References 184
Appendix I Full recorded data, signal traces, and penetration hole images 206
Appendix II Supplementary material and data 248

List of Tables

Table 2.1 Top ten on orbit breakup events before 2016, ranked according to the number of catalogued debris produced. 12

Table 2.2 Examples of past time of flight space dust and debris detectors flown aboard space missions, and the type of detection used. 21

Table 2.3 A review of recent CubeSat sized detectors and CubeSat missions for orbital debris and cosmic dust detection. 26

Table 2.4 Projectile parameters used in the Pailer and Grün (1980) thin film penetration study. 42

Table 2.5 Deceleration results for projectiles of different densities, all with mass = 10^{-11} g, v_i = 3 km s^{-1}, and perpendicular incidence, from Pailer and Grün (1980). 43

Table 2.6 Deceleration results for Fe projectiles of different masses and a 60° angle of incidence to the film, from Pailer and Grün (1980). 43

Table 3.1 Research active Light Gas Gun facilities in the UK. 48

Table 3.2 General conditions used to obtain a range of velocities. 59

Table 4.1 Key shot parameters for seven shots to determine detector/prototype performance. 85

Table 4.2 The time between the onset of the small preceding peaks and the onset of the larger peaks of interest, and the sensor to impact separation for shots Veri.1 to Veri.3. . 96

Table 4.3 Experimental parameters for the light flash related shots. 98

Table 4.4 Penetration hole diameter (d_h) in the 1st and 2nd Kapton films. 104

Table 4.5 Speed measurement results. 106

Table 4.6 Wave speed in the Kapton film as calculated from this experimental data. ... 107

Table 5.1 Comparison between the measured projectile speed from manually picked (MP) and algorithm autonomously picked (AP) onset times. 115

Table 5.2 Shot parameters for the nineteen successful shots performed to determine effects of Kapton film penetration on small projectiles, and results for their associated penetration holes 117

Table 5.3 Deceleration results for the shots in the Dec. shot programme, featuring small projectiles with larger f:d_p. 132

Table 6.1 Comparison between data generated from MASTER here and data from a past simulation presented in Wozniakiewicz and Burchell, 2019. 153

Table 6.2 'Target Orbit Settings' for the simulation of LDEF data. 155

Table 6.3 Input parameters for MASTER's 'Satellite Properties' used for LDEF. 155
Table 6.4 'Target Orbit Settings' for the simulation of HST data. 161
Table 6.5 Input parameters for MASTER's 'Satellite Properties' used for HST. 161
Table 6.6 Data from a crater survey on plates from Tray B9 of the LDEF mission, with an area less than the largest face of a 6U CubeSat (0.06 m^2). 167
Table 6.7 'Target Orbit Settings' used for a circular polar orbit of 98.7° inclination and altitude of 800 km. 171
Table 6.8 Input parameters for MASTER's 'Satellite Properties' used for the propagation of future CubeSat missions. 171

List of Figures

Fig. 2.1 A monochrome image of the DART spacecraft impact into Dimorphos, showing the ejecta produced. 8

Fig. 2.2 Comet 1P/Halley, taken by W. Liller, March 8, 1986. 9

Fig. 2.3 Evolution of the number of tracked objects in Earth-orbit by class. 10

Fig. 2.4 The size regime for each population of orbital debris. 13

Fig. 2.5 The damage produced by a 1 mm stainless steel sphere, and a 1.5 mm soda-lime glass sphere impacting 3.15 mm thick aluminium plates at ~ 4.0 km s^{-1} 15

Fig. 2.6 Schematic of the Whipple shield design and principle. 15

Fig. 2.7 An example of the Whipple shield design, previously impacted at Kent by a 4.3 mm diameter solid nylon sabot at 7.19 km s^{-1}. 16

Fig. 2.8 Sentinal-1A solar array before (left) and after (right) an impact by a ~ 1 cm particle at ~ 11 km s^{-1}. 16

Fig.2.9 Schematic of the Debris Resistive Acoustic Grid Orbital NASA-Navy Sensor (DRAGONS) detector. 23

Fig. 2.10 Schematic of the one-dimensional impact model. 28

Fig. 2.11 Hugoniot Curve schematic. 28

Fig. 2.12 Schematic of the excavation stage of the cratering process. 32

Fig. 2.13 Diagram of the impact features produce in a brittle target material. 36

Fig. 2.14 Schematic for the evolution of cratering into penetration for impacts into increasingly thinner targets. 37

Fig. 2.15 X-ray shadowgraph of a Cd projectile impact into a Cd plate at 5 km s^{-1}. 38

Fig. 3.1 The Light Gas Gun in the University of Kent's Impact Facility. 48

Fig. 3.2 A schematic representation of the University of Kent's light gas gun. 50

Fig. 3.3 A schematic representation of the working principle of the compression stages of a two-stage light gas gun. 51

Fig. 3.4 A nylon piston with black O-rings in place, towards the front of the piston. 52

Fig. 3.5 Unscored and scored burst discs before and after rupturing. 53

Fig. 3.6 Microscope images of a split sabot. 55

Fig. 3.7 A stop plate after having been impacted. 56

Fig. 3.8 A schematic of a PVDF film with their specific axis nomenclature and electric polarisation shown. 61

Fig. 3.9 A quarter sized sensor that has been removed from a detector, laying on top of a piece of Kapton. 63
Fig. 3.10 NASA's New Horizons spacecraft in the Kennedy Space Center. 64
Fig. 3.11 A front facing view of a prototype detector used in this thesis. 66
Fig. 3.12 A schematic showing the sensors placement used for the prototype. 68
Fig. 3.13 A prototype detector shown positioned in the target chamber. 69
Fig. 3.14 The projectile capture system shown mounted on the target chamber. 70
Fig. 3.15 Optical images (transmitted light at an angle of 45°) of penetration holes in the detector's Kapton films after impact by a 1 mm stainless steel sphere at 2 km s^{-1}. 71
Fig. 3.16 A schematic representation of the time of flight method, applied to a projectile penetrating two Kapton films separated by a distance *x*. 72
Fig. 3.17 Typical acoustic signals recorded for a 1 mm stainless steel sphere impacting at ~ 2 km s^{-1}. 74
Fig. 3.18 The key time period of acoustic signals in Fig. 3.17 plotted in sensor pairs across multiple plots to make identification of features in each signal possible. 74
Fig. 3.19 The key time period of acoustic signals from a 1 mm stainless teel 420 sphere shot at ~ 4 km s^{-1}. 75
Fig. 3.20 The key time period of acoustic signals from a 1 mm stainless steel 420 sphere shot at ~ 2 km s^{-1}, with a relatively broad, split peak. 77
Fig. 3.21 Microscope images of a penetration hole in the first film, viewed from the incident direction of the 1 mm stainless steel 420 sphere that impacted at ~ 4 km s^{-1}. 82
Fig. 3.22 Microscope images of a penetration hole in the first film, (a) backlight, and (b) backlight at an angle 45°. 83
Fig. 4.1 The key time period of acoustic signals in shot Veri.1. 86
Fig. 4.2 The key time period of acoustic signals in shot Veri.2. 86
Fig. 4.3 The full trace of signals in shot Veri.3. 87
Fig. 4.4 The key time period of acoustic signals in shot Veri.3. 87
Fig. 4.5 The key time period of acoustic signals in shot Veri.4, with signs of non-acoustic noise that contaminated the onset of the signals of interest. 88
Fig. 4.6 The key time period of acoustic signals in shot Veri.4 plotted on a single graph with an extended y-axis to show the full magnitude of the non-acoustic noise peak. 88
Fig. 4.7 The key time period of acoustic signals in shot Veri.5. 89
Fig. 4.8 The key time period of acoustic signals in shot Veri.6. 89
Fig. 4.9 The key time period of acoustic signals in shot Veri.7. 90

Fig. 4.10 Acoustic signals for a shot conducted with an empty sabot at ~ 2 km s^{-1}. 92
Fig. 4.11 The time period of interest for the acoustic signals in the empty sabot shot. ... 92
Fig. 4.12 Demonstration of how tap tests were performed. 93
Fig. 4.13 Acoustic signals from a tap test on the first film of the detector. 93
Fig. 4.14 Images of the other two methods used to try and determine whether any acoustic contamination occurs between films. 94
Fig. 4.15 Isolated films in the target chamber for the shot to determine whether any acoustic contamination occurs between films. 95
Fig. 4.16 A schematic of the experimental setup for light flash experiments. 99
Fig. 4.17 Light flash experimental setup, analogous to the prototype detector. 99
Fig. 4.18 Photodiode and PVDF signals recorded for a 0.8 mm stainless steel 420 sphere impacting two consecutive Kapton films. 101
Fig. 4.19 Expanded time region of interest from Fig. 4.18. 102
Fig. 4.20 Penetration holes in 1st and 2nd 12.5 µm Kapton films. 103
Fig. 4.21 Penetration hole in a 2nd 12.5 µm Kapton film. 103
Fig. 4.22 Three random examples of spherical projectiles taken from the 1 mm stainless steel 420 supply to confirm the tolerance of the projectile size. 105
Fig. 5.1 Algorithm used for automated determination of signal onset time. 113
Fig. 5.2 The raw acoustic data compared to the processed data for shot Veri.3. 114
Fig. 5.3 Schematic of the impact geometry for inclined incidence shots. 116
Fig. 5.4 Example of a penetration hole with a 'thin film-like' morphology (TFL). 119
Fig. 5.5 Example of a penetration hole with a 'barrel-like' morphology (BL). 120
Fig. 5.6 Schematic representation of the four penetration hole morphologies. 121
Fig. 5.7 Example of a penetration hole with a 'crater-like' morphology (CL). 122
Fig. 5.8 Example of penetration holes in the 1st (a) and 2nd (b) film with a 'directional' morphology (Di). 123
Fig. 5.9 Elastic Plastic Impact Computation code simulation snapshot for aluminium sphere impacting into an aluminium plate at 2.4 km s^{-1}, from Rogers *et al*., 2023. 124
Figure 5.10 Normalised hole diameter (d_h/d_p) plotted against film thickness over projectile diameter (f/d_p). 125
Fig. 5.11 Projectile diameter (d_p) plotted against hole diameter (d_h). 126
Fig. 5.12 Projectile diameter over film thickness (d_p/f) plotted against hole diameter over film thickness (d_h/f). 128
Fig. 5.13 The key time period of acoustic signals in shot Dec.7. 129

Fig. 5.14 The key time period of acoustic signals in shot Dec.18. 130
Fig. 5.15 The key time period of acoustic signals in shot Dec.11, showing signs of non-acoustic noise. 130
Fig. 5.16 Acoustic signals for shot Dec.6, which were contaminated with unexpected debris arriving close in time to the projectile. 131
Fig. 5.17 Data from the Veri. and Dec. shot programmes plotted as v_i/v_p vs. m_f/m_p. 134
Fig. 5.18 Data from the Veri. and Dec. shot programmes, plotted as v_i/v_p vs. m_f/m_p, compared to past deceleration data from Simpson and Tuzzolino (1998), and Capaccioni and McDonnell (1986). 135
Fig. 5.19 Data from the Veri. and Dec. shot programmes, plotted as v_i/v_p vs. $(m_f/m_p)^{0.5}$, compared to past deceleration data from Simpson and Tuzzolino (1998), and Capaccioni and McDonnell (1986). 136
Fig. 6.1 Near-Earth environment volume discretisation scheme implemented by MASTER. 147
Fig. 6.2 Geometric model of a 6U CubeSat in the ESABase2 geometry window. 151
Fig. 6.3 LDEF lifted from the cargo bay of the space shuttle Columbia after retrieval. ... 154
Fig. 6.4 MASTER 8.0.3 predicted cumulative particle flux for the space-facing end of LDEF. 156
Fig. 6.5 Flux vs. surface normal impact velocity, for impacts on an orientated surface modelling the space-facing end of LDEF as simulated and output by MASTER 8.0.3. 157
Fig. 6.6 Comparison between MASTER 8.0.3 predicted crater lip diameter flux and the measured crater lip diameter flux for the space-facing end of LDEF. 158
Fig. 6.7 Flux vs. surface impact angle (measured from normal incidence), for impacts on an orientated surface modelling the space-facing end of LDEF. 160
Fig. 6.8 Comparison of MASTER 8.0.3 predicted conchoidal cracking diameter flux for the HST solar arrays (between 04/1990 – 12/1993) and data measured from a returned solar array wing. 162
Fig. 6.9 3D spatial density (S.D.) distribution of dust and debris vs. altitude and declination, output by MASTER 8.0.3. 163
Fig. 6.10 Spatial density of the different space debris and the meteoroid background populations as a function of altitude, as predicted by MASTER 8.0.3. 164
Fig. 6.11 Spatial density of the different space debris and the meteoroid background populations as a function of diameter, as predicted by MASTER 8.0.3. 165

Fig. 6.12 Tray B9 post de-integration from LDEF, showing the small plates used in the investigation herein. 166
Fig. 6.13 Cumulative particle flux data for particle diameter (d_p), for a surface pointing 8° from the velocity vector in a LDEF-like orbit as predicted by MASTER 8.0.3. 168
Fig. 6.14 Flux vs. surface normal impact velocity, for impacts on a surface modelling the LDEF Tray B9 pointing direction, as simulated and output by MASTER 8.0.3. 169
Fig. 6.15 Cumulative flux data for crater-lip diameter (d_r), for impacts into a surface pointing 8° from the velocity vector in a LDEF like orbit as predicted by MASTER 8.0.3. 169
Fig. 6.16 Comparison between the output predicted cumulative flux from MASTER 3.0.8 for a 1 m^2 cross-section sphere and the cumulative flux for a 6U CubeSat predicted by ESABase2/Debris. 172
Fig. 6.17 Three-dimensional flux results for a 6U CubeSat with its largest face pointing along the velocity vector. 173
Fig. 6.18 The time in days expected for a particle (debris or meteoroid) ≥ a given size will impact the ram face (top) and entire surface area (bottom) of a 1U, 1.5U, 3U, and 6U CubeSat in a circular orbit, with an inclination of 98.7°, and altitude of 800 km (where the largest surface area face is pointing in the ram direction). 174

List of Acronyms

ADLER	Austrian Debris Detection Low Earth (orbit) Reconnoiter
ALADDIN	Arrayed Large-Area Dust Detectors in INterplanetary space
APID	Austrian Particle Impact Detector
ARGOS	Advanced Research and Global Observation Satellite
ARMADILLO	Attitude Related Manoeuvres And Debris Instrument in Low (L) Orbit
ASTERISC	Advanced Satellite Toward Exploration of dust enviRonment with In-Situ Cosmic dust sensor
BL	Barrel-Like morphology
CDD	Cosmic Dust Detector
CDM	Cosmic Dust Analyzer
CFRP	Carbon Fibre Reinforced Plastic
CL	Crater-Like morphology
CONOPS	Concept of Operations
COTS	Commercial Off The Shelf
CPE	Cell Passage Event
DART	Double Asteroid Redirection Test
DEBIE	Debris In-Orbit Evaluator
DELTA	Debris Environment Long-Term Analysis model
DFMI	Dust Flux Monitor Instrument
Di	Directional Morphology
DIDSY-IPM	Impact Plasma and Momentum subsystem of the Dust Impact Detection System
DISC	Dust Impact Sensor and Counter
DRAGONS	Debris Resistive Acoustic Grid Orbital NASA-Navy Sensor
DRAMA	Debris Risk Assessment and Mitigation Analysis
DUCMA	Dust Counter and Mass Analyser
ESA	European Space Agency
EURECA	EUropean REtrievable CArrier
GEO	Geostationary Earth Orbit
HEL	Hugoniot Elastic Limit
HRD	High Rate Detector
HST	Hubble Space Telescope

IADC	Inter-Agency Space Debris Coordination committee
IAU	International Astronomical Union
IDPs	Interplanetary Dust Particles
IKAROS	Interplanetary Kite-craft Accelerated by Radiation Of the Sun
ISS	International Space Station
JAXA	Japanese Space Agency
LAD-C	Large Area Debris Collector
LDEF	Long Duration Exposure Facility
LEO	Low Earth Orbit
LGG	Light Gas Gun
LMRO	Launch and Mission Related Objects
MASTER	Meteoroid and Space Debris Terrestrial Environment Reference
MEO	Medium Earth Orbit
MLI	Multi-layer insulation
NaK	Sodium-potassium alloy
NASA	National Aeronautics and Space Administration
ODPO	Orbital Debris Programme Office
ORDEM	Orbital Debris Engineering Model
PD	Payload Debris
PDD	Piezoelectric Dust Detector
PL	Payload
PM	Payload Mission related object
POEM	Program for Orbital Debris Environment Modelling
PVDF	Polyvinylidene Fluoride
RB	Rocket Body
RD	Rocket Debris
RF	Rocket Fragmentation debris
RM	Rocket Mission
RORSAT	Radar Ocean Reconnaissance Satellite
S.D.	Spatial Density
SDS	Space Debris Sensor
SOLID	SOLar panel based Impact Detector
SPADUS	SPAce DUSt (a particular detector)
SRM	Solid Rocket Motor

STS	Space Transportation System
StSt420	Stainless Steel 420
TFL	Thin Film-Like morphology
TLE	Two Line Element
TOF	Time of Flight
UI	Unidentified

Chapter 1: Introduction and Thesis Outline

1.1 Introduction

Since the beginning of the space age, when humankind began to launch spacecraft into orbit in the 1950's, the pollution of the near-Earth orbital environment has been increasing, with debris being created and left behind from the ever increasing rocket and spacecraft activities. Debris can vary in size from large upper stage rocket bodies to very small particles, such as dust produced in solid rocket motor (SRM) firings, and ejecta from impacts into spacecraft from natural cosmic dust and anthropogenic debris relating to human activity (e.g. see Wozniakiewicz and Burchell (2019) for a review). Large debris > 10 cm in size can be readily tracked from Earth and thus avoidance manoeuvres to avoid a catastrophic collision can be performed (Liou and Johnson, 2006; NASA, 2020, 2021). However, due to high impact speeds (for low Earth orbit (LEO) typical mean debris impact speeds are in the range 7 km s^{-1} to 14 km s^{-1} (Kessler *et al*., 1989; Burchell *et al.*, 2013)), even millimetre-sized debris can cause fatal – end of mission - damage to spacecraft. Such debris cannot be tracked and avoided, thus mm-sized debris poses an invisible yet lethal threat to spacecraft that can only be mitigated with spacecraft shielding. In fact, due to the large population of mm-sized debris (compared to larger sized debris) and hence more frequent impacts, mm-sized debris is considered to pose the largest mission ending threat (NASA, Office of Inspector General, Office of Audit, 2021).

As modern society increases its demand for space-based infrastructure, whether that be telecommunications, global positioning, or surveillance and global imaging, so too has the supply. As well as traditional national agencies, this has heralded the way for commercial launch and services providers in recent years such as SpaceX, which have significantly increased the launch rate. This in turn has significantly increased the growth rate of orbital debris, with ~ 8000 tracked objects in Earth-orbit on the first day of the year 1997, ~ 9000 in 2007, ~ 15000 in 2011 and ~ 32000 in 2023 (ESA Space Debris Office, 2023). The situation is far worse when considering the un-trackable populations of smaller sized debris, which are much larger. Using statistical modelling through their MASTER-8 software, ESA predict that there are 36,500 objects > 10 cm, 1 x 10^6 objects sized between 1 cm and 10 cm, and 130 x10^6 objects sized from 1 mm to 1 cm in orbit as of 06/06/2023 (ESA Space Debris Office, 2023b). This poses a twofold threat; not only is there more debris that can cause fatal damage to spacecraft, but there are also more spacecraft on which we as a society

have a greater reliance. This ultimately leads to a larger and more frequent number of impacts and collisions, potentially causing spacecraft losses, and further increasing the problem of orbital debris in a cascade effect. This could lead to the dreaded Kessler syndrome (Kessler, 1991), whereby the critical density of LEO is reached, resulting in a self-propagating debris collision mode that will render the LEO environment unusable for spaceflight for some time. At low altitudes below 300 km, debris tends to clear due to atmospheric drag in the order of months. However, debris ejected and/or thrown into higher orbits can remain in orbit for longer. Below 600 km debris last in the order of years, at 800 km lifetimes are measured in centuries, and above 1000 km this time increases rapidly to a thousand years and more.

The only way to provide adequate shielding and mitigate against debris that cannot be tracked is to measure the debris particle environment with in-situ detectors and quantify their threat. Similarly, an accurate measure of the debris environment is required to inform us on sustainable practises for launch and operation of spacecraft, which directly influences policies, regulations, laws, and remediation put in place to improve and future proof the sustainability of the space environment and economy. This emphasises the importance of in-situ detectors that can provide data to inform on the above. Of the two types of in-situ detector, 'active' and 'passive', only active detectors can directly measure the speed of impacting particles, and hence provide a more detailed knowledge of the environment, and more readily distinguish between natural dust particles and anthropogenic debris (by determining the trajectory/orbit from the speed and direction of impact). This is due to active detectors measuring and transmitting data, while passive detectors must be retrieved and investigated. With the fast growing and dynamic state of the debris environment, active detectors have the added value of producing data in real-time, providing up to date information and the ability to inform on time critical events.

One such type of detector that can measure the speed of incident particles are thin film time of flight (TOF) detectors. In particular, Kapton's favourable properties and proven flight heritage suggest that it would be suitable for application in thin film TOF detectors. One way to separate between debris and natural dust detection is by their speed (debris is typically lower speed than dust that is coming from interplanetary space). Note that a fuller separation is possible if the orbit can be determined i.e. particle speed and direction. This poses the question: what speed measurement accuracy can Kapton based TOF detectors achieve? What are the implications of the film impact on the detection, will the impactor

be disrupted or decelerated? Furthermore, the risks and threat of orbital debris are not homogeneous in the near-Earth environment. Thus, detectors are required for different detections in different orbits, each effecting the detector and mission design. There is a recent movement in the space industry away from traditional large and expensive satellites to smaller and cheaper satellites, such as CubeSats. Can CubeSats, and in particular nano-satellites (< 10 kg) that are often given a bad reputation as 'space junk' due to ease of access to space and their typically short operational lifetimes, provide a useful detector platform to increase detection capacity?

Accordingly, this thesis advances the development of detectors with regards to; understanding the true speed of impactors and the performance of Kapton thin film TOF detectors, and understanding the current debris environment and the feasibility of future small satellite detector design i.e. mission parameters, detector size and producing sufficient detection area. All of this is with a focus on the mm-sized population that has the highest mission ending threat.

1.2 Research Objectives

The objectives of the research presented in this thesis aimed to develop new techniques and methods for in-situ orbital debris detection. The main, and first two, objectives relate to the current development of an active debris sensor, the 'Debris Resistive Acoustic Grid Orbital NASA-Navy Sensor' (DRAGONS), in conjunction with my industry partners AstroAcoustics, whom are part of the DRAGONS team. These objectives focused on the speed determination capabilities of the DRAGONS sensor. The third objective was related to applying the rapidly increasing small satellite, and particularly CubeSat, industry to orbital debris detection and harnessing their benefits, such as their quick time to launch and relatively cheap budget. The objectives were as follows:

1. To determine the speed measurement accuracy achievable with the DRAGONS concept (based on the acoustic detection of particle impacts on successive thin Kapton films), for orbital debris in the millimetre-size range of interest.
2. Determine the effects of film penetration on the particles detected, and on particle detection. This was with a focus on the deceleration and/or disruption experienced

during passage of the projectiles. A knowledge of this is required to determine accurate information about the incident particles.

3. Perform analysis on the feasibility of using small CubeSat (defined here as less than six CubeSat units in size) sized detectors for orbital debris detection, using the latest space environment modelling software.

1.3 Thesis Outline

Chapter 2 provides an overview of the near-Earth space dust and orbital debris environment, including discussion of their origins/sources and the threat that they pose to spacecraft missions. Past space dust and orbital debris detectors are introduced, and the impact physics and processes relevant to the development of detectors is reviewed.

Chapter 3 details the experimental procedure for the research presented, including data collection and analysis. There is a focus on introducing the Light Gas Gun that was used to perform the impact experiments, the design of the prototype detector used in the study, and the analysis of acoustic data for time of impact determination. Techniques for the determination of impactor speed, penetration hole size, and projectile disruption are also detailed.

Chapter 4 presents result on the hypervelocity impact of the prototype detector with millimetre-sized particles. Speed measurement accuracy, and penetration hole features are presented. Obstacles that had to be overcome, including the determination of the signals of interest, and noise in the data, are also detailed. This involved the investigation of light flash phenomena.

Chapter 5 concerns result from hypervelocity impacts on the detector by sub-millimetre projectiles that may experience deceleration and/or disruption. The deceleration observed is presented and discussed. The change of penetration hole characteristics with impactor size is shown and discussed with relevance to the accuracy of the detector.

Chapter 6 details ESA's Meteoroid and Space Debris Terrestrial Environment Reference (MASTER) model used for simulation of the near-Earth dust and debris environment. The spatial distribution of dust and debris was simulated to give an understanding of the environment. Impact flux simulations of past missions were carried out to verify the

accuracy of data being output from the user defined inputs. Then simulations of CubeSat's and CubeSat sized detectors were performed (including the use of ESABase2), to analyse the feasibility of using CubeSats for dust and debris flux measurements.

Chapter 7 summarises the conclusions from the research herein, and outlines future work that has presented itself from the study that should be considered and carried out for further development.

References: References for the material cited in the main text.

Appendix I: This appendix contains tables of the raw data used for the calculation of the detector measured projectile speed, and Kapton wave speed measurements not shown in the main text. Then there is a table that relates shot ID's to shot date, to allow cross referencing with Kent's LGG facility archives. Full signal traces, the key time period of interest, and penetration hole features imaged from the projectile incidence direction, which were not included in the main text are presented here. Finally, the raw signals from the light flash experiments that were not shown in the main text are included.

Appendix II: Presented here is the derivation of the scaling of the ratio of film mass over projectile mass as the film thickness and projectile diameter is scaled by a factor of two, the Python code use for the autonomous signal onset determination algorithm discussed in Chapter 5, and the average flux (averaged over all faces) vs. diameter for the different sizes of CubeSat discussed in Chapter 6.

Chapter 2: Background

2.1 Introduction

This chapter introduces the key background research and theory required to understand the rationale for this research and the results discussed within. The focus is on particles in the near-Earth environment, the threat that they pose to spacecraft and space sustainability, and the detectors and methods used to measure and quantify them. Relevant underlying physical processes are also discussed.

2.2 Cosmic Dust

Cosmic dust can be classified into several groups depending on its origin and where it resides; these are interplanetary dust, interstellar dust, and intergalactic dust. Starting with the latter of these, intergalactic dust populates the medium between galaxies. Research suggests that it is transported here from galactic discs via winds and radiation pressure and it has been found to affect the measurement of cosmological parameters, through galactic distance measurements (Ménard *et al.*, 2010). Similarly, interstellar dust is found within the interstellar medium causing a similar extinction and scattering of star light (Trümpler, 1930), with dense clouds visible as dark nebulae against the background of the Milky Way. The predominant source of interstellar dust are stars that are in the late stages of their evolution, which produce heavy elements (Grün *et al*., 2019). A further source are supernova explosions from stars in their final stage of evolution (Leitner & Hoppe, 2019). Accretion of interstellar dust into dark interstellar clouds leads to the formation of stars, through gravitational collapse leading to heating of the core and eventually fusion begins. Following this, further condensation and accretion of dust in the protoplanetary disk around newly formed stars produces planetary objects (Dorschner, 2001) creating a planetary system. This system is populated by interplanetary dust leftover from the early stages of the solar system, and created in processes taking place throughout the solar system, as described below in Section 2.2.2.

2.2.1 Interplanetary Dust

Interplanetary dust describes cosmic dust in our solar system, defined by the International Astronomical Union (IAU) Commission F1 as: “Finely divided solid matter, with particle sizes in general smaller than meteoroids, moving in, or coming from, interplanetary space”

(Koschny *et al.*, 2019). In turn, meteoroids are defined by the IAU as: "A solid natural object of a size roughly between 30 µm and 1 m, moving in, or coming from, interplanetary space" (Koschny *et al.*, 2019). This gives a slightly ambiguous definition of the size of interplanetary dust particles, for which many sources differ. However, the smaller sized meteoroids, also known as micrometeoroids, are usually defined as the largest of the interplanetary dust particles, ranging in size from 50 µm to 2 mm (Corsaro *et al.*, 2016). Due to the relevance of the < 1 cm population to the research discussed within this thesis, interplanetary dust shall be defined throughout this research as natural particles smaller than 1 cm, moving in, or originating from, interplanetary space. Common constituents of interplanetary dust include carbonaceous material ($\sim$ 2.5 g cm^{-3} – 3 g cm^{-3}), silicates such as magnesium-iron silicates (Mg-Fe silicates, $\sim$ 2.5 g cm^{-3} – 2.9 g cm^{-3}), iron-nickel sulphides (Fe-Ni S, $\sim$ 4.5 g cm^{-3} – 6 g cm^{-3}), and metals such as iron and nickel (Fe $\sim$ 7.9 g cm^{-3} and Ni $\sim$ 8.9 g cm^{-3}, respectively)(Graham *et al*., 2001; Moussi *et al*., 2005, Grün *et al*., 2019).

Interplanetary dust is so ubiquitous within the solar system that it produces a phenomenon called the Zodiacal light, which can be observed with the naked eye in favourable conditions. This is seen as a diffuse white cone of light that extends from the sun along the ecliptic, resulting from the scattering of sunlight by dust particles in the interplanetary medium (Weinberg & Sparrow, 1978). Observations of the Zodiacal light including spectroscopic and polarimetric measurements allow information about the properties of the dust within the Zodiacal cloud to be inferred, such as the size, composition, morphology, and spatial density (Koschny *et al.*, 2019; Leinert *et al*., 1998). Approximately 40,000 tonnes of interplanetary dust is accumulated by Earth each year (Love & Brownlee, 1993). Although a large percentage of this dust is vaporised as it enters the atmosphere a considerable mass of particles reach the surface, which are known as micrometeorites. When collected in the Earth's stratosphere, these particles are known as interplanetary dust particles (IDPs), and both provide a source of cosmic dust that can be studied in the laboratory (Wozniakiewicz, 2017) .

2.2.2 Origins of Interplanetary Dust

The predominant sources of interplanetary dust are thought to be minor solar system bodies, i.e., asteroids and comets (Grün *et al.*, 2001; Wozniakiewicz, 2017; Grün *et al*., 2019). Thus, interplanetary dust has significant scientific value, providing insight into the conditions, constituents, and processes taking place on these bodies, as well as providing a history of the processes taking place in the early solar system. These relatively fragile minor

planetary bodies produce dust particles as a result of impacts, collisions, and the release of binding volatiles (such as volatile species including O_2 and N_2 species trapped in ices). Most asteroids orbit within the main asteroid belt located between Mars and Jupiter. Collisions between asteroids result in meteoroids and dust particles being ejected at velocities that cause their orbits to leave this region, making them a significant source of dust. Asteroid breakups are evidenced by asteroid families, i.e. groups of asteroids that have very similar orbital elements implying a common origin in their past, generated from the breakup of larger asteroids (Hirayama, 1923; Grün *et al*., 2019). As well as break-up events, even sub-critical impacts can produce significant amounts of dust. NASA's Double Asteroid Redirection Test (DART) spacecraft which impacted Dimorphos in the Didymos system can be used as an example (Fig. 2.1 from Rivkin & Cheng, 2023). Although an experiment to test planetary defence capabilities for redirecting near-Earth objects that pose a threat to humanity, the impact can be considered an analogue to an asteroid-on-asteroid collision and gives an appreciation of the amount of ejecta produced in such an event that would contribute to the interplanetary dust population.

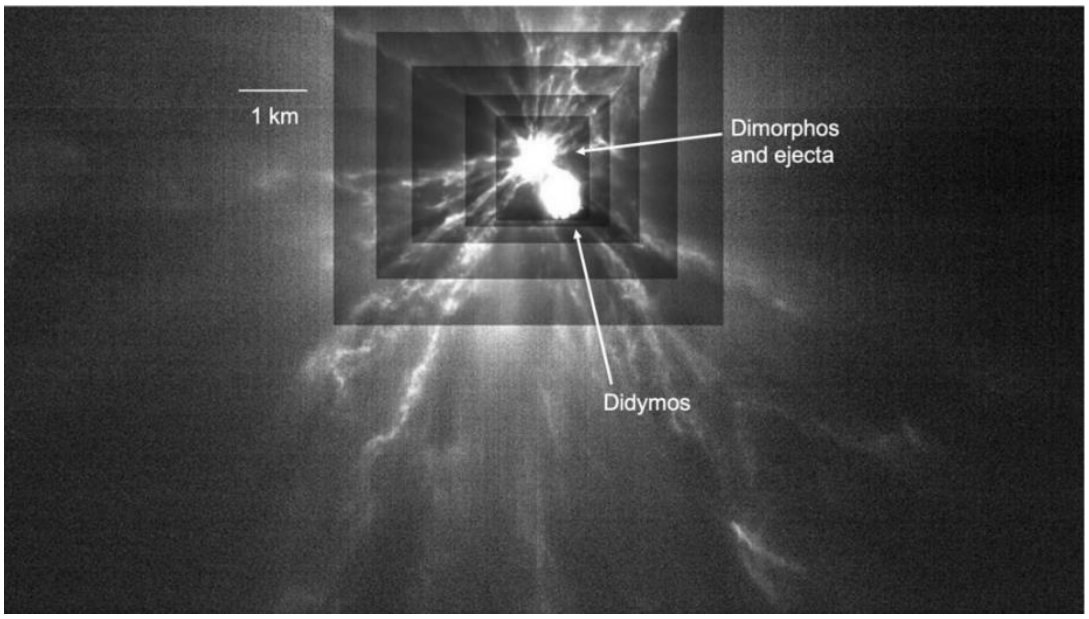

Fig. 2.1: A monochrome image taken from the accompanying LICIACube CubeSat of the Didymos system after the DART impact into Dimorphos. Filaments of ejecta can be seen emanating from the impact as bright streaks. The contrast of the image has been increased with each larger box to make all ejecta appear the same brightness in the image. An estimated 1 km scale bar has been included. Reproduced from Rivkin & Cheng, 2023.

Comets can have highly elliptical orbits that take them from the cold far reaches of the solar system, to close approaches to the sun at their perihelion. As icy bodies pass close to the sun, volatiles can sublimate, carrying with them solid particles. Solar radiation pressure then causes smaller particles to be moved away from the parent body, and similarly their

ejection velocities can cause their orbit to disperse from that of their parents over time (Koschny *et al*., 2019). A body, typically a comet, that continuously releases particles forms a trail that follows the orbit of the parent (Fig. 2.2). There are two tails, the dust tail that is slightly curved (driven by radiation pressure), and the ion tail that is tinged blue in the figure and points directly away from the sun in a very straight line (driven by the solar wind). Eventually, these are dispersed by non-gravitational forces - such as radiative forces (Burns *et al*., 1979), including the Poynting-Robertson effect (Robertson, 1937), and the Yarkovsky effect - forming a meteoroid stream. A stream entering the Earth's atmosphere produces a large density of meteors, in an event known as a meteor shower and can be a re-occurring annual event. Other sources of interplanetary dust include impacts causing ejecta on other solid bodies, such as the moon and outer solar system Kuiper belt objects (Horányi *et al*., 2014). Some of the dust, even in the inner solar system, can even have an interstellar origin. Such grains are distinguishable by their small size, hyperbolic orbits and fast velocities, offering insight into processes in the interstellar region (Dorschner, 2001; Draine, 2003; Strub *et al*., 2019).

Fig 2.2: Comet 1P/Halley, taken by W. Liller, Easter Island, part of the International Halley Watch (IHW) Large Scale Phenomena Network, March 8, 1986. Dust particles emitted from the nucleus form a tail that extends from left to right in the image (Bell, E. V., NSSDCA).

2.3 Orbital Debris

The term orbital debris is used in this work to define the anthropogenic (i.e. caused by humans or their activity) debris in orbit around the Earth, to distinguish it from space debris which some authors use to include cosmic dust. Ever since the first human activities in

space, the population of orbital debris has been increasing significantly (Fig. 2.3). In recent years the sudden increase in growth of tracked objects can be attributed to the increased supply and demand of commercial launch and space services, as well as improvements in tracking technologies. There is another factor contributing to the increase shown in Fig. 2.3 from 2015. Since 2015, a change in policy has seen previously excluded 'unidentified' (UI) objects now included in ESA's space object tracking catalogue. Unidentified objects are defined as those that cannot be traced back to a launch event and whose nature cannot be identified (ESA Space Debris Office, 2023). With more and larger constellations of satellites being proposed and accepted by licensing agencies for launch, the outlook for orbital debris is that it is set to increase at an even greater rate.

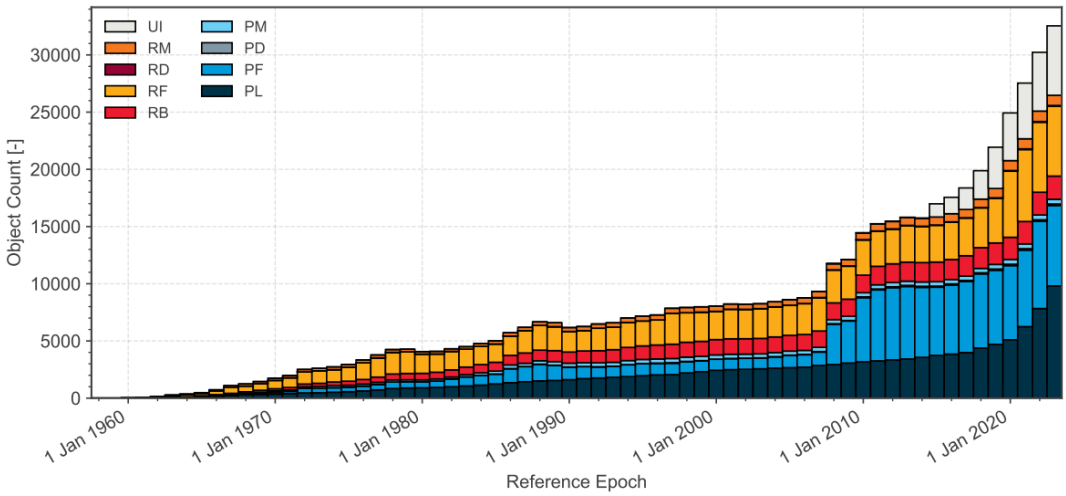

Fig. 2.3: Evolution of the number of tracked objects in Earth-orbit by class: UI – unidentified, RM – rocket mission related object, RD – rocket debris, RF – rocket fragmentation debris, RB – rocket body, PM – payload mission related object, PD – payload debris, PF – payload fragmentation debris, PL – payload. Reproduced from (ESA Space Debris Office, 2023).

2.3.1 Orbital Debris Sources

The primary sources of orbital debris < 1 mm in size are solid rocket motor (SRM) firings (producing SRM dust and slag composed of aluminium oxide (Al_2O_3) particles), impact ejecta, and surface degradation (including paint flakes). For debris > 1 mm the primary sources are explosion/fragmentation and collision events. In total, there are eight main populations of debris in Earth-orbit, including (Horstmann *et al*., 2020):

1. **Ejecta** - originating in hypervelocity impacts from natural space dust and orbital debris impacts into spacecraft. Ejecta is predominantly comprised of small target material-derived particles, but also projectile remnants.

2. **Paint Flakes** - caused by the degradation of spacecraft surface coatings from atomic oxygen, thermal cycling and ultraviolet radiation.
3. **SRM Dust** - small Al_2O_3 particles, typically spheres, which are produced by the reaction of oxygen with aluminium added to the propellant to reduce burn instabilities, and exhausted during SRM burns.
4. **SRM Slag -** larger fragments of Al_2O_3 produced in a slag pool in the motor and more commonly exhausted at the end of a SRM burn.
5. **Sodium-potassium (NaK) Droplets -** NaK alloy NaK-78, used as coolant in the Buk nuclear reactors aboard the Radar Ocean Reconnaissance Satellite (RORSAT) spacecraft, was ejected into space from 16 RORSAT satellites producing NaK droplets. Two leak events from the TOPAZ reactors, aboard Cosmos-1818 and Cosmos-1867, have also added to the population of NaK droplets in low Earth orbit (LEO) (Matney, 2019).
6. **Multi-Layer Insulation (MLI) -** with two main production mechanisms, fragmentation events and degradation related delamination.
7. **Explosion/Fragmentation and Collision Fragments -** particles originating from spacecraft fragmentation and collision events. Such events produce large quantities of small < 1 mm particles as well as a smaller number of larger debris objects. The NASA hypervelocity impact experiment to replicate a catastrophic fragmentation event of a 56 kg spacecraft (DebriSat) showed that there are five main shapes of debris produced in fragmentation events. These shapes include; straight and bent needle/rod/cylinder, flat and bent plates, and nugget/spheroid/parallelepiped (Cowardin *et al.*, 2021). Spontaneous fragmentation events can occur, for example if a piece debris were to impact a pressurised tank, propellant tank, or battery. Although, more noteworthy causes of fragmentation include accidental collisions such as the Iridium 33 – Cosmos 2251 collision in 2009, and intentional destruction such as the Fengyun-1C Chinese anti-satellite missile test in 2007. A table of the ten most significant break ups that occurred before 2016 is shown in Table 2.1.
8. **Launch and Mission Related Objects (LMRO)** - describe the large objects related to launch and space missions, including operational and dysfunctional satellites, upper rocket body stages etc. that are intact, i.e.

have not experienced a collision or fragmentation event that would see them classed as a fragment.

The size range covered by each of these populations and the meteoroid background population is shown in Fig. 2.4 (Horstmann *et al.,* 2022). Typical debris materials include aluminium, aluminium oxide, steel, titanium, and carbon fibre (Graham *et al*., 2001; Moussi *et al*., 2005).

Table 2.1: Top ten in orbit breakup events before 2016, ranked according to the number of catalogued debris produced. Here RB stand for Rocket Body, IC Intentional Collision, AC Accidental Collision, AE Accidental Explosion, and UN unknown. Modified from (NASA, 2016).

Rank	Satellite/ Object	Year of Breakup	Altitude of Breakup	Catalogued Debris Produced	Cause of Breakup
1	Fengyun-1C	2007	850	3428	IC
2	Cosmos 2251	2009	790	1668	AC
3	STEP-2 RB	1996	625	754	AE
4	Iridium 33	2009	790	628	AC
5	Cosmos 2421	2008	410	509	UN
6	SPOT-1 RB	1986	805	498	AE
7	OV2-1/LCS 2 RB	1965	740	473	AE
8	CBERS 1/SACI 1 RB	2000	740	431	AE
9	Nimbus 4 RB	1970	1075	376	AE
10	TES RB	2001	670	372	AE

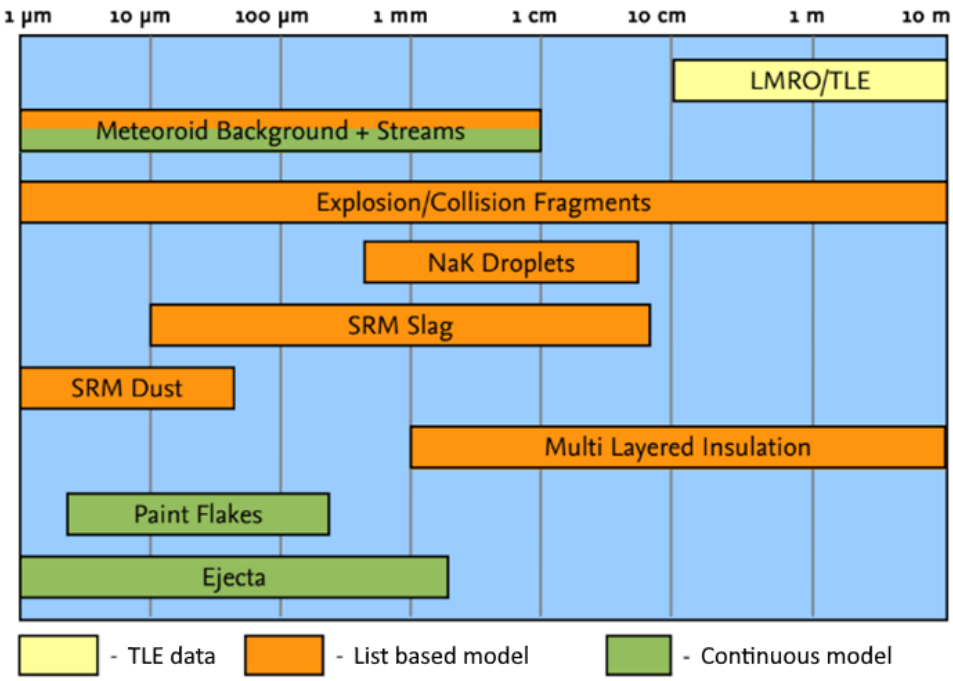

Fig. 2.4: The size regime for each population of orbital debris, with the corresponding method for determining the quantity/spatial density for each population in the ESA's MASTER model marked by colour. LMRO stand for Launch and Mission Related Objects, TLE for Two Line Element, and SRM for Solid Rocket Motor. Reproduced from (Horstmann et al., 2022).

2.3.2 Risks from Orbital Debris

Due to the large impact speeds of orbital debris, with mean impact speeds in LEO of 10 km s^{-1} and as high as 14 km s^{-1} for sun-synchronous polar orbiting spacecraft (Hamilton *et al.*, 2017), even mm-sized debris can cause fatal damage. This is also true for interplanetary dust that have even larger mean impact speeds (which can extend up to 15 km s^{-1} - 20 km s^{-1}). An example of the damage produced by a 1 mm diameter stainless steel 420 (StSt420), a particular grade/alloy of stainless steel, sphere impacting a 3.15 mm thick aluminium plate at only 4.5 km s^{-1} is shown in Fig. 2.5a. A penetration hole from a 1.5 mm diameter soda-lime glass sphere (a silicate, 2.5 g cm^{-3}) impacting a 3.15 mm aluminium plate at 4.0 km s^{-1} is shown in Fig. 2.5b for comparison. Such significant damage and penetration can be catastrophic if it hits, for example, electronics, a pressure vessel (Schafer & Schneider, 1997) or a fuel tank. Indeed, the resulting debris cloud can cause further damage as it passes into the interior of the spacecraft. This coupled with the relatively large population, and inability to track and avoid mm-sized debris gives it the largest mission ending threat of all debris (NASA, 2021).

The only way to mitigate against something that cannot be tracked is to shield against it. For smaller debris less than a few hundred μm, a few mm of aluminium armour plating is sufficient. However, as impactor size scales up, thicker and thicker aluminium plating cannot simply be added as shielding due to its mass (since excess mass can cause launch difficulties and impact on cost) and potential effects on other spacecraft design constraints, e.g. the overall charge state of the spacecraft, and thermal consideration. Instead, a range of shielding designs and technologies are employed, e.g. the Whipple shield (Whipple, 1947) or honeycomb core sandwich panels (Warren *et al*., 2021). The Whipple shield first proposed by Fred Whipple has arguably the most flight heritage of any design. The design consists of a first layer of a material (typically aluminium) of a similar thickness to the impactor that is being shielded against. This is known as the 'bumper' layer or shield, with a stand-off distance from the surface of the spacecraft or a second further layer of shielding (Fig. 2.6 and Fig. 2.7). The working principle is that the impact with the first layer disrupts the impactor, leading to multiple smaller fragments that carry less momentum and energy, and that can be wholly absorbed and shielded against by subsequent layers. Honeycomb sandwich panels work off a similar principle to the Whipple shield, with an internal honeycomb material stiffening the overall structure to help make it rigid. A further elaboration is the "stuffed" Whipple shield, which has the interstitial space filled with a material to arrest the disrupted projectile and bumper layer. More recently composite materials such as Carbon Fibre Reinforced Plastic (CFRP) are being investigated for their applications to spacecraft shielding (e.g. Taylor *et al*., 1997; Lamontagne *et al*., 2001; Higashide *et al*., 2015; He & Chen, 2023). To develop adequate spacecraft shielding and ascertain what degree of shielding is required for spacecraft in different orbits, an understanding of the distribution of orbital debris and the threat that it poses is required. A crucial first step in understanding this population and quantifying its threat is to collect data on this population, for which we need detectors.

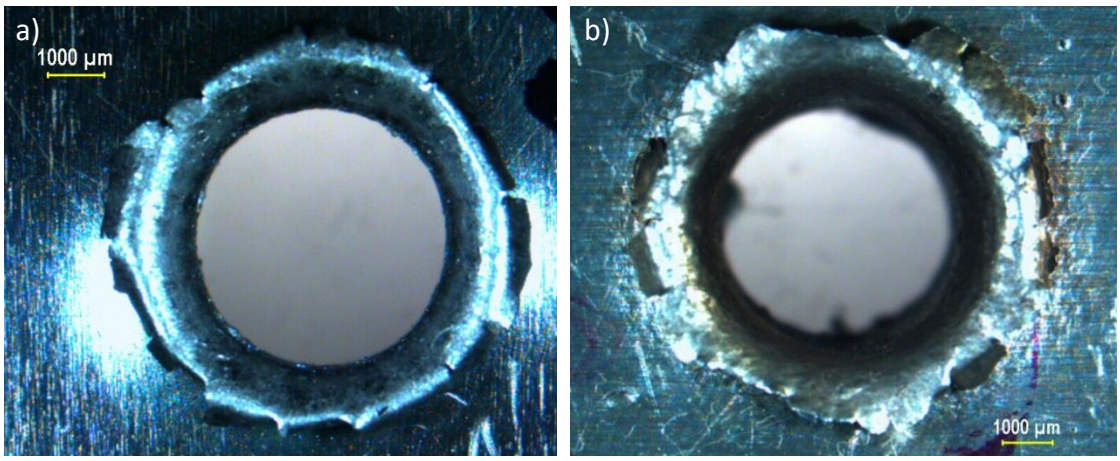

Fig. 2.5: (a) The damage produced by a 1 mm stainless steel sphere impacting a 3.15 mm thick aluminium plate at 4.5 km s^{-1}. The projectile wholly penetrated the plate leaving a 4.42 ± 0.01 mm diameter penetration hole. (b) The damages produced by a 1.5 mm soda-lime glass sphere impacting a 3.15 mm thick aluminium plate at 4.0 km s^{-1}. The penetration hole had a diameter of 4.46 ± 0.02 mm.

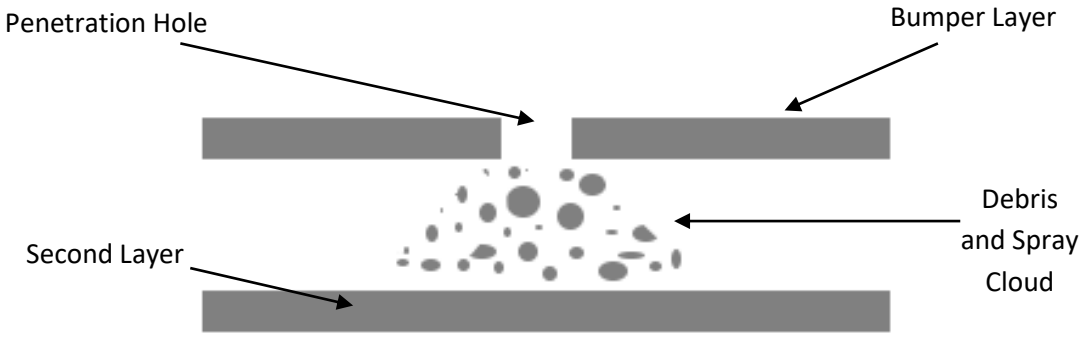

Fig. 2.6: Schematic of the Whipple shield design and principle. An impactor that penetrates the first layer is disrupted to produce a cloud of target and projectile material debris and ejecta, which carries less momentum and energy, and is easier for the second layer to wholly absorb.

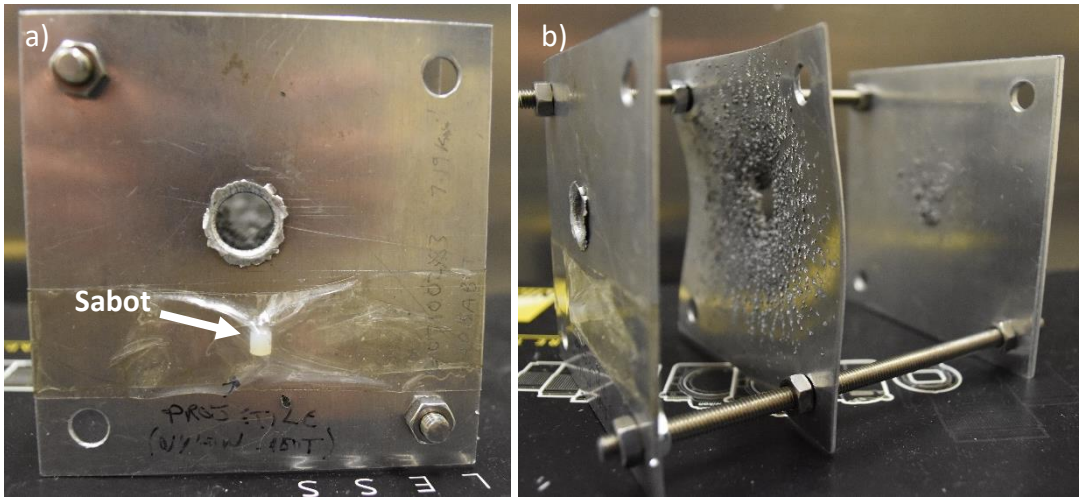

Fig. 2.7: An example of the Whipple shield design, previously impacted at Kent by a 4.3 mm diameter solid nylon sabot at 7.19 km s^{-1}. (a) Face on view showing the 12 ± 1 mm penetration hole in the front 1.5 mm thick aluminium plate, and an example of the sabot that created it. (b) Side view showing the impacts in the second 1.5 mm thick aluminium plate from the spray produced by the disrupted projectile and removed target material. Any debris that penetrated the second plate was wholly absorbed and stopped by the third 3.0 mm thick aluminium plate.

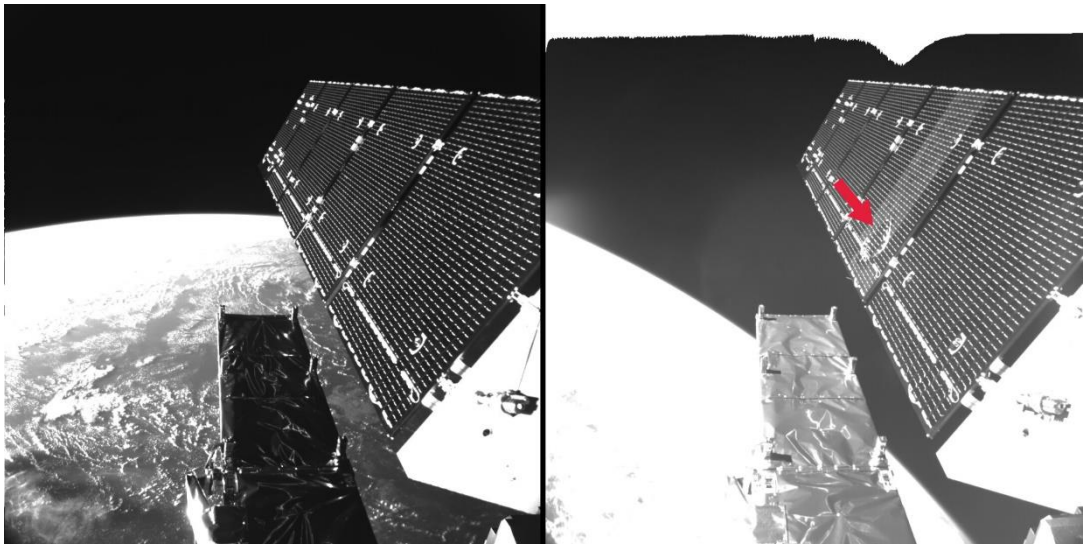

Fig. 2.8: Sentinal-1A solar array before (left) and after (right) an impact by a ~ 1 cm particle at ~ 11 km s^{-1}. The damage area indicated by the red arrow had a ~ 40 cm diameter. (ESA, 2016).

Debris of a few centimetres in size causes much greater damage and cannot be shielded against. One example of such an impact is the impact into the Sentinal-1A solar array reported by Krag *et al*., (2017). The piece of debris was estimated to be ~ 1 cm in size and

likely impacted at the average speed of 11 km s^{-1} for a spacecraft in a Sentinel-1A like orbit. This resulted in an impact damage feature measuring ~ 40 cm in diameter (Fig. 2.8), causing a permanent partial loss of power, and appreciably changing the 2-ton satellite's orbit and altitude.

Even tracked debris can still cause collisional damage, if the quantity and quality of measurements of the debris and satellites two line elements (TLE's) are low, resulting in a false negative conjunction, or if the satellite is unpowered and cannot perform evasive manoeuvres. Typically, a warning of a predicted conjunction within a few km is enough to warrant evasive manoeuvres for high risk and/or important satellites. Such a collision is believed to have occurred in 1996 between the CERISE microsatellite and a catalogued piece of debris from the explosion of the third stage of an Ariane V16 rocket body (Alby *et al*., 1997). The outcome was a close conjunction between the satellite and piece of debris, resulting in an attitude and altitude change in both the debris and satellite, and the production of a third trackable piece of debris. Consequently, CERISE began tumbling as part of the gravity gradient boom had been severed in the likely collision. Ultimately, CERISE was re-stabilised using the onboard magnetorquers and novel magnetic control algorithms (Sweeting *et al*., 2004).

2.3.3 Measurement and Quantification

While objects ≥ 10 cm can be easily tracked from Earth with telescopes and radar, this is not the case for smaller objects (Liou *et al*., 2015). Ground based radar observations can be used to detect debris down to ~ 3 mm in LEO, however, at this size individual debris is un-trackable. Instead ground based radar statistically sample the population by maintaining fixed pointing angles and detecting objects that pass through their field of view. The only way of detecting particles < 3 mm in size is with space-based detectors, referred to as in-situ detectors.

Broadly, there are two main types of in-situ detectors. The first of these, referred to as 'passive' detectors, are deployed in space, simply left to be impacted by particles, and then retrieved to be studied in the laboratory. These include returned space exposed surfaces, such as: the Long Duration Exposure Facility (LDEF) specifically placed in orbit to measure the effects of the space environment on materials (O'Neal & Burton Lightner, 1991), the EUropean REtrievable CArrier (EURECA) spacecraft (Drolshagen *et al.*, 1996), returned solar

panels from the Hubble Space Telescope (HST) (Drolshagen *et al*., 1997), and the Space Transportation System (STS) also known as the space shuttle (Bernhard *et al*., 1997). One advantage of these systems, is the large area of the returned surfaces and, except for the STS, the long exposure times, which combined give flux measurements even for the larger particles. However, these are rare missions, with none in recent years, so the resulting flux data are no longer current.

The second type are 'active' detectors, which measure particle characteristics in real-time and transmit the data to Earth. Monitoring the evolution of the debris environment with time is crucial for understanding and supporting efforts to address the problem of orbital debris in space sustainability. For this application, active detectors are favoured for their time stamped data and speed of data availability (i.e. not having to wait for a retrieval mission), and as such this thesis focuses on the development of active detectors. There are issues with such detectors, they tend to be more complex in design, and usually have only a small active area. As a result of the added complexity of in-situ measurements, including providing a detection area large enough to collect a representative sample of impacts, current data on the debris flux in LEO for the size range of a few 100 µm to a few mm is uncertain or outdated, leaving the flux poorly constrained (Wozniakiewicz & Burchell, 2019). Thus, detectors capable of measuring the sub-mm and mm sized populations are required, now more than ever considering the rapidly increasing debris population.

Observations of individual small debris particles cannot alone provide sufficient understanding of this population and its distribution to inform future space mission design and sustainability initiatives. Not only does this sample a small percentage of the population, but continued production of orbital debris particles, and the constant evolution and decay of existing orbital debris, means that methods for predicting the future population are also required. To make future predictions and provide a more complete picture of the small-scale orbital debris environment, modelling is employed. The two main software tools for this are the Meteoroid and Space Debris Terrestrial Environment Reference (MASTER) model (developed and maintained by the European Space Agency, ESA (Horstmann *et al*., 2020; Braun *et al*., 2021)), and the Orbital Debris Engineering Model (ORDEM) (developed and maintained by the National Aeronautics and Space Administration, NASA (Vavrin *et al*., 2019)). Both models are similar at a high level, concerning function and development. They start by producing a debris population based on data for intact spacecraft and breakup/source models applied to catalogued events, and then simulate its evolution and distribution (Horstmann *et al*., 2021). A full description of

the MASTER Model is given in Chapter 6. The main differences between MASTER and ORDEM is that MASTER is an event-based model that uses the validation data collected by observations and detectors to reweight the modelled events. ORDEM on the other hand, is a data-driven model that uses validation data to reweight the modelled populations (Krisko *et al*., 2015; Horstmann *et al*., 2021). There is also some variation in the validation data used for each model, and the output from MASTER is in terms of source, while the output from ORDEM is in terms of density. Data from these models can be used in mission analysis software, such as ESA's Debris Risk Assessment and Mitigation Analysis (DRAMA) software available at https://sdup.esoc.esa.int/ (accessed 10/05/2023), and ESABase2 available at https://esabase2.net (accessed 10/05/2023), to assist with mission design.

2.4 Past Detectors

Active dust detectors have been flown in space since the dawn of the space age, initially to identify the risk to spacecraft from cosmic dust and then to detect cosmic dust at various locations in the solar system (Grün, 2001). Detectors can be based on a variety of different detection techniques. For example: acoustic (piezoelectric) detection of the acoustic waves generated by the impact of a particle on a surface acoustic (e.g. the 'Impact Sensor' subsystem of the Grain Impact Analyser and Dust Accumulator (GIADA) instrument flown aboard the Rosetta mission to Comet 67P (Sordini *et al*., 2018)), plasma detection using charged electrodes to measure the charged particles produced in the plasma created by a particle impact on a target material (e.g. such as the Impact Plasma and Momentum subsystem of the Dust Impact Detection System (DIDSY-IPM) flown aboard the Giotto probe to comet 1P/Halley (McDonnell, 1987)), or a combination of several techniques such as the Debris In-Orbit Evaluator (DEBIE) dust detector, which employed both of the preceding methods to measure the dust flux for micron sized particles in LEO (Schwanethal *et al*., 2005). Bauer *et al*., 2014 provides a convenient review of different detectors.

One consideration for detectors in orbit is how to distinguish between orbital debris impacts and interplanetary dust impacts. One method is to examine residue at the impact site. Elements characteristic of interplanetary dust include Mg, Si, Fe, S, and Ni, while debris is primarily dominated by Al (Wozniakiewicz, 2017), thus it is possible to distinguish between the two populations using the composition. However, this is more readily applied to passive detectors where the residue can be examined in the laboratory back on Earth,

whereas an active detector would require a mass spectrometer to be incorporated into the detector design. Thus in space itself, the most effective way of differentiating between the two populations is considering the impact speed and trajectory of the incident particle, to determine whether it matches that of a debris particle ($\sim$ 7 km s^{-1} to 14 km s^{-1}) or an interplanetary dust particle in an unbound orbit (i.e. a hyperbolic trajectory originating from interplanetary space) and with larger impact speeds of typically $\sim$ 15 km s^{-1} to 20 km s^{-1} (Burchell *et al*., 2013). Accordingly, time of flight (TOF) style detectors with their speed and direction determination capabilities are popular for applications as space dust and debris detectors, with many designs previously flown in space missions (Table 2.2). Subsequently, there has been recent research by among others NASA and the Japanese Space Agency (JAXA) into developing new TOF detectors (e.g. Burchell *et al*., 2013; Liou *et al*., 2015; Nakamura *et al*., 2015; Hamilton *et al*., 2017; De Simone *et al*., 2019; Schimmerohn *et al*., 2021; Cornwell *et al*., 2023). All these detectors feature either the use of 12.5 µm thick polyimide films and/or the use of acoustic detection for impactor speed determination.

Table 2.2: Examples of past time of flight space dust and debris detectors flown aboard space missions, and the type of detection used.

Mission	Detector	Detector Type	Reference
Pioneer 8 and 9 solar orbiters and the Lunar Ejecta	Cosmic Dust Detector (CDD)	Two layers of ionisation film grid and rear piezoelectric (acoustic) plate	Berg 1969
Lunar Ejecta and Meteorites (LEAM) to collect meteorites and lunar eject on the moon	CDD	Two layers of ionisation film grid and rear piezoelectric (acoustic) plate	Berg 1973
The Earth Orbiting Advanced Research and Global Observation Satellite (ARGOS) in LEO	SPAce DUSt (SPADUS)	Two layers of polyvinylidene fluoride film that produce a charge response upon impact	Tuzzolino *et al*., 2001
Cassini to sample dust in interplanetary space and the saturnian environment	Cosmic Dust Analyzer (CDM)	Two layers of charge grid, and ionisation detector	Srama *et al.,* 2004
Attitude Related Manoeuvres And Debris Instrument in Low (L) Orbit (ARMADILLO)	Piezoelectric Dust Detector (PDD)	1st ionisation mesh, followed by a charged mesh and final piezoelectric plate/ionisation target for TOF measurement	Brumbaugh *et al*., 2012

2.5 The Debris Resistive Acoustic Grid Orbital NASA-Navy Sensor

One of these detectors under development, and that was indeed deployed in LEO on the International Space Station (ISS) (altitude ~ 400 km) as the Space Debris Sensor (SDS) detector in January 2018 (Hamilton *et al*., 2017; Anz-Meador *et al.*, 2019), is the Debris Resistive Acoustic Grid Orbital NASA-Navy Sensor (DRAGONS) (Burchell *et al*., 2013; J.-C. Liou *et al*., 2015). SDS was planned for a 2-year mission, during which time it would collect data on the dust and debris environment in the size range of 50 µm to 500 µm to act as a proof-of-concept mission. Although, large impactors approaching the mm scale could be detected, the likelihood of a detection of these lower flux particles with the 1 m^2 detection area of the SDS in the 2-year time frame was deemed unlikely. Unfortunately, due to electronics and communications failures SDS was only operational for 26 days (Anz-Meador *et al*., 2019). In this time the SDS detected five likely impact candidates ranging from an estimated 30 µm to 110 µm in size. This enabled the demonstration of in-flight impact detection, time of impact detection, and location determination. Unfortunately, none of these were large enough to penetrate the first layer intact and reach the second layer. Thus, due to successive layers not being impacted, an in-flight demonstration of the determination of impactor direction, speed, and density (from energy) was not possible. Similarly, particle size measurements using the resistive gird could not be demonstrated (Anz-Meador *et al*., 2019). DRAGONS was developed by NASA'S Orbital Debris Programme Office (ODPO). The University of Kent Centre for Astrophysics and Planetary Science has been supporting DRAGONS development as a contractor for ~ 10 years and the work related to thin film TOF detectors presented in this thesis was carried out for the development of DRAGONS.

The design and working principle of DRAGONS is illustrated in Fig. 2.9 (Hamilton *et al.*, 2017). It consists of two 12.5 µm polyimide Kapton film layers separated by a known distance (0.15 m for the SDS model) and a third solid backstop. Each of the three layers of the detector are equipped with four polyvinylidene fluoride (PVDF) acoustic sensors that determine the time of particle impact. Using three of these sensors and their relative impact times, triangulation of the impact location can be determined in a process known as multilateration (Corsaro *et al*., 2016), with the fourth sensor acting as a redundancy. The first Kapton film of the SDS model of DRAGONS was also equipped with 75 µm wide resistive lines that can measure impactor size from the change in resistance produced by the severing of these lines. Comparing impact locations on subsequent films allows the

determination of the impactor's trajectory, which can be used, in combination with the host spacecrafts attitude, to infer the impact direction. Applying the TOF method, the difference in time between the impacts on the first and second films can be used in conjunction with the known separation to determine impactor speed, using the relation that speed is equal to distance over time. The combination of impact speed and direction, provides the orbit estimate (providing the orientation of the detector is known). The final backstop, which absorbs all of the impactor's kinetic energy, can estimate impact energy from the amplitude of the measured acoustic signals, thus allowing estimates of impactor mass. This, combined with the size measured on the resistive grid, provides an estimate of density. Before launch the SDS model of DRAGONS achieved performance of ~ 80 mm average deviation for location determination and ~ 18% average deviation for speed determination (Hamilton *et al.*, 2017). Thus, there is room for significant improvement in speed determination for DRAGONS.

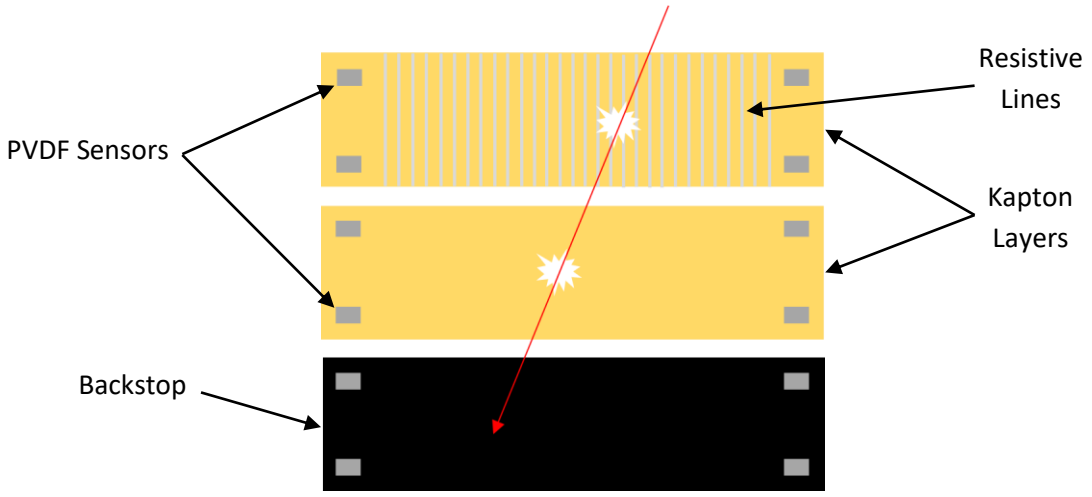

Fig. 2.9: Schematic of the Debris Resistive Acoustic Grid Orbital NASA-Navy Sensor (DRAGONS) detector. The red line depicts the path of an incident projectile. Multiple Kapton layers are used for time of flight (TOF) speed determination. Resistive lines on the first film provide impactor size determination. Multiple PVDF sensors are used for time of impact and location determination. The backstop plate is used for energy measurement and density estimation.

2.6 Old Space *vs.* New Space

A change is currently taking place in the space industry, from what is known as 'old space' to 'new space'. In the old model for the space industry there was the moto 'it has to be right first time'. As a result, during planning, space missions underwent extensive research, development, and rigorous testing. This coupled with expensive components led to space missions being very time consuming and costly, and as such the space industry was dominated by national space agencies. By contrast, in the new space model there is a larger

appetite for risk (assuming it does not include human space flight), whereby missions (telecommunications satellites, etc.) are developed cheaper, on shorter time scales, with the model being that of launching more but accepting there will be a higher failure rate. This has been further compounded by the ever-increasing reliance on technology and communication of modern society, and the emergence of commercial launch providers (e.g. SpaceX), providing more frequent and cheaper access to space. In fact, the new model for space can be exemplified by the development of SpaceX's Starship launch vehicle/spacecraft. Models SN8, SN9 and SN11 all experienced catastrophic failure during flight tests, and the latest model SN20 (integrated with the Super Heavy Rocket stage) also experiencing a "rapid unscheduled disassembly" (Todd, 2023) mid-flight, but was labelled as a successful learning experience by SpaceX. While the value of the lessons learned in the development process, which has always existed and experienced failures, cannot be understated, this "flight test until it is successful" approach represents the new space model, not the old space model.

Unfortunately, the new space model itself is inherently not sustainable, and places greater pressure and importance on the orbital debris problem. However, to offset this and head towards a more sustainable future, both policy and industry goals are placing ever-increasing importance on space sustainability. This has led to the development of sustainable technologies, such as reusable lower rocket stages (e.g. SpaceX's self-landing Falcon 9 lower rocket stage), and reformed regulations and practices. In 2007 the Inter-Agency Space Debris Coordination committee (IADC) recommended that all spacecraft in LEO must de-orbit within 25 years of the end of their mission, with this the current requirement to meet ESA's space sustainability compliance regulations. A recent (29/09/2022) regulatory change by the United Sates of America's Federal Communications Commission (FCC) has seen this time frame reduced to 5 years for US-licensed satellites and those licensed elsewhere that wish to enter the US market. Such policies and interest have allowed a whole branch dedicated to space sustainability to develop in the industry, with companies that look to offer debris removal (e.g. Astroscale, and ClearSpace), in-orbit servicing, and refuelling (e.g. OrbitFab) as services.

As with computers and the smart-phone revolution, the miniaturisation of technology has driven a particular change in new space known as the 'small satellite revolution', where for many applications, small and relatively cheap satellites are increasingly being chosen over the more traditional larger satellites. Nanosatellites (satellites with a mass ≤ 10 kg) are

becoming particularly popular, due to the improved launch availability for such small satellites in rideshare opportunities, and the modular design standard of the CubeSat. To reduce costs, CubeSats must conform to criteria governing their form factor and mass. This is achieved with the standardised CubeSat unit, known as a 'U'. Each 1U is a cube with 10 cm edges (i.e. 10 cm × 10 cm × 10 cm, volume 1,000 cm^3) with an associated mass of originally typically 1 kg but more recently up to 2 kg (California Polytechnic State University, 2017, 2022).

Common CubeSat sizes are 1U, 1.5U, 3U, and 6U; with a typical mass of 1 kg, 1.5 kg, 3 kg, and 6 kg, respectively. The standardisation of CubeSats allows companies, such as NanoAvionics and AAC Clyde Space, to produce 'commercial off the shelf' (COTS) CubeSat buses and components. These factors make CubeSats relatively cheap to produce and quick to market/launch, thus increasing accessibility to space, and embodying the essence of new space. Unfortunately, ease of access to space coupled with often relatively short operational lifetimes (typically < 5 years, while their orbit lifetimes follow those of debris objects at different altitudes, outlined in the introduction, with the same considerations) and a lack of end-of-life de-orbiting strategies, has given CubeSats a bad reputation for being "space junk" i.e. contributing to the concerning levels of orbital debris. However, the move to using smaller satellites for many applications has made the development of CubeSat detectors and debris sensing missions an active area of research (e.g. see Table 2.3 for a review of recent CubeSat missions and detectors). Detectors under development include: e.Cube (Colombo *et al*., 2021), STRATHcube (Creed *et al*., 2021), Move-III (Oikonomidou *et al.*, 2022), and the Dust Impact Sensor and Counter (DISC) due to fly on the Comet Interceptor mission in 2029 that uses a piezoelectric (acoustic) plate based on the GIADA sensor (Della Corte *et al*., 2021; Della Corte and others 2023). Thus, CubeSats can support solutions to space sustainability.

To provide meaningful statistical data, in-situ detectors need detection areas large enough to ensure that they sample a representative number of particles within their mission lifetime. For a 3-year mission at an altitude of 700-1000 km, a 1 m^2 detection area with an optimal pointing direction is considered a minimum (Hamilton *et al*., 2017). Other proposed detectors aimed to have even larger detection areas e.g. the Large Area Debris Collector (LAD-C) (Liou *et al.*, 2006), proposed with an area of 10 m^2. To provide large enough detection areas, without employing detection area increasing technologies, the accumulation of area over multiple CubeSats would be required. Thus, the use of CubeSats

for debris and dust flux measurement is posed with an important question: Will the accumulation of detection area over many individual CubeSats lead to statistically meaningful data?

Table 2.3: A review of recent CubeSat sized detectors and CubeSat missions for orbital debris and cosmic dust detection.

Mission	Detector	Detector Type	Reference
Horyu-II, a technology demonstration nanosatellite 2012	The space dust impacts detector	Resistive grid, 90 mm X 90 mm, ~ 30 g, and cost ~ €200.00	(Faure *et al*., 2013)
Flown on TechnoSat in 2017, due to fly on CompactSat in 2024	The SOLar panel based Impact Detector (SOLID)	Solar panel substrate mounted Resistive grid	(Bauer *et al*., 2014, 2016; Bauer, 2021)
The 3U CubeSat ARMADILLO, 2019 - 2022	PDD	1st ionisation mesh, followed by a charged mesh and final piezoelectric plate/ionisation target for TOF measurement	(Brumbaugh *et al*., 2012; Mcdonald, 2022)
'Austrian Debris Detection Low Earth (orbit) Reconnoiter' (ADLER-1) 3U CubeSat 2022 - current	Austrian Particle Impact Detector (APID) and a PL2/CW radar	APID – piezoelectric plate Radar for mm and sub-mm particle detection at ~ 100 m	(Groemer & Stumptner, 2021; Austrian Space Forum, 2023)
ADLER-2 6U CubeSat 04/2023 - current	APID-2 and An enhanced radar	APID-2 – Ceramic piezoelectric sensor and a Continuous-wave radar	(Austrain Space Forum, 2023)

2.7 Hypervelocity Impacts

The large speeds on the order of km s^{-1} involved in impacts between orbiting bodies tends to lead to impacts that enter the hypervelocity regime, wherein the impact speed exceeds the sound speed in both target and impactor materials. This occurs for the majority of materials for impacts above approximately 2 - 3 km s^{-1} and so impacts in excess of these speed are commonly known as hypervelocity impacts (Burchell *et al*., 1999). Fechtig *et al*.

(1978) gives a good overview of the impact processes involved in hypervelocity impacts, which are discussed below.

2.7.1 Initial partition of Energy: Contact and Compression

During a hypervelocity impact, the initial transfer of energy from the projectile to the target takes place during the contact and compression stage. During this stage, both the impactor and target are rapidly compressed, which produces shockwaves in both materials as the impactor pushes target material out of the way (Collins *et al*., 2012). For large targets this leads to the cratering process, which is discussed here. By contrast, thinner targets can experience varying degrees of penetration, where the rear of the target fails, which is discussed with relevance to detector design and development in Section 2.8.

The energy transfer can be considered using a one-dimensional model (Fig. 2.10), with the conservation of mass, momentum, and energy across a shock wave described by the Rankine-Hugoniot equations Eq. 2.1 to Eq. 2.3 (Ahrens, 1993; Ahrens & Johnson, 1994):

$$\rho_1 = \rho_0 \frac{(U_s - u_0)}{(U_s - u_1)}, \tag{2.1}$$

$$\mathrm{P}_1 - \mathrm{P}_0 = \rho_0 (u_1 - u_0)(U_s - u_0), \tag{2.2}$$

$$\mathrm{E}_1 - \mathrm{E}_0 = \frac{1}{2}(\mathrm{P}_1 + \mathrm{P}_0)\left(\frac{1}{\rho_0} - \frac{1}{\rho_1}\right) = \frac{1}{2}(u_1 - u_0)^2. \tag{2.3}$$

Here U_s = shock velocity, u = particle velocity, ρ = density, P = pressure, and E = internal energy per unit mass (specific energy). Subscripts 0 and 1 refer to the unshocked and shocked states in front of and behind the shock front. The total energy imparted into the target is equally divided between the internal energy and the kinetic energy (Eq. 2.3).

There is another relation between these parameters that describes the state on either side of the shock front, the Hugoniot curve (Fig.2.11), which links the jump in pressure ($P - P_0$) to the change in specific volume ($V_1 - V_0$) across the shock front. Note $V = 1/\rho$. Individual points along the Hugoniot are not successively achieved during a shock, this curve instead represents the locus of shock states corresponding to a specific initial state. The initial and shocked (Hugoniot) state are joined by a straight line called a Rayleigh line (Ahrens & Johnson, 1994). Another curve that describes the expansion of the compressed material is the Isentrope. From these two curves and the Rayleigh line, the increase in specific internal energy corresponds to the area of the triangle ABC, and the area below the Isentrope BCD

is equal to the elastic energy used in the expansion. The difference between these two energies represents the thermal energy lost to irreversible heating (Fechtig *et al*., 1978).

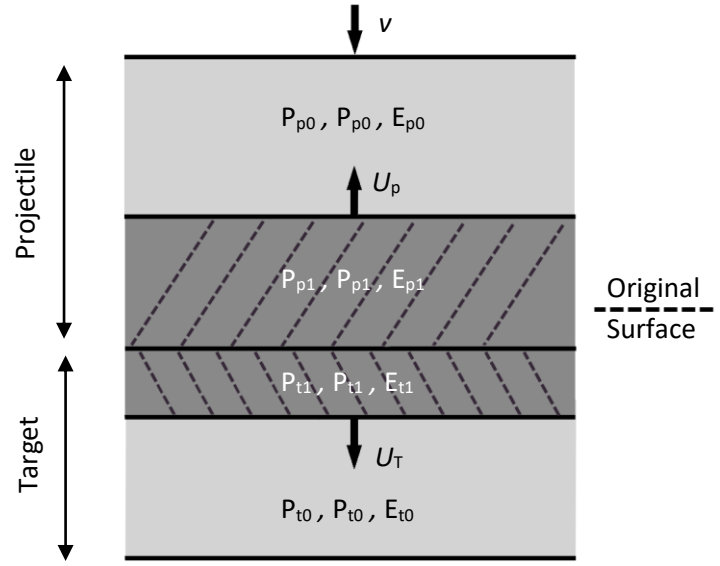

Fig. 2.10: Schematic of the one-dimensional impact model. *v* = impact velocity, *U* = shock velocity, P = Pressure, E = internal energy. Subscripts p = projectile, t = target, 0 = uncompressed material, 1 = compressed material. The original target surface height is shown to the right. (Fetchtig *et al*., 1978)

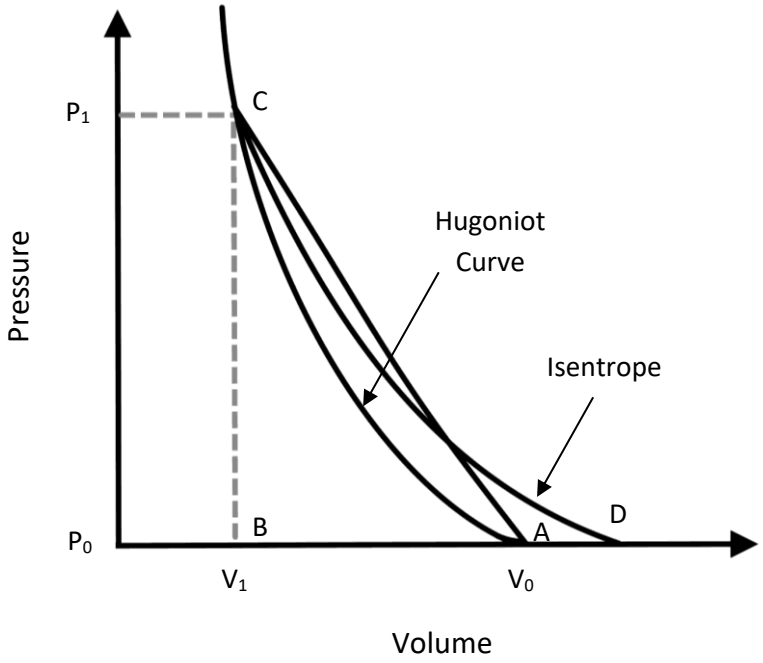

Fig. 2.11: Hugoniot Curve schematic. P = pressure, V = Volume. Subscripts 0 and 1 are the uncompressed and compressed states respectively. Area of the triangle ABC = the increase in specific internal energy. Area below the Isentrope BCD = the elastic energy used in the expansion. (Fetchtig *et al.*, 1978)

2.7.1.1 Shockwaves

Shockwaves propagating in most materials, that have not undergone a significant phase change, can often be described by a linear shockwave equation of state:

$$U_s = c_0 + Su \tag{2.4}$$

Where u is the particle velocity behind the shock front, S is an empirical constant and c_0 is the ambient pressure bulk sound speed given by:

$$c_0 = \sqrt{\frac{K_0}{\rho_0}} = \sqrt{{c_L}^2 - \frac{4}{3}{c_S}^2}\ , \tag{2.5}$$

where K_0 is the isentropic bulk modulus, c_L the longitudinal sound speed, and c_S the shear sound speed (Marsh, 1980; Wood *et al.,* 2017). Note that these sound speeds for the longitudinal and shear waves both have the same dependence on density and their respective modulus (longitudinal and shear modulus respectively) as c_0. However, as shown in Eq. 2.5, longitudinal elastic waves propagate faster than the bulk sound speed in a given material.

Below a certain pressure and strain, known as the Hugoniot Elastic Limit (HEL), the material undergoes elastic deformation, and the shock wave is a purely elastic wave traveling at the speed c_L. At stresses between the HEL and the strong shock limit the material begins to experience plastic deformation, in what is known as the elastic plastic region. For this region a two-wave structure is produced, an elastic precursor followed by a viscoelastic wave propagating at a slower speed. For the highest pressures the material enters the strong shock regime, or limit. Deformation is plastic and there is a single shock wave produced, which exceeds the speed of the elastic wave in the material (Graham, 1993). In the strong shock regime, when the shear strength of a material is overcome and the shock becomes overdriven, a material can exhibit hydrodynamic ('fluid -like') behaviour (Bourne & Bourne, 2022). In this regime the material begins to flow (hydrodynamic flow) much like a fluid, whilst still in the solid phase (Agu *et al.,* 2019).

As shock waves propagate through a medium, the peak pressure and peak particle velocity decreases roughly as $1/r^2$ as energy is lost through geometric spreading and attenuation, until it decays into a shock wave with an elastic precursor and then into an elastic wave (Melosh, 1989). While P drops behind the shock front, u remains at around 1/3 to 1/5 of its

peak value. After compressing the material, the shock wave will reach a free surface or zero-stress boundary at which point a rarefaction wave (also known as expansion, unloading, decompression, relief, and release waves) is set up. This wave is responsible for returning the material to ambient pressure, with material flow in the same direction as the pressure gradient, which is opposed to the direction of wave propagation (Boslough & Asay, 1993). Rarefaction wave speeds are generally so high that the rarefaction wave produced at the back of the projectile can overtake the shock wave propagating into the target. Their speed can be estimated using a Murnaghan-type equation of state, using the sound speed in the compressed material c_R, which is the rarefaction wave speed and is approximated by (Melosh, 1989):

$$c_R \approx \sqrt{\frac{(K_0 + n\mathrm{P})}{\rho}}, \tag{2.6}$$

Where:

$$n = 4S - 1\,. \tag{2.7}$$

Here c_R is in the rest frame of the target material and does not consider the residual particle velocity in the target material (u_t), which will further increase the speed of the rarefaction wave relative to the shockwave that is propagating into unshocked stationary material (i.e $c_R + u_t$ in the reference frame of the target). Once the rarefaction wave catches the main shock wave, the shock is rapidly attenuated. Note that the walls of a projectile are also free surfaces that set up rarefaction waves, and for spherical projectiles rarefaction waves can be produced at the time of contact.

2.7.1.2 Impact Pressure the Planar Impact Approximation

Calculating the pressure produced in an impact is not trivial. There are several methods for calculating the expected pressure produced in a hypervelocity impact, for example the 'late-stage effective energy' method, which takes into account projectile dimensions (Mizutani *et al.*, 1990; Parnell *et al.*, 2010). However, one of the most commonly used methods for estimating peak impact pressure is the planar impact approximation (Melosh, 1989). This considers the impact between an infinitely wide plate of projectile material with a thickness of the projectile diameter and an infinitely wide plate of target material. The main assumption is that after contact, both projectile and target are raised to the same

pressure and travel together with the same particle velocity, due to the projectile material not being able to interpenetrate the target material, and thus:

$$u_t = v - u_p \, . \tag{2.8}$$

The conditions between the shocks can then be calculated by applying the Hugoniot equations and relative equations of state, and the equality of particle velocity and pressure. Care must be taken to apply the Hugoniot equations in a reference frame at rest. Solutions to this approximation are not trivial. However, when both materials have linear equations of state the easiest solution can be found for u_t from (Melosh, 1989):

$$u_t = \frac{-B \pm \sqrt{B^2 - 4AC}}{2A} \quad . \tag{2.9}$$

Here:

$$A = \rho_{0T} S_T - \rho_{0p} S_p \, , \tag{2.10}$$

$$B = \rho_{0T} c_T + \rho_{0p} c_p + 2\rho_{0p} S_p v \, , \tag{2.11}$$

$$C = -\rho_{0p} v \left(c_p + S_p v \right) , \tag{2.12}$$

Where subscripts p and t donate projectile and target, respectively.

Other quantities can then be calculated using the Hugoniot equations and equation of state. The peak impact pressure (shock pressure) is calculated using Eq. 2.2 and Eq. 2.9 to Eq. 2.12 as (Collins *et al*., 2012)

$$\mathrm{P} = \rho_{0t} u_t (c_t + S_t u_t) \, . \tag{2.13}$$

The peak pressure in the target material occurs in an area just below the impact, known as the isobaric core, which is roughly the size of the projectile. Due to the assumptions made, this approximation only holds if the lateral dimensions of the projectile are small compared to the distance the shock has propagated, and provides an upper limit to the pressure expected in an impact event. For penetration of thin films, such as those studied in this thesis, shock pressures do not reach their peak values (Capaccioni & McDonnell, 1986), nor would the pressure exceed that required to penetrate the film. Thus, this formulation for pressure and means of calculating u_t and U_t does not apply for the Kapton films used in this thesis. Similarly, at speeds above $\sim$ 2 km s^{-1} the projectile will have already removed the

area of Kapton film shocked by the impact, before the shock wave would propagate into the rest of the Kapton film. It is then assumed that only small elastic strain waves from around the edge of the impact will propagate into the material. Thus, acoustic signals in the Kapton films will travel at a constant wave speed.

2.7.2 Cratering, Excavation and Ejecta

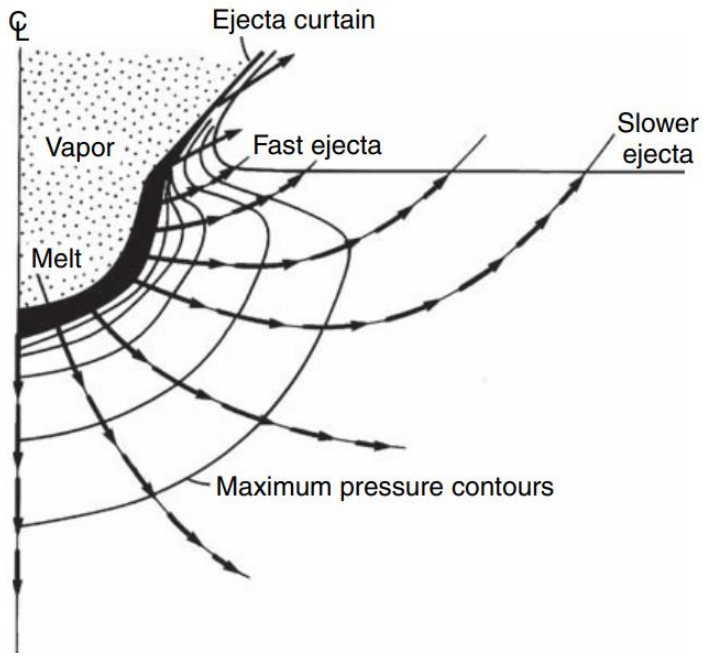

Fig. 2.12: Schematic of the excavation stage of the cratering process. The line on the left indicates the centre line of the crater. The lines with arrows represent streamtubes along which material flows downward and outward from the crater. The density of peak pressure contours intersected by a streamtube represent the max pressure of the shocked material. The location where stream tubes meet the surface represents the location of this material in the ejecta curtain. Ejecta emerging near the impact site travel at faster speeds than ejecta emerging at larger distances. Reproduced from Melosh, 2011.

When the rarefaction wave in the projectile reaches the projectile target boundary, releasing the pressure in the projectile, the contact and compression stage comes to an end. As the hemispherical shock wave (Walsh *et al.*, 1964) in the material continues to propagate, the residual particle velocity behind the shock wave excavates target material forming a crater. The excavation velocity field has a downward outward direction that ejects target material out of the crater at angles close to 45° at the rim, as ejecta Fig. 2.12 (Melosh, 2011). This ejecta has relatively low speeds, much slower than the shock wave velocity. Gault *et al*. (1963) found from aluminium projectile impacts into basalt targets that most of the slow speed ejecta was ejected at angles ≥ 50°, measured from the target surface

to the ejecta velocity vector. During the early stages of the contact phase, the fastest ejecta emanates from the projectile-target interface with very low (shallow) ejection angles. It can be travelling at speeds observed to be as much as three times the speed of the impact (Gault *et al*., 1963) in a process known as jetting.

Simple impact craters in ductile materials tend to be hemispherical or bowl shaped, depending on the target material and impact characteristics. However, more complex craters can form in the modification stage for larger impacts (above 2 – 3 km diameter craters on Earth) (Melosh, 2011; Melosh, 1989). Shortly after the excavation process has formed the crater, a change in the motion of the removed material within and beneath the crater takes place. Material starts to flow down and back towards to centre of the crater, lowering the rim wall and starting to help infill the crater. More infilling can occur as some of the more vertically launched ejecta lands within the crater. Finally, for the largest craters elastic rebound of the underlying compressed material may also play a role in changing the crater shape by producing a central peak (Melosh, 2011).

2.7.2.1 Oblique Impacts

In space the most likely/most frequent impact angle is 45° (a mathematical derivation of this quality is given in Pierrazzo & Melosh, (2000)), thus the study of oblique impacts is necessary. In oblique impacts the shockwave becomes weaker with decreasing impact angle (with the angle measured from the target surface to the impactor velocity vector) and becomes asymmetric, with the largest shock downrange of the projectile velocity vector (Pierrazzo & Melosh, 2000). For highly oblique incidence with low impact angles $\sim 10°$, there is an elongation of the crater diameter along the impactor velocity vector. Ejecta from the jetting phase of oblique impacts shows a preferential direction downrange (Melosh, 1989; Pierrazzo & Melosh, 2000).

2.7.3 Melting, Vaporisation, and Impact Ionisation/Light Flash

The large pressures and temperatures induced by the high energy of hypervelocity impacts easily break atomic bonds, leading to the melting (Pierazzo *et al*., 1997) and even evaporation/vaporisation of projectile and target material. For example, molten material is found as glass lining craters in lunar rocks produced by micrometeoroid impacts (Fechtig *et al*., 1978). Indeed, the elevated pressures and temperatures can be so great that they can cause vaporised material to ionize, producing positive and negative ions, and electrons in a

plasma cloud. The high internal pressure of the plasma cloud then causes it to expand into the surrounding area of low pressure. Ionisation from particle impacts is the principle employed by Ionisation detectors to detect microparticle impacts on metal target materials. The charge produced (Q) in such an impact can be described by the empirical law:

$$Q \sim mv^b, \tag{2.14}$$

Where m = mass and v = velocity. Various studies (Friichtenicht, 1964; Auer & Sitte, 1968; Adams & Smith, 1971; Dietzel *et al*., 1973) find the constant b to range from 2.6 to 3.5 (Fechtig *et al*., 1978), although later measurements suggested values in the range 3 to 5 (Burchell *et al*., 1999).

The expanding plasma cloud also emits light, the spectrum (different wavelengths) of which can be used to determine the effective plasma temperature (Eichhorn, 1976; Tsembelis *et al*., 2008). Observation of impact flashes have been used to probe hypervelocity impacts since as early as 1955 (Atkins, 1955), with studies of the light flash produced by microparticle impacts into metal targets also being conducted (e.g. Eichhorn, 1975, 1976). The energy of the light flash produced (E_{LF}) was found to relate to impactor mass (*m*) and velocity (*v*) according to:

$$\mathrm{E}_{FL} = Cm^a v^c\,, \tag{2.15}$$

Where C is a constant, a $\sim$ 1, and b $\sim$ 3. The absolute magnitude of the light flash was also found to be dependent on the ambient pressure, although constant below $\sim 10^{-3}$ mbar (see Burchell et al., 1996 for a more detailed review of light flash research and discussion of ionisation and light flash from hypervelocity impacts into water ice for example). Both the intensity of ionisation and light flash being proportional to approximately the third power of the impact velocity shows that both have a significant dependence on impact velocity.

2.8 Development of Thin Film Detectors

To determine results from many designs of passive detectors, including space exposed surfaces, the relationship between impactor and impact crater is required (McDonnell & Sullivan, 1992). To this end, many empirical crater scaling relationships have been developed, some of which are based on theory (e.g. Watts *et al*., 1993), but most on experiment (e.g. Cour-Palais, 1987; Hörz *et al.*, 1991). Empirical relations tend to be specific

to the materials and scales from which they are derived. Berthoud & Mandeville (1993) give a review of empirical impact equations for both cratering in large semi-infinite targets, and penetration in thin films, with a discussion of which equations are suited for applications to which target materials and size scales. Cratering relationships, such as the NASA meteoroid damage equation for metal plates (NASA, 1970; Berthoud & Mandeville, 1993):

$$\frac{\mathrm{P}_d}{d_p} = K_\infty {d_p}^{0.056} {\rho_p}^{0.519} v^{0.667} , \tag{2.16}$$

tend to be in terms of penetration depth (P_d) attained by a certain diameter projectile (d_p) impacting at a given speed (v), considering projectile and target properties such as projectile density (ρ_p) and a target material constant (K_∞) that can often be related to a material parameter, such as yield strength. For the NASA equation above, P_d and d_p are in cm, v is in km s^{-1}, ρ_p is in g cm^{-3}, and K is 0.4 for Al and 0.25 for stainless steel. From P_d, crater diameter (d_C) and other crater parameters can then be calculated using the relative formulae that relates P_d to d_C, etc.

Another impact feature observed in brittle materials that is often required for the interpretation of impact features on space exposed surface, is the conchoidal spallation diameter d_{CO} (Drolshagen *et al*., 1997). Under tensile stress caused by the uplifting of the central pit/crater, brittle materials exhibit conchoidal fracturing. The conchoidal zone shows both radial and circular features and usually determines the visual extent of an impact feature, extending to several times the distance of the original bowl shaped crater, e.g. Fig. 2.13, with the maximum damage diameter (d_{max}) usually referring to the damaged region slightly greater than the conchoidal fracture zone for small impacts (Drolshagen *et al.*, 1997).

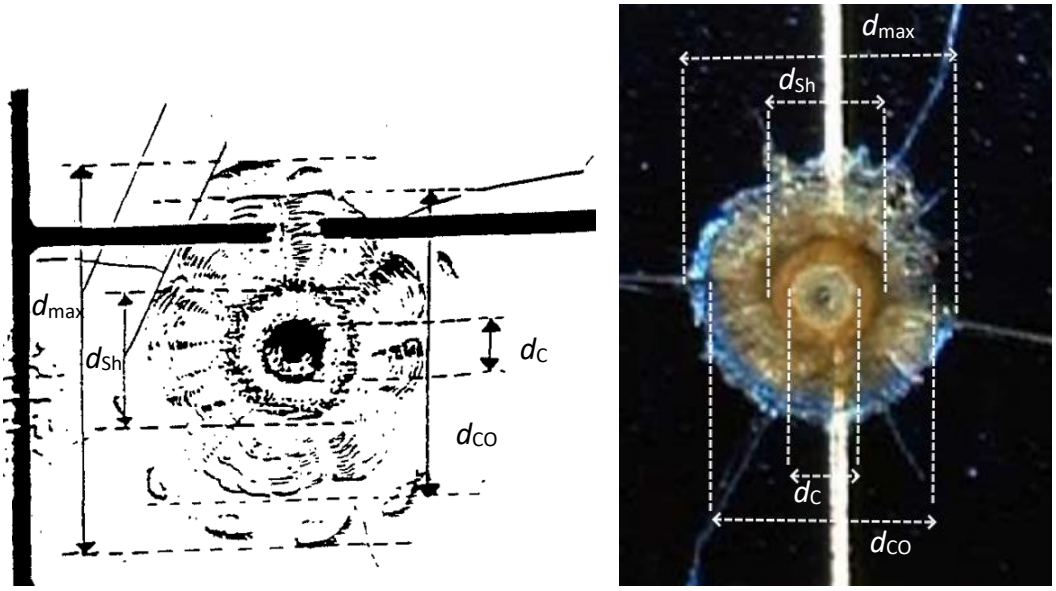

Fig. 2.13: Diagram of the impact features produced in a brittle target material shown on the left, and an impact feature on a Hubble Space Telescope solar array on the right. The diameter/extent of the d_C = crater, d_{sh} = shatter zone, d_{CO} = conchoidal fracture zone, and d_{max} = maximum damage features are shown. Figures modified from Drolshagen *et al*., 1997 and Moussi *et al*., 2005.

2.8.1 Penetration of Thin Films

As alluded to earlier, at some ratio of target thickness (T) to projectile diameter (T/d_p) known as the ballistic limit, the rear of the target will begin to fail and the projectile will begin to penetrate the target. A comprehensive study of this process was conducted by Hörz *et al*. (1994) using dimensionally scalled impacts of soda-lime glass spheres into Al 1100 targets at 6 km s^{-1}, with d_p ranging from 0.005 mm to 3.175 mm and T ranging from infinite half-spaced geometeries to 0.8 µm thick films. The change from the cratering process to the penetration process as a function of T/d_p is well described by Fig. 2.14 (Hörz, 2012). It was found that penetration holes were characterized by almost identical morphologies at equivalent T/d_p, no matter the size of the projectile. However, the relative hole diameter (d_h/d_p) decreases systematically with decreasing T/d_p, from as large as $d_h \approx 4d_p$ for thick targets to $d_h = d_p$ for thin films. A modest dependence on the absolute projectile size was observed, with the samllest projectiles producing comparatively small craters, yet relatively large penetration holes (Hörz *et al*., 1994). Larger mm-sized projectiles were more prone to fragmentation than small projectiles (suggesting that a shock-pulse duration in the projectile and target may be a useful approach), and the dispersion angle of the debris cloud was found to depend on T. An example of the ejecta

and debris cloud (both target and material) produced by a Cd sphere impacting a Cd plate at 5 km s^{-1} is presented in Fig. 2.15. Extensive images of the craters and penetration holes produced his work are shown within Hörz *et al*. (1994) making it an excellent compendium of source material. A similar study that scaled impact velocity from 1 – 7 km s^{-1}, as well as varying T, while keeping d_p constant, was also conducted by Hörz *et al*. (1995). They reported that $d_h = d_p$ was typically reached at $T/D_p < 1/50$ regardless of v, i.e. $d_h = d_p$ for $d_p >> T$. For $1/50 < d_p < 1$ the relation between d_h and v was complex, with variable exponents for v over a narrow interval in d_p/T, however, the general trend was that both D_h and D_c increased with increasing impact velocity.

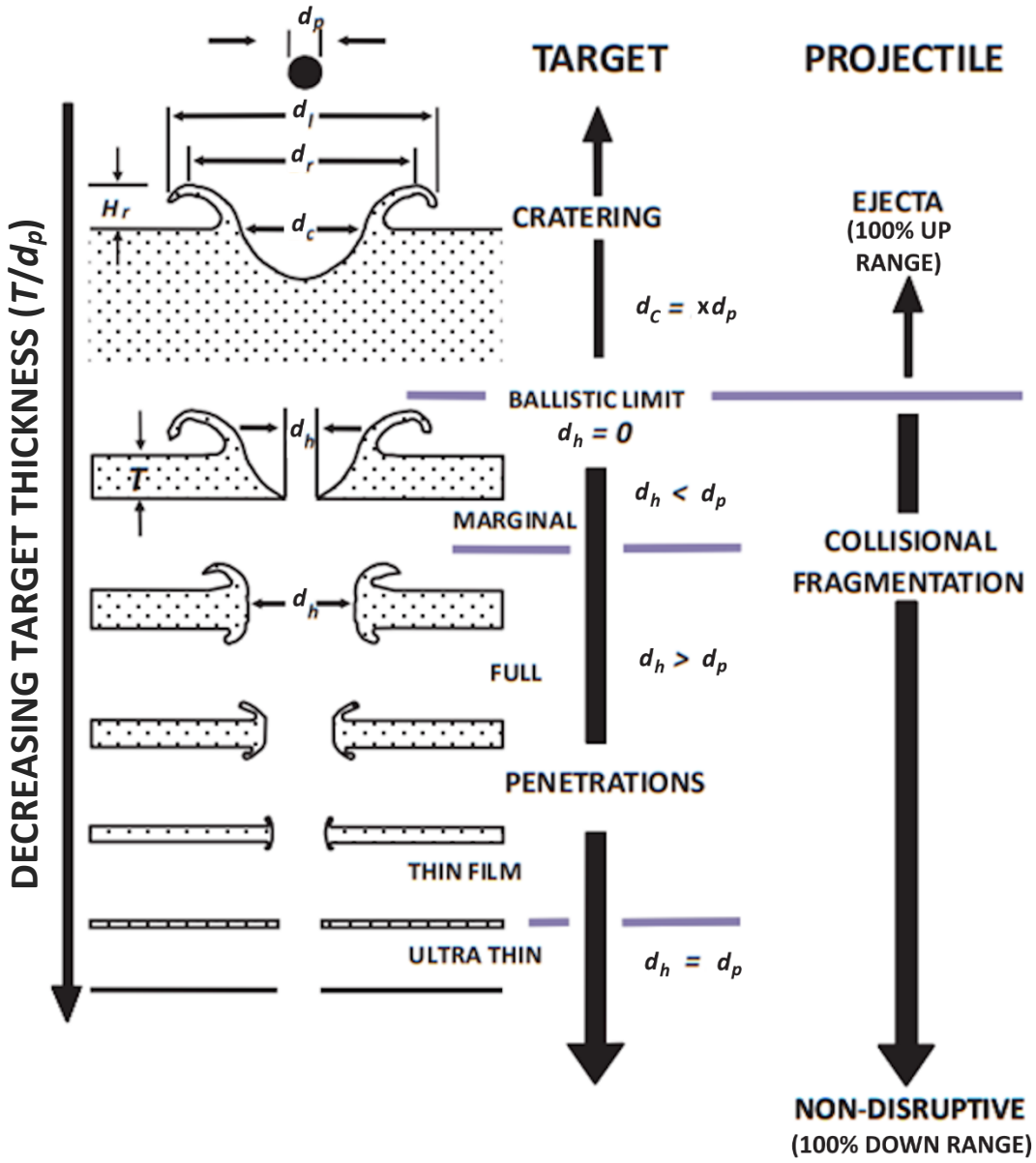

Fig. 2.14: Schematic for the evolution of cratering into penetration for impacts into increasingly thinner targets. Target and projectile fate for decreasing T/d_p is listed. T = film thickness, d_p = projectile diameter, d_l = outer lip diameter, d_r = rim diameter at highest point, d_c = crater diameter, H_r = rim height above the surface, X = constant. Modified from Hörz, 2012.

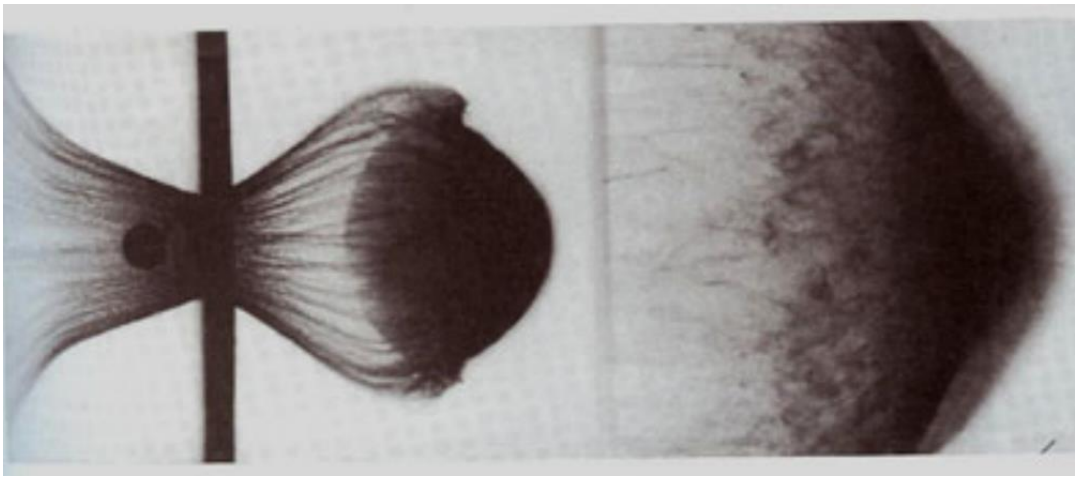

Fig. 2.15: X-ray shadowgraph of a Cd projectile impact into a Cd plate (target thickness/projectile diameter = 1/6) at 5 km s^{-1}. The image on the left is time stepped, with three x-ray tubes fired at subsequent times, onto the same film. Thus, all three images and time steps are superimposed onto the one image. The image to the right is a partial enlargement from a fourth tube that was taken slightly later to show the dispersion of the disrupted projectile. This shows the presence of a web of molten material. Reproduced from Hörz, 2012.

In a similar vein of research to that of cratering relations, is research into perforation limits, with applications to spacecraft shielding and the development of thin-film detectors (McDonnell, 1999). There has been much work in formulating relations that describe the penetration of plates/films, with perforation limit or ballistic limit equations (e.g. Fish & Summers, 1965; Pailer & Grün, 1980; Carey *et al*., 1985; McDonnell & Sullivan, 1992; Gardner *et al*., 1997; Christiansen & Kerr, 2001), the size of d_h i.e. hole growth equations (e.g. Carey *et al*., 1985; Gardner *et al*., 1997), and on projectile fate (e.g. Grün & Rauser, 1969; Pailer & Grün, 1980; Gwynn *et al*., 1997; Hörz, 2012), for given impactors and targets.

Ballistic limit equations such as that derived by Pailer and Grün (Pailer & Grün, 1980):

$$f_{BL} = \frac{1}{\varepsilon^{0.06}{\rho_t}^{0.50}} {m_p}^{0.40} (v cos\theta)^{0.88} {\rho_p}^{0.33}, \qquad (2.17)$$

usually describe the foil thickness at the ballistic limit (f_{BL}) of an impact by an impactor, characterised by the mass (m_p) or size of the impactor, and some constant, in this case described by material properties – here film (i.e. target) ductility (ε). Note that here $v$cosθ is the velocity component perpendicular ($v_\perp$) to the film, and ρ_t is the density of the target and ρ_p the projectile, with units in cm, g cm^{-3}, g, and km s^{-1}. Note that this relation was based on experiments with target materials ranging from plastics to stainless steel and gold, projectile masses ranging from 10^{-14} g to 1 g with densities from 0.9 g cm^{-3} to 19.3 g cm^{-3}, at impact speeds from $v_\perp \sim$ 1 km s^{-1} to 20 km s^{-1}. This data included both penetration and

cratering data, thus the relationship was intended as a general penetration formula that describes penetration thickness or crater depth over five orders of magnitude, from 10^{-5} cm to 1 cm, achieving accuracies of approximately 50 % (Pailer & Grün, 1980).

A study by Grün & Rauser (1969) on the penetration of Fe projectiles into thin films found similar results to Hörz *et al*. (1994). For relatively slow < 0.5 km s^{-1} impacts of Fe projectiles into Al films that only just penetrated the film, the penetration holes were of a comparable size to the particle diameter and the film was punched out leaving a flap of film, but not removed completely. For faster particles entering the hypervelocity impact regime, typical hypervelocity penetration holes were observed, with similar looking entrances and exits. At velocities above 2 km s^{-1}, $d_h > d_p$, by a factor governed by the film thickness and the velocity. d_h was found to be proportional to v and the normalised hole diameter, d_h/d_p, decreased with decreasing f. For very thin films and/or big projectiles, such that $d_p >> f$, $d_h/d_p = 1$ representing the ultra-thin film limit (Hörz, 2012). Similar behaviour was observed in Au films, and no deviation from $d_h/d_p = 1$ was observed for impacts into 1 µm carbon and 0.05 µm nitrocellulose films.

Hole penetration diameter formulae have a similar form to the cratering and ballistic limit formulae, with the inclusion of film thickness (f). For example, the equation for Fe projectiles into Al films from Carey et al. (1985) is:

$$\frac{d_h}{d_p} = 1 + 1.5\left(\frac{f}{d_p}\right)v^{0.3}\left[1 + \left(\frac{f}{d_p}\right)^2 v^{-n}\right]^{-1}, \qquad (2.18)$$

where n is:

$$n = 1.02 - 4e^{-0.9v^{0.9}} - 0.003(20 - v) \qquad (2.19)$$

for 2 km $s^{-1} < v < 20$ km s^{-1} and then n is constant (n = 1.02) for v > 20 km s^{-1}.

Neish & Kibe (2001) collected data on penetration holes in Kapton films for impacts at ~ 5 km s^{-1}, in the development of a damage equation for Kapton multi-layered insulation. Results for d_p were collected for d_h/f in the range $\sim 0.6 \leq d_h/f \leq 10$. Their results were found to fit a modified version of the Gardner *et al*. (1997) hole growth equation of the form (Neish & Kibe, 2001):

$$\frac{d_p}{f} = 0.337 + \frac{d_h}{f}\left[1 - 0.8912^{\frac{d_h}{f}+0.06502}\right]. \qquad (2.20)$$

A later study on the penetration of thin Kapton films, this time focusing on 12.5 µm thick films, was conducted by Nakamura *et al*. (2015). The majority of their data was collected at or above ~ 5 km s^{-1}, however, they noted that there was not an appreciable relation between d_h and v for impacts involving stainless steel 304 spheres (d_p = 309 µm) into 12.5 µm Kapton films at 2 km s^{-1} to 6.5 km s^{-1}. They found the relationship between d_p and d_h could be described by the formula:

$$d_p = 1.39^{-1}\, {d_h}^{1.28}. \tag{2.21}$$

They also reported the results for inclined incidence impacts from 90° to 15°, as measured from the target surface. At 60° the major-axis diameter (the axis of an ellipse with the largest diameter) was only ~ 6% larger than the diameter at 90° (d_{h90}). However, at 30° the major axis was ~ $2d_{h90}$ and at 15° ~ $4d_{h90}$, showing significant elongation with increasing angle of incidence. Note that the minor-axis diameter was comparable to d_{h90}.

To measure the projectile fate after penetration of a single film, witness plates are employed. These are usually highly polished metal plates positioned behind the film targets. For studies using multiple films, the projectile fate can be determined from subsequent films. Grün and Rauser (1969) studied the fate of iron projectiles at velocities of 4 km s^{-1} and 8 km s^{-1}. At 4 km s^{-1} particles of approximately 1 µm began to break up on impacting 0.8 µm Al-foils, and 0.1 µm Au films. Whereas, at 8 km s^{-1}, 1 µm particles broke up on impacting 0.5 µm Al-foils, and 0.1 µm Au films, with only a small amount of ablation for 0.2 µm Al films. The spray angles of projectile fragments in impacts at 8 km s^{-1} were 20° for 0.5 µm Al-films and 45° for 0.8 µm Al films, leading to a distribution of fragments over a circular area, with the larger fragments concentrated at the perimeter. Fe particles penetrating 0.1 µm carbon, and 0.05 µm nitrocellulose films showed no signs of disruption over the entire velocity and mass range studied.

Another relevant study concerned the fate of glass projectiles incident on PVDF films (Simpson & Tuzzolino, 1989). For f/d_p in the range 0.6 - 0.3, i.e. PVDF films (28 µm) about half the thickness of the projectile, they found fragmentation effects to be relatively mild, with the incident particle breaking into a few large fragments with a total mass approximately half the incident particle mass, and small spray angles < 3°. On the other hand, for penetrations of 6 µm films no disruption was observed. A single particle with a mass approximately equal to the incident mass, was observed to leave a single crater in the thicker witness film. They concluded that more than half of the particles impacting with

$m > 10^{-9}$ kg in the velocity range ~ 2-12 km s^{-1} will penetrate a thin 28 µm PVDF film without significant disruption/spallation.

2.8.2 Deceleration of Projectiles Penetrating Thin Films

As well as disruption and alteration of the projectile, the forces experienced during the interaction with the film can act to decelerate the projectile. To have a more accurate measure of the properties of the incident projectile an understanding of this process is required. Unlike the research into the penetration of films, there has not been a great deal of research concerning the deceleration of projectiles penetrating films, with only four studies giving a thorough treatment of the topic that could be found in the literature. The earliest of these studies was conducted in 1969 by Grün and Rauser (1969), and the most recent by Simpson and Tuzzolino (1989). A detailed review of these four studies on particle deceleration through thin films now follows.

The earliest study (Grün & Rauser, 1969) used a Van de Graaff accelerator to accelerate iron spheres with diameters of a few µm and masses in the range 10^{-10} g to 10^{-12} g to velocities ranging from 2 to 12 km s^{-1}. These projectiles were impacted into various films, including: Evaporated self-supporting Al and Au films that were 0.1 µm to 1 µm thick, 1 µm carbon films, and 0.05 µm nitrocellulose films. They found that their data could be summarised by the following empirical expression:

$$\frac{v_p}{v_i} = (1 + C_1 + C_2 m^a {v_i}^{2a+1})^{-1}. \quad (2.22)$$

Where v_i and v_p are the velocities (in cm s^{-1}) before and after penetrating the film respectively, m is the projectile mass (in g), and C_1 and C_2 are constants that are dependent on the film material. For the measured region, it was found that a was a function of the material only. In the case of the Al films, it was found that $a_{Al} = -0.5 \pm 0.05$, thus the velocity loss was independent of the incident velocity and could be expressed as a function of the particle mass over the entire velocity range. This was not the case for the Au films, with $a_{Au} = -0.85 \pm 0.09$, however, little more information on the deceleration produced by Au films was presented. It should be noted that, due to the nature of Van de Graaff accelerators (Fechtig et al., 1978), the mass of an accelerated particle is inversely proportional to its velocity according to $m \sim v^{-4}$, thus particles of larger velocity have smaller mass.

The relative velocity loss, velocity loss (Δv) over initial velocity, given by:

$$\frac{\Delta v}{v_i} = \frac{(v_i - v_p)}{v_i} \,, \tag{2.23}$$

for the biggest particles (10^{-10} g) penetrating the thinnest (0.2 µm) Al film was approximately 5%. Whilst $\Delta v/v_i$ for the smallest particles (10^{-12} g) penetrating the thickest (0.8 µm) Al films was approximately 30%, no measurable velocity loss was detected for the carbon and nitrocellulose films, hence any deceleration was smaller than the experimental error of 2%.

Another study by Pailer and Grün (1980), investigated the deceleration produced by the protective entrance film covering one of the sensors of the HELIOS micrometeoroid experiment (Dietzel *et al*., 1973) and the effect it has on particle detection. This film consisted of 0.3 µm of parylene coated with 0.075 µm of aluminium. Fe, Al, glass, and polyphenylene projectiles were accelerated using a Van de Graaff dust accelerator as summarised in Table 2.4. The magnitude of the deceleration was found to be correlated to particle density, with particles of greater density being decelerated less, as shown in Table 2.5. Absolute mass and angle of incidence also had a considerable effect on deceleration, with results for Fe projectiles with an angle of incidence 60° from perpendicular, summarised in Table 2.6. Comparing the 10^{-11} g results in Table 2.6 to the results for 10^{-11} g Fe in Table 2.5 shows that an angle of incidence of 60° leads to a factor of 2.25 increase in deceleration. Similarly, polyphenylene projectiles impacting at 60° were no longer detected behind the film suggesting that they experienced considerable deceleration to speeds below the 1 km s^{-1} threshold for the ionisation detector used, or they were stopped completely (Dietzel *et al*., 1973).

Table 2.4: Projectile parameters used in the Pailer and Grün (1980) thin film penetration study. Reproduced from Pailer and Grün (1980).

Projectile Material	Density (g cm^{-3})	Mass Range (g)	Speed Range (km s^{-1})
Iron	7.85	2 x10^{-10} – 5 x10^{-13}	1.4 – 13.3
Aluminium	2.7	4 x10^{-11} – 2 x10^{-12}	3.0 – 7.5
Glass	2.4	2 x10^{-10} – 6 x10^{-12}	1.5 – 4.2
Polyphenylene	1.25	5 x10^{-11} – 3 x10^{-13}	2.0 – 11.0

Table 2.5: Deceleration results for projectiles of different densities, all with mass = 10^{-11} g, v_i = 3 km s^{-1}, and perpendicular incidence (Pailer & Grün, 1980).

Projectile Material	Density (g cm^{-3})	$\frac{\Delta v}{v_i}$ (%)
Fe	7.85	4
Al	2.7	8
Glass	2.4	9
Polyphenylene	1.25	14

Table 2.6: Deceleration results for Fe projectiles of different masses and a 60° angle of incidence to the film (Pailer & Grün, 1980).

Projectile Material	Mass (kg)	$\frac{\Delta v}{v_1}$ (%)
Fe	10^{-10}	4
Fe	10^{-11}	9
Fe	10^{-12}	20

A later study by Capaccioni and McDonnell (1986) investigated the deceleration of Fe projectiles; with m in the range 3 x10^{-12} g to 1 x10^{-10} g, and v in the range 2.5 km s^{-1} to 5 km s^{-1} penetrating multiple mylar films, ρ = 1.39 g cm^{-3} and f = 2.4 µm, and single 5.4 µm films. Again, a Van de Graaff accelerator was used and therefore the study was also subject to the same condition as the previous studies, i.e. that faster projectiles had smaller masses. In agreement with the previous studies, $\Delta v/v_i$ over the entire velocity range was found to be a function of mass only. Maximum decelerations of $\Delta v/v_i \sim 70$ % were observed for projectiles with incident velocities of 5 km s^{-1} and mass of 5 x10^{-12} g penetrating two, and 8 x10^{-12} kg penetrating three mylar films, respectively. The smallest deceleration ($\sim$ 13 %) was recorded for a projectile of v_i = 2.5 km s^{-1} and m = 5 x10^{-11} g, impacting a single 2.4 µm mylar film.

Further to this, they compared their single film results to those of the two earlier studies described, focusing on the mass of the incident projectile and the mass of the film

intersected by the cross-sectional area of the projectile. Substantial agreement was found between the experimental data and scaling based on the conservation of momentum, according to:

$$\frac{v_i}{v_p} = 1 + \frac{m_f}{m_p}, \tag{2.24}$$

where m_f is the film mass and m_p the projectile mass, with discrepancies no greater than 20% for $m_f/m_p < 1$. Note that:

$$\frac{m_f}{m_p} = \frac{3\rho_f}{2\rho_p}\frac{f}{d}\,. \tag{2.25}$$

Similar to the calibration study for the HELIOS film; Simpson and Tuzzolino (1989) conducted a calibration experiment for their PVDF film based detector SPADUS (Tuzzolino *et al*., 2001). The experiment used a plasma drag accelerator to impact glass projectiles (ρ = 2.5 g cm^{-3}) in the mass ranges 5 x10^{-8} g to 1 x10^{-6} g and 9.3 x10^{-8} g to 4.8 x10^{-7} g, at 28 µm and 6 µm thick PVDF films, respectively, over a velocity range from 1.8 km s^{-1} to 12 km s^{-1}. These films had ~ 60 nm thick aluminium electrodes evaporated onto the front and back surfaces of the film (Simpson *et al*., 1989). Combined, these two electrodes represent an Al film 0.12 µm thick, ~ 0.4% the thickness of the 28 µm film and ~ 2% of the 6 µm film, and was considered negligible. It is worth mentioning that the Munich plasma gun accelerator used features a thin (< 0.1 µm), nitrocellulose film known as a Munich film, used to determine particle mass, that also produces negligible deceleration.

The results from the 28 µm PVDF film showed > 50% of projectiles were decelerated by less than ~ 20 %. While within experimental error, no deceleration was observed for projectiles penetrating the 6 µm films, i.e. $\Delta v/v_i$ < ~ 5%. In a later publication describing the SPADUS detector (Tuzzolino *et al*., 2001), it was admitted that the above study was not comprehensive enough to comprise a full calibration of the deceleration associated with detections for this detector. As a result, an approximate estimate based on conservation of momentum was used to determine v_i. This took the form of an expression that linked the initial velocity to the combined mass of the projectile and the sensor film removed upon penetration (Tuzzolino *et al*., 2001):

$$\frac{|v_p|}{|v_i|} = \left[1 + \frac{3}{2}\,G^2\,\frac{\rho_f}{\rho_p}\frac{f}{d_p}\right]^{-1}. \tag{2.26}$$

Here G is a constant relating particle and hole diameter, such that $d_h = Gd_p$. From the calibration data, G was taken as 1 for $f < 20$ µm. Differences between the values calculated from Eq. 2.26 and the limited calibration data, ranged from ~ 10% to a factor of ~ 2, representing only reasonable agreement and leading to an estimated uncertainty for SPADUS's velocity measurements as large as a factor of two.

In a similar study, although not a deceleration study, Burchell *et al*. (1998) mentioned deceleration in a study on the role of particle charge in impact ionisation. The study concerned iron spheres with a mass between 10^{-15} g to 10^{-10} g penetrating 50 nm thick cellulose films with a vacuum deposited 20 nm thick layer of gold-palladium. In these experiments, velocities were between 1 km s^{-1} and 5 km s^{-1}. No deceleration was measured (within experimental errors $\Delta v \sim 2$ %) in good agreement with all of the previous studies.

2.9 Conclusions

This chapter has introduced the origins of interplanetary dust and the reasons for its study. The different source populations of orbital debris have been introduced, along with the different methods for detection, and models used for predicting the populations of small un-trackable debris and future population trends. Due to their high impact speeds, both dust and debris of even mm-size can cause catastrophic damage to spacecraft. With the rapidly increasing number of debris objects in orbit, worsened by the new rapid launch culture that is making space more accessible, a better knowledge of the mm and sub-mm sized populations is required to quantify the threat that these un-trackable populations pose. This is required to enable the effective shielding of spacecraft missions, and to provide information on the evolution of the orbital debris environment to support solutions for space sustainability.

To measure the mm and sub-mm sized populations, in-situ debris detectors are required, with active detectors favoured for determining the time evolution of the population. The physics of the hypervelocity impact cratering process in semi-infinite targets was introduced for their use in decoding particle measurements from impact features on space exposed surfaces and passive detectors. Past active dust and debris detectors were then described, showing that TOF style detectors are favoured for their speed and trajectory determination, which allow for the distinction between orbital debris and interplanetary dust. Many of the TOF designs feature the use of thin films. The move towards using smaller satellites such as nanosatellites (≤ 10 kg) and CubeSats (that conform to the modular

CubeSat design) has seen the application of detectors to small satellite mission become an active area of research. An important question for the use of small area detectors, however, is whether the accumulation of a large enough area from multiple detectors will lead to meaningful data.

From the physical process taking place in hypervelocity impacts it is seen that at some ratio of film thickness to particle diameter, particles will be decelerated and/or be disrupted, causing inaccurate determination of incident impactor properties. Thus, for the development of specific thin film TOF detectors two important questions exist: Firstly, at what size do particles begin to be disrupted and will this affect the size range of interest? Secondly, if particles are decelerated before they are disrupted, what is the magnitude of deceleration? It should also be noted that compared to impacts on semi-infinite targets, the use of thin films in hypervelocity impacts is a relatively poorly studied field, and relies on several empirical studies for key observations and inferences.

Chapter 3: Experimental Equipment and Method

3.1 The Light Gas Gun

To test the cosmic dust and debris detector being developed within this thesis, it was necessary to simulate, in the laboratory, the kind of hypervelocity impacts that it will encounter in orbit around the Earth. There are several different types of apparatus that can be used to accelerate particles to the required speeds for hypervelocity impact research. These include: electrostatic dust accelerators (such as the 3 MV linear electrostatic dust accelerator at the Dust Accelerator Lab, University of Colorado Boulder), which can accelerate particles with masses from 10^{-15} g - 10^{-9} g to velocities of 0.5 km s^{-1} to 115 km s^{-1} (Shu *et al*., 2012), plasma accelerators, which can accelerate masses from 10^{-8} g - 10^{-4} g to velocities of up to 20 km s^{-1} (Schneider & Schäfer, 2001), and explosive 'shaped' charge accelerators, with performance characteristics ranging from accelerating projectiles of 8 g up to 4.5 km s^{-1}, and 0.08 g up to 16.5 km s^{-1} (Fechtig *et al*., 1978). However, a more versatile apparatus capable of accelerating clouds of µm sized projectiles as well as single mm and cm sized projectiles to velocities ranging from 1 – 8 km s^{-1} is the two-stage Light Gas Gun (LGG), first developed by Crozier in 1946 and Hume in the 1950s (Crozier & Hume, 1957; Tang *et al*., 2020).

Although first developed over seventy years ago (Crozier & Hume, 1957) there are still relatively few research active LGG facilities. Table 3.1 lists UK facilities that are currently research active, and the recent review by Rogers *et al*., 2022 gives a fuller account of facilities worldwide. One reason for the small number of facilities is due to the traditional LGG using explosives or gun powder to compress the light gas in the pump tube. These require specialist handling and storage and consequently LGG facilities take up a relatively large amount of space and are challenging to run within the university environment. This has led to a particular focus of research on producing LGGs that use an alternative to 'powder gas' (the hot gas produced by the ignition/burning of gunpowder) in the first stage. Examples include using the pressure differential between a pre-compressed gas in the first stage and the light gas in the second stage (e.g. Lamberson & Boettcher, 2018), and the combustion of flammable gases (e.g. Tang *et al*., 2020). However, powder gas driven first stages tend to attain higher projectile velocities and are still widely used.

Table 3.1: Research active Light Gas Gun facilities in the UK, with the bore (diameter of the launch tube barrel) and maximum (max) projectile velocity of each. The bore diameter for the Manchester gun could not be found. Modified from Rogers *et al*., 2022.

Facility	Bore (mm)	Max Velocity (km s^{-1})	Reference
University of Kent	4.5	8.4	(Hibbert *et al*., 2017)
Cranfield University	7.6	~ 7	(Wood *et al.*, 2017)
The Open University	4.7	~ 7	(McDonnell, 2006)
Imperial College London	10.0	4	(Jones *et al.*, 2014)
First Light Fusion (Oxford)	12.7	6.5	(Ringrose *et al*., 2017)
University of Manchester	-	2	(University of Manchester, 2023)

The two-stage LGG at the University of Kent is shown in Fig 3.1. It is capable of accelerating single projectiles from 0.1 – 3.0 mm in diameter to speeds of up to 8.4 km s^{-1}, and was used to collect the results described Chapters 4 and 5. The following discussion of the design and operation of LGGs uses the University of Kent's LGG to exemplify the general concept, as well as familiarise the reader with the specific setup used within this study.

Fig. 3.1: The Light Gas Gun in the University of Kent's Impact Facility. The gun starts with the powder chamber in the bottom left corner of the image and continues to the target chamber in the middle right of the image.

3.1.1 Design and Operation of LGGs

The basic principle of a traditional (two-stage) LGG is that a powder gas initially accelerates a piston that compresses a 'light gas' of low molecular mass (normally hydrogen or helium) in the pump tube. The gas is compressed until it reaches a pressure sufficient to rupture an aluminium 'burst' disc, and its sudden release from pressure, and ability to rapidly expand into the launch tube, is used to accelerate the desired projectile which sits within a sabot just the other side of the aluminium burst disc (Barker *et al*., 1993). The degree to which the gas is compressed dictates the speed achieved (with higher pressures generating greater acceleration) and can be controlled by scoring of the burst disc such that it ruptures at different pressures (as described later). Using the light gas to accelerate the projectile in this way removes the primary limiting factor for muzzle velocity in conventional guns, namely the relatively large molecular mass of the propellant powder gas (Crozier & Hume, 1957). Figure 3.2 and 3.3 show a schematic representation of the design and operation of the Kent LGG, with its individual components discussed in more detail below.

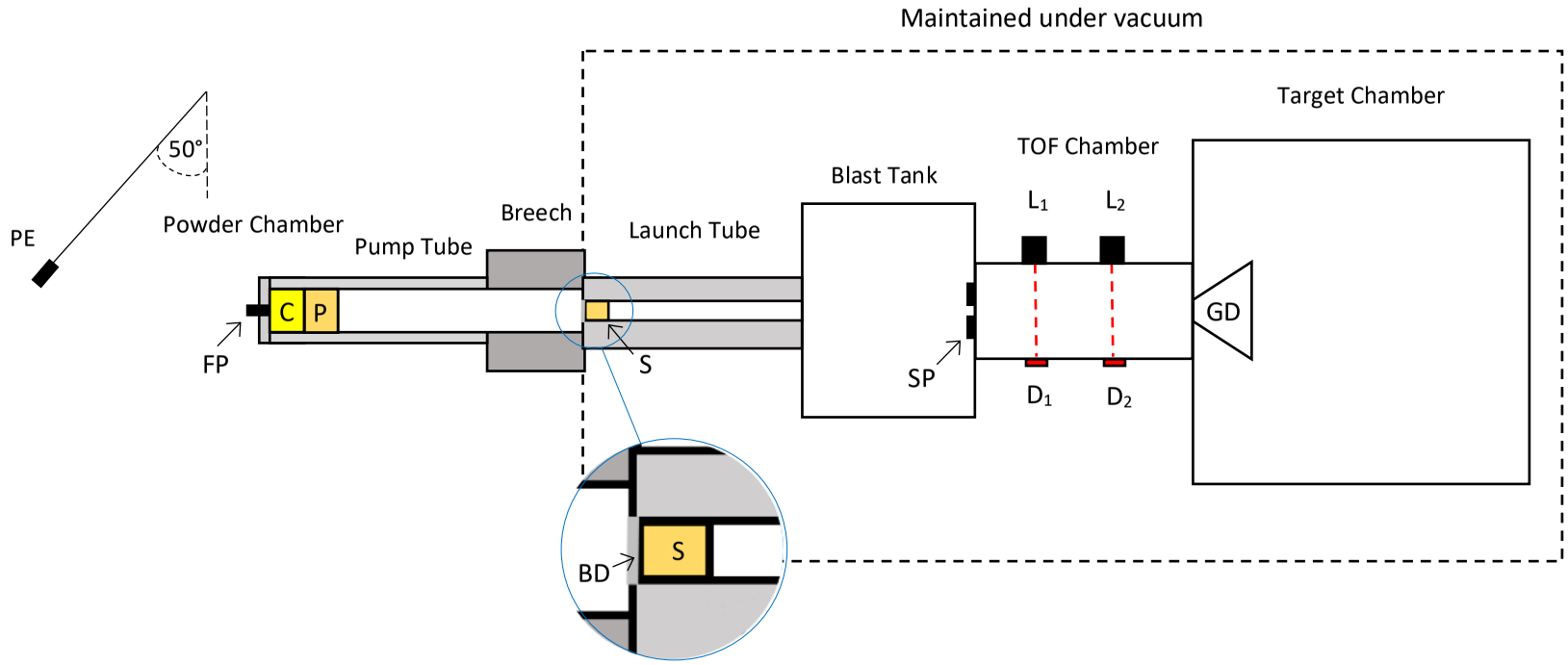

Fig. 3.2: A schematic representation of the University of Kent's light gas gun. The dashed line represents all of the components maintained under vacuum during operation. Modified from figure 8 in Burchell et al., 1999. List of acronyms:

PE – Pendulum	C – Cartridge	BD – Burst Disc	SP – Stop Plate	D_x – Photodiode
FP – Firing Pin	P – Piston	S – Sabot	L_x – Laser Diode	GD – Gas Diverter

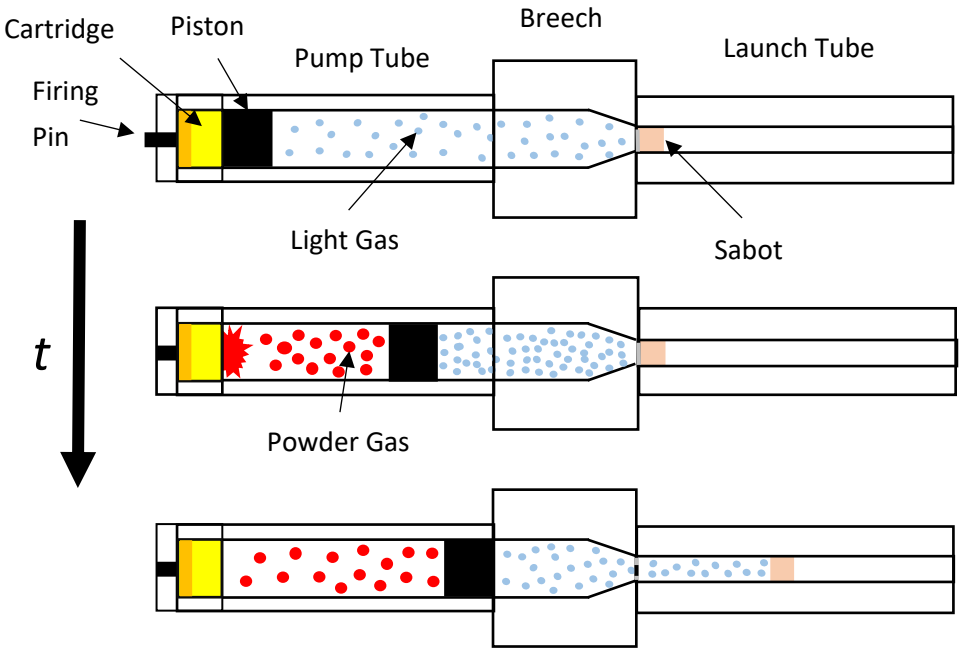

Fig. 3.3: A schematic representation of the working principle of the compression stages of a two-stage light gas gun, modified from Fig. 3 of Schneider & Schäfer (2001). The arrow labeled ***t*** represents the direction of time, with events lower on the page being later in time. The higher molecular mass powder gas is represented by the larger (red) circles, and the lower molecular mass light gas is represented by the smaller (blue) circles. In the top image the light gas has been pumped into the pump tube and breech to the pre-pressure. In the middle image the cartridge has been detonated, burning the powder and producing the expanding powder gas that pushes the piston and compresses the light gas into the breech, the far end of which is sealed with a burst disc behind the sabot. In the bottom image the large pressure has ruptured the burst disc allowing the compressed light gas to expand into the launch tube, accelerating the sabot and projectile housed within.

Pendulum

The first component in Fig 3.2 is the pendulum. This is positioned 50° from vertical and is used to strike a firing pin placed in contact with the primer (inside the shot gun cartridge being used), detonating the gunpowder in the cartridge. The pendulum is held in position on a pivot at 50° from vertical by a rod, which is withdrawn automatically on command (via an electric circuit) releasing the pendulum. There is a heavy mass at the end of the pendulum, and the regular and reproducible impulse arising as the swinging pendulum reaches the vertical and strikes the firing pin is sufficient to ignite the primer. The use of an electric circuit to release the pendulum is a safety feature that allows the gun to be operated remotely from outside the room.

Cartridge

Cartridges used in the LGG are 20 mm in diameter, with a type CC1 209M primer. They are loaded in the laboratory with a typical charge of 10 g of Alliant Reloader 19 or 22 powder. The detonation of the cartridge, which is housed within the powder chamber, produces the powder gas that accelerates the piston as shown in Fig. 3.3.

Pump Tube

The Pump Tube has an internal diameter of 12.7 mm and length of 600 mm. This tube contains the piston at one end and a light gas in the front of it. The light gas is pumped into the tube under pressure from a small refillable gas cylinder. This pre-pressure (that is there before the gun is fired) helps determine the ultimate firing velocity. As the piston accelerates through the pump tube the light gas is compressed until a certain pressure is reached, at which stage the burst disc ruptures, allowing the light gas to expand into the launch tube, see Fig. 3.3.

Piston

The pistons are made of nylon 66 and have a typical mass of 12 g and a diameter of 12.7 mm, which is the same as the bore of the pump tube to ensure a tight fit. Further to this, there are circular rubber 'O' rings positioned along the piston to help produce a good gas-tight seal with the pump tube (Fig. 3.4).

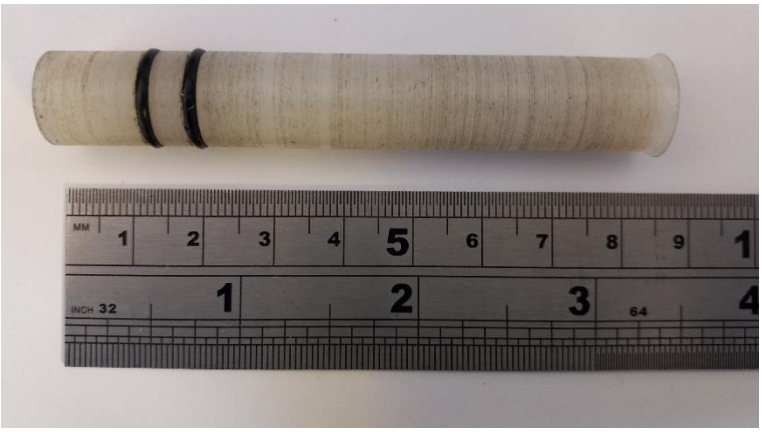

Fig. 3.4: A nylon piston with black O-rings in place, towards the front of the piston. A ruler is present for scale.

Breech

The breech is a reinforced chamber designed to withstand the large pressures produced by the compression of the light gas. It connects the pump tube and the launch tube (that are separated by the burst disc), using a system of clamps and 'O' rings. In addition, the reduction in diameter from the pump tube to the launch tube helps further increase the pressure in the expanding light gas by throttling the gas flow.

Burst Disc

Separating the pump tube from the launch tube, the burst disc determines the pressure at which the light gas releases from the pump tube into the launch tube, by rupturing at the desired pressure. To determine the pressure at which the disc ruptures, and consequently the achievable velocity, different (softer or harder) aluminium alloys are used, either with or without crosshair-shaped scoring (Fig. 3.5). The weaker, scored discs provide speeds of 5 km s^{-1} and less, and non-scored discs are used for speeds greater than 5 km s^{-1}. The scoring also allows the burst disc material to be retained attached to the disc after it ruptures. This reduces the amount of material that flows down the launch tube and that may otherwise inadvertently reach the target.

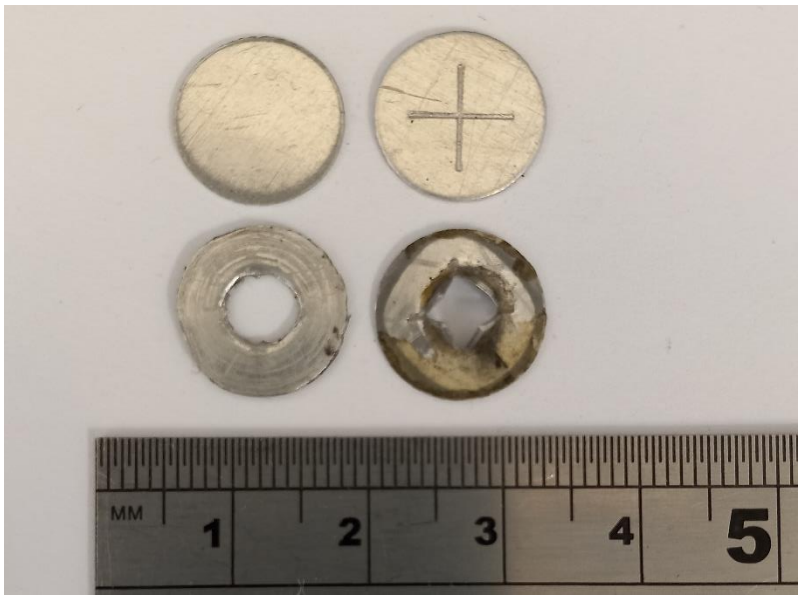

Fig. 3.5: Unscored and scored burst discs (left and right) before and after rupturing (top and bottom). A ruler is present for scale.

Launch Tube

The launch tube acts as a traditional gun barrel, containing the sabot and projectile that are accelerated before entering the blast tank. It is made of EN24T steel, hardened to a Rockwell C scale (RC) hardness of 50 – 51C. It has a bore diameter of 4.5 mm, length of 0.7 m and is rifled such that the projectile performs one complete revolution as it travels along the tube. There are also some variants of the launch tube that are smooth bore, but these are not used in this work so are not described. The sabot is placed in position at the breech end of the tube before connecting the burst disc, the breech, and then filling the pump tube with the light gas. Before firing, the launch tube, and successive chambers down-range of the burst disc and sabot (see Fig. 3.2), are evacuated down to typically 0.5 mbar, to minimise drag forces that will otherwise slow the projectile in flight. The low pressure also prevents shock waves building up in the launch tube, which would prevent optimum acceleration of the sabot.

Sabot

Sabots used can either be a single piece of nylon (typical mass of 78 mg) or consist of four interlocking pieces of Isoplast 202EZ thermoplastic resign (which is known as a split sabot shown in Fig. 3.6), with an external diameter of typically 4.30 mm (to match the bore of the launch tube) and a typical length of 4.50 mm. The central hole in a spit sabot is used to mount the projectile, and its diameter therefore depends on the projectile size if a single projectile is used. Unless a solid sabot is used and fired directly at the target, the sabot's primary functions are to house the projectile, produce a tight fit to the launch tube and accelerate the projectile through the tube. Split sabots have serrated internal edges that lock together to from a single unit while confined by the tube. Due to the rifling within the launch tube, the sabot gains a rotational velocity that causes the four segments to separate once the sabot leaves the confines of the tube, resulting in the parts of the sabot being thrown off the horizontal main gun axis while the centrally mounted projectile remains on axis.

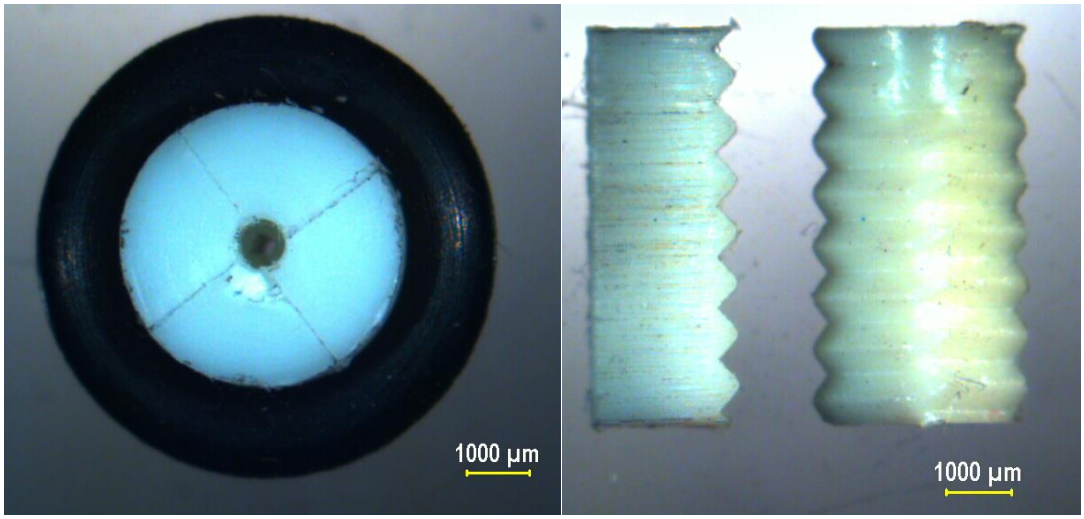

Fig. 3.6: Microscope images of a split sabot. Left: The segments are assembled and held together by the black rubber O-ring around the outside of the sabot. The small central cavity is where the projectile is housed. Right: Two segments in different orientations showing the serrated interlocking edges. Note that only the top part of each sabot segment (down to about 1/5 its length) is bored out to contain the projectile.

Projectiles

Projectiles used in the gun fall into two main categories, single projectiles, and buckshot. Single projectiles usually consist of small spheres ranging from 0.1 – 3.0 mm and are made of glass, nylon, ruby, aluminium, stainless steel, copper, and phosphor bronze, amongst other materials. Provided that it can fit within the sabot and survive the large acceleration and jerk (acceleration/time) encountered during firing, any size and shape of projectile can be fired. Most single projectiles are spherical, but some are cubes and any shape can be accommodated, provided its centre of gravity can be placed in line with the centre of the sabot to ensure flight along the main axis of the gun with minimal deviation. However, for extremely small projectiles of less than 0.1 mm, loading them onto the central axis of the sabot becomes critical and any small deviation can cause the projectile to deviate from this axis and fail to reach the target.

Buckshot is comprised of many small (sub-millimetre) projectiles and is produced by loading a mass of small spheres, or in some cases powder, into the sabot. The buckshot travels as a projectile cloud with a diameter at the target limited by the opening angle produced by the hole in the stop plate (see the next section) measured from the end of the launch tube.

Blast Tank and Stop Plate

Once accelerated and separated from the sabot, the on-axis projectile continues through the blast tank (width 0.3 m and length 0.9 m) and exits into the light gate chamber, while the parts of the sabot which drift off axis are stopped in the blast chamber by the stop plate (see Fig. 3.7). The stop plate, a piece of high carbon steel, is placed at the exit of the blast tank and has an 8 mm (or 10 mm) diameter hole at its centre that is aligned with the main gun axis. The size of the central hole is chosen for each shot based on the size and density of the projectile, which determines the likelihood of the projectile staying perfectly on axis or drifting off slightly. A polyvinylidene fluoride (PVDF) impact sensor, discussed in greater detail in Section 3.2, is attached to the stop plate to provide additional timing information that can be used, along with a light curtain at the muzzle, to confirm the velocity measurement given by the light curtains in the time of flight (TOF) chamber (see below), although with a reduced accuracy of ± 4% (Burchell *et al*., 1999).

Fig. 3.7: A stop plate after having been impacted; the hole that lets the projectile through is seen at the centre and the other two (left and right) are for mounting in the blast tank. Top right is the PVDF impact sensor attached with a G-clamp. Large craters produced by the four sabot segments traveling at high speed are seen around the central hole. In between these are rectangular impact marks with jagged lines, produced by slower moving sabot segments from a previous lower speed shot.

The stop plate is removed after each shot and examined to identify whether any sabot segments passed through the central hole or the projectile hit the plate. Similarly, when using the stop plate for timing measurements the distance from the nearest sabot segment impact and the PVDF sensor is recorded and considered when calculating the velocity measurement. Stop plates are used for several shots, until impact features make identification of new features difficult. Previous impact craters are marked with a marker (remnants of green marker can be seen in Fig. 3.7) to enable new features to be identified on old features.

Time of Flight Chamber

This chamber acts as the primary projectile speed measurement system. It contains two light curtains comprised of 3 mW CW laser diodes, lenses and apertures. Each curtain produces a rectangular sheet of light (5 mm width and 1 mm depth) transverse to the direction of projectile flight, that is refocused at the bottom of the chamber onto a photodiode. The currents of the photodiodes are monitored by a trans-impedance amplifier connected to an oscilloscope (sampling at 50 MHz). When the projectile passes through each light curtain, a rise in current is produced due to the change in illumination. The time difference between the two signals and the known separation of 0.499 m are used to give a measurement of the projectile's speed, with an accuracy of ± 1% for projectile velocities up to 7 km s^{-1}.

Target Chamber

The final chamber is the target chamber, which has internal dimensions 1.15 m × 1.15 m × 1.15 m. This is where the projectile impacts the target under investigation. At the front of the chamber there is a metal cone gas diverter attached to the hole through which the projectile enters. This diverts the majority of any light gas and following debris/gas from the first stage away from the central axis. Electrical feedthroughs and windows are present to allow the instrumentation of targets and the use of cameras. Targets can be mounted on the door at the end of the chamber, on free standing rigs designed to hold targets, or in a range of different mounts capable of rotating, heating, and simulating a body of water (Hibbert *et al.*, 2017). The target chamber is one of the chambers that is evacuated to approximately 0.5 mbar pre-shot, with pump down taking around 40 minutes. This minimises the drag forces that would decelerate the projectile after passing through the TOF chamber and similarly stop the production of sonic waves.

After a shot has been fired, the target chamber is re-pressurised by air that is flowed through the blast tank and into the target chamber, and out again via a series of filters that trap particles as small as 5 μm. The procedure takes 10 minutes and removes any vapours and particulates from within the target chamber that arose from the shot. This is done to make it safe for the chamber to be opened to the laboratory and operating staff.

3.1.2 Velocity Dependence

As mentioned earlier, the primary principle of an LGG that allows it to obtain such high speeds is the use of a light gas as the accelerating propellant, as a lighter gas can accelerate faster than a heavier one, i.e. its expansion velocity is proportional to its mean molecular mass. This can be seen from Eq.s 3.1 and 3.2, which describe the maximum theoretical muzzle velocity of a projectile (Seigel, 1965):

$$v_{max} = \frac{2}{(\gamma - 1)} a_0. \tag{3.1}$$

Here γ is the ratio of the specific heats and a_0 is the initial sound speed of the propelling gas. The speed of sound in a gas is given by the equation:

$$a_0 = \sqrt{\frac{\gamma R \mathrm{T}}{m}}, \tag{3.2}$$

where R is the gas constant, T the temperature, and m the molecular mass of the gas. Thus, by substituting Eq. 3.2 into Eq. 3.1 it is seen that the maximum speed is proportional to $m^{-1/2}$, hence the lighter the gas the greater the speed. Even in specially strengthened powder guns capable of withstanding high pressures, muzzle exit speeds are typically limited to around 3.5 km s^{-1} (Seigel, 1965).

As well as the molecular mass of the propelling gas, there are a few other parameters that determine the speed of the projectile. These include: the mass (quantity) of gun powder used, the powder burn rate, the masses of the piston, sabot, and projectile, the pressure of the light gas in the pump tube before firing and compression, the strength of the burst disc, and the residual gas pressure (i.e. vacuum) in the launch tube pre-shot. Careful selection of these parameters allows the velocity for a shot to be chosen from a range of 1.2 – 7.7 km s^{-1}, with an approximate agreement of ± 0.3 km s^{-1} between the speed selected pre-shot and that actually achieved. Table 3.2 shows the general conditions used to obtain a range of velocities.

Table 3.2: General conditions used to obtain a range of velocities, reproduced from (Burchell *et al.*, 1999). The gas pressures given are the pre-shot pressures of the light gas in the pump tube before the gun is fired.

Velocity (km s^{-1})	Gas	Variables
1.2 - 2.2	Nitrogen	40 – 70 bar and 8 - 10 g of gunpowder
3.3 - 4.3	Helium	45 – 70 bar and 10 g of gunpowder
4.4 - 5.7	Hydrogen	35 – 70 bar and 8 - 10 g of gunpowder

3.1.3 LGG Summary

Section 3.1 has discussed the design and working principles of the LGG and has outlined how different shot speeds are achieved. In operation, the gun is typically fired twice a day depending on the nature of the experiment, e.g. how long it takes to set up the target and/or in-situ measurement apparatus. After each shot, the pump and launch tubes are cleaned, the stop plate inspected, and the shot speed calculated. The gun operator typically undertakes these duties, whilst the user inspects and removes the target from the target chamber.

The ability of the University of Kent's LGG to accelerate single projectiles from 0.1 mm – 3.0 mm in diameter to speeds ranging from 1.2 – 7.7 km s^{-1}, make it ideal for simulating orbital debris impacts, in the size range of interest, which a detector would encounter in Earth orbit.

3.2 Detector Materials

In this thesis, detectors are tested which consist of layers of Kapton film, instrumented with PVDF acoustic impact sensors. This section therefore discusses the relevant properties of PVDF and Kapton, and includes a review of relevant past PVDF detectors.

3.2.1 Introduction to PVDF

Polyvinylidene fluoride (PVDF) is a semi-crystalline polymer with piezoelectric properties whereby, due to an intrinsic volume polarisation (dipole moment/volume) within the bulk (Simpson & Tuzzolino, 1985; Xin *et al*., 2016), piezoelectricity causes an electric charge to be produced in response to an applied strain. PVDF has a number of properties that make

it well suited for use in space-based detectors (Measurement Specialties Inc., 1999; Tuzzolino, 1996; Tuzzolino *et al*., 2003) such as:

- It is a relatively inexpensive material that is flexible, easily fabricated into thin films, and highly resistant to radiation, moisture, and contaminants.
- It has good thermal resistance, with an operating temperature of - 40 °C to 80 °C. For space applications, sensors coated with a Chemglaze Z-306 coating can achieve ranges from -200 °C to 115 °C.
- It has high dielectric and mechanical strengths.
- No operating voltage is required (although associated measurement electronics in a detector do require an operating voltage).

PVDFs suitability for use in space has seen detectors that incorporate PVDF flown in many space missions including:

1. The Dust Counter and Mass Analyser (DUCMA), which was flown aboard the Vega 1 and 2 spacecraft missions. This instrument analysed the flux and mass distribution of particles across the coma of comet 1P/Halley in 1996 and was built at the University of Chicago (Simpson *et al*., 1986).
2. The SPAce DUSt (SPADUS) instrument, launched in 1999 aboard the Advanced Research and Global Observation Satellite (ARGOS). This orbited the Earth in a sun-synchronous polar orbit with an altitude of 850 km. It was designed to measure the speed/trajectory, flux, and mass distribution of near-Earth space dust (both cosmic dust and orbital debris) (Tuzzolino *et al*., 2001).
3. The Dust Flux Monitor Instrument (DFMI) flown aboard the Stardust mission (launched 1999), which was designed to measure the flux and mass distribution of particles on its passage through the coma of comet 81P/Wild 2 in 2004 (Tuzzolino *et al*., 2003).
4. The High Rate Detector (HRD) flown aboard the Cassini spacecraft (launched 1997). HRD is very similar in design to DUCMA, also having been designed and built at the University of Chicago. Its main objective was to measure the particle flux and mass distribution throughout the ring system of Saturn (Srama *et al*., 2004).
5. The Arrayed Large-Area Dust Detectors in INterplanetary space (ALADDIN) flown aboard JAXA's solar sail demonstrator IKAROS (Interplanetary Kite-craft Accelerated by Radiation Of the Sun). ALADDIN was launched in 2010 aiming to measure the flux of dust $\geq$ 10 μm in the zodiacal cloud between 0.7 AU and 1.1 AU

with higher temporal and spatial resolution than any previous in-situ measurement (Hirai *et al*., 2014).

6. The Space Debris Sensor (SDS) deployed by NASA on the exterior of the international space station (ISS). Launched in 2017, its main goal was to determine the distribution of sizes, densities, speeds, and orbits of the debris population in low Earth orbit (Hamilton *et al.*, 2017).

Most of these detectors featured one or more layers of PVDF film that, as stated, produced a charge signal upon impact by high-speed small particles, due to the depolarisation that results from the complete destruction of dipole moments in and around the penetration hole.

3.2.2 Properties of PVDF Sensors

The piezoelectric properties of PVDF can be significantly increased along a given direction by stretching it along that direction while above its curie temperature and cooling it while maintaining the strain. This is a result of the crystalline domains tending to align. Improving the piezoelectric properties in this way allows PVDF to be fabricated into acoustic sensors that use a thin layer of PVDF to detect acoustic signals from the voltage produced by the associated strain produced in the material by the vibrating waves.

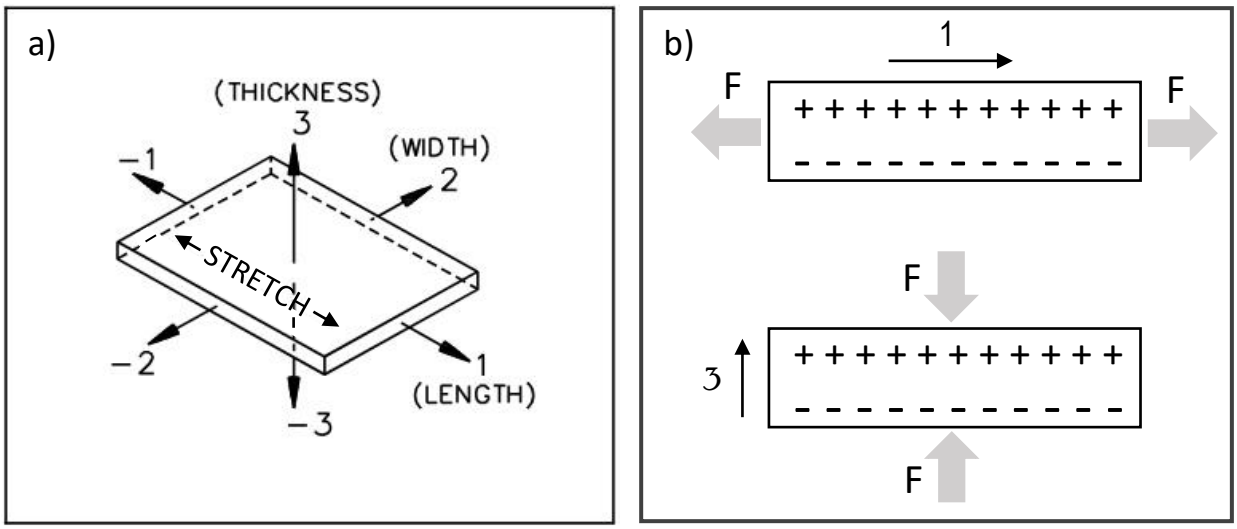

Fig. 3.8: (a) A PVDF film with their specific axis nomenclature shown. The stretch direction is along its length axis '1' (modified from Measurement Specialties Inc., 1999). (b) A cross-section through the thickness of a PVDF film with electrodes attached to the upper and lower surface. Numbered arrows denote the directional axis. '+' and '-' symbols represent the electrical polarisation of the material. Arrows labelled F represent an applied force (strain), with the g_{31} (stress perpendicular to the polarisation) and g_{33} (stress parallel to the polarisation) modes shown top and bottom respectively (modified from Xin *et al*., 2016).

Due to the thin nature of piezo film, electrodes can only be attached to the upper and lower surfaces. Accordingly, the polarization axis is always along the '3' axis (Fig. 3.8b) . There are two main transformation mechanisms in PVDF film: the g_{31} mode, which is when the strain applied is perpendicular to the polarization (top of Fig. 3.8b) and the g_{33} mode, which is when the strain is in the direction parallel to the polarisation (bottom of Fig. 3.8b). These are named after their respective piezo coefficients for voltage (g_{3n}), where the subscript '3' and 'n' denote the axis of electrical polarisation and applied strain, respectively. The g_{31} mode produces a larger voltage per force applied than the g_{33}, primarily due to the smaller surface area along this axis (thickness by width for g_{31} vs width by length for g_{33}). Note that the g_{33} mode is not applicable when applied to a compliant membrane, and the g_{32} coefficient, i.e. a strain transverse to the stretched direction (Fig. 3.8a), can be as much as ten times smaller than g_{31} due to anisotropy in this direction (Gusarov, 2015). Hence, PVDF sensors are essentially in-line strain sensors, sensitive to longitudinal waves and far less sensitive to transverse (shear) waves.

PVDF sensors have a wide range of applications from portable medical health monitoring to architectural structure monitoring (Xin *et al*., 2016). Similarly, this style of sensor can be used to monitor the acoustic signals produced by impacts, which is the operational design of the SDS detector (Hamilton *et al*., 2017). Indeed, the initial development of the PVDF sensors used within the research in this thesis was originally funded by the NASA Science Missions Directorate's Planetary Instrument Definition and Development Program in 2003. NASA had determined, via hypervelocity impact testing and analysis, that PVDF was the best sensor material available for space detectors (Liou *et al*., 2015). This was a result of PVDF having such a high sensitivity, low mass, and being commercially available as a thin, flexible sensor that is easily applied to a surface without significantly constraining the substrate, a critical feature for a sensor applied to thin films. Previous hypervelocity impact experiments carried out at the University of Kent (DRAGONS project sponsored by AstroAcoustics/NASA) confirmed that PVDF sensors were indeed suitable for detecting cosmic dust and orbital debris impacts (Corsaro *et al*., 2010; Burchell *et al*., 2011).

3.2.3 Sensors Used in this Research

Sensors used in this research campaign were commercial PVDF sensors manufactured by TE Connectivity Measurement Specialties (formerly Measurement Specialties inc.) and supplied by Digi-Key Electronics, with the model number FDT1-028K (Note that this is a 'model number'/specification ID, not a part number for the supplier). The standard sensor

dimensions for the active (electrode) area are 12 mm X 30 mm X 0.23 mm. Past (unpublished) research by the DRAGONS team found that shorter sensors have a better response to high frequencies, with a quarter of the original length seeming optimal. As it is the high frequency acoustic signals that are of interest in an impact, quarter-sized sensors (12 mm X 7.5 mm X 0.23mm) (Fig. 3.9) were used to instrument the prototype detector described in Section 3.3. Quarter sized sensors were produced by cutting the original sensors. Care should be taken during cutting not to damage the silver ink electrodes, and to use a sharp blade to minimise the production of a rough edge or filaments of material, which could cause the sensor to short or fail.

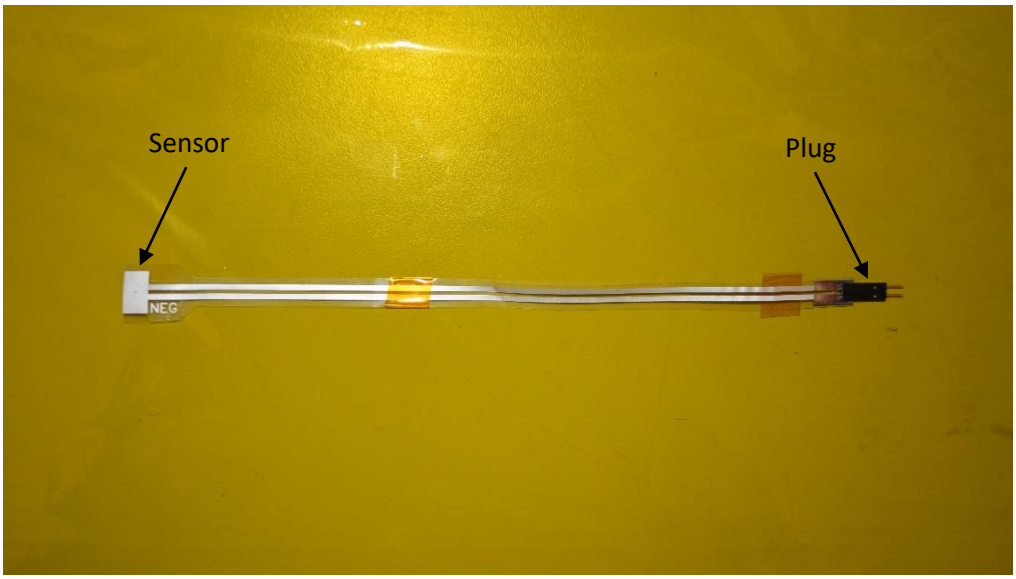

Fig. 3.9: A quarter sized sensor that has been removed from a detector, laying on top of a piece of Kapton. The grey rectangle shown on the left is the active area of the sensor, and the black plug, with two pins, shown on the right is for connecting a measurement system for data read out. The cables connecting the sensor and plug are 20 cm long. The negative side of the sensor comes labelled as "NEG". There are two pieces of Kapton tape, one near the plug end, and one near the middle of the long tail, which were used to hold the sensor tail in place on the detector.

3.2.4 Kapton Polyimide Film

Kapton is a polyimide film that was invented by the company DuPont de Nemours, Inc. (known as DuPont) and is a registered trademark of theirs. A polyimide is a synthetic, plastic

polymer comprised of imide groups. Kapton has a range of excellent properties (DuPont, 2021) including:

- Thermal resistance, being able to tolerate both high and cryogenic temperatures (ranging from 4 to 673 K). This is ideal for the temperature extremes experienced in space, e.g. between full illumination and eclipse for Earth orbit, or traveling into outer space.
- Good mechanical properties such as high strength and low shrinkage.
- Chemical resistance to known organic solvents.
- Low outgassing under vacuum (Willis & Hsieh, 2000).
- Radiation resistance capable of withstanding the energetic particle environments of space (Gouzman *et al*., 2019).

Kapton's favourable properties make it ideal for aerospace applications, and as such it is space qualified and has been used in a range of applications since the 1960's. Notable applications include; electrical wire insulation (Berkebile & Stevenson, 1981), electrical insulation in photovoltaic cells, and most commonly in multilayer insulation (MLI) (Finckenor & Dooling, 1999; Henderson, 1989; Smith *et al*., 2016). The NASA New Horizons spacecraft (now on its way through the Kuiper belt), shown before its launch in 2006 in Fig. 3.10, demonstrates the distinctive golden look of MLI that results from the yellow-orange of Kapton (Fig. 3.9) over a layer of aluminium film.

Fig. 3.10: NASA's New Horizons spacecraft in the Kennedy Space Center clad in multilayer insulation featuring Kapton, demonstrating its golden appearance (VOAnews, 2015).

One issue for the deployment of Kapton in LEO is Kapton's susceptibility to erosion from atomic oxygen (single atom oxygen O_1) that is highly reactive, and prevalent in LEO with

fluxes of ~ 1.9 x10^{20} atoms cm^{-2} $year^{-1}$ (Banks, 1990). However, thin metal coatings such as aluminium (Cooper *et al*., 2008), gold, platinum (Silverman, 1995), and palladium (Dignam *et al*., 2022) significantly prevent erosion due to impact of O_1 allowing prolonged use of Kapton in LEO. Other inorganic compounds can also be used as coatings, with silicone oxides (of the form SiO_x) found to be particularly effective (Qi *et al*., 2022).

Coatings tend to be thin (typically a few nanometres) to reduce cost, since many coatings are extremely pure, and in some cases, precious metals. There are also issues related to coating thickness, where thicker coatings tend to exhibit imperfections, such as cracks, that subsequently allow atomic oxygen to erode the underlying Kapton. Similarly, only the space exposed surface of the Kapton layer tends to be coated. This is to reduce atomic oxygen undercutting, which is when an atom becomes trapped between two surface coatings, causing more damage than if the atom were able to pass through (Banks *et al*., 2002).

The coating thickness is also limited by its reaction to impact. Research conducted at the University of Kent (Dignam *et al.*, 2022) found that these coatings can suffer delamination upon impact if they are too thick, leading to the recommendation that coatings of palladium be no more than 50 nm thick to mitigate against such coating damage/delamination during particle impact. To protect against atomic oxygen, however, the same research found that a coating of at least 25 nm is recommended to prevent significant erosion by atomic oxygen, demonstrating the careful balance that must be considered between protection from atomic oxygen and delamination effects.

Despite the use of coatings in LEO, during this research no coated films were subject to experiment. This was primarily to reduce cost and increase availability of the Kapton samples. Therefore, uncoated type “HN” general purpose Kapton (ρ = 1.42 g cm^{-3}) was used for the prototypes within this study. Coatings such as a 25 nm thickness as suggested above, would represent 0.2 % of the total film thickness for a 12.5 µm Kapton film (with a single side coated), and are unlikely to significantly affect the deceleration experienced by a particle.

3.3 Experimental Method

3.3.1 Construction of the Prototype Thin Film Detector

To determine the speed of projectiles after film penetration, and hence deceleration, two prototype thin film TOF detectors of the same design were produced (see Fig. 3.11). Use of two prototypes allowed 12.5 µm and 25 µm thicknesses of Kapton films to be used during the same time period, without having to remove and replace films and sensors when switching from one thickness to the other. Similarly, having two prototypes ensured that the shot programme would continue without delay if one suffered damage and was declared out of action for a period of time due to, for example, catastrophic film damage from debris (including accidental impacts by whole sabots) or sensor damage/failure.

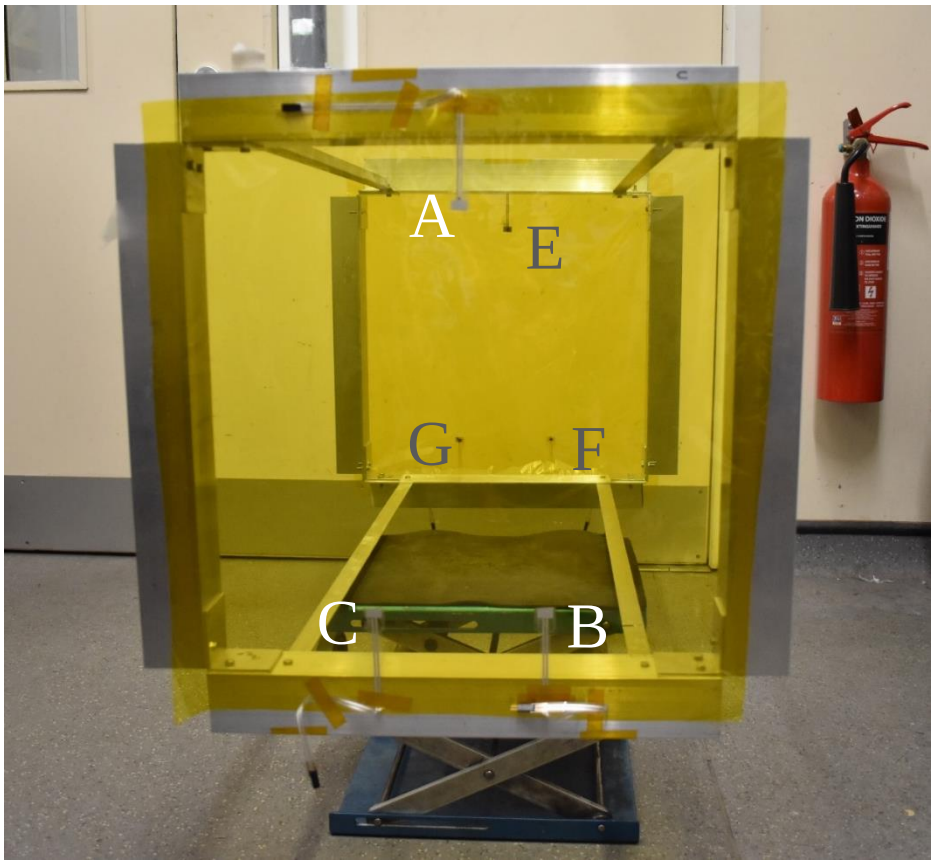

Fig. 3.11: A front facing view of the detector mounted on a rubber insulated mounting platform. Sensors A, B, C (labelled in white text) are located on the first film. Sensors E, F and G (labelled in grey text) are on the second film.

The prototypes consisted of two aluminium frames each of which support a Kapton film of identical thickness (*f*) and exposed surface area 40 cm X 40 cm = 1600 cm^2, with a separation

between Kapton films (x) of 0.754 ± 0.001 m. This maximised x while fitting in the target chamber with enough room for a projectile capture system at the rear, and enough space at the front for the gas diverter. Maximising x decreases its relative uncertainty and similarly increases the time of flight between the two films, thus also reducing this relative uncertainty in timing. Each film is equipped with three PVDF sensors, which were positioned in identical locations on each film to produce pairs of sensors. On the first film were sensors A, B and C, while on the second were D, E and F, with sensors paired as follows: A with E, B with F, and C with G (Fig. 3.11). These sensors provide time of impact measurements for each film and were chosen for their properties described earlier in section 3.2.2, such as not constraining the films, as well as having been shown by previous studies to provide accurate timing measurements (Liou *et al*., 2006; Corsaro *et al*., 2016).

3.3.2 Sensor Positioning

Three pairs of sensors were used to enable an average speed measurement to be computed. This is also representative of this style of detector that would have at least three sensors per plane for impact location triangulation. A fourth (or more) redundancy sensor for better average determination was not included due to supply constraints. When this research began in 2020 the COVID-19 pandemic was at its height, affecting production and supply chains worldwide, resulting in a limited supply of PVDF sensors available within the University.

The signal onset time for each sensor on a plane is different and not the time of impact, as it includes a time delay associated with the propagation of the acoustic waves through the Kapton film. To reduce the need to compensate between sensors (on different films) in a pair for differences in impact location (relative to the individual sensor in each pair) and the associated propagation times through the Kapton from impact site to sensor, and hence the related uncertainties, sensors were located directly behind one another along the direction of projectile flight (assuming normal incidence). This ensured that the distance from the centre of the impact to the centre of sensor, and thus the signal propagation time, would be the same for each sensor in a pair. Hence, the time difference between sensors in a pair (Δt) is equal to the time taken to traverse the film separation (x). Sensor location matching was achieved by producing the prototypes such that the frames were the same size and directly in line with one another. This led to the bottom left corner of each frame essentially being the (0,0) of a two-dimensional plane, with the second film a distance x

behind the first. Using this as a reference point the location of each sensor could be measured by hand, with differences in position on the order of the uncertainty (1 mm).

Sensors were positioned 56 mm from the edge of the nearest aluminium frame (Fig. 3.12). This was done to maximise the area for shots to be conducted, whilst ensuring there would be 60 µs between the first acoustic waves arriving at the sensor and the arrival of any reflected waves. This was predicted using the wave speed in Kapton, previously determined by the DRAGONS team from unpublished data as 1875 ± 25 m s^{-1}, and was considered a sufficient time not to contaminate the onset of the acoustic waves. To improve detection sensitivity, the sensors could be placed in the corners (the black dashed rectangles in Fig. 3.12) to increase the acoustic component inline with the sensor (the g_{31} mode), the most sensitive direction as described in Section 3.2.2. However, this kind of configuration did not lend itself to having two sensors close together, while maximising the area to shoot, and avoiding edge reflections. Thus, an isosceles triangle configuration for the sensors (exemplified in Fig. 3.12) was used. Having two sensors relatively close together and the third relatively far away, typically gives the largest difference between two sets of impact-to-sensor path lengths on a plane (A & B, and A & C) most consistently (excluding the most central region). Maximising this distance improves the uncertainty in the calculation of the wave speed in the Kapton, using the difference in known path length and time difference between in-plane sensors, as discussed later.

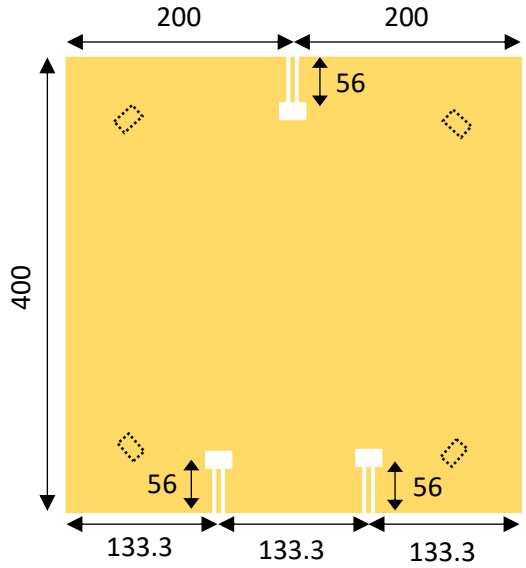

Fig. 3.12: A schematic showing the placement of sensors (white rectangles with tails) on the Kapton films (Yellow) used here on the prototype. All measurements shown are in mm and carry an uncertainty of 1 mm. Hollow black dashed rectangles illustrate where sensors would be positioned to optimise sensitivity. However, this was not done due to limited availability of sensors and the need to maximise the separation used for wave speed calculations.

The only difference in configuration between the first and second film is that the sensors were adhered to the ram side of the first film and the aft side of the second film, for ease of accessibility. For consistency the negative electrical lead (labelled NEG) was used as the return lead and adhered face up. Polarity is not important here and the decision to have negative facing up was arbitrary. Sensors were adhered to the Kapton film using a low viscosity cyanoacrylate that cures hard/stiff, a condition required to provide efficient transmission of strain to the sensor. A low viscosity allows for a thin layer of adhesive, which is also desirable to maximise transmission of strain. Care should be taken not to damage the silver ink on the upward facing PVDF sensor surface by accidently rubbing the adhesive on it during sensor application.

3.3.3 Experimental Procedure

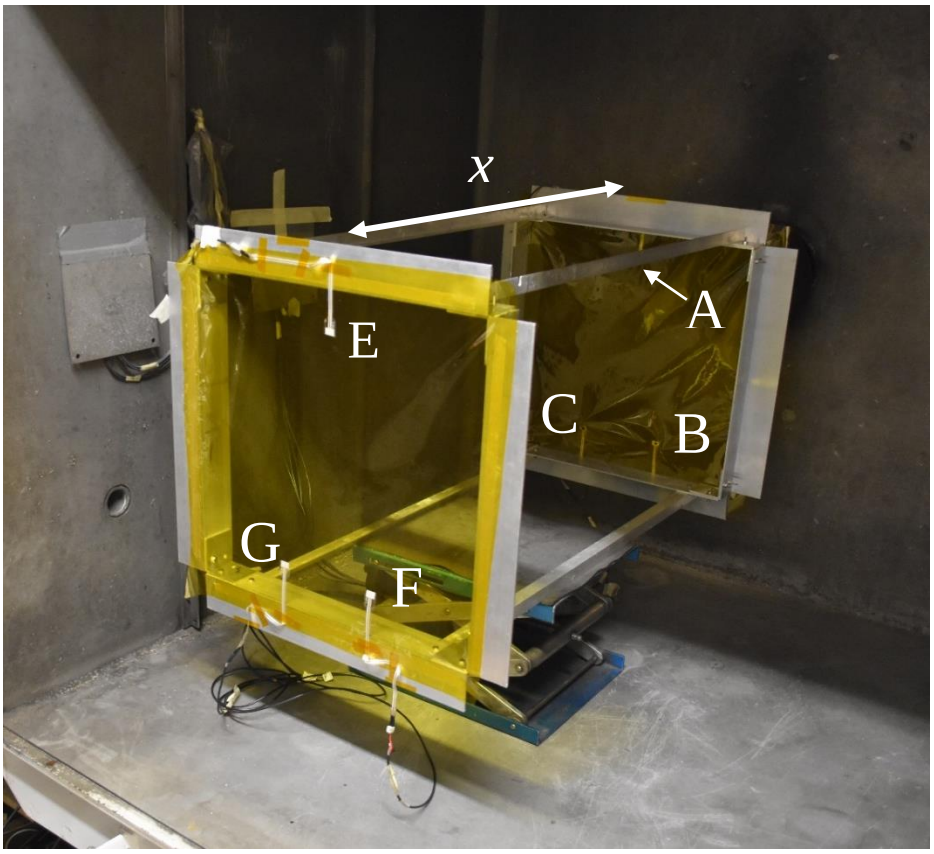

Fig. 3.13: A prototype detector shown positioned in the target chamber. The separation (*x*) between the two Kapton layers (each 40 x 40 cm) is marked with a double headed arrow. The projectile enters from the right of the image through a port hidden behind the position of the 'A' marker, and proceeds at normal incidence through the two layers (towards the left of the image). Sensors A, B and C are on the first layer as seen by the projectile (sensor A's location is obstructed by a strut that comprises the aluminium frame structure and is marked by an arrow). Sensors E, F and G are on the second layer.

The specific experimental parameters and conditions (projectile size, speed, etc.) for each set of data and results are discussed in the relevant Chapters later. Below is a general description of the experimental procedure used to collect data on the deceleration and disruption of projectiles penetrating Kapton films.

Hypervelocity impact experiments (referred to within this text as 'shots') were carried out using the University of Kent's LGG for projectiles with diameter (d_p) in the range 0.2 mm to 1.0 mm, impacting the Kapton films of a prototype detector at speeds in the range 2.0 km s^{-1} to 5.5 km s^{-1}. With a wave speed of 1875 ± 25 m s^{-1} in the Kapton films, even at 2.0 km s^{-1} the impacts will be entering the hypervelocity regime, and at 4 km s^{-1} and above impacts are well within the hypervelocity regime. Therefore, impacts at this speed will be representative of penetrations occurring at the larger velocities of debris and dust impacts, ~ 10 km s^{-1} and ~ 15 km s^{-1}, respectively.

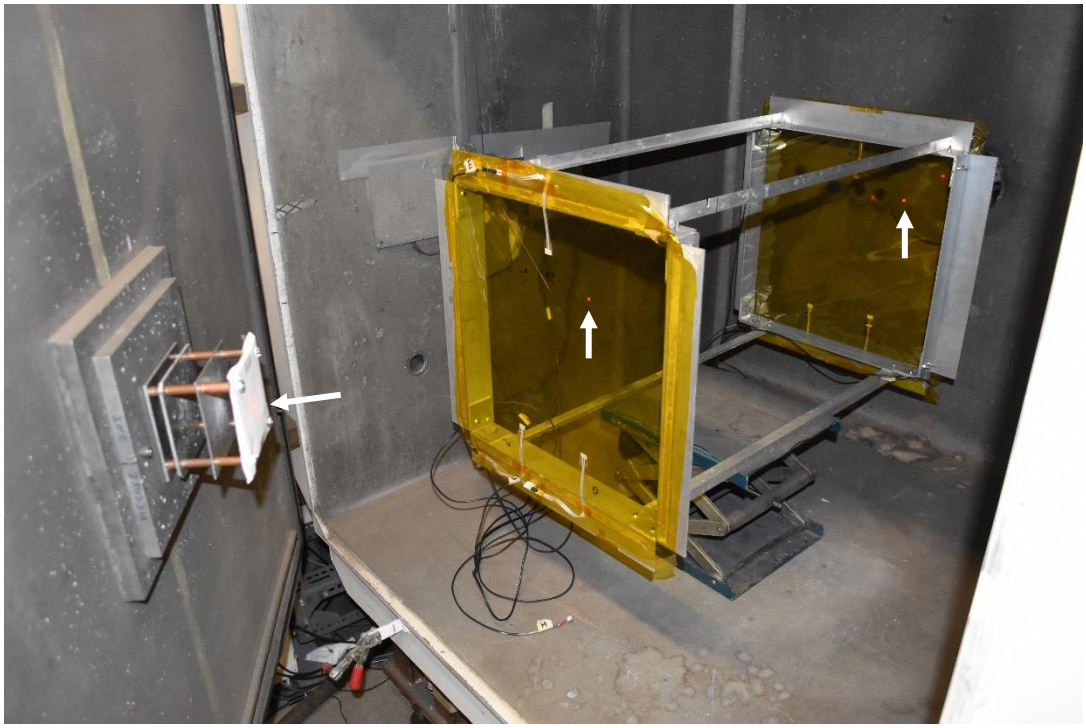

Fig. 3.14: The projectile capture system shown mounted on the target chamber door (left of the image). When the door is closed, the front face of the capture system (the white paper) is in line with, and orthogonal to, the expected trajectory of the projectile. The dot from a red laser (marked with white arrows) can be seen on the Kapton sheets and paper of the capture system. The laser is used to align the barrel with the target and is removed before a shot.

The prototype was mounted in the target chamber on a rubber insulated mounting platform (Figs. 3.13 and 3.14) that has been found to prevent the transmission of any gun vibration in previous experiments. Down-range of the second film, the back stop which usually captures the projectile before it hits the chamber door was replaced with an ejecta capture system (Fig. 3.14) to stop ejecta spraying the rear surface of the second film. The system used to do this consisted of an initial aluminium plate with a hole in the centre that was covered in paper, followed by three aluminium plates in a Whipple shield configuration. This system was effective at stopping the ejecta reaching the Kapton film.

In a shot, the projectile passes through both Kapton layers before being captured behind the target. Subsequent inspection of the films by optical microscope in the laboratory allows for comparison of the holes in each Kapton layer. Two similar appearing holes suggests intact passage of the projectile through the first layer, as in the example shown in Fig. 3.15. However, if multiple holes are found in the second layer, this implies the projectile was disrupted whilst passing through the first layer. It was later found that this did not occur for the relatively strong steel projectiles used in this thesis. The study of stainless steel impactors has significance as one of the constituents of space debris, and with an Fe content of ~ 85%, StSt420 has approximately the same density as Fe ($\rho_{StSt420} \approx 7.8$ g cm^{-3} ~ $\rho_{Fe} \approx 7.9$ g cm^{-3}) and thus has relevance to space dust. Stainless steel also has benefits for use in LGG experiments. The relatively large density of stainless steel and thus momentum for a given size projectile increases the likelihood that the projectile will remain on the gun axis, and make it into the target chamber, allowing the successful use of smaller sized projectiles.

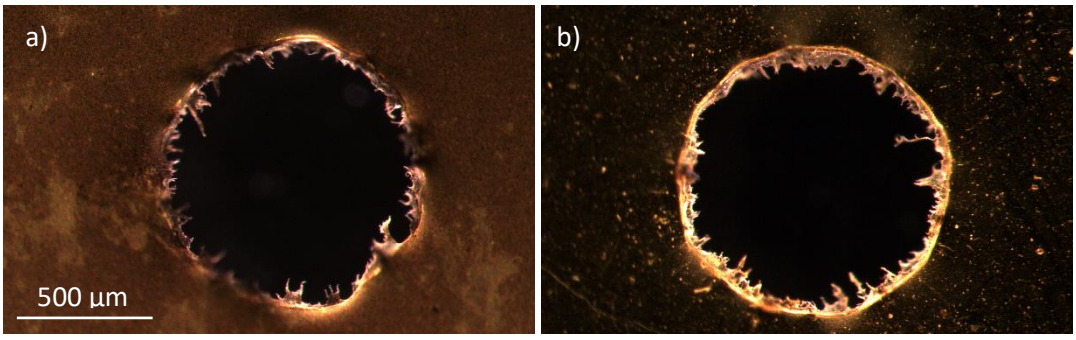

Fig. 3.15: Optical images (transmitted light at an angle of 45°) of penetration holes in the detector's Kapton films after impact by a 1 mm stainless steel sphere at 2 km s^{-1}. (a) The hole in the first film. (b) A similar hole in the second film, suggesting that the projectile was not appreciably disrupted. Both images are to the same scale as shown in (a). The hole size was found to be 1000 µm ± 1% for (a) and 1001 µm ± 1% for (b) comparable to the 1000 µm projectile.

To determine the speed of the projectile between the two films, and hence post penetration of the first film, the time of flight obtained from the PVDF sensors is combined with the known separation of the two layers. This speed can be compared to the incident speed of the projectile measured up-range by the LGG's light gate system.

3.3.4 The Time of Flight Method to Calculate Speed

The time of flight method (see Fig. 3.16) uses the time taken, Δ*t*, for a body to traverse a known distance, *x*, to determine the speed of the body, *v*, using the relation Eq. 3.3:

$$v = \frac{x}{t_2 - t_1} = \frac{x}{\Delta t} \quad . \tag{3.3}$$

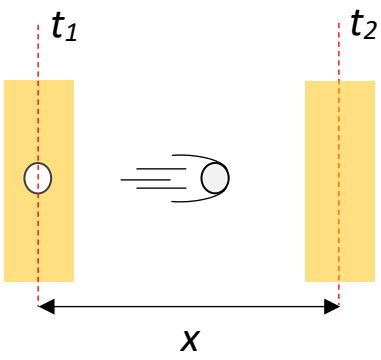

Fig. 3.16: A schematic representation of the time of flight method applied to a projectile penetrating two Kapton films separated by a distance *x*. t_1 and t_2 represent the times of impact on the first and second film respectively.

In the case of the TOF detector described above, Δ*t* is calculated from the difference in time of impact on each film, which is determined by measuring the acoustic signals produced during projectile impact. These signals are measured using the PVDF sensors glued to the films, with their output voltages being recorded on a standard laboratory PC running Lab View SignalExpress, with acquisition triggered by the impact of the discarded sabot on the LGG stop plate. The sampling parameters were set to take 12000 samples at a rate of 2.5 MHz, producing output files 4.8 ms in length with a sampling resolution and thus error of 0.4 μs. For a given shot, three values of the projectile speed are calculated using the Δ*t* from each pair of sensors on the two layers (i.e. A and E, B and F and C and G), which are averaged to provide a single speed measurement for the projectile. The uncertainty in the

speed is obtained by combining the resultant uncertainty in the transit time with the uncertainty in the separation of the Kapton films (x), as discussed further in Section 3.3.8.

3.3.5 Signal Onset Determination

A typical set of raw acoustic signals from a hypervelocity impact can be seen in Fig. 3.17 and Fig. 3.18, in this case from a 1 mm stainless steel 420 (StSt420) sphere traveling at $\sim$ 2 km s^{-1}. The arrival time of an acoustic signal or 'onset time' was identified manually (a 'manual pick') and taken as the onset of the largest peak-to-peak (P-P) amplitude in the first set of peaks. This provides a standardised approach for onset determination and was chosen as it is the most identifiable point in a trace. This component of the acoustic signal is assumed to arrive at the same relative time for each sensor. For time determination, only the relative magnitude was considered, and no treatment of normalisation for signal intensity loss due to signal spreading and attenuation was applied. The first largest P-P amplitude was used, as peaks of similar or larger magnitude arriving later in time could be produced by reflections of the acoustic waves at boundaries and/or superposition of waves, and hence would not be representative of the signal produced directly by the impact. The onset of the largest P-P amplitude was identified as the first recorded data point on the slope of the peak (or trough) belonging to the set of two adjacent peaks and troughs, or vice versa, with the largest P-P amplitude. This data point usually had a magnitude of 0.030 V from the zero point (- 0.027 V), i.e. a value of 0.003 V or - 0.057 V, for peaks and troughs respectively. This is 0.028 V above the amplitude of the background electronic noise, which had a P-P amplitude of 0.005 V. Before the large acoustic signals of interest arrive, smaller preceding acoustic signals can be seen in some of the data (see the circled regions in Fig. 3.17). Although these are thought to be acoustic and originate from the impact, they are less consistent in shape/magnitude and are not always present. Further to this, on the first film their maximum peak amplitude is typically 0.03 V from the zero point, significantly smaller than the maximum of the signals of interest and only just comparable to the first point on the slope of the maximum peak of interest, which is taken as the onset time. Thus, they cannot be mistaken for the signals of interest.

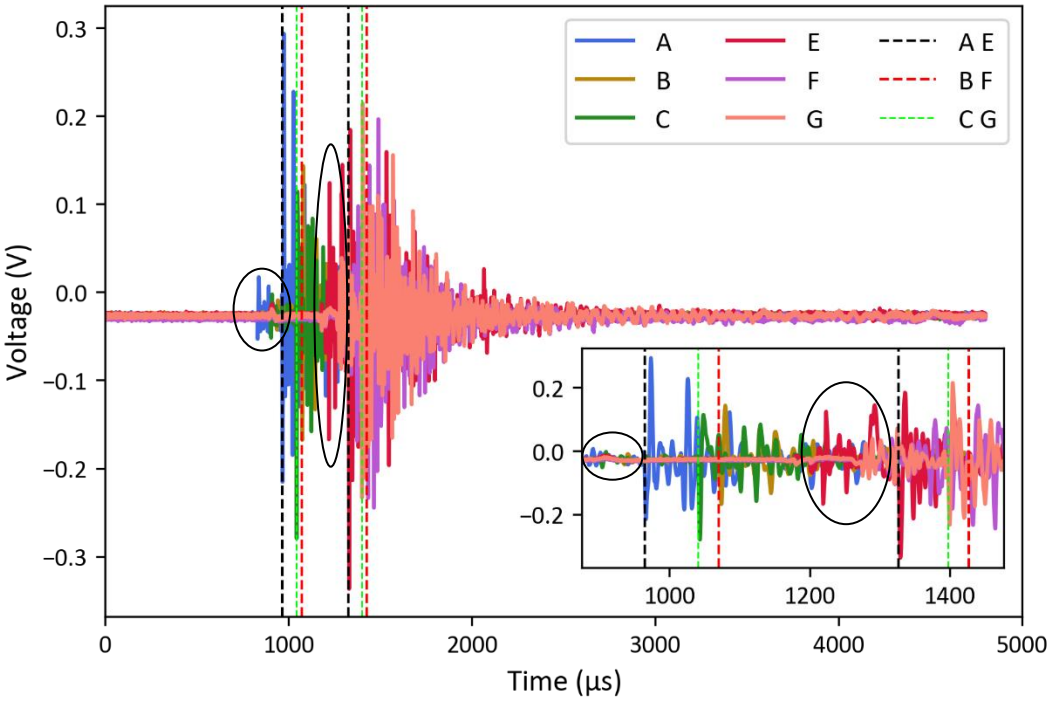

Fig. 3.17: Typical acoustic signals recorded for a shot (a 1 mm stainless steel sphere at ~ 2 km s^{-1}). Dashed vertical lines represent the onset times for sensors in each pair of sensors. Smaller acoustic peaks, discussed in the main text, that precede the onset of the large signals of interest are enclosed in black ellipses. The inset shows the region of interest magnified, with the smaller acoustic peaks circled again. Here only the preceding peaks in E are fully enclosed in the ellipse for the latter traces E, F and G.

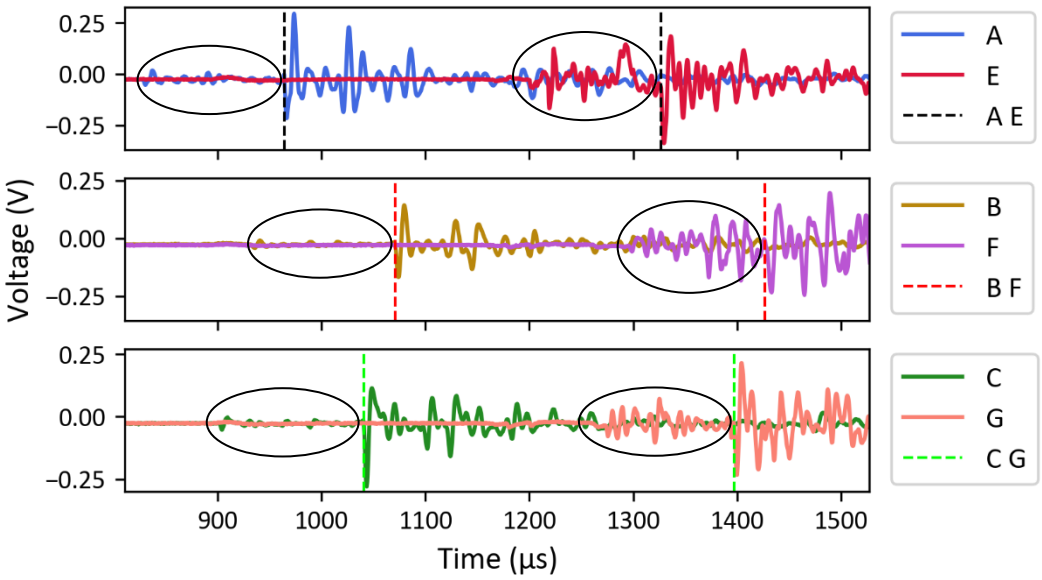

Fig. 3.18: The key time period of acoustic signals in Fig. 3.17 plotted in sensor pairs across multiple plots to make identification of features in each signal possible. Vertical dashed lines represent the onset times for each sensor in a pair. Smaller acoustic peaks that precede the onset of the large signals of interest are enclosed in black ellipses.

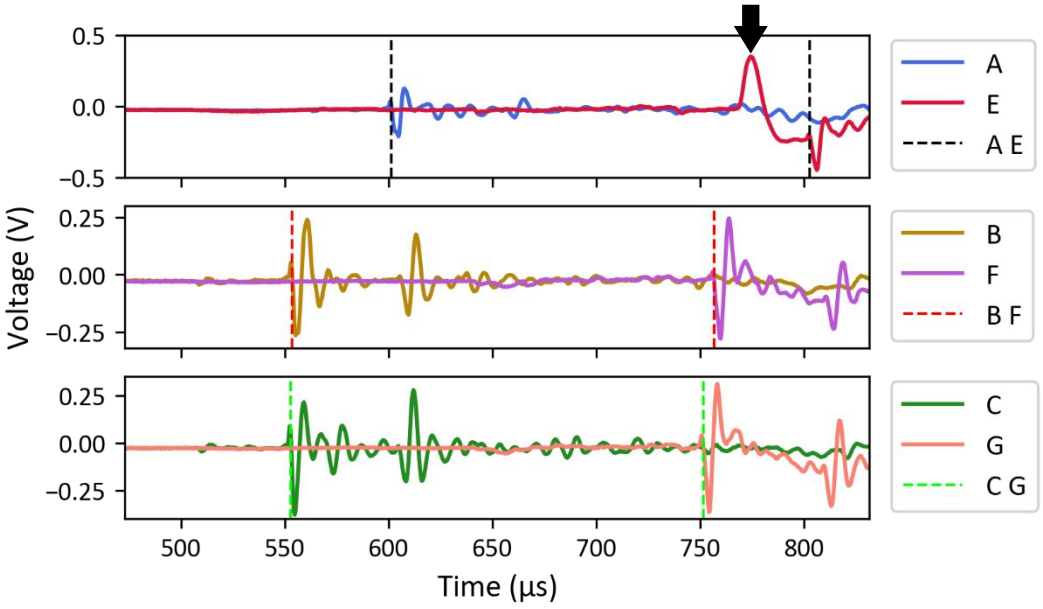

Fig. 3.19: The key time period of acoustic signals from a 1 mm stainless steel 420 sphere shot at ~ 4 km s^{-1}. The single peak with a recovery tail in E, marked by the black arrow, is a non-acoustic noise peak.

Automated signal processing techniques and algorithms for determination of the arrival time of an acoustic emission, such as the 'first crossing threshold' and the 'Akaike information criteria' techniques, have their performance compared and measured against manual picks in Pearson *et al*. (2017). There it is shown that the method that compares most favourably to manual picks, achieved an arrival time estimation accuracy of ± 2 sample points for 95% of events, when compared to manual picks. Thus, it is considered that the identification of onset time by an intelligent picker (manual pick) provides the most accurate selection of onset time, to which other methods are compared. For this reason, and the fact that the finite and manageable size of the number of shots to be analysed allows it, manual picks, as described above, were used for time of onset determination throughout this work to reduce errors. It is, however, noted that the automation of this process would be beneficial for a flight model detector flown in space. Among other benefits, processing raw data into results on board will greatly reduce the payload data rate, thus effecting the overall data and link budget of the platform. To this end some treatment of the automation of onset time determination has been considered in Chapter 5, Section 5.2.

To supress low frequency vibrational modes that are not of interest here and often accompanied by noise, a four-pole 15 kHz high pass filter was applied in the preamplifier stage of the electronics. However, non-acoustic noise is observed in some of the data, typically consisting of a single peak followed by a recovery tail, such as the peak marked with a black arrow in Fig. 3.19. These peaks are distinct from, and cannot be mistaken for, the acoustic signals of interest that have positive to negative (or vice versa) oscillatory behaviour that decays with time, which is characteristic of the acoustic waves that produce them.

3.3.6 Uncertainties

A full investigation of signal shape in PVDF sensors attached to thin films would be very useful, but is beyond the scope of this thesis. Here I note that signals are variable, and some traces have signals that do not always start with a sharp, well-defined, strong peak, which dominates all subsequent peaks. The main observed variants are the presence of broader peaks (see Fig. 20) and a train of several peaks of similar magnitude (such as trace F in Fig. 3.18). The difference in signal shapes, particularly broadness, effects how quickly the leading edge of the peak rises, thus effecting the difference between magnitudes of two adjacent sample points, and which sample point is considered to be the first lying on the slope of the peak. This leads to an uncertainty related to the reproducibility of the pickers choice of the first sample point. To try and account for the impact of this on signal arrival time, and hence accuracy of speed determination, the uncertainty in time of onset was taken as δt = 1 μs, over twice the sampling resolution for this measurement, leading to $\delta\Delta t = \sqrt{1^2 + 1^2} \approx 1.4$ μs. The separation of the two Kapton films was measured by hand in the laboratory using a metre rule and the uncertainty was taken as the precision of the rule δx = 1 mm. With incident speeds of 2 km s^{-1} and 4 km s^{-1} producing flight times of 377 μs and 189 μs, these measurement errors represent an error in flight time of 0.4% and 0.8%, respectively, whereas the error in separation is ~ 0.1% (for a separation of 0.754 m).

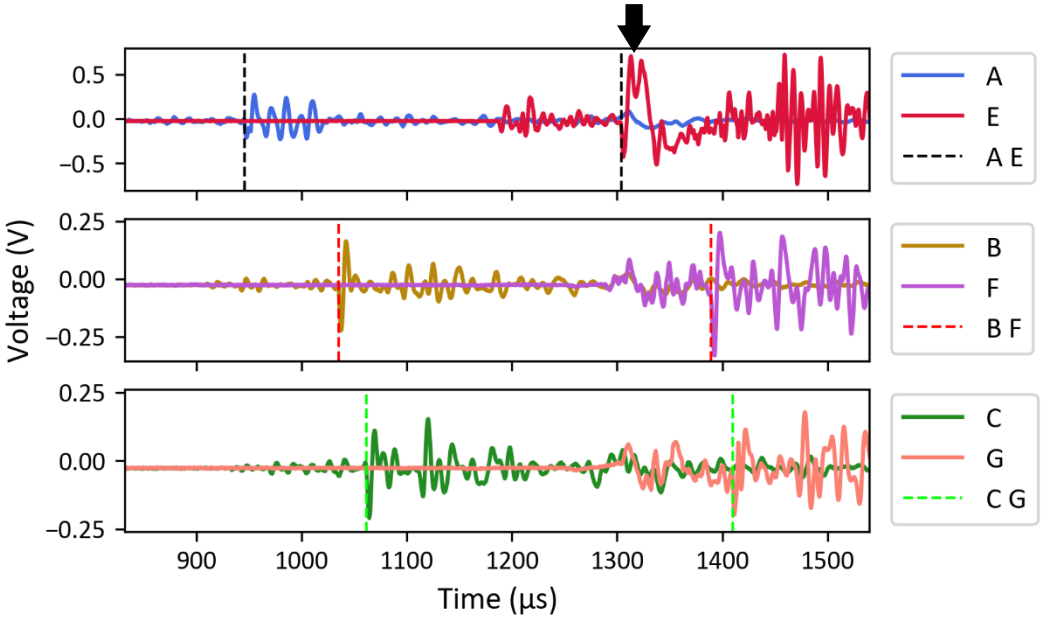

Fig. 3.20: The key time period of acoustic signals from a 1 mm stainless steel 420 sphere shot at ~ 2 km s^{-1}. A relatively broad, split peak marked with an arrow is seen in trace E.

The measurement uncertainties in x and Δt (Eq. 3.3) are independent and uncorrelated, so the general error propagation method for a variable using partial derivatives can be used to calculate the uncertainty in v. The general formula for error propagation is (Kirkup, 2019):

$$\delta z^2 = \sum_{i=1}^{n} \left(\left(\frac{\partial z}{\partial y_i} \right) \delta y_i \right)^2, \tag{3.4}$$

where z is a function of n variables from y_1 to y_n, each with uncertainty δy_i. Applying Eq. 3.4 to Eq. 3.3 results in an expression for the uncertainty in v based on the precision of the measuring apparatus, Eq. 3.5:

$$\delta v^2 = \left(\left(\frac{\partial v}{\partial x} \right) \cdot \delta x \right)^2 + \left(\left(\frac{\partial v}{\partial \Delta t} \right) \cdot \delta \Delta t \right)^2$$

$$\rightarrow \delta v^2 = \left(\left(\frac{1}{\Delta t} \right) \cdot \delta x \right)^2 + \left(\left(\frac{-x}{\Delta t^2} \right) \cdot \delta \Delta t \right)^2$$

$$\rightarrow \delta v^2 = \left(\frac{\delta x}{\Delta t} \right)^2 + \left(\frac{x \delta \Delta t}{\Delta t^2} \right)^2 . \tag{3.5}$$

For shots where the projectile flight was not perfectly normal to the detector, the impact location on the second film could deviate from the first. This is primarily caused by imperfect horizontal alignment of the mounting platform, as much as 1° from parallel to the chamber floor, and to a lesser extent the projectile being pushed slightly of axis as the sabot separates, with a maximum angular deviation of 0.2°. Combined, these can lead to a maximum lateral difference between impact location on the first and second film of 16 mm. However, in the actual data deviations were spread with typical values < 5 mm. Note that 0.2° is the maximum deviation when considering that the projectile is pushed off axis after leaving the end of the launch tube, if it is pushed off axis by the sabot separating further down the gun this angle would increase. Small deviations in projectile flight have a negligible effect on the flight distance x, with a difference in impact location of 16 mm leading to ~ 0.17 mm deviation in x, far smaller than the uncertainty in this measurement. However, depending on proximity to a given sensor, the difference in relative transit time of the acoustic wave in the Kapton films can be significant. A 16 mm difference in location corresponds to a 32% difference in transit time (Δt_{travel}) for a sensor to impact separation (S) of S = 50 mm. To account for this difference, a correction to Δt in Eq. 3.3 is applied by the subtraction or addition of Δt_{travel} depending on whether S on the first film (S_1) is smaller or larger than S on the second film (S_2), respectively. Note that this sign convention only holds for $\Delta t = t_2 - t_1$ and not $\Delta t = t_1 - t_2$. Δt_{travel} can be calculated by rearranging Eq. 3.3 for Δt and substituting the difference in wave pathlength ($\Delta S = |S_2 - S_1|$) for x and the known wave velocity in Kapton films v_{wave} = 1875 ± 25 m s^{-1} for v. This additional component of Δt increases the uncertainty in this value such that $\Delta t = \sqrt{\delta t^2 + \delta t^2 + \delta \Delta t_{travel}{}^2}$. $\delta \Delta t_{travel}$ is comprised of the uncertainties in ΔS, $\delta \Delta S = \sqrt{1^2 + 1^2} \approx 1.4$ mm (here $\delta S_1 = \delta S_2$ = 1 mm) and the uncertainty in the known wave speed δv_{wave} = 25 m s^{-1}, and is given by Eq. 3.6:

$$\left(\frac{\delta \Delta t_{travel}}{\Delta t_{travel}}\right)^2 = \left(\frac{\delta \Delta S}{\Delta S}\right)^2 + \left(\frac{\delta v_{wave}}{v_{wave}}\right)^2, \tag{3.6}$$

where the expression is shown in terms of relative uncertainties, and comes from dividing both by sides of the general expression in Eq. 3.4 by the quantity to which the uncertainty relates. This and all equations described were applied where necessary to each set of data (shot).

There are several sources of random errors, which individually and/or collectively can dominate the measurement uncertainty related to precision. These include:

- Significant differences in peak shape that cause the onset of the signal of interest to be misidentified i.e. differ from the true onset of the signal of interest. This is a particular issue when a train of peaks with similar magnitudes occurs. Consider for example that the second peak in the first group, or train, of large peaks is larger than the first. Under the standardised condition for onset determination, it would be the onset of the second peak that is chosen, even though, similar in magnitude, it could be the first peak that was the true onset. If we take trace A in Fig. 3.20 as a hypothetical example, if the second trough and peak P-P amplitude were slightly larger than the first P-P amplitude, then the onset of this trough would have been taken as the onset time. This is 16 µs later in time than the first trough, and this time difference would represent an error of 4.2% and 8.5% for shots at 2 km s^{-1} and 4 km s^{-1}, respectively.
- Contamination from non-acoustic noise. This occurs when the non-acoustic noise and its associated recovery tail occurs close enough in time to the arrival of the signals of interest, such that they are either dominated by the noise, not detected (due to the dead time of the sensor associated to the recovery tail), or affects the peak shape such that it is miss-identified. This was observed to affect speed determination by as much as 15% in the verification shot programme. In cases where the effects were identified as significant, contaminated data sets and their associated determined speeds were removed from consideration.
- Errors in the calculation of the additional Δt_{travel} due to differences in impact location. This error arises from the fact that the sound speed in Kapton can vary due to material or temperature variations. In the literature the Young's modulus can range from 2.5 to 5.5 GPa. With a density of 1.42 g cm^{-3} for Kapton this leads to a longitudinal wave speed of between 1200 m s^{-1} and 2000 m s^{-1}, depending on the source material and temperature. Members of the DRAGONS team can recall recording a wave speed value for a 25 µm film of close to 2200 m/s, while another gave a value of ~ 1650 m/s (private communication with R. Corsaro 18/06/2021). The wave speed for Kapton quoted in this thesis was calculated by the DRAGONS team over many shots and includes averaging over minor variations in conditions. If we assume a difference between the true wave speed (in the lab that day, as it were) and the experimentally derived value, of

225 m s^{-1} (i.e. a wave speed of 1650 m s^{-1}) its effect can be estimated. A 16 mm separation gives $\Delta t_{travel} \approx 8.5$ µs and 9.7 µs when calculated with the two wave speeds. Thus, a difference of 225 m s^{-1} between the true wave speed in a given set of conditions and the previously determined wave speed, gives a difference in Δt_{travel} of 1.2 µs, corresponding to a 0.3% and 0.6% error in speed measurement at 2 km s^{-1} and 4 km s^{-1} respectively. However, 16 mm is the maximum expected deviation in location and typical variations in wave speed, in the laboratory on a given film, are smaller than this, thus this error is typically smaller than this.

To account for these random errors, averaging the speed over all three pairs is employed. When random errors dominate, it is better to use the standard error in the mean calculated from statistical considerations rather than propagating the measurement uncertainties.

Propagating errors for an average in the standard way is achieved by using Eq. 3.7:

$$\delta v_{Avg} = \frac{\sqrt{\delta v_{AE}{}^2 + \delta v_{BF}{}^2 + \delta \Delta v_{CG}{}^2}}{3}, \tag{3.7}$$

where v_{AE}, v_{BF}, and v_{CG} are the velocities calculated from each pair of sensors respectively, and 3^{-1} is the constant term from the average. However, this would tend to underestimate the uncertainty. To calculate the standard error (SE_v) in the mean from the variance (σ_v') in the data, Eqs. 3.8 – 3.10 were used:

$$\sigma_v{}'^2 = \frac{1}{n}\sum_{i=1}^{n}\left(v_i - v_{avg}\right)^2, \tag{3.8}$$

$$\sigma_v = \sigma_v'\sqrt{\frac{n}{n-1}}, \tag{3.9}$$

$$SE_v = \frac{\sigma_v}{\sqrt{n}}. \tag{3.10}$$

Here σ_v is the best estimate of precision. The uncertainty was calculated in both ways and typically returned $SE_v > \delta v_{avg}$. However, in data with a small spread of values, SE_v could be smaller than δv_{avg}. This would seem unphysical as the uncertainty should not be smaller than the precision the apparatus and procedure can realistically achieve and is a result of chance cancelation of the uncertainties. Thus, δv_{avg} is considered a minimum uncertainty

and it is the larger of the two uncertainties that is taken as the uncertainty in the average speed, the speed output by the detector.

For an example shot at 2 km s $^{-1}$, three separate speeds are obtained, v_{AE} = 2080.6 ms^{-1}, v_{BF} = 2083.6 ms^{-1}, and v_{CG} = 2085.2 ms^{-1} giving an average speed measurement of v_{avg} = 2083.13 ms^{-1}. The spread of individual speed measurements leads to a standard deviation in the average speed, v_{avg} of σ_v = 1.4 m s^{-1}. However, combining the individual measurement uncertainties from each speed measurement gives an uncertainty in v_{avg} of δv_{avg} = 5.4 m s^{-1}. The larger of these separate methods is then taken as the estimate of the uncertainty in the average speed, giving a final overall speed measurement of 2083 ± 5 m s^{-1}.

A similar procedure was carried out for the calculation of uncertainty in the wave speed in the Kapton film ($WS_{mn.}$), as measured from the data set, via Eq. 3.11 and Eq. 3.12:

$$WS_{AB} = \frac{|s_B - s_A|}{\Delta t_{AB}}, \tag{3.11}$$

$$\left(\frac{\delta WS_{mn}}{WS_{mn}}\right)^2 = \left(\frac{\delta \Delta s_{mn}}{\Delta s_{mn}}\right)^2 + \left(\frac{\delta \Delta t_{mn}}{\Delta t_{mn}}\right)^2. \tag{3.12}$$

Here Δs_{mn} is comprised of the difference between impact to sensor displacements from two sensors on the same film, and Δt_{mn} is the difference in onset time between the two sensors on the same film.

The uncertainty associated with the average value of WS_{mn} was calculated in an analogous manner to the calculations of V_{Avg} and SE_v, using Eq. 3.7 to Eq. 3.10 with the different variables substituted.

3.3.7 Microscopy

Microscopy was conducted to determine penetration hole size and morphology. As well as being a useful data set, this was used to confirm a successful shot (i.e. that the projectile reached the first film) and determine whether the projectile was appreciably disrupted by its passage through the first film. For the majority of penetration features, transmission microscopy (the sample lit from beneath) was used, with only a few cases using reflected light (reflection microscopy), which are clearly identified as such in the text.

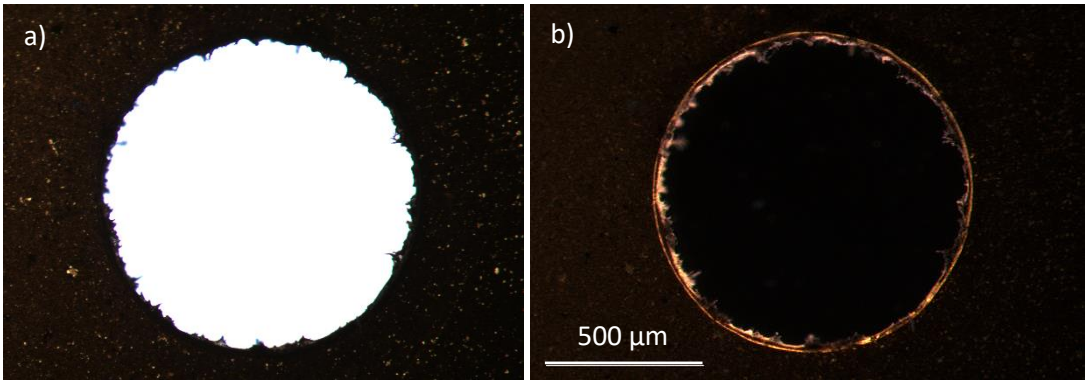

Fig. 3.21: Microscope images of a penetration hole in the first film, viewed from the incident direction of the 1 mm stainless steel 420 sphere that impacted at ~ 4 km s^{-1}. (a) backlight and (b) backlight at a 45° angle. The angled backlighting highlights the edge of the penetration hole (the outer thin bright circle). Both images are to the same scale shown in (b).

Regular backlight transmission microscopy on the first film did not lead to well-lit and clear images of the outer edge of the penetration hole (see Fig. 3.21a) due to the layer of gunpowder and soot deposited on the film extinguishing the light. Adjusting the backlighting so that the light was projected onto the film at a 45° angle greatly improved the visibility of the edge of the penetration hole, and other features raised from the front or back surface of the film (Fig. 3.21b). This method highlighted such features as they were the most illuminated from what was effectively side lighting. Traditional backlighting did produce relatively good images of the penetration holes on the second film (Fig. 3.22a), however, angled backlighting was used for the second film as well to improve consistence between measurements on the first and second film.

Penetration hole diameter was determined by taking the average of the horizontal and vertical diameters of the hole (see Fig. 3.22b), and the diameter was measured from the outer edges of the bright rim, viewed from the incident direction of the projectile (front of the film). For less circular holes, the largest axis was aligned with either the horizontal or vertical axis, thus typically the smallest axis was along the other (orthogonal axis). Measurements were taken from the outer edge, as this is the most consistent point to identify, due to the inner edge and its visibility differing depending on the quantity and morphology of Kapton filaments produced in the impact. Typically, the rim region was ~ 25 µm wide. The errors associated with this measurement are a combination of the judgment error in where the edge of the whole is (taken to be 8 pixels for clear edges and 16 pixels for unclear edges on dirty first films that are converted to µm using calibration with a graticule), the uncertainty in the calibration against the graticule, and the standard error in the mean from the largest and smallest axis that accounts for variation in hole

shape. 8 pixels is ~ 5.0 µm for a magnification of 6.3 and ~ 2.7 µm for a magnification of 11.5.

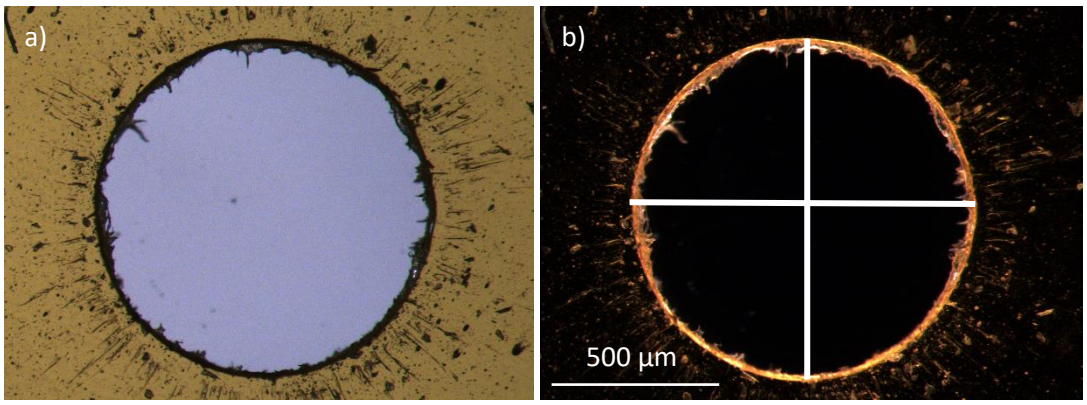

Fig 3.22: Microscope images of a penetration hole in the first film, viewed from the incident direction of the 1 mm stainless steel 420 sphere that impacted at 4 km s^{-1}. (a) backlight and (b) backlight at a 45° angle. Both images are to the same scale shown in (b). The orthogonal diameters from which the average penetration hole diameter is calculated can are shown in (b).

3.4 Conclusion

This chapter introduces the key experimental apparatus used for the research within this study. The materials, design, and construction of the prototype detector, under development in this work, are introduced, and described. Finally, the experimental method is described, and in so doing, so are the working principles of the prototype detector. The experimental method focuses on the determination of signal onset, to enable velocity measurements, and the related uncertainties. While the general principles and procedure for the experiments and the measurements taken are described here, individual experimental parameters are discussed with the corresponding results sections. Other variations of the experimental setup are also introduced later in the thesis, where appropriate.

Chapter 4: Determination of Detector Performance and Results for Large Projectiles

4.1 Introduction

A key question for investigation in the development of thin film, acoustic, TOF cosmic dust and debris detectors is that of detector performance, namely what is the accuracy of the impactor speed measurement made by such detectors? This question is of importance for two reasons. Firstly, thin film detectors need to provide accurate speed measurements to be capable of distinguishing between cosmic dust and orbital debris, and hence determine the threat they pose. Secondly, knowledge of the prototype's accuracy is required to determine whether direct measurement of impactor speed from the prototype is a suitable method for the particle deceleration studies to be conducted, presented in Section 5.3.2. This chapter presents the experimental parameters used to investigate this question, and results for larger 1 mm sized projectiles.

4.2 Experimental Parameters

To determine the speed measurement accuracy of the prototype detector, the speed of the projectile as measured by the detector was compared to the incident projectile speed as measured by the light gate system up-range in the gun. To eliminate any uncertainty in this comparison arising from deceleration upon impact with the detectors first film, a projectile that would likely not experience deceleration or be disrupted was required. Stainless steel 420 (StSt420) spheres with a diameter (d_p) of 1 mm were therefore used. With their relatively high strength, and d_p = 1 mm vs film thickness f = 12.5 µm giving a f:d_p = $\frac{1}{80}$, no deceleration or disruption was expected (Gardner *et al.*, 1997). Seven successful shots with orthogonal projectile incidence, at speeds of $\sim$ 2 km s^{-1} and 4 km s^{-1} were conducted. The parameters of each shot are given in Table 4.1. Note that for shot Veri.7 the frames were mounted separately, such that they were free standing, without the connecting trusses. The connecting trusses were usually used to provide a well determined and repeatable separation between the films, but shot Veri.7 was performed to check that there was no acoustic contamination between the two Kapton films via the trusses.

Table 4.1: Key shot parameters for seven shots to determine detector/prototype performance. Shot ID is the name given to each shot for reference. d_p is the projectile diameter and v_{LGG} is the speed of the incident particle as measured by the LGG's light gate system. Angle of incidence is measured from normal (perpendicular) incidence.

Shot ID	d_p (mm)	v_{LGG} ± 1 % (m s^{-1})	Angle of Incidence (°)
Veri.1	1	2084	0
Veri.2	1	2192	0
Veri.3	1	2132	0
Veri.4	1	3900	0
Veri.5	1	3779	0
Veri.6	1	3740	0
Veri.7	1	2097	0

4.3 Results

Acoustic signals from each of the seven 'Veri.' shots are shown below in Fig. 4.1 to Fig. 4.9. Acoustic data is presented in sensor pairs to allow for better distinction between traces and direct comparison between signal onset times from each sensor. Vertical dashed lines in the figures mark the time of onset for acoustic signals at each sensor, determined according to the criteria set out in Section 3.3.5. In most cases only the crucial part of the data including the onset of the signals are shown. However, the full traces of Veri.3 (Fig. 4.3) are shown to give another example of a full set of signals, without repeating the data shown in section 3.3.5 from Veri.1. Full traces of all shots can be found in the Appendix I.

It is assumed, unless there is reason to believe otherwise, that the first thing to impact the target is the projectile. This assumption is based on where the projectile is positioned in relation to the contents of the stages of the gun up-range of the projectile (towards the powder chamber). As discussed in Section 3.3.1, shots can feature unintentional gun debris, of which there are two main types, unexpected and expected. Unexpected debris is a result of an unexpected incident, such as a sabot segment passing through the hole in the stop plate or hitting the edge, resulting in a sabot segment or multiple smaller pieces of isoplast as debris, respectively. By contrast, expected debris, is debris associated with the first stage of the gun, including unburnt powder and soot which often travels the length of the gun (and here can blacken the target around the impact site). Expected debris comes down after the projectile and impacts the target late enough in time that it does not tend to

contaminate the data. On the other hand, unexpected debris can follow the projectile much closer in time, and contaminate the data. In instances where impacts occur close in time, issues arise with the fact that there is no way of confirming that a piece of debris did not lead the projectile. An example of data contaminated by unexpected debris can be found in Section 5.3.2, Fig. 5.14. Fig. 4.3 is an example of a set of data that shows signals from later arriving pieces of debris, which did not affect the data from the projectile impact.

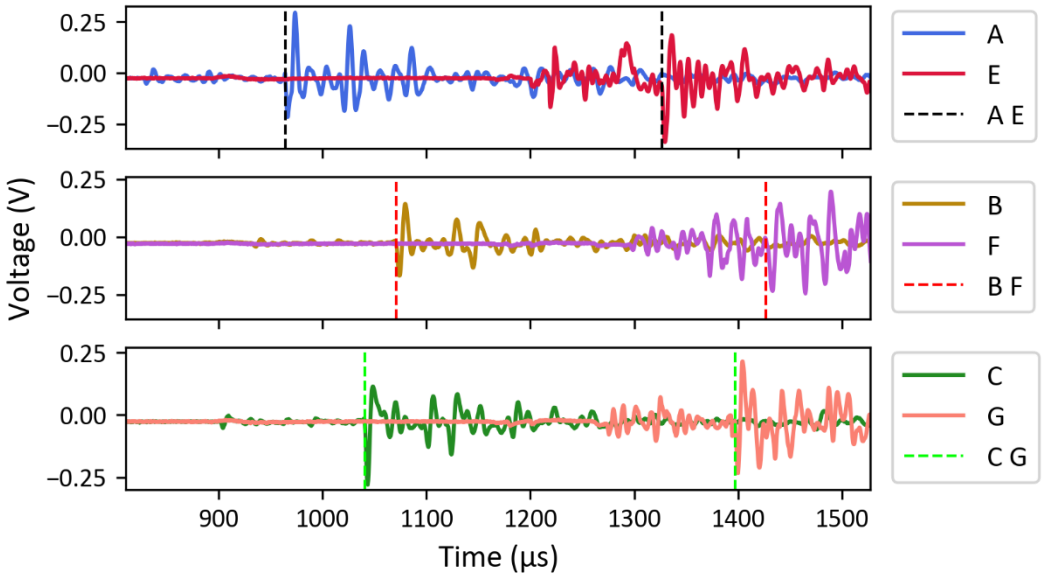

Fig. 4.1: The key time period of acoustic signals in shot Veri.1, d_p = 1 mm, v_{LGG} = 2084 m s^{-1} with normal incidence. Vertical dashed lines represent the onset times for each sensor in a pair. Note that the onset times differ due to a non-central impact on the Kapton film, resulting in different path lengths and thus different signal arrival times at each sensor on a given film.

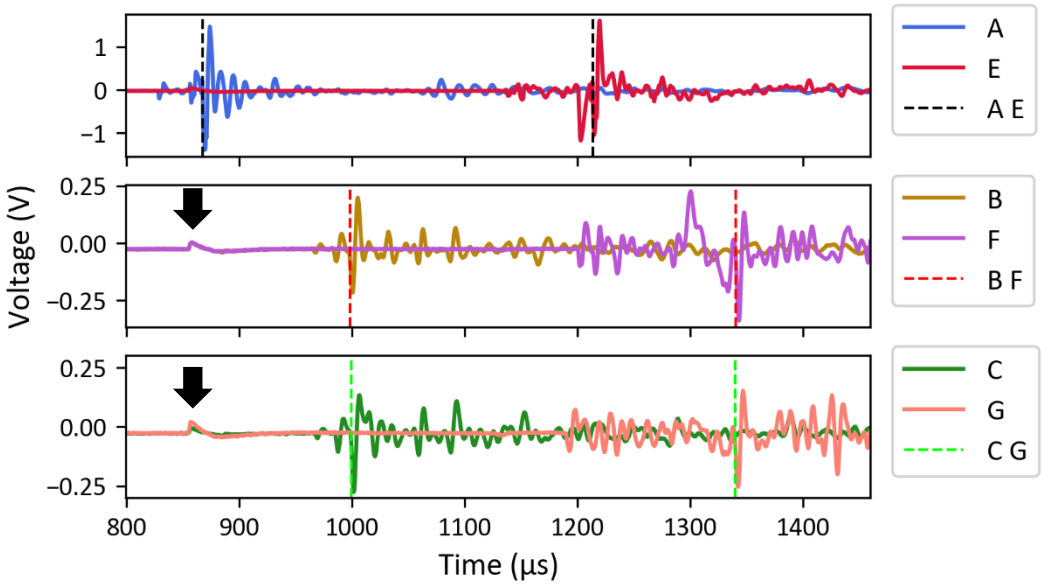

Fig. 4.2: The key time period of acoustic signals in shot Veri.2, d_p = 1 mm, v_{LGG} = 2192 m s^{-1} with normal incidence. Vertical dashed lines represent the onset times for each sensor in a pair. Black arrows indicate small non-acoustic noise signals.

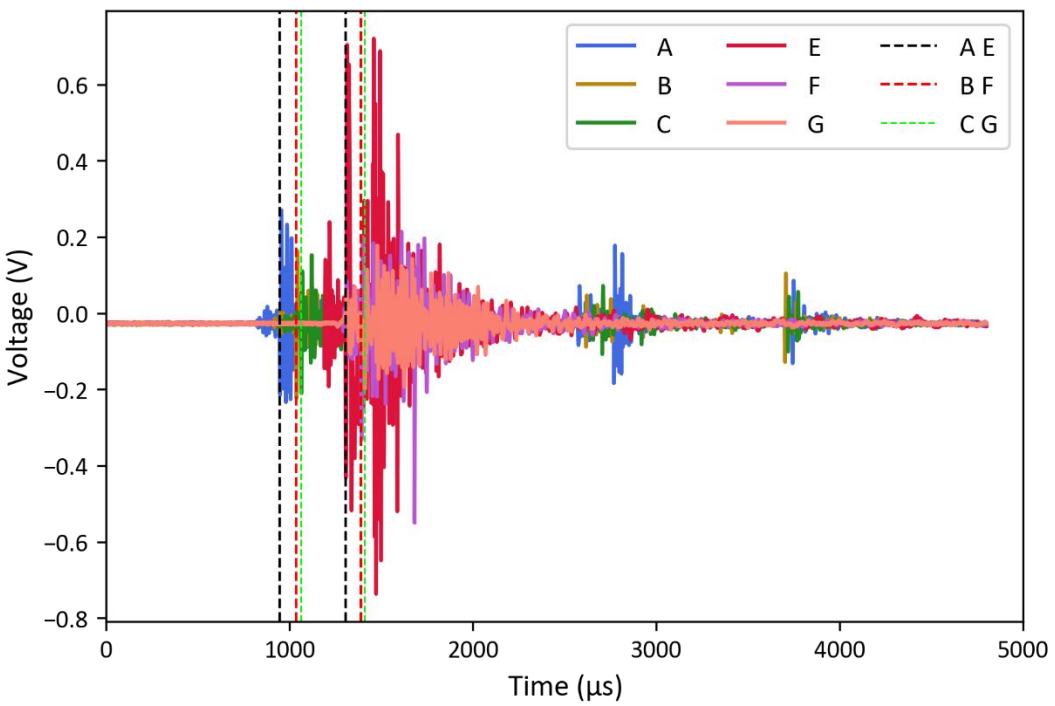

Fig. 4.3: The full trace of signals in shot Veri.3, d_p = 1 mm, v_{LGG} = 2132 m s^{-1} with normal incidence. Vertical dashed lines represent the onset times for each sensor in a pair. Signals from later arriving pieces of debris can be seen arriving around 2571 µs and 3699 µs.

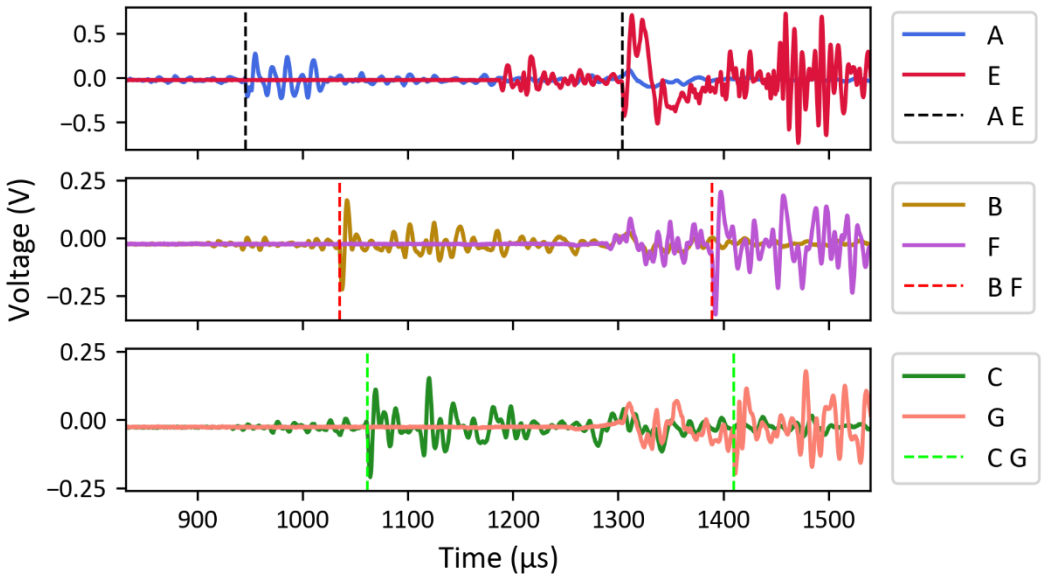

Fig. 4.4: The key time period of acoustic signals in shot Veri.3, d_p = 1 mm, v_{LGG} = 2132 m s^{-1} with normal incidence. Vertical dashed lines represent the onset times for each sensor in a pair

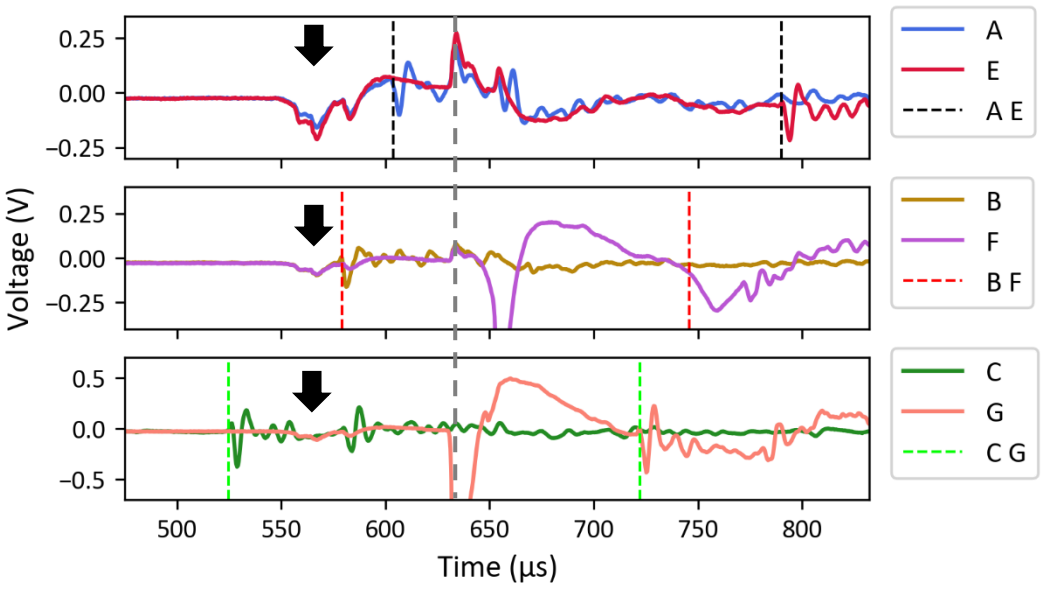

Fig. 4.5: The key time period of acoustic signals in shot Veri.4, d_p = 1 mm, v_{LGG} = 3900 m s^{-1} with normal incidence. Black, red, and green vertical dashed lines represent the onset times for each sensor in a pair. Black arrows indicate small non-acoustic noise signals, and the dashed grey line indicates the onset of a large non-acoustic noise peak, which ultimately contaminated the onset of the acoustic signal of interest in trace F.

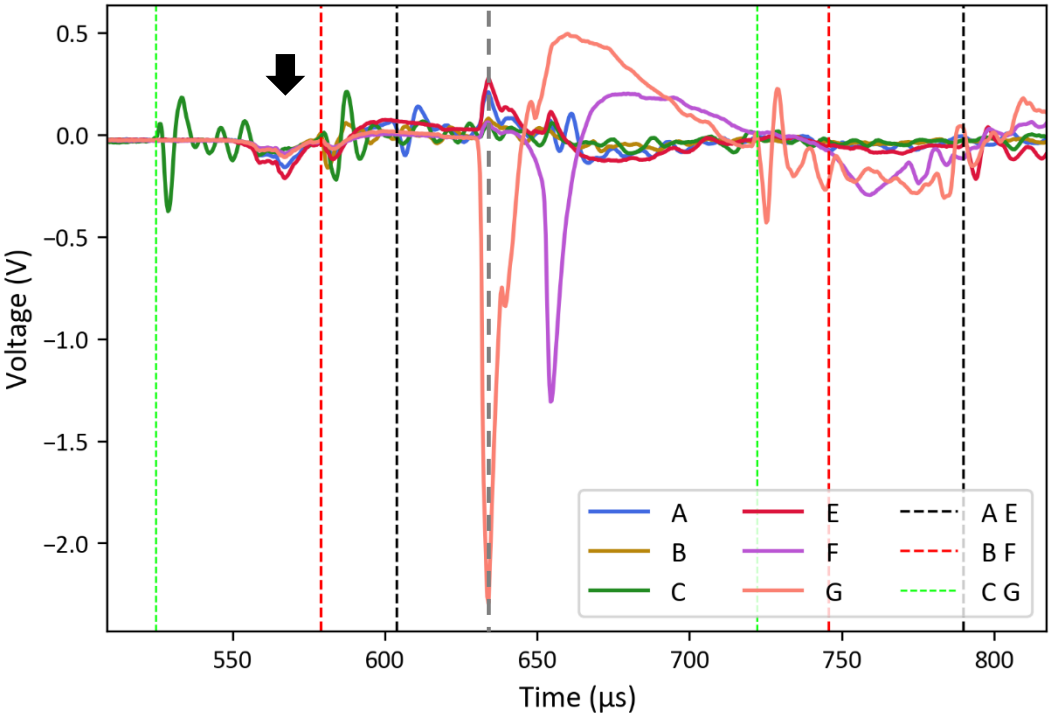

Fig. 4.6: The key time period of acoustic signals in shot Veri.4, d_p = 1 mm, v_{LGG} = 3900 m s^{-1} with normal incidence. Traces are plotted on a single extended y-axis to show the full magnitude of the non-acoustic noise signals, marked with the grey dashed line. Black, red, and green vertical dashed lines represent the onset times for each sensor in a pair. The black arrow indicates small non-acoustic noise signals.

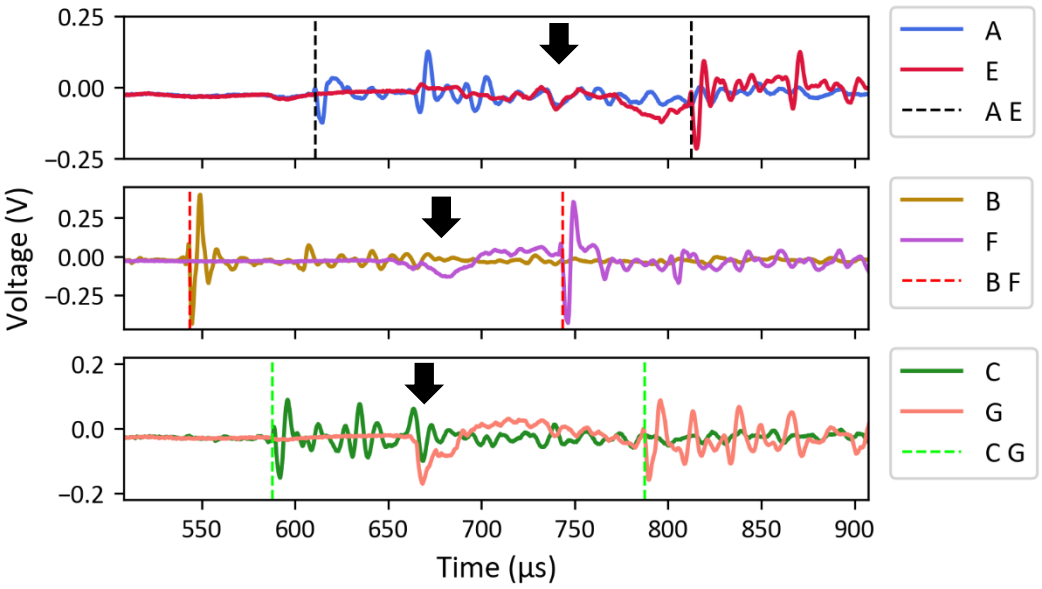

Fig. 4.7: The key time period of acoustic signals in shot Veri.5, d_p = 1 mm, v_{LGG} = 3779 m s^{-1} with normal incidence. Vertical dashed lines represent the onset times for each sensor in a pair. Black arrows indicate non-acoustic noise signals.

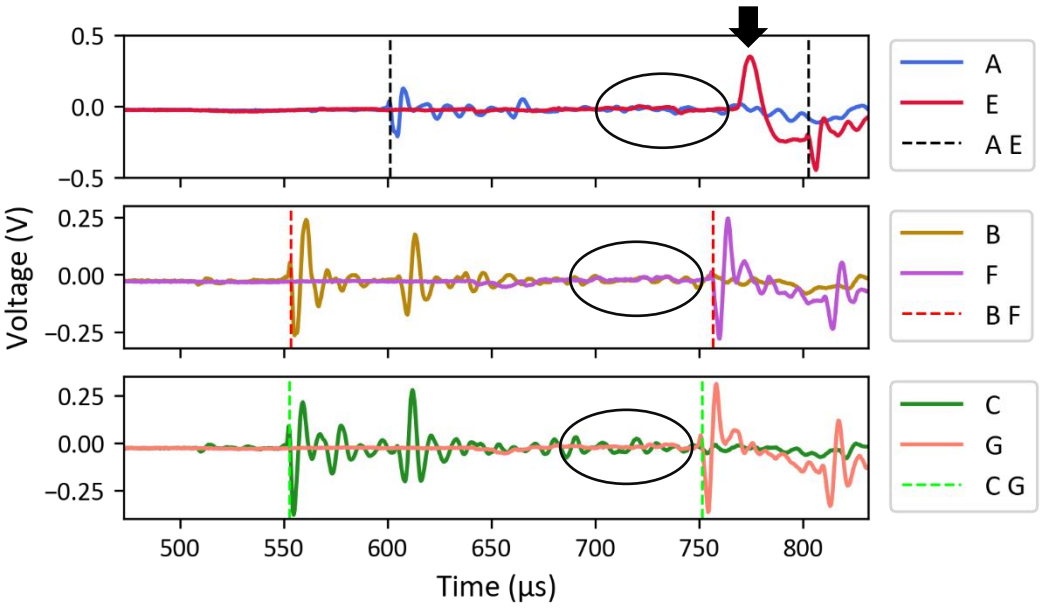

Fig. 4.8: The key time period of acoustic signals in shot Veri.6, d_p = 1 mm, v_{LGG} = 3740 m s^{-1} with normal incidence. Vertical dashed lines represent the onset times for each sensor in a pair. A black arrow indicates a non-acoustic noise signal. The circled regions highlight the locations in which preceding acoustic peaks that are relatively large compared to those seen in the first film, are typically seen for d_p = 1 mm projectiles at 2 km s^{-1} (e.g., Fig. 4.1, Fig. 4.2, and Fig. 4.4).

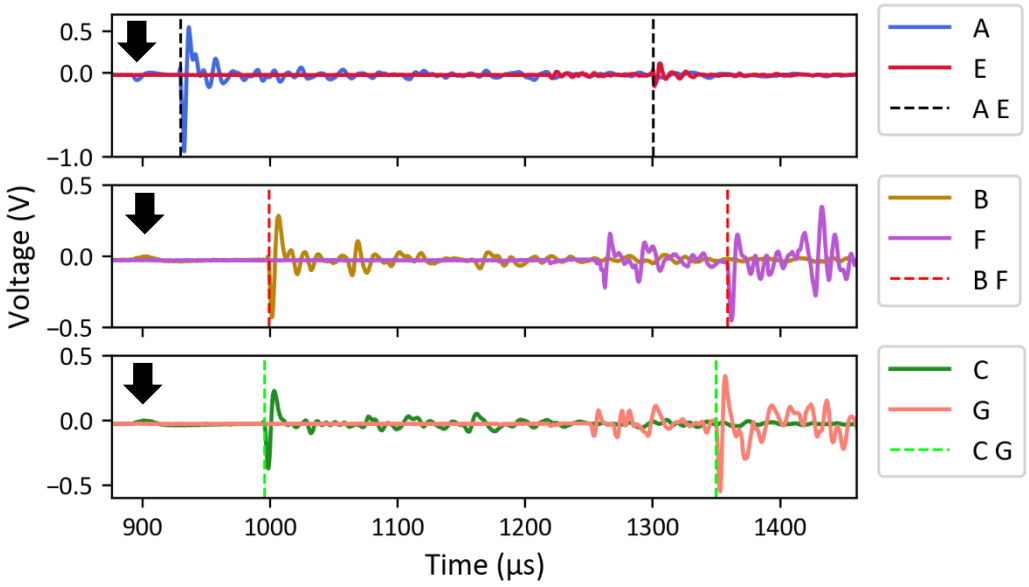

Fig. 4.9: The key time period of acoustic signals in shot Veri.7, d_p = 1 mm, v_{LGG} = 2097 m s^{-1} with normal incidence. Vertical dashed lines represent the onset times for each sensor in a pair. Black arrows indicate small non-acoustic noise signals. For this shot, the frames that support the Kapton films were mounted separately, with no connecting structure. The acoustic signals seen in the second film show similar characteristics to those observed in shots with a connecting structure (e.g., Fig. 4.1, Fig. 4.2, and Fig. 4.4). The reduced magnitude in trace E is a consequence of sensor E beginning to fail. Shortly after this shot, when the sensors were tested prior to another shot, sensor E had failed entirely and required replacing.

4.3.1 Determination of Signal Features

The characteristic shape of acoustic signals is their positive to negative (or vice versa) short period oscillatory behaviour. However, signal shape can vary significantly between shots, and to a lesser extent between sensors on the same film, for a given shot (see Fig. 4.1 to Fig. 4.9 for variability). Variation is somewhat expected, as individual impacts are different, and propagation effects along any one path will cause differences in the acoustic signal observed.

The smaller peaks that precede the signals of interest, described in the experimental chapter, can be seen in all of the 2 km s^{-1} shots, except for trace A, B and C in Fig. 4.9, although these may have been affected by the presence of non-acoustic noise, marked with the black arrows. Their oscillatory nature suggests that these preceding peaks are acoustic in origin. Why then, do these peaks precede what is believed to be the onset of the impact signal? One possible explanation for these peaks is that they are produced by a gas blast from co-moving gas proceeding the projectile, essentially a bow wave of gas. To test this

potential source, a shot with an empty sabot was conducted. For this shot, all parameters were kept consistent with a shot for a 1 mm StSt420 sphere at a nominal speed of 2 km s^{-1}, with the only exception that a projectile was not loaded into the sabot. Thus, the only thing to pass through the stop plate, enter the TOF chamber and subsequently reach the prototype in the target chamber, would have been co-moving gas accelerated in front of and around the sabot, followed by any later arriving gunpowder, soot and debris from the first stage of the gun.

For the empty sabot shot, the sabot attained a speed of 2176 m s^{-1} ± 4%, measured by the timing taken from the muzzle laser and stop plate. Only powder and soot hit the first film, with no significant debris, and no penetration of the film. Reflective of this, the acoustic signals detected in the empty sabot shot (Fig. 4.10 and Fig. 4.11) only showed one set of peaks, corresponding to the deposition of powder and soot. These signals cannot be mistaken for a projectile impact; as they arrived later in time than expected for a projectile impacting the same location, with a much-reduced intensity (~ 0.04 V max amplitude), and a different signal shape. The gradually increasing signal intensity is quite different from a projectile impact signal, which feature an early and significant maximum amplitude followed by a decaying intensity. This suggests that if present a gas blast proceeding the sabot did not produce signals in the first film. Neither were there any signals detected in the second film. Thus, a gas bow wave produced by the sabot and projectile accelerating in the evacuated chambers is unlikely to be the cause of the small preceding peaks observed. Observing no signals in the second film in this shot also confirms that no gun vibration is transferred to the detector through the insulated mount it stands on.

As well as small signals preceding the acoustic signals of interest on the first layer of Kapton, there are also some larger acoustic-like signals that precede the signals of interest on the second layer. These signals in traces E, F, and G of a shot (see examples in Fig. 4.1, 4.2, 4.4 and 4.9) could be supposed to arise from acoustic waves from the impact on the first film propagating through the connecting trusses into the second film. Initially to test the possibility of acoustic signal contamination between films, in-situ tap test were conducted to see if signals transferred from one to the other. Tap testing consisted of hitting a single film with short sharp taps from a screwdriver handle (demonstrated in Fig. 4.12) while recording the PVDF sensor outputs. No sign of signal transfer was observed (Fig. 4.13).

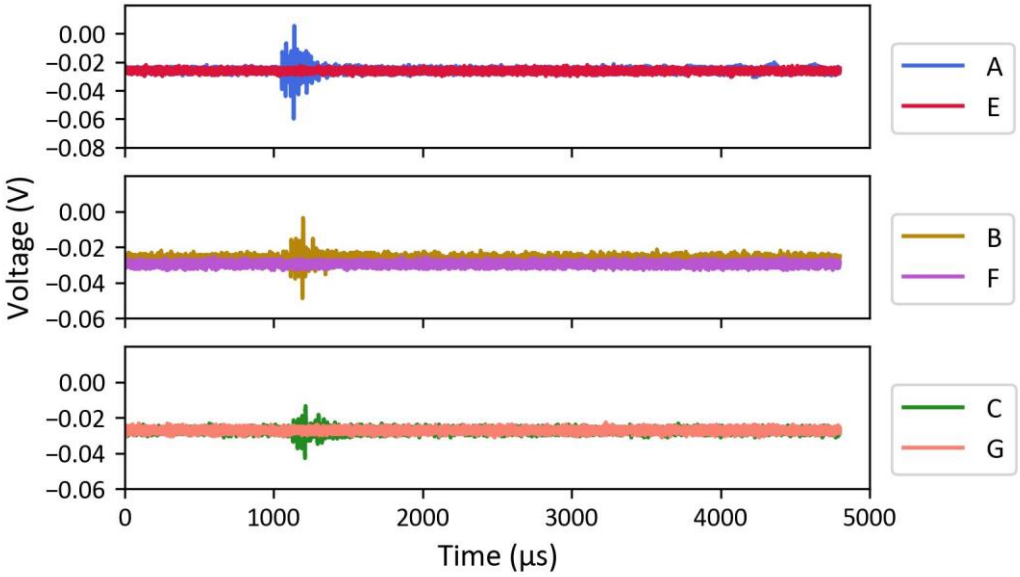

Fig. 4.10: Acoustic signals for the shot conducted with an empty sabot at ~ 2 km s^{-1} (recorded sabot speed 2176 m s^{-1} ± 4%). Only one set of signals were recorded on the first film, arriving later than expected and corresponding to the later arriving powder and soot from the first stage of the gun.

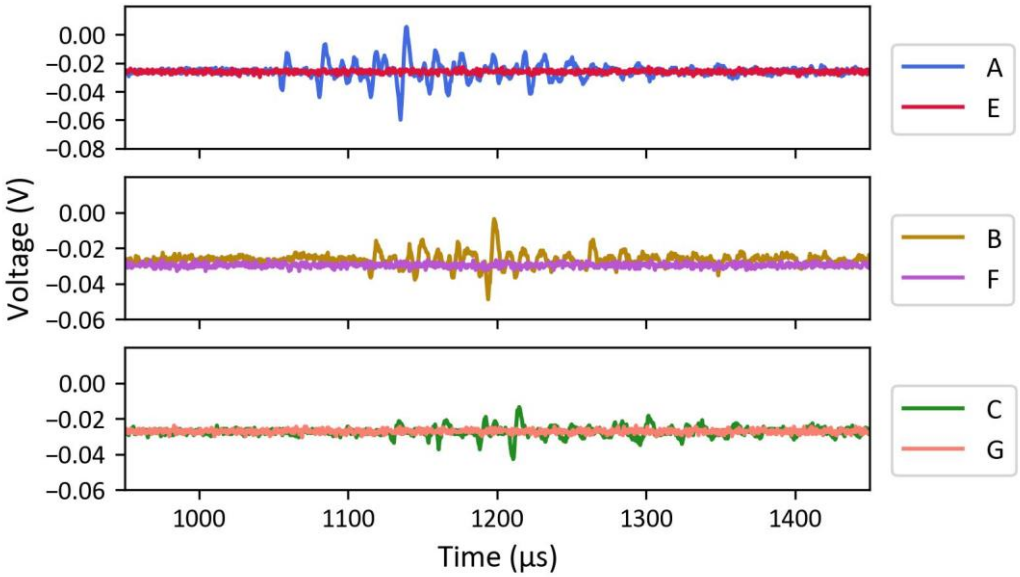

Fig. 4.11: The time period of interest for the acoustic signals in the empty sabot shot. These cannot be mistaken for signals relating to a projectile impact, arriving later than expected, with a low magnitude, and a gradual increase and decrease in intensity.

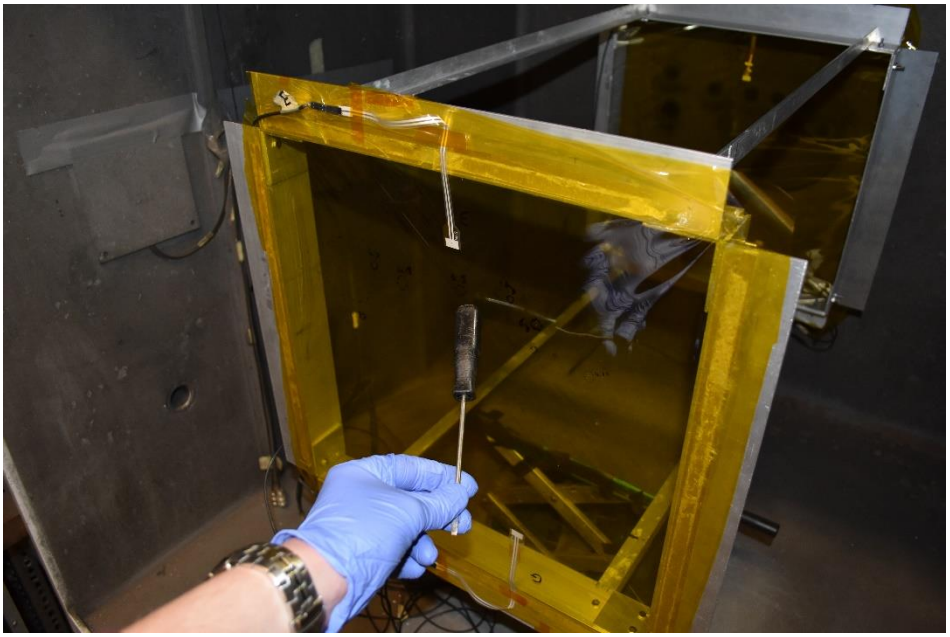

Fig. 4.12: Demonstration of how tap tests were performed. Note these used the same experimental setup as shots, i.e. the same mount and readout system etc., only with the projectile impact replaced with a screwdriver tap, and data acquisition trigger by acoustic waves reaching the closest sensor instead of the stop plate.

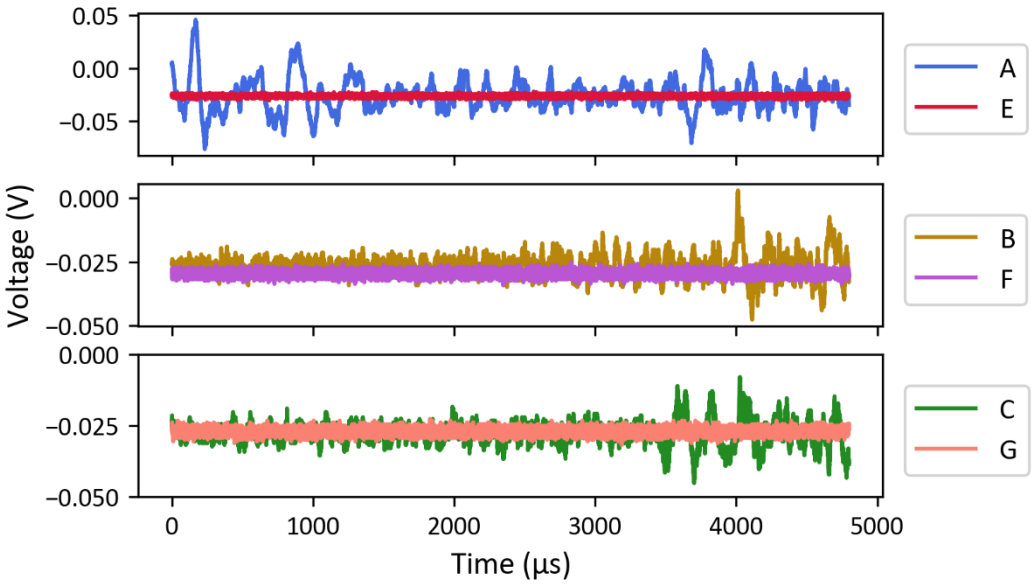

Fig. 4.13: Acoustic signals from a tap test on the first film of the detector, showing no transmission of acoustic signals from the first film to the second via the aluminium supporting structure.

To further determine whether acoustic waves produced in a hypervelocity impact are transmitted from the first film to the second via the trusses used in the prototype to maintain a fixed separation, it was decided to carry out some hypervelocity impact experiments. Shot parameters were kept consistent with a 1 mm StSt420 shot at 2 km s^{-1},

and three methods of determining acoustic contamination employed. The first test shot involved cutting an 8 cm diameter hole into the second film, such that when aligned with the gun barrel the projectile would impact the first film and pass through the second film without impact (Fig. 4.14a). This would produce acoustic waves in the first film but not the second and show if any transmission was occurring via the frame. Unfortunately, the shot with this set up was inconclusive due to more debris than normal, including a fragment of the burst disk that hit the second film near the edge of the hole.

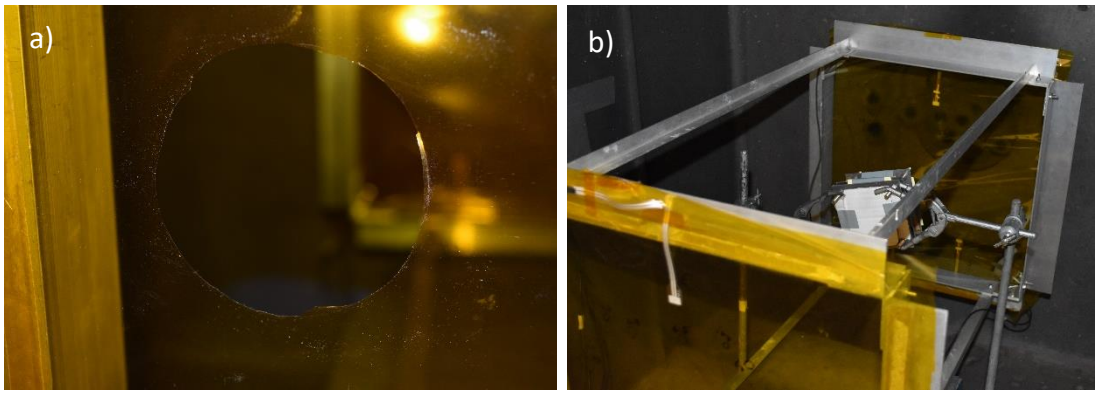

Fig. 4.14: (a) Experiment to test transmission of acoustics through the prototype frame, by cutting a hole in the second film, removing the second impact surface and thus any observed acoustics must have been transmitted. (b) Experiment to test the transmission of acoustics by stopping the projectile from hitting the second film, using a projectile capture system.

To reduce the likelihood of the second film being impacted another approach was tried. This time a standard prototype with complete films (no hole) was used, and a projectile capture system (composed of three individual, separated, aluminium plates with catchment paper and card) was placed between the two films to stop the projectile before impacting the second film, after it had passed through the first (Fig. 4.14b). The resulting PVDF signals were different in shape, magnitude, and the order of arrival, thus could not be mistaken for the acoustic noise seen in a normal shot. Considering the signals observed it could be that some form of ejecta/spall from the capture system hit the second film, thus also creating acoustic signals in the second film, and was therefore deemed inconclusive.

In light of these inconclusive experiments, an altogether different approach was tried. This sought to remove the possibility of transmission by removing the trusses, and effectively having two layers of Kapton physically isolated from each other. The test (shot Veri.7) was to see whether the preceding signals in traces E, F and G remained. The 12.5 µm film

prototype was disassembled so that each of the film frames could be separately mounted in the target chamber, and isolated from one another (Fig. 4.15). Rubber insulation (3 mm thick) was applied between the frames and the mounting platforms as before. 3 mm of rubber and 44 mm of chip-board were used to further insulate the platforms from the floor of the chamber. The separation between isolated films was 0.750 ± 0.002 m. The increase in uncertainty was due to difficulty in measuring the separation inside the target chamber.

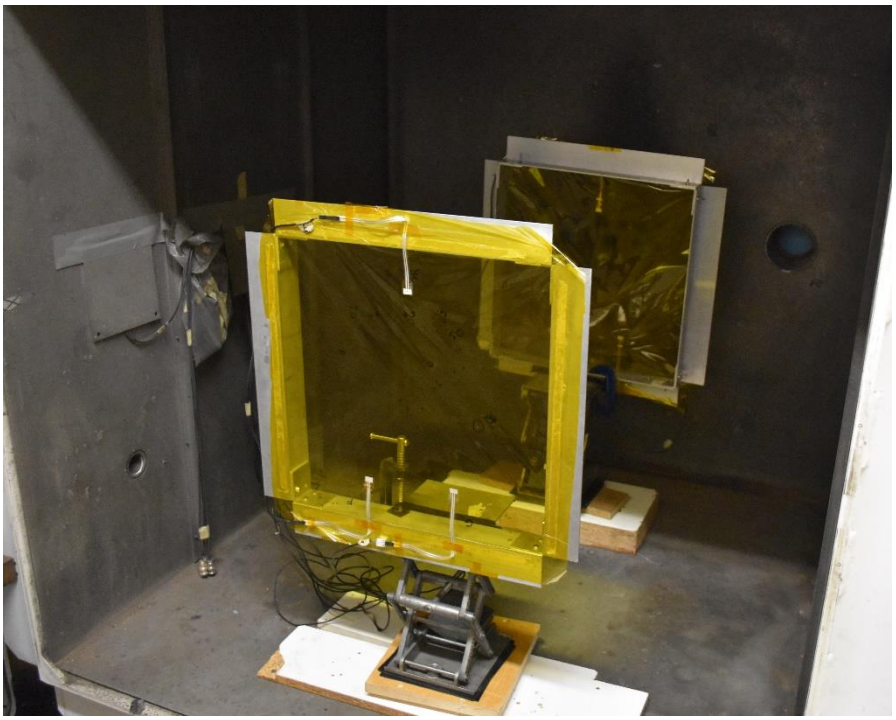

Fig. 4.15: Isolated films in the target chamber for the shot to determine whether any acoustic contamination occurs between films. Films are aligned with one another along the gun barrel axis, separated by 0.750 ± 0.002 m. Rubber, and rubber and chip-board were used to insulate the frames from the mounts and the mounts from the floor of the chamber, respectively.

Fig. 4.9 shows the acoustic signals from the separately mounted films. Traces F and G clearly show preceding signals that are characteristic of those seen in shots with the connecting frames present. Trace E is less clear as a faulty sensor affected the overall intensity measured. Similar peaks, in shots with and without connecting trusses, suggest the original prototype design (which includes 5 acoustic discontinuities between the two films) was not responsible for the preceding signals observed on the second film, but they are inherent to some aspect of the impact process, such as fast ejecta from the rear of the front film, or originate from the impact on the second film itself. To investigate this further, hydrocode

modelling (using a software such as Autodyn) could be the focus of future work, to see if modelling also predicts these preceding waves to originate from the impact.

All preceding peaks are thought to originate from the impact of the projectile itself. This is because firstly, there were preceding peaks present for the first film, yet there is no ejecta incident on this film from an up-range film, and for successful shots it is unlikely that there would be any debris traveling ahead of the projectile. Secondly, if the order of the onset times of the signal of interest are considered, it is noticeable that the preceding peaks arrive in the same order and with similar time intervals between sensors (i.e. the time difference between the signal of interest in A and B is similar to the time difference between the first preceding peak in A and B). This is indicative of the source of the preceding peaks being located at the site of the impact and the acoustic wave subsequently reaching each sensor located further from the site. This observation is true for the preceding peaks in both the second and first film. Considering the time difference between the first preceding peak and the signal of interest in a sensor trace, for shots Veri.1 to Veri.3 (given in the first line for each shot in Table 4.2), the time difference is not linked to the separation between the impact and sensor (shown in the second line for each shot in Table 4.2). Thus, the difference in arrival time between these two acoustic components, seemingly from the same impact, is unlikely to be due to a difference in wave propagation speed, such as the difference in wave speed between a longitudinal and transverse wave. In general, a smaller spatial separation should lead to a smaller time difference between preceding peaks and peaks of interest, and this is not seen.

Table 4.2: The time between the onset of the small preceding peaks and the onset of the larger peaks of interest for each sensor in shots Veri.1 to Veri.3 are given in the first line of each shot. The impact to sensor separation for each shot is given in the second line for each shot.

Shot ID	A (± 1.4 µs) (± 1 mm)	E (± 1.4 µs) (± 1 mm)	B (± 1.4 µs) (± 1 mm)	F (± 1.4 µs) (± 1 mm)	C (± 1.4 µs) (± 1 mm)	G (± 1.4 µs) (± 1 mm)
Veri.1	136.4 145.0	126.4 145.0	138.4 349.0	130.4 338.0	138.4 287.0	123.2 278.0
Veri.2	39.2 113.5	76.4 119.5	32.6 281.5	140.0 280.0	32.0 325.5	149.0 328.0
Veri.3	122.0 31.0	116.4 34.5	126.0 280.5	94.2 277.5	129.6 277.5	105.0 276.0

4.3.2 Non-acoustic Noise

Non-acoustic noise was thought to originate from the light flash produced by the plasma created in the impact. The smaller peaks that are more homogeneous across all sensors (even on different films) are thought to be caused by photons, with the fast speed of light causing noise in different sensors effectively simultaneously. However, there would still be some variation in intensity due to the relative position of each sensor and thus the effective sensor area within a line of sight. The larger magnitude noise peaks seen in traces F and G in shot Veri.4 (Fig. 4.6), which are separate in time, are thought to originate from charged ions produced in the plasma, due to their uncharacteristically large amplitude and given that ions will be emitted less homogeneously and thus sensor response is likely more variable. While impact induced plasma lasts for a very short time, the relatively long tails seen in the non-acoustic noise are likely to be a result of the sensors saturating, and thus represent the sensors recovering. Induced plasma and light flash intensity is known to be proportional to approximately v^3, so will be more likely at higher speeds (see Section 2.7.1). This is consistent with the data here, with non-acoustic noise features present in all three of the 4 km s^{-1} shots, while only present in two of the four 2 km s^{-1} shots and with a lower magnitude.

To confirm light flash as the source of this noise, or otherwise, experiments were conducted towards the end of the PhD, in conjunction with the DRAGONS team. These experiments aimed to record the light flash with photodiodes, to see whether light flash could be used for speed determination. My main contribution to these experiments was on the second Kapton film, to which I included the addition of PVDF sensors to allow the comparison between any noise and the light flash observed.

The experiment was set up analogously to the TOF experiments conducted with the prototype, as described in Section 3.3, only this time photodiodes were responsible for the time of impact determination. Fig. 4.16 shows a schematic of the experimental setup, and Fig. 4.17 shows a picture of the setup in the target chamber, with a thick black material shroud to reduced light reflection off of the target chamber side walls. This time the frames holding the Kapton films were plastic with internal Kapton dimensions of 18 cm x 18 cm (324 cm^2), and a film separation of 0.555 ± 0.001 m. Two photodiodes mounted on a black plastic plate (with a hole at their centre to allow passage of the projectile) were positioned 21 ± 1 mm in front of each film, facing towards the film, thus providing four photodiodes in total. The second Kapton film was instrumented with two PVDF sensors, one on the front

and back of the film, and a third PVDF sensor adhered to the frame (as shown in Fig. 4.17). Note that due to the supply issues with sensors, the two sensors on the Kapton film were closer to 1/6 sized sensors than 1/4, since a rough edge was produced when initially cut and requiring it to be recut to a shorter clean edge. Furthermore, the third (1/2 sized) frame mounted sensor was reused from an initial test set up experiment, thus this featured the original Kapton film it was adhered to sandwiched between the sensor and frame (i.e. PVDF sensor|glue|Kapton|glue|frame). Seven successful shots were conducted with the experimental parameters outlined in Table 4.3, most of which were at ~ 5 km s^{-1} to improve the likelihood of light flash production. Note that all shots were at normal incidence, and that the 0.8 mm projectiles were StSt420 spheres, while all other projectiles in this series of shots were StSt304 spheres. This difference in the grade of steel was due to the available smaller sized projectiles in the projectile supply being StSt304.

Table 4.3: Experimental parameters for the light flash related shots. The 0.8 mm diameter (d_p) projectile was a StSt420 sphere, while all other projectiles were StSt304 spheres. Whether a flash was deemed as present was based on measuring a noticeable photodiode response.

Shot ID	d_p (mm)	v_{LGG} ± 1 % (m s^{-1})	Flash Present
Light.1	0.8	4925	Yes
Light.2	0.5	5157	Yes
Light.3	0.5	4941	Yes
Light.4	0.5	4892	Yes
Light.5	0.5	3816	Yes
Light.6	0.5	2000	No
Light.7	0.3	5131	Yes

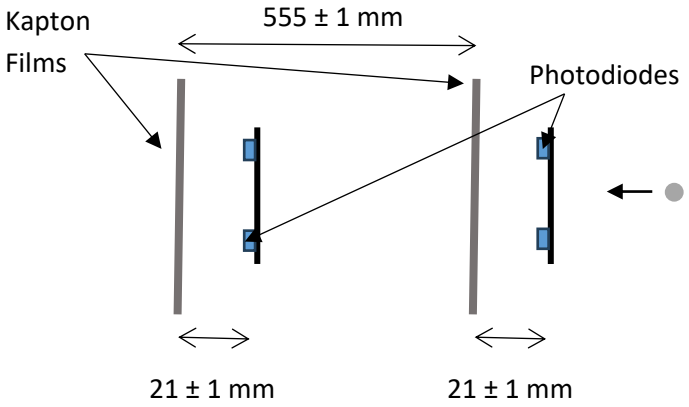

Fig. 4.16: A schematic of the experimental setup for light flash experiments. The direction of the projectile is shown from the right of the figure (the front of the chamber). The second Kapton film (thick grey line on the left of the figure) is equipped with PVDF sensors. The blue squares show the placement of photodiodes.

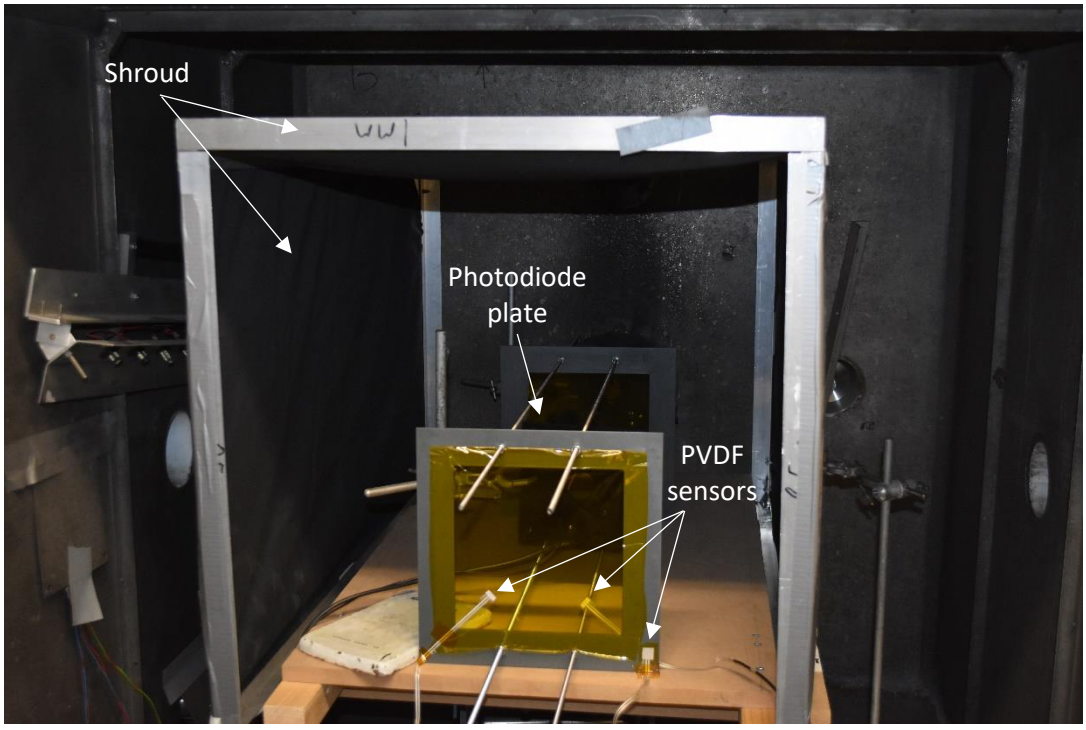

Fig. 4.17: A TOF experiment setup, analogous to the prototype detector, to determine whether light flash can be used for projectile speed determination, viewed from behind the second Kapton frame. The second plate holding the second set of photodiodes can be seen through the second Kapton film. PVDF sensors adhered to the second Kapton film/frame are shown. The left most sensor in the image is adhered to the rear of the film, the rightmost adhered to the frame, and the other adhered to the front of the film.

The results recorded for Light.1 are presented in Fig. 4.18 and Fig. 4.19. Traces 1 – 4 are the photodiode responses, with 1 and 2 being the first two photodiodes in front of the first Kapton film, and 3 and 4 being the second two in front of the second film. Traces 5 - 7 are the PVDF response, 5 is on the front of the film, 6 on the rear, and 7 on the frame. The photodiodes respond in the order that the films are impacted (1 and 2 first, then 3 and 4), in this case producing a negative, step-like response from high voltage to low voltage, confirming the presence of a light flash. The PVDF signals showed small single peaks with a recovery tail, characteristic of the non-acoustic noise observed in the earlier verification shots (Veri. programme presented above), arriving ahead of the acoustic signals. This non-acoustic noise signal coincided in time with the photodiode response for an impact on the second film, suggesting that this noise could well be produced by electromagnetic (EM) waves. Although there is some variation in the shape of photodiode response, the other shots showed similar noise like signals in the PVDF coinciding with the onset of light flash (traces for Light.2 to Light.7 can be seen Appendix I). Significant light flash was not observed for the 0.5 mm sphere at 2 km s^{-1} (Light.6 – the experiment with lowest speed), further suggesting that light flash and thus noise are less likely at lower speeds. Not all shots with observed light flash (significant photodiode response) gave rise to interference in the PVDF sensors.

Interestingly the PVDF sensor on the frame did not pick up the interference from the light flash. This could be due to the frame shielding 50% of the sensor surface area. Conversely the noise may be due to charge or charged particles traveling across the Kapton surface, thus the sensor on the frame would not have picked up the charge. However, this does not agree with the simultaneous observation of such signals on different films produced earlier (Fig. 4.2, Fig. 4.5, and Fig. 4.6). Both PVDF sensors on the film show similar acoustic responses, suggesting that there is negligible difference between a sensor adhered to the front or back of the film (as is the case for the first and second films of the prototype respectively). The frame mounted sensor did not pick up significant acoustic signals, with only insignificant oscillations on the level of the electronic noise noticed in the traces. This further suggests that acoustic waves are not likely to propagate from the film into the film frame, with an appreciable intensity required to be able to propagate along an adjoining structure into another frame and subsequently another film and its mounted PVDF sensors.

In the 26 days of operation, the SDS experiment (flight test of the DRAGONS detector concept) reported that they recorded 19 events that they identified as “Flash” with the

characteristics of a "Large impulse signal showing simultaneously on multiple sensors, directly followed by flat line" (Anz-Meador *et al.*, 2019). These characteristics closely match those of the simultaneous non-acoustic noise identified in this thesis. The above experiments that observe non-acoustic noise to coincide with the production of impact induced light flash suggest that the hypothesised origin of this non-acoustic noise relating to light flash ("Flash") originating from the impact is very likely.

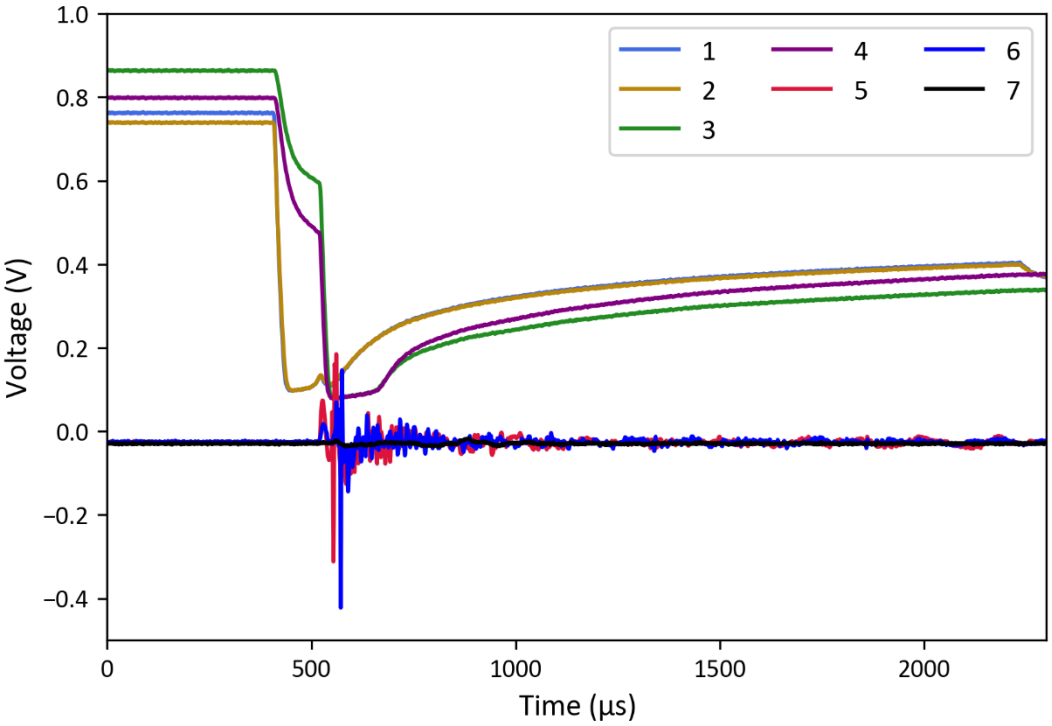

Fig. 4.18: Photodiode (1 – 4) and PVDF (5 – 7) signals recorded for a 0.8 mm stainless steel 420 sphere impacting two consecutive Kapton films separated by 555 ± 1 mm at ~ 5 km s^{-1} (Light.1). Photodiodes 1 and 2 were looking at the first film, 3 and 4 at the second, and the PVDFs 5 and 6 were attached to the front and back of the second film respectively, while PVDF 7 was attached to the frame of the second film. Coincidence of the light flash from the second film with noise in the two Kapton mounted PVDF sensors can be seen at ~ 520 µs. Note that photodiodes 3 and 4 do start responding at the same time as 1 and 2. This initial drop is due to some light from the impact flash on the first Kapton film reaching 3 and 4. 3 and 4 then show a greater and faster response when the impact occurs on the second Kapton film.

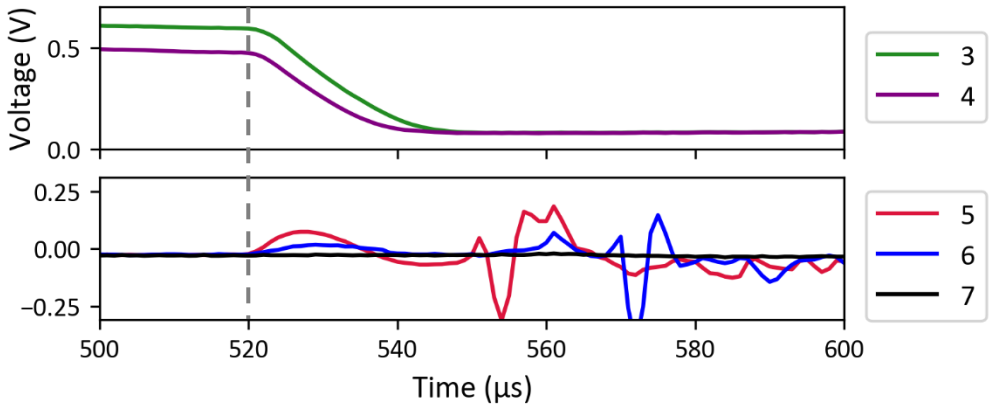

Fig. 4.19: Expanded time region of interest from Fig. 4.18 of photodiodes (top) and PVDF signals (bottom) recorded for a 0.8 mm stainless steel 420 sphere impacting two consecutive Kapton films separated by 555 ± 1 mm at ~ 5 km s^{-1} (Light.1). Photodiodes 3 and 4 were facing the second Kapton film, and the PVDFs 5 and 6 were attached to the front and back of the second film respectively, while PVDF 7 was attached to the rear frame of the second film. Coincidence of the light flash from the second film with noise in the two Kapton mounted PVDF sensors is marked with a grey dashed line.

4.3.3 Projectile Penetration

Inspection of the first and second film post shot showed similar looking penetration holes of roughly the same size in both (see Fig. 4.20 for an examples of penetration holes in the first and second film at 2 km s^{-1} and 4 km s^{-1}). This suggests that the 1 mm StSt420 spheres were not appreciably disrupted upon impacting a 12.5 µm Kapton film. During penetration, the edge of the Kapton was left with strand like filaments, likely produced by the hydrodynamic flow of material. The friction and pressure induced during impact increase as the projectile speed increases. This leads to more Kapton entering the hydrodynamic phase and/or being vaporized during impact, which can be seen from there being fewer and smaller filaments in the shot at 4 km s^{-1} (Fig. 4.20c and d) than at 2 km s^{-1} (Fig. 4.20a and b). On the second film in a shot (Fig. 4.21), it is possible to see that more Kapton and removed filaments were thrown outwards, and at a much shallower angle (measured from the film surface) for higher speed impacts, depositing on the film. This can be seen as bright illuminated lines on the back of the film, radiating from the penetration hole. A difference between impact features in the 2 km s^{-1} and 4 km s^{-1} impacts could explain why the small preceding peaks are less significant for the 4 km s^{-1} impacts. The cleaner the penetration hole the less complex the acoustic wave set up in the film. Similarly, more vaporised Kapton, as seen in the 4 km s^{-1} shots suggest a greater luminescent plume and thus light flash.

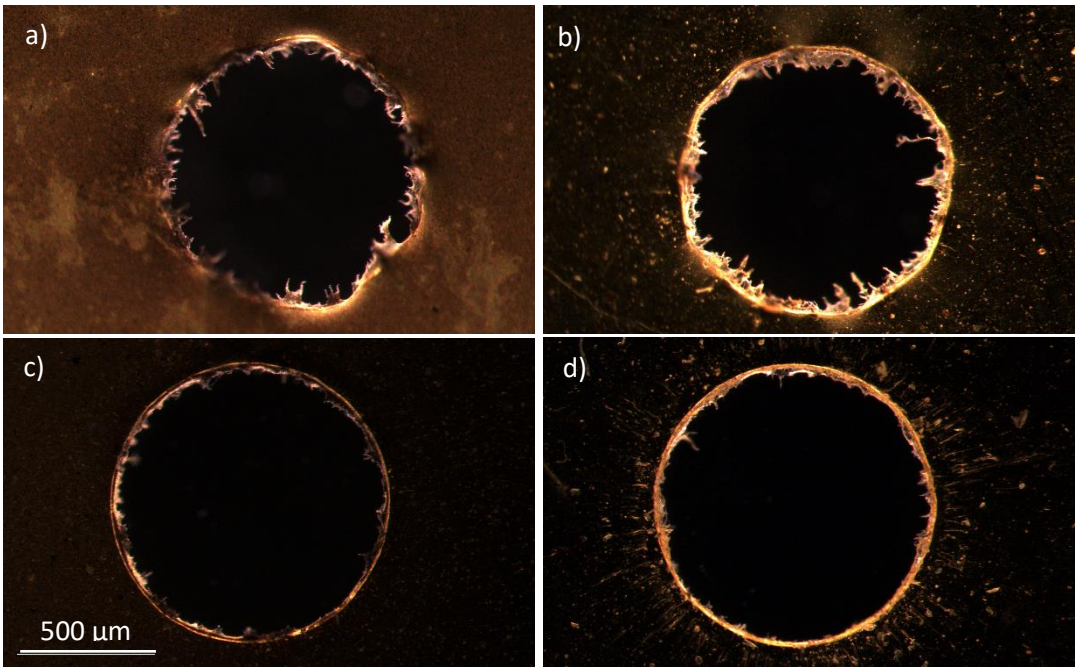

Fig. 4.20: Penetration holes in 12.5 µm Kapton films, viewed from the incident direction of the 1 mm steel spheres. (a & b) Holes in the 1st and 2nd film with diameters of 995 ± 23 µm and 994 ± 12 µm respectively, after impact at ~ 2 km s^{-1} (shot Veri.2). (c & d) Holes in the 1st and 2nd film with diameters of 1025 ± 7 µm and 1036 ± 6 µm respectively, after impact at ~ 4 km s^{-1} (shot Veri.4). All images are to the same scale with the same scale bar shown in the bottom left.

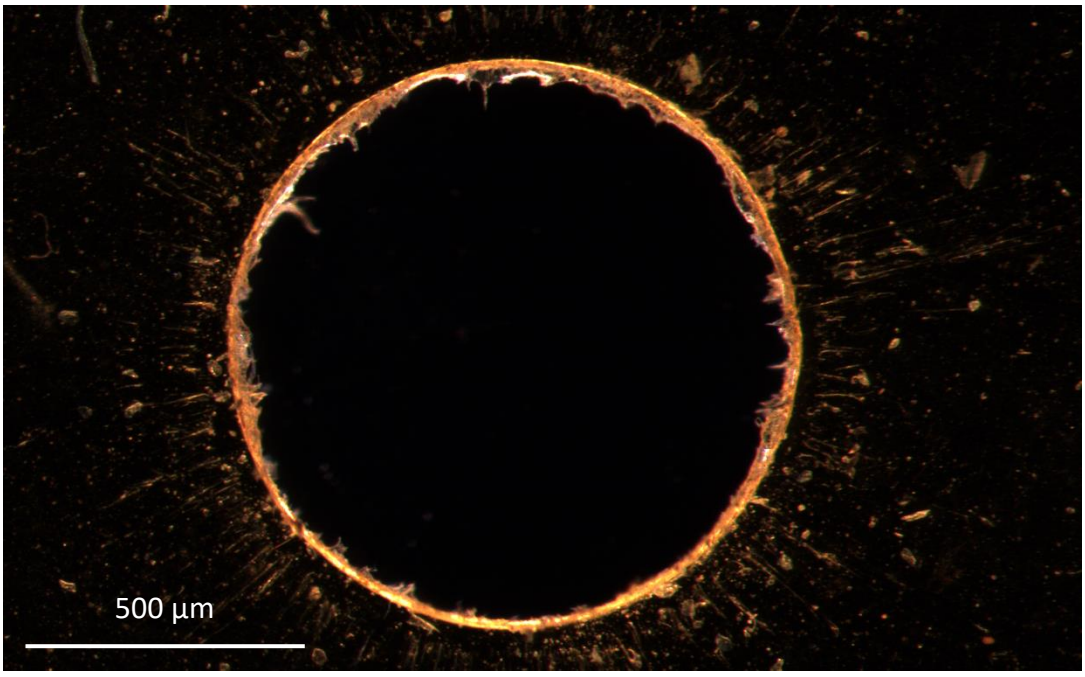

Fig. 4.21: Second film viewed from the direction of the projectile after penetration by a 1 mm stainless steel 420 sphere at ~4 km s^{-1} (shot Veri.4). Removed Kapton and Kapton filaments can be seen draped across the film as bright illuminated lines radiating from the penetration hole.

Table 4.4: Penetration hole diameter (d_h) in the 1st and 2nd Kapton films from each shot. Shot Veri.1 to Veri.3, and Veri.7 were at 2 km s^{-1}, Veri.4 to Veri.6 were at 4 km s^{-1}. All projectiles were 1 mm in diameter.

Shot ID	Veri.1 2 km s^{-1} (µm)	Veri.2 2 km s^{-1} (µm)	Veri.3 2 km s^{-1} (µm)	Veri.4 4 km s^{-1} (µm)	Veri.5 4 km s^{-1} (µm)	Veri.6 4 km s^{-1} (µm)	Veri.7 2 km s^{-1} (µm)
1st film	1029 ±26	995 ±24	1006 ±24	1025 ±10	1021 ±10	1018 ±10	982 ±12
2nd film	1009 ±13	994 ±12	1007 ±10	1036 ±10	1038 ±10	1024 ±10	979 ±10

Penetration hole diameter (d_h) for each shot can be seen in Table 4.4. These diameters are the average of the diameters measured along the vertical and horizontal of the penetration holes in the images taken by optical microscopy. Three random examples of 1 mm StSt420 spherical projectiles were taken from the projectile supply and measured under the microscope to confirm the tolerance of d_p (Fig. 4.22). The three projectiles had diameters d_p = 1000 µm ± 10 µm, d_p = 998 µm ± 10 µm, and d_p = 1000 µm ± 10 µm, i.e. all 1 mm within measurement uncertainties. At 2 km s^{-1} the hole diameter in the first film had d_h = 1000 µm ± 10 µm , the slight deviation in Veri.7 still lies within the combined absolute uncertainty for the hole and projectile. Similalrly, for the 4 km s^{-1} impacts d_h = 1000 µm are within the combined absolute uncertainties of d_h and d_p. However, there is a general increase in d_h between Kapton layers 1 and 2, allbeit small, likely caused by more Kapton removed from layer 1 adhered to the edge of the projectile. Thus, for 12.5 µm Kapton films at a ratio of f:d_p = $\frac{1}{80}$, penetration hole diameter tends towards d_h = d_p at low speed, which is the ultra-thin film limit (Hörz, 2012). This result is useful for the development of damage equations for Kapton, such as that given by Neish and Kibe (2001). A damage equation for Kapton would have to satisfy d_h = d_p at or before d_h/f = 80. For penetrations in the second film, d_h tends to be a little larger than d_h in the first film, with the increase in d_h between the layers greater at 4 km s^{-1}. This could be because as the impact speed increases a greater amount of removed Kapton could accumulate on the projectile and lead to the larger d_h observed.

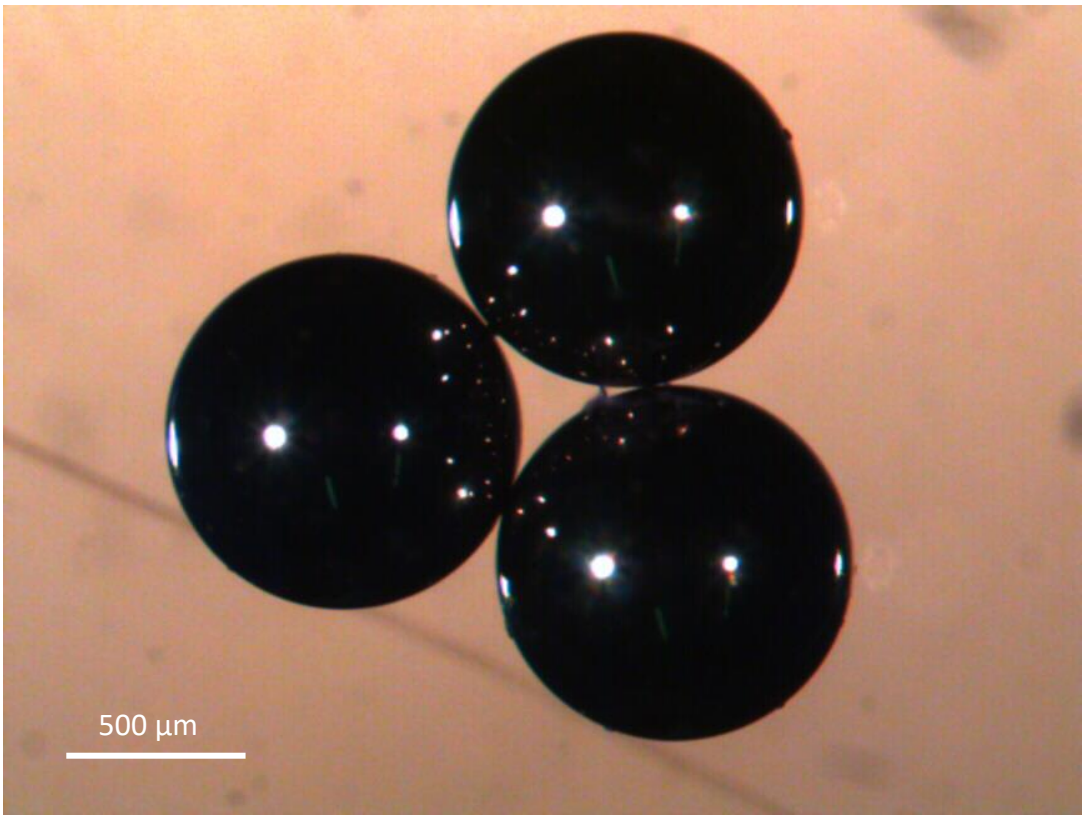

Fig. 4.22: Three random examples of spherical projectiles taken from the 1 mm stainless steel 420 supply. They had diameters d_p = 1000 µm ± 10 µm, d_p = 998 µm ± 10 µm, and d_p = 1000 µm ± 10 µm, i.e. 1 mm within measurement uncertainties.

4.3.4 Speed Measurement Accuracy

The results from the speed measurements from each pair of sensors (v_{AE}, v_{BF}, and v_{CG}) and the average speed from all three pairs of sensors (TOF Avg.) for each shot are shown in Table 4.5. The non-acoustic noise described in section 4.3.2 and present in data from shot Veri.4, contaminated the onset of the acoustic signal in trace F leading to an anomalous value for v_{BF} (marked with a '*' in Table 4.5). Thus, TOF Avg. was recalculated for shot Veri.4 using the two values from v_{AE} and v_{CG} (marked with '**' in Table 4.5). Excluding the anomalous result, there are twenty separate speed estimates from pairs of PVDF sensors. Of these only two differ from the LGG speed > 1σ (v_{CG} in shots Veri.2 and Veri.3 which differ from v_{LGG} by 1.83 and 3.23 respectively). The final speed measurements from the TOF detector (the average TOF Avg.) differed from the incident speed measurement by no more than ~ 0.5%, well within the ~ 1% uncertainties. Hence, no deceleration was observed and

in ideal conditions the acoustic TOF detector is capable of accurately measuring the speed of mm sized projectiles to within ± 1%.

Table 4.5: Speed measurement results, showing speeds determined from pairs of sensors (v_{AE}, v_{BF}, v_{CG}), the average speed measured by the TOF detector (TOF Avg.), the incident particle speed as measured by the LGG's light gate system (v_{LGG}), and the difference between TOF Avg. and v_{LGG} ($\Delta_{TOF, LGG}$). The value marked with a ' * ' is an anomalous value caused by a noise artefact in the data. The value marked with a '**' is the average recalculated excluding the anomalous value.

Shot ID	v_{AE} (m s^{-1})	v_{BF} (m s^{-1})	v_{CG} (m s^{-1})	TOF Avg. (m s^{-1})	v_{LGG} ± 1 % (ms^{-1})	$\Delta_{TOF, LGG}$ (m s^{-1})
Veri.1	2081 ± 9	2084 ± 10	2085 ± 10	2083 ± 5	2084	1 ± 22
Veri.2	2191 ± 11	2192 ± 11	2210 ± 11	2198 ± 6	2192	6 ± 22
Veri.3	2124 ± 10	2125 ± 10	2174 ± 10	2141 ± 6	2132	9 ± 22
Veri.4	3937 ± 33	4470 ± 43*	3872 ± 32	4093 ± 21 3905 ± 23**	3900	193 ± 44 5 ± 45**
Veri.5	3770 ± 33	3780 ± 30	3802 ± 31	3784 ± 18	3779	5 ± 42
Veri.6	3740 ± 27	3720 ± 30	3783 ± 31	3748 ± 17	3740	8 ± 41
Veri.7	2083 ± 13	2073 ± 13	2094 ± 13	2084 ± 8	2097	13 ± 22

The example of noise contamination in Veri.4 led to a 15% difference between the measured value of v_{BF} and v_{LGG} and a 5% difference between the originally calculated value of TOF Avg. and v_{LGG}. Five of the seven shots showed signs of one or more instances of non-acoustic noise, with only one (Veri.4) showing signs of significant speed measurement contamination. This suggests that there was a 5/7 probability of non-acoustic noise being detected in a shot and if present, a 1/5 chance of it significantly affecting the speed measurement obtained. Combined this gives a 1/7 probability of non-acoustic noise significantly affecting the speed measurement obtained. Considering individual sensors, out of the fifty-six traces recorded across all shots, twenty-five showed signs of one or more instances of non-acoustic noise, with only one trace leading to a significantly affected speed measurement. Thus, representing a 1/56 probability of non-acoustic noise affecting the speed measurement. However, as applied here identification of a contaminated data set can allow it to be removed from consideration and stop it affecting the final speed measurement from the detector.

Table 4.6: Wave speed in the Kapton film as calculated from the difference in path lengths and travel times for sensors on the same film. WS_{AB} corresponds to the wave speed calculated from the differences between sensors A & B, etc. WS is the average of the four values. The onset times from which the difference in travel time were calculated are the same as those used in calculations for projectile speed in Table 4.4. The previously measured value for the wave speed was 1875 ± 25 m s^{-1}. The value marked with a '*' is an anomalous value, caused by a noise artefact present in the data. The value marked with a '**' is the average recalculated excluding the anomalous value.

Shot ID	WS_{AB} (m s^{-1})	WS_{AC} (m s^{-1})	WS_{EF} (m s^{-1})	WS_{EG} (m s^{-1})	WS (m s^{-1})
Veri.1	1917 ± 29	1868 ± 39	1930 ± 31	1889 ± 42	1901 ± 18
Veri.2	1913 ± 23	1873 ± 23	1916 ± 24	1917 ± 24	1904 ± 12
Veri.3	1875 ± 33	1828 ± 25	1879 ± 35	1967 ± 29	1887 ± 16
Veri.4	1694 ± 112	1860 ± 38	803 ± 41*	1947 ± 46	1576 ± 33 1833 ± 42**
Veri.5	1938 ± 46	2044 ± 140	1922 ± 44	1905 ± 121	1952 ± 49
Veri.6	1852 ± 62	1996 ± 65	1894 ± 66	1907 ± 59	1911 ± 32
Veri.7	1921 ± 44	1864 ± 45	1879 ± 52	1941 ± 62	1901 ± 26

Achieving an accurate measurement of the incident projectile speed with an acoustic TOF detector relies on accurate determination of the time of impact and thus signal onset time. Noise contamination affecting the determination of the onset time as above is a case in point for this. Therefore, it is important to determine whether the criteria used for determining the signal onset time gives a good representation of the true onset and time of impact of the projectile. An independent measure of the accuracy of the time of onset can be achieved using the previously and independently measured wave speed in Kapton films (1875 ± 25 m s^{-1}). Comparing the wave path length difference between sensors on the same film e.g. A & B, and A & C, and the difference between time of signal onset, the wave speed can be determined directly from the experimental data. Hence, time of impacts that return a wave speed of 1875 ± 25 m s^{-1}, within uncertainties, can be considered to be accurate measures of the signal onset time and correspond to the same time of impact, agreed by multiple detectors. The results from this analysis of the 1 mm projectile data are shown in Table 4.6 where WS_{AB} is the wave speed calculated from the difference in A & B, etc., and WS is the average wave speed from the four calculations, which can be used as a course check of the overall reliability of the final speed measurement.

Excluding the anomalous result in Veri.4, Table 4.6 shows significant agreement with the previously measured value for the wave speed (the average WS taken over all results excluding B and F in Veri.4 is 1909 ± 9 m s^{-1}). This suggests that the criteria used to determine the time of signal onset and correspondingly the time of impact, described in the experimental chapter (Section 3.3.5), gives an accurate determination of the onset of the signal of interest. Furthermore, if the impact location is known then this method can independently verify the validity of a final speed measurement or measurement from a pair of sensors. For example, WS_{EF} in Veri.3 agrees with the measured wave speed in Kapton, suggesting that the onset time for E and F are accurately determined. Whereas WS_{EG} returned a slightly different value, suggesting that the onset time was not so accurately determined for G. The same is true for C when comparing WS_{AB} and WS_{AC}. These small inaccuracies in onset determination would explain the slight over estimation of v_{CG} in Veri.3. Similarly, the anomaly produced by noise contamination can be identified with this validation technique. WS_{EF} from Veri.4 shows a significantly different value for the wave speed, while WS_{EG} is all but within uncertainties. Thus, this implies a significant error in the onset determination for sensor F in Veri.4, and could predict that v_{BF} would return an anomalous result. Applying similar considerations as before to WS_{AB} and WS_{AC}, would suggest that the onset time for B is slightly inaccurate. There would be no doubt that the combination of B and F would lead to the anomalous result in v_{BF}.

4.4 Summary

The experimental parameters and procedures for the investigation of detector performance and accuracy for relatively large 1 mm sized projectiles was discussed. The main feaures of the observed acoustic signals from the impacts on the on the Kapton films were also discussed. The acoustic signals of interest were identified as the first of the largest oscilitory peaks, with smaller preceding oscilitory peaks likely to originate from the impact, however less consistent. Non-acoustic noise, characterised by a single peak with a recovery tail, was identified in some of the data sets, with greater impact speed tending to lead to more noise. Light flash experiments with photodiodes that showed coincidence between the onset of photodidode signals and non-acoustic noise in PVDF sensors, suggest that this non-acoustic noise originates from the impact light flash (EM waves) and/or charged ions produced in the impact plasma. This noise was found to contaminate the onset of signals of interest and affect the speed measurment capability. Considering individual detector output speed measurments (the averaged value over three sensor pair measurements), the

probability of noise affecting the measurment was as large as 1/7. Considering the total number of traces recorded, the probability of non-acoustic noise affecting an individual measurement was as low as 1/56. It is possible to improve the probability of contaminated results affecting a measurment by removing the speed measurement result from a contaminated sensor pair, using wavespeed measurement cross-referenceing to determine whether accurate time of onset was achieved for each sensor. This produced accurate speed determination in all seven shots. Given the apparent sensitivity of PVDF sensors to EM waves, it is recommended that further invesitgation is conducted into the effects of the EM and charged particle environment of space on PVDF sensors, to identify whether they require sheilding.

TOF cosmic dust and debris detectors rely on their ability to accurately determine the speed of an incident particle. It is therefore recommended that an average speed measurment from multilpe pairs of sensors is used to reduced the effects of small errors in time of impact determination, arising from differences in signal shape. For 1 mm stainless steel spherical projectiles, under ideal conditions, it is shown that acoustic, Kapton thin film TOF detectors can do this to better than 1% accuracy. Furthermore, 1 mm stainless steel spheres do not experience significant disruption or deceleration upon impact with 12.5 ± 0.2 µm Kapton films, up to the $\sim$ 4 km s^{-1} speeds examined here, although already in the hypervelocity regime for Kapton this is expected to hold as velocity is scaled. Finally, at a ratio of $f{:}d_p = \frac{1}{80}$, i.e. for $d_p >> f$, at the speeds used here, pentration holes in 12.5 µm Kapton films tend toward the ultra thin film limit, $d_h = d_p$. This suggests that detectors based on this method are applicable for detecting 1 mm sized space debris.

Chapter 5: Small Projectile Results and Deceleration

5.1 Introduction

This chapter focuses on the study of small projectile impacts and the effects that thin Kapton films have on small particles, for which f:d_p is larger than the 1/80 ratio studied in Chapter 4. The chapter begins with an exploration of automated signal and onset time detection, not only for its relevance to a flight-model detector as noted in Section 3.3.5, but also for its application to the acoustic signals under investigation here, which had less accurate signal onset determination. The experimental parameters that were used are then outlined, and results for penetration hole formation and particle deceleration are presented and discussed.

5.2 Automated Signal Detection

Although the full development of advanced automated detection algorithms/software was outside of the scope of this thesis, an attempt to produce such an algorithm was made to investigate its application to the detector described. It was also thought that the use of an algorithm based on a more mathematical line of reasoning could have benefits for determining the onset time for the seemingly more variable data presented in this chapter.

Several attempts at an algorithm for onset determination were made; however, the majority followed the same process, based on identifying when a certain percentage of the total signal in the specified window had arrived, described in the algorithm diagram/flow chart in Fig. 5.1. Most of the algorithm development consisted of refining individual steps within the process. The key steps/processes that received most refinement were the filter to be applied, definition of an appropriate window over which to integrate, and what percentage of total signal arrival to take as the onset of the signal. Determining the optimal parameters for these steps was achieved by using five of the seven sets of "Veri." data from Section 4.3 as a training data set, and the data from Veri.5 and Veri.7 (chosen at random) as a test data set, to provide an unbiased evaluation of the algorithm's performance. Parameters were iteratively refined, after each iteration the algorithm was applied to the training data and the corresponding velocity measurement compared to the detector

measured speed, until a best set of parameters across all sets of data was found. The logic used for the algorithm refinement processes was as follows:

Signal Window

A signal window should be picked to avoid noise in the data, as its inclusion would contaminate the data considered for determining the '10% of signal arrival' condition (itself justified below). For the training data the best and subsequently chosen window was found to be - 50 µs and + 300 µs around the peak with the largest magnitude (t_{peak}). This window did not tend to include significant noise, except for the data in trace F of Veri.4, for which the data of interest was contaminated by noise (although the algorithm made a better onset determination in this case of noise, with a speed determination within 1% of the other sensor pairs, than the manual pick). t_{peak} needs to be identified in the raw signal before the filtering/processing occurs, as this is more representative of the magnitudes related to the impact, which was identified as important for onset determination. A window based on the first signal above the noise was attempted, however, this was often the less consistent small peaks or non-acoustic noise, which would be unsuitable and did not return results as accurate as a window centred on the largest peak. For a flight-model algorithm, automated noise detection and cleaning could be applied to ensure the widow excludes noise.

Signal Filtering

The variability between acoustic signals lead to different parameters providing varying levels of algorithm performance between data sets. Thus, the ideal signal filter would try to make the different acoustic signals appear more similar without losing important information, so that a single algorithm applying the same processes and looking for the same conditions would provide results that are more homogeneous. The best filter for this was found to be a band pass filter between the frequencies of 100 kHz – 200 kHz, with a Hilbert transform applied. Note: Here I zeroed the data before applying filtering and processing, although this should strictly not be necessary as an offset would be in both integrals.

Onset Determination

The onset condition needs to be defined such that it coincides with the time of signal onset. A running integral to identify when a certain percentage of the total signal within the window has arrived (the onset condition) was chosen to determine the time of onset. This

should reduce the dependency on signal shape (e.g. a single peak being broader and/or larger and slightly later in time) compared to considering a single largest peak, as it takes into consideration a larger portion of the signal. A Hilbert transform is applied to find the signal envelope, which is then easily integrated with no negative and positive peak cancellation. An onset condition of 10% was found to best fit the training data.

An example of processed signals with the algorithm determined onset times can be seen compared to the raw signals with the manually picked onset times in Fig. 5.2 (shot Veri.3). Across all seven sets of data the difference between the average speed measurement from the detector based on manually picked onset times and algorithm autonomously picked onset times (Table 5.1) had a mean deviation of 60 ± 22 m s^{-1} for 2 km s^{-1} shots and a mean deviation of 79 ± 41 m s^{-1} for 4 km s^{-1} shots. The variability in agreement is caused by the variability between acoustic signals from different shots and is likely to be a limiting factor for autonomous detection. However, achieving reasonable agreement with an algorithm after what was only exploratory analysis has proven the applicability of such algorithms for autonomous onset detection. Given enough time, and a large enough data set, it would be possible to develop a better algorithm using artificial intelligence, such as neural networks to determine the optimal algorithm.

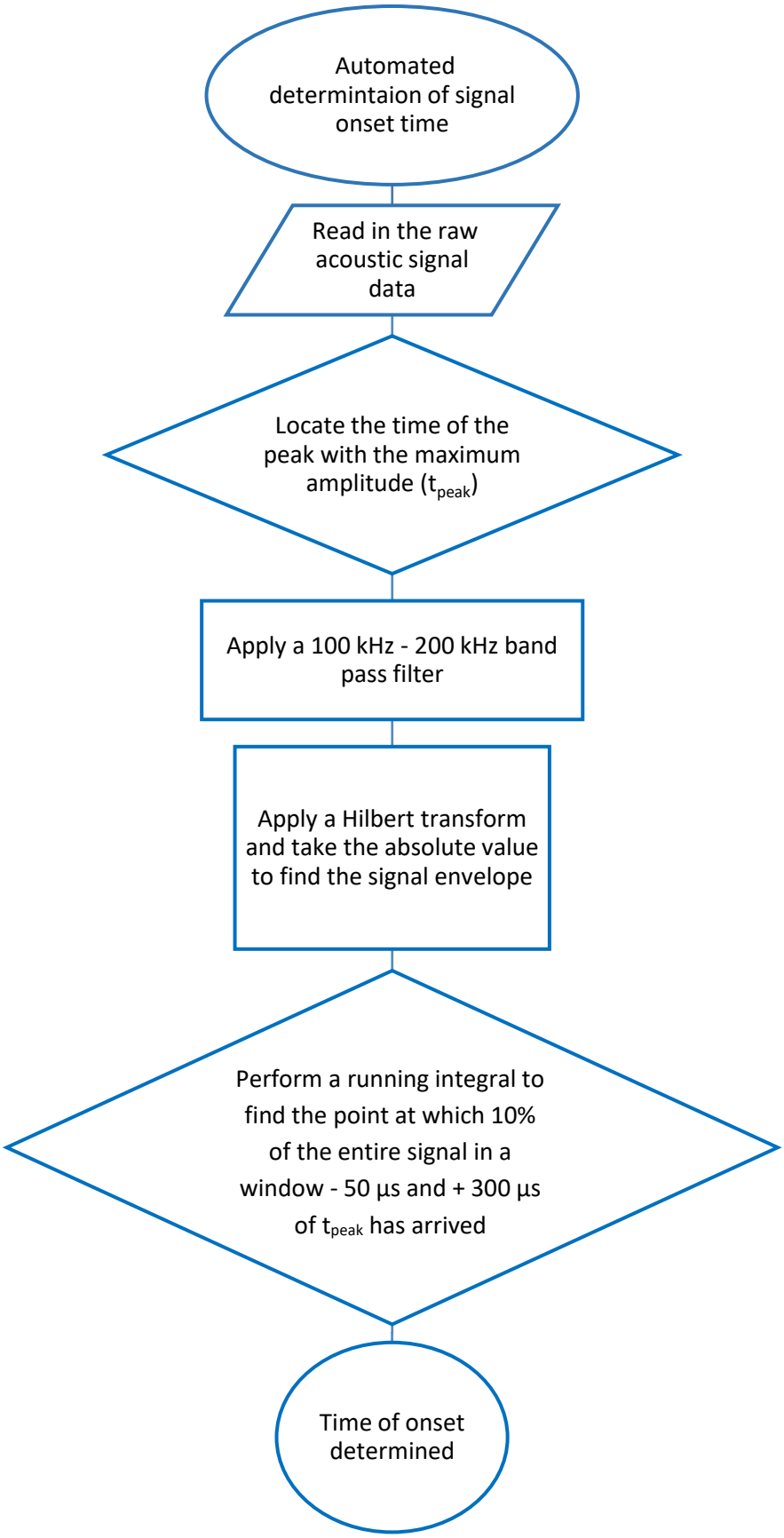

Fig. 5.1: Algorithm used for automated determination of signal onset time. The order of processes is sequential from top to bottom.

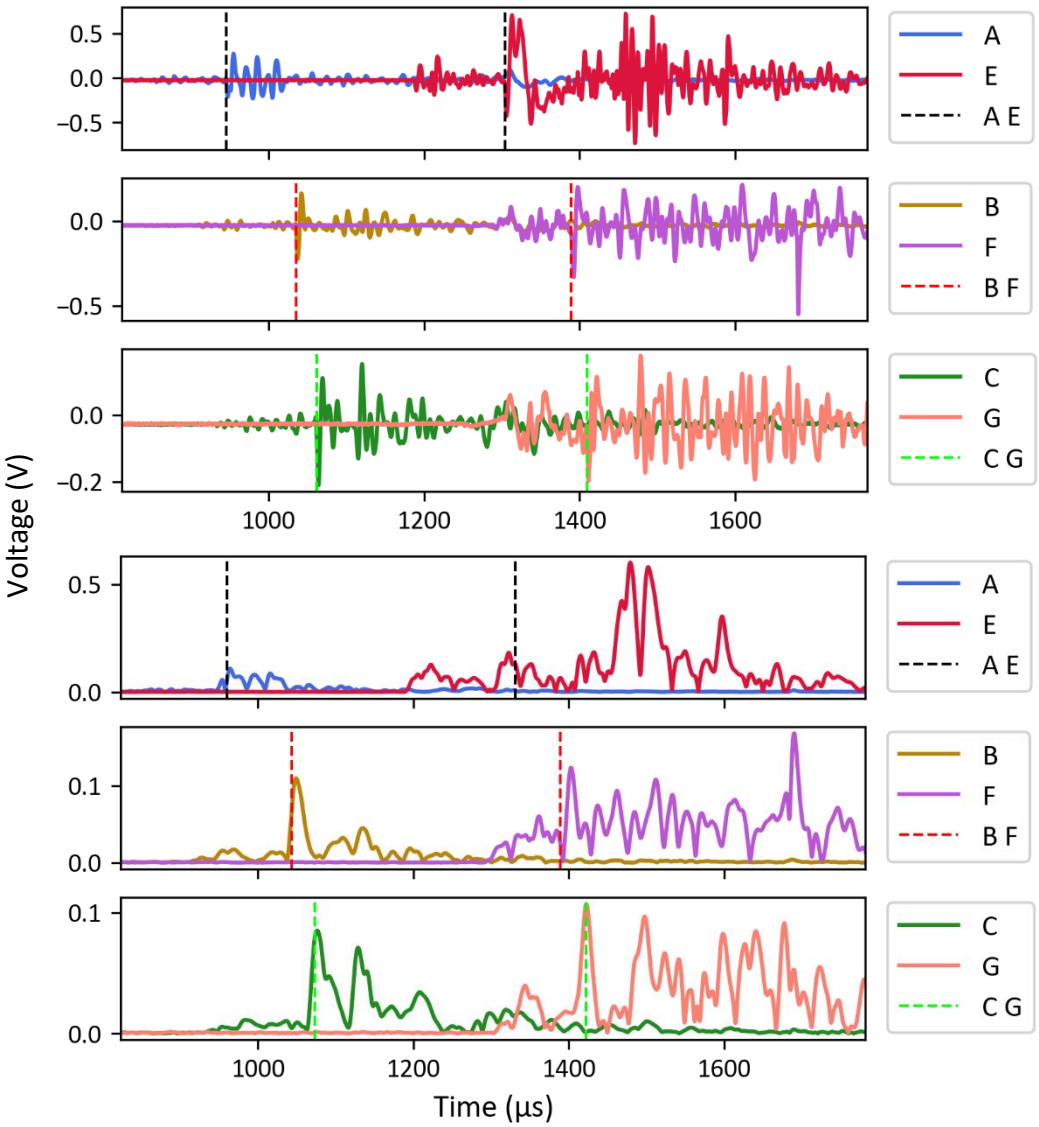

Fig. 5.2: The raw acoustic data from shot Veri.3 is shown in the top three panels (dashed vertical lines show the manual pick time of signal onset). The bottom three panels show the same data from shot Veri.3 after filtering with a 100 kHz – 200 kHz band pass filter, and taking the signal envelope. A running integral was then performed to determine the algorithm determined time of signal onset, shown with the vertical dashed lines.

Table 5.1: Comparison between the measured projectile speed (TOF Avg.) with manually picked (MP) onset times and algorithm autonomously picked (AP) onset times. The incident velocity as measured by the Light Gas Gun up-range (v_{LGG}) is also included.

	Veri.1	Veri.2	Veri.3	Veri.4	Veri.5	Veri.6	Veri.7
v_{LGG} (m s^{-1})	2084	2192	2132	3900	3779	3740	2097
MP TOF Avg. (m s^{-1})	2083	2197	2141	3904	3784	3747	2084
AP TOF Avg. (m s^{-1})	2166	2302	2133	3779	3785	3857	2126
Δ AP.MP (m s^{-1})	+ 83	+ 105	- 8	- 125	+ 1	+ 110	+ 42

5.3 Experimental Parameters

Analogous to determining the accuracy of the detector in chapter four, to determine the deceleration (if any) for projectiles with larger f:d_p the detector measured speed (i.e. after passage through the first film) was compared against the LGG measured speed. For projectiles with $d_p \leq 0.4$ mm an uncertainty in v_{LGG} of 4% was used, instead of the 1% uncertainty for larger projectiles that can be measured with the light gate. This is because as the smaller projectiles do not always trigger the light gate system, it is the sabot speed measurement with its larger uncertainty that is used for speed determination. Due to the lower success rate of shots with smaller d_p, a 25 µm film prototype was used as well as a 12.5 µm film prototype (film thickness of the first and second film was always the same in any given shot) to investigate a larger range of f:d_p. While f:d_p obviously scales directly i.e. 1:1, it is not so obvious for quantities such as projectile mass (m_p) and films mass (m_f), and thus momentum before and after penetration. However, it is indeed the case that m_p and m_f scale directly with a full derivation of this quality provided in Appendix II. Shots with comparable f:d_p and different values for f and d_p were conducted to investigate whether the effects for projectile and film scaling hold true.

Shots for 0.1 mm were attempted but failed due to the projectile coming off axis and not reaching the target. Successful shots were collected from 0.2 mm into both films up to 0.8 mm into the 25 µm films, spanning f:d_p = 1/8 to f:d_p = 1/32. All of the successful shots presented here used StSt420 spheres, although there was time to attempt one shot with a

titanium sphere (d_p = 0.189), which was unfortunately unsuccessful. Two shots with f:d_p = 1/16 were conducted with inclined incidence of 15° from normal incidence. Inclined incidence was achieved by rotating both Kapton frames by the same relative 15° rotation within the supporting structure (Fig. 5.3). Rotating the whole detector in the target chamber would neither have fit, nor would have allowed for as large an angle, as at the chosen separation the projectile would miss the second film. In total thirty shots were conducted. Nineteen of these were deemed successful shots (assigned the ID Dec.), where successful designates that the projectile made it to the target (however, some of these shots contained debris). A full list of experimental parameters for the nineteen successful shots can be found in Table 5.2.

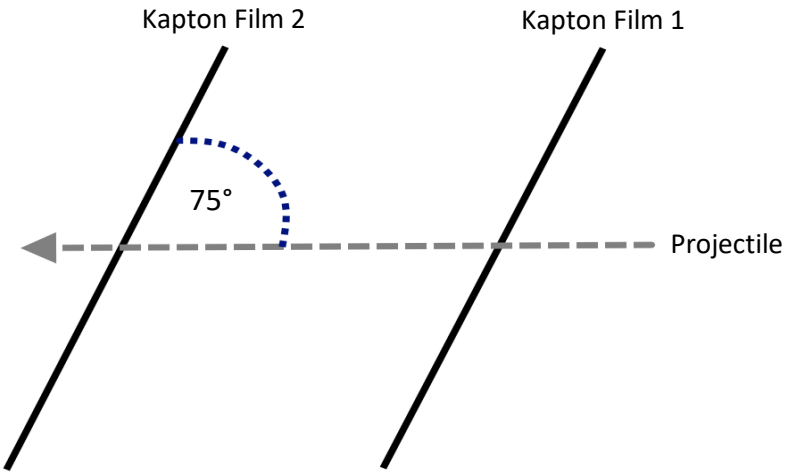

Fig. 5.3: Schematic of an overhead view of the impact geometry for the inclined incidence shots conducted. The shots were inclined 15° from normal incidence. The grey arrow defines the direction of the projectile's velocity vector.

Table 5.2: Shot parameters for the nineteen successful shots performed to determine effects of Kapton film penetration on small projectiles, and results for their associated penetration holes. Shot ID is the name given to each shot for reference. f is the film thickness, d_p the projectile diameter, v_{LGG} is the speed of the incident particle as measured by the LGG's light gate system. Angle of incidence (inc.) is measured from normal (perpendicular) incidence to the Kapton surface. d_h is the penetration hole diameter measured at the film surface. d_{lip} is the inner most or outer most (depending on the morphology) diameter measured from the lips. Both d_h and d_{lip} have two values given, the first representing the impact on the first film and the second representing the impact on the second film. The morphology for each penetration is labelled (BL: Barrel-like, CL: Crater-like, Di: Directional, TFL: Thin film-like).

Shot ID	f (µm)	d_p (mm)	f:d_p	v_{LGG} ± 4 % (m s^{-1})	Inc. (°)	d_h (µm)	d_{lip} (µm)	Morphology
Dec.1	25	0.2	1/8	1959	0	237 ± 5 256 ± 5	196 ± 14 201 ± 7	BL
Dec.2	12.5	0.2	1/16	1900	0	244 ± 22 227 ± 4	191 ± 32 175 ± 7	BL
Dec.3	12.5	0.2	1/16	2160	0	208 ± 8 239 ± 4	183 ± 9 181 ± 13	BL
Dec.4	12.5	0.2	1/16	1746	0	224 ± 10 226 ± 4	177 ± 18 156 ± 5	BL
Dec.5	12.5	0.2	1/16	1742	0	214 ± 23 223 ± 3	181 ± 16 167 ± 3	BL
Dec.6	25.0	0.4	1/16	1963	0	445 ± 4 449 ± 5	336 ± 8 336 ± 5	BL
Dec.7	25.0	0.4	1/16	2005	0	445 ± 6 449 ± 4	370 ± 11 338 ± 10	BL
Dec.8	25.0	0.4	1/16	1953	0	445 ± 11 449 ± 5	378 ± 30 354 ± 7	BL
Dec.9	25.0	0.4	1/16	3999	0	482 ± 5 485 ± 9	538 ± 10 548 ± 10	CL
Dec.10	25.0	0.4	1/16	4466	0	486 ± 8 490 ± 5	576 ± 8 566 ± 5	CL
Dec.11	25.0	0.4	1/16	5216	0	501 ± 8 508 ± 14	566 ± 5 571 ± 6	CL
Dec.12	25.0	0.4	1/16	1920	15	438 ± 8 464 ± 13	-	Di
Dec.13	25.0	0.4	1/16	2039	15	446 ± 21 454 ± 6	-	Di

Table 5.2 Continued.

Shot ID	f (µm)	d_p (mm)	f:d_p	v_{LGG} ± 4 % (m s^{-1})	Inc. (°)	d_h (µm)	d_{lip} (µm)	Morphology
Dec.14	25.0	0.8	1/32	1830	0	795 ± 38 828 ± 35	-	TFL
Dec.15	25.0	0.8	1/32	2013	0	811 ± 38 836 ± 34	-	TFL
Dec.16	25.0	0.8	1/32	1879	0	783 ± 40 834 ± 33	-	TFL
Dec.17	12.5	0.4	1/32	2094	0	420 ± 17 429 ± 8	-	TFL
Dec.18	12.5	0.4	1/32	2160	0	427 ± 11 429 ± 6	-	TFL
Dec.19	12.5	0.4	1/32	1963	0	424 ± 9 424 ± 4	-	TFL

5.4 Results

The two main questions under investigation in this chapter relating to the affect of Kapton on smaller projectiles was whether particle disruption occurred and whether deceleration occurred. They require consideration of two set of results concerning penetration hole-size and consistency between films, and the speed measurement from the detector i.e. after penetrating a Kapton film. These sets of results are discussed separately below.

5.4.1 Penetration Hole Formation

In all cases, even for the smallest projectile (200 µm) into the thickest film (25 µm) with f:d_p = 1/8, there was no appreciable disruption of the relatively strong StSt420 projectiles, with similar sized penetration holes observed in both films. Penetration holes came in four main morphologies, with different distinct features and the assignment of shots to morphologies is given in Table 5.3. The first of these was found to occur for f:d_p = 1/32 and is called 'thin film-like' (TFL) morphologies as they resemble the penetrations hole from projectiles with d_p >> f. The TFL morphology is characterised by a penetration hole that is approaching d_h = d_p, with filaments that are more individually defined and remain close to the penetration hole rim (Fig. 5.4). Shots with f:d_p = 1/32, to which these morphologies

belonged, were only conducted at 2 km s^{-1}. It is expected that as projectile speed increases more of these filaments would be removed, as with the results in Section 4.3.3.

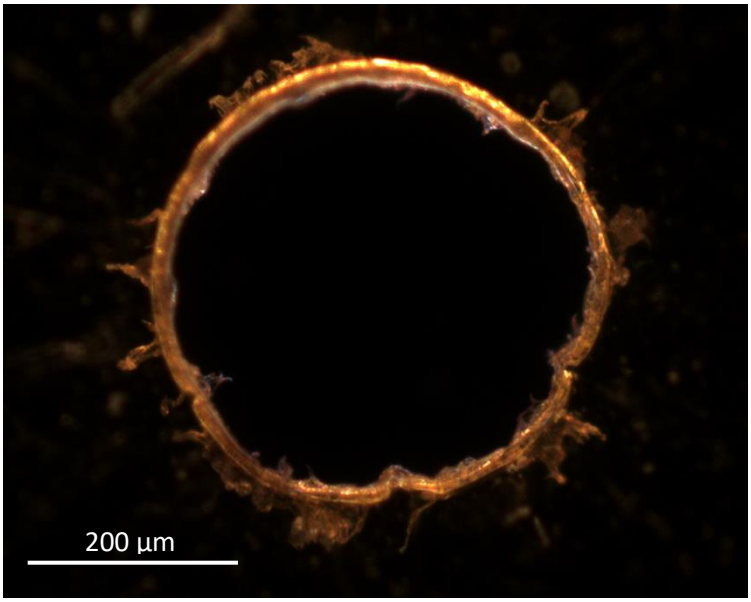

Fig. 5.4: Penetration hole in a second 12.5 µm Kapton film (downstream of a first film) viewed from the incident direction of a 400 µm stainless steel sphere at ~ 2 km s^{-1} (Dec.18). The diameter is 429 ± 10 µm. This is a 'thin film-like' morphology (TFL), with the hole diameter approaching the projectile diameter, and relatively small distinct Kapton filaments remaining close to the edge of the penetration hole.

The second morphology, called 'barrel-like' (BL), is present for larger f:d_p (> 1/16) for shots at speeds of 2 km s^{-1}. The BL morphology is characterised by a maximum $d_h > d_p$ at the film surface, and more continuous (joined) filament/Kapton lip structures, more akin to crater lips, extending above and below the surface. These lips protrude inwards from the penetration hole edge, creating a smaller hole diameter as measured from the lips ($d_{lip} < d_p$). Inner lip diameter was taken as the average of the vertical and horizontal diameters measured from the inner most lips (as shown in Fig. 5.5 and Fig. 5.6).

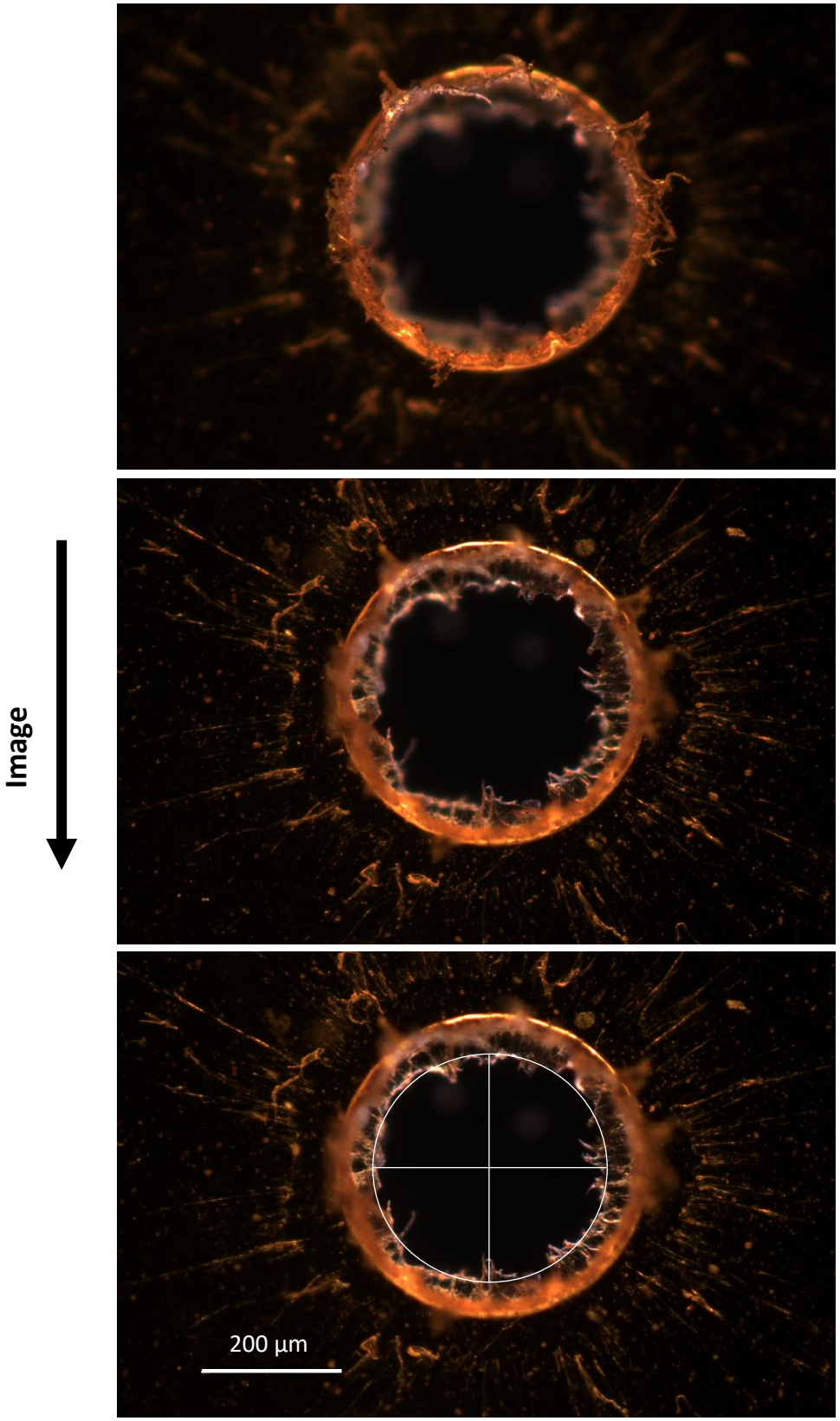

Fig. 5.5: Penetration hole in a second 25 µm Kapton film (downrange of a first film) viewed from the incident direction of a 400 µm stainless steel sphere at ~ 2 km s^{-1} (Dec.7). From top to bottom the images are focused above the film surface, at the film surface, and beneath the film surface, showing the barrel-like morphology (BL). This morphology shows filaments that form continuous lips that protrude inwards. The diameter at the surface is 449 ± 4 µm and the inner diameter of the lips is 338 ± 10 µm ± 1%. Horizontal and vertical inner lip measurements used to determine the average lip diameter are demonstrated with white lines.

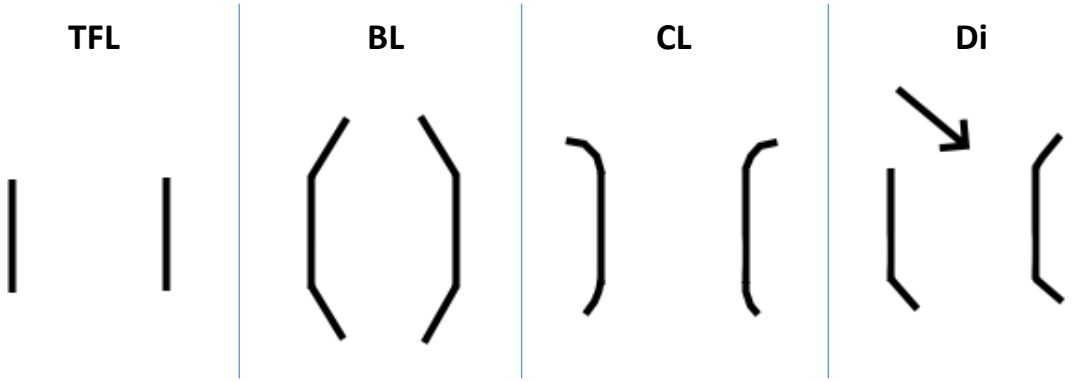

Fig. 5.6: Schematic representation of a side view of the four penetration hole morphologies, thin film-like (TFL), barrel-like (BL), crater-like (CL), and directional (Di). Only Kapton lips have been illustrated above and below the penetration hole in the film (depicted by the parallel vertical lines), with no small individual filaments such as those seen in the TFL morphologies shown. The arrow in the Di morphology diagram represents the direction of the incident projectile that causes the lip structures in the corresponding directions shown.

The third morphology was found for higher speed impacts (shots of ~ 4 km s^{-1}) with f:d_p = 1/16 and is dubbed 'crater-like' (CL). CL penetration holes are characterised by $d_h > d_p$ at the film surface (more so than for the BL morphologies), with Kapton lips close to the penetration hole rim. On the front of the film, they resemble tradition crater lips, which roll outwards from the penetration hole, whereas the structures on the rear of the film left a clean circular circumference with hydrodynamic flow of Kapton and few small filaments. The outer lip diameter was measured analogously to inner lip diameter (Fig. 5.7).

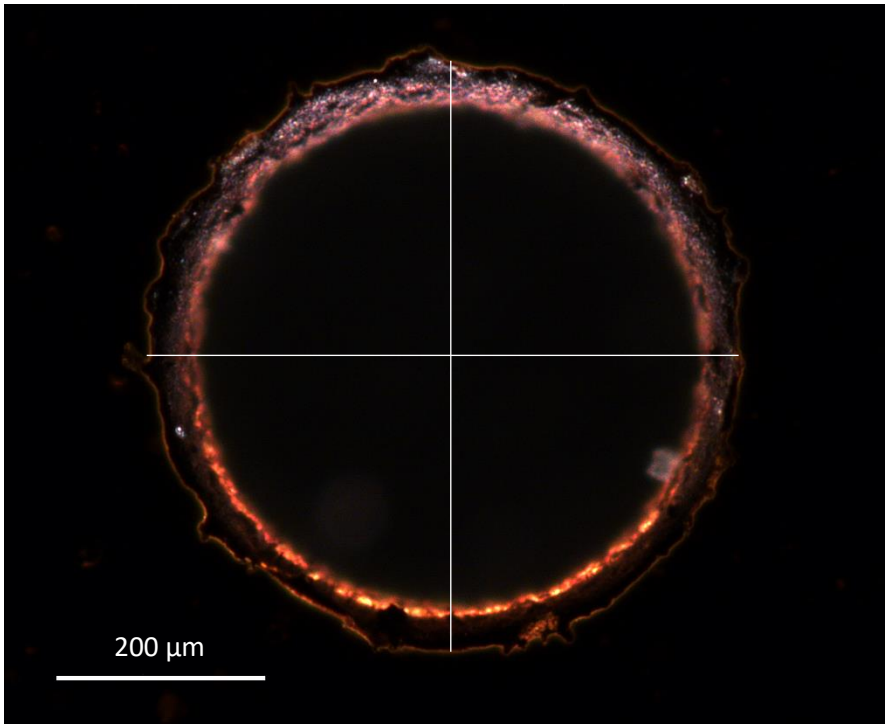

Fig. 5.7: Penetration hole in a first 25 µm Kapton film viewed from the incident direction of a 400 µm stainless steel sphere at ~ 5 km s^{-1} (Dec.11). The diameter at the film surface is 507 µm ± 2%, and the outer lip diameter is 568 µm ± 1%. This morphology is 'crater-like' (CL), with a hole diameter greater than the projectile diameter, and Kapton lips on the front of the film that resemble crater lips. Structures on the rear of the film left a clean circular circumference with hydrodynamic flow of Kapton, but few filaments. The first film was used to demonstrate the crater-like morphology, as opposed to the often-clearer second film, as the dark powder residue shows a shadow on the lip where it curls over.

The final morphology was observed in shots with an angled direction of incidence, showing directional properties and hence is called the 'directional' (Di) morphology. Di had $d_h > d_p$ and slightly larger than for BL holes. By careful orientation of the sample during microscopy, the horizontal diameter was aligned along the direction of projectile incidence and the vertical diameter aligned orthogonal to it. Despite the incident impact the difference between the vertical and horizontal diameters was not significant ~ 2%. However, this difference is likely to increase with increased angle of incidence, as seen in Nakamura *et al*., 2015. On the other hand, the ejecta lip formed at the edge of the penetration hole was different to the other morphologies. That is, there were clear directional effects, with more

top lip formed in the direction of the incident projectile (see Appendix I for an image with a focused top lip) and in an outwards direction unlike the BL morphology, and less lip formation elsewhere (Fig. 5.8). The converse is true for the bottom lip, with less lip formed downrange of the direction of the projectile flight in an outwards direction (the direction of projectile travel) while there was more lip formed and protruding inwards on the other side, not in the path of the projectile. Hence, it could also be possible to infer impact direction from the penetration hole morphology in thin Kapton films.

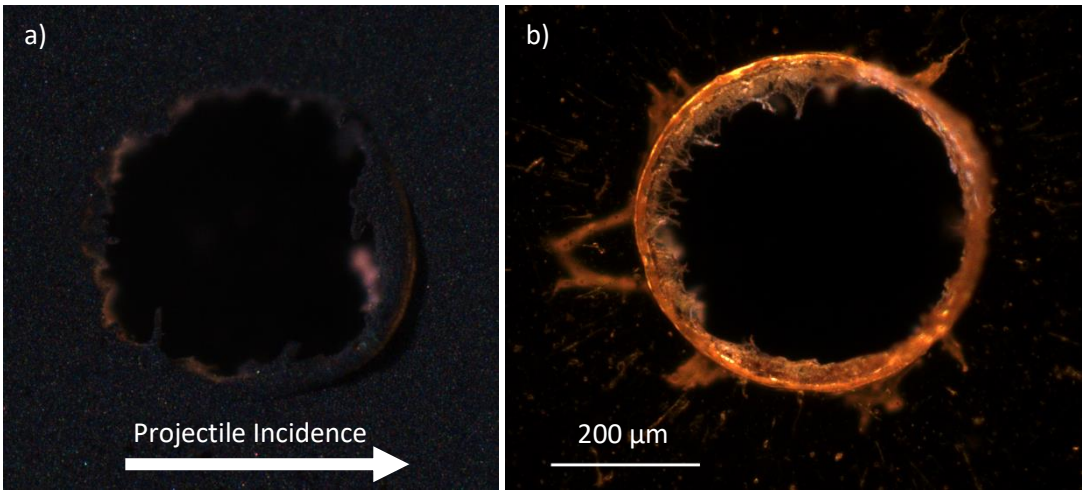

Fig. 5.8: Penetration holes in the first (a) and second (b) 25 µm Kapton films, viewed from the incident direction of a 400 µm stainless steel sphere impacting at ~ 2 km s^{-1} with an incidence angle of 15° from normal incidence (Dec.13). The first film was imaged with reflected light as this best shows the ejecta on the front of the film, seen as a bunched-up lip of Kapton on the right side of the penetration hole (downrange of the projectiles direction of flight). The second film also shows directional ejecta, with the front ejecta predominantly to the right of the penetration hole seen as the raised out of focus Kapton, obstructing the view of the bright rim of the penetration hole at the film surface. Ejecta at the back of the second film can only be seen for the left of the penetration hole (i.e. not down range of the projectile), with ejecta at the back of the right side of the penetration hole having more Kapton removed and/or pushed outwards from the hole. The direction of projectile incidence shown in (a) also applies to (b), and the scale bar shown in (b) also applies to (a).

TFL morphologies show an increase in d_h for the second film, whereas the BL morphologies do not show an appreciable increase in d_h for the second film. Thus, the material forming the lips in BL penetrations, which is removed for TFL penetrations, is in support of removed material coating the projectile and increasing the effective projectile diameter at the second film.

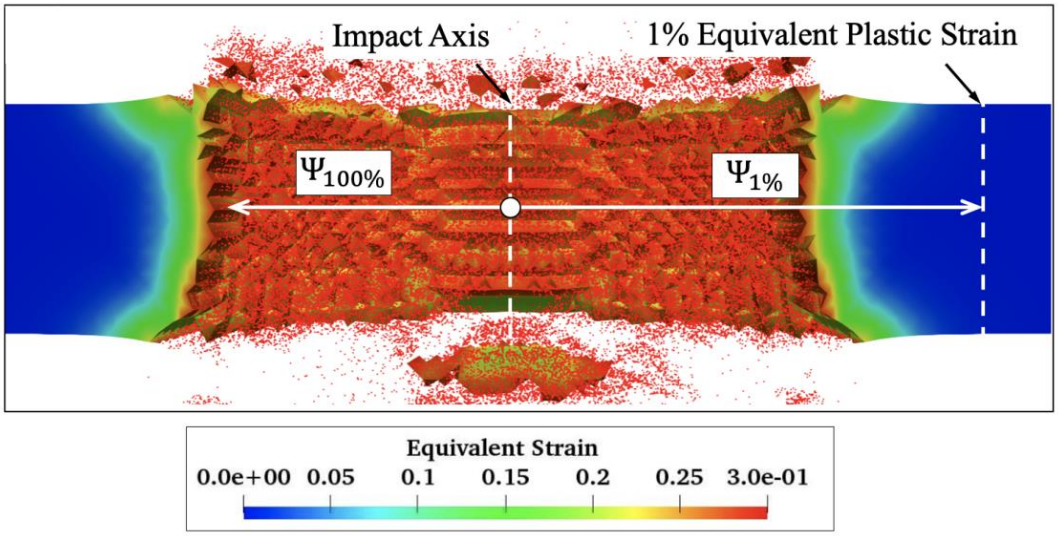

Fig. 5.9: Elastic Plastic Impact Computation code simulation snapshot for a 1.98 mm 2017-T4 aluminium sphere impacting a 1.59 mm Al6106-T6 plate at 2.4 km s^{-1}, showing the formation of outward curved lips at the top (top of image) and bottom of the penetration hole. The resulting equivalent plastic strain field is shown with a colour heat map, the radius of the 1% and 100% equivalent plastic strain region are marked with labelled arrows. Due to the large value of f:d_p (0.8), and similar material for projectile and target, the projectile was disrupted after penetrating the plate. Reproduced from Rogers *et al*., 2023.

BL morphologies are quite unusual, having raised lips that form inwards from the penetration hole rim. The raised lips for full penetration ($d_h \geq d_p$ at the film surface) are expected to curve outwards from the penetration hole rim, as shown previously in the work by Hörz, 2012 (Fig. 2.14) presented in Section 2.8 that showed this behaviour in a study that covered the range of f:d_p studied here. This can also be seen in more recent work by Rogers *et al*., 2023, with Elastic Plastic Impact Computation code simulations for the penetration of Al6106-T6 plates with 2017-T4 aluminium spheres. These simulations show the top and bottom edges of the penetration hole curving outwards (Fig. 5.9). So, why are the Kapton lips forming inwards. One explanation could be that it is speed related, and ~ 2 km s^{-1} is close to the sound speed of the Kapton films (with the measured wave speed = 1875 ± 25 m s^{-1}), thus the impact would only just be entering the hypervelocity regime. However, this is not observed for penetration holes for the 1 mm projectiles at ~ 2 km s^{-1} that can be characterised as TFL morphologies, see Section 4.3.3. Although they do show inward pointing filaments, so do the penetration holes for 1 mm at ~ 4 km s^{-1}. It is more likely that this phenomenon is related to the kinetic energy (KE) in the impact. At large projectile sizes and consequently mass, even slower speed impacts have large enough KE to induce hydrodynamic flow, and destroy the bonds within the material, leading to wholly removed material. At smaller projectile sizes and masses, the velocity becomes more important; with slower, low KE projectiles not imparting enough energy to remove as much

material. Thus, this altered material has the ability to relax back towards its original position, with inner diameters $d_{lip} < d_p$. It is expected that such impacts would greatly exceed the elastic properties of the Kapton, so the closing up of the penetration hole could be a result of altered material past the extent of d_p flowing inwards. Either way, the tendency of material to move in the direction opposing the force exerted by the projectile is interesting. The two studies in the literature presented above both focus on impacts into aluminium, thus the relaxing of the modified material to form this barrel shape is likely to be specific to the Kapton, and the more plastic properties of polymers in general, compared to the more ductile properties of a metal. Future analyses of the impacts with hydrodynamic code simulations could help to confirm/identify the cause of the morphologies recorded.

Full results of penetration formation, outer penetration hole diameter (at the film surface), lip diameter, and the hole morphology are presented in Table 5.3. d_h is found to increase as f:d_p increases (Fig. 5.10), as expected from the literature (Grün & Rauser, 1969; Hörz *et al.*, 1994). Similarly, increased impactor speed increases d_h, with greater KE producing a larger radius of altered Kapton.

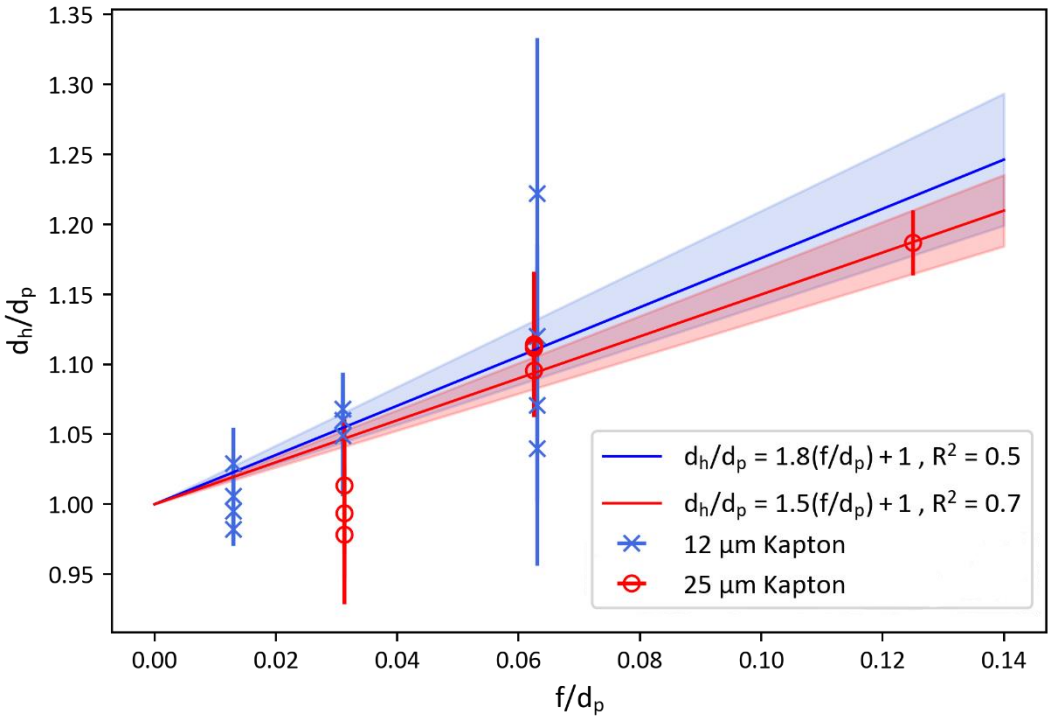

Fig. 5.10: Normalised hole diameter (d_h/d_p) plotted against film thickness over projectile diameter (f/d_p) for 12.5 µm (blue crosses) and 25 µm (red circles) thick Kapton films, impacted at ~ 2 km s^{-1} by spherical steel projectiles d_p = 0.2 mm, 0.4 mm, 0.8mm, and 1.0 mm. The + 1 in both fits is a fixed constant that obeys the constraint that $d_h = d_p$ for infinitesimal f/d_p (the ultra-thin film limit). For the 12.5 µm the gradient is 1.8 ± 0.3, and for the 25 µm film the gradient is 1.5 ± 0.18, the errors are shown as shaded regions.

To infer the size of an impactor from the size of the penetration hole in the Kapton film, which is also required to determine the expected deceleration using a calibration curve, a relation relating d_p to d_h is required. To do this for the data collected here and for comparison to past results, first a fit directly relating d_p and d_h was tried. From Fig. 5.11 a fit of this kind was determined for the 12.5 µm films to be:

$$d_p = 0.64 \pm 0.08 \, {d_h}^{1.064 \pm 0.019}, \tag{5.1}$$

and for the 25 µm films to be:

$$d_p = 0.31 \pm 0.04 \, {d_h}^{1.18 \pm 0.02}, \tag{5.2}$$

where d_p and d_h are in µm. Comparing the fit to the 12.5 µm film data (Eq. 5.1) to literature, we find Nakamura *et al*. (2015) found similar values, with the gradient reported as 0.72 and the power in the fit as 1.28. Most of their data was collected at 5 km s^{-1}, although it is noted in Nakamura *et al.* (2015) that there was no appreciable relation between d_h and impact velocity, this may contribute to the discrepancy observed. More likely to cause discrepancy is that the fit in Nakamura *et al.* (2015) covers a smaller absolute size range of 50 µm ≤ d_p ≤ 516 µm compared with this study which covers the range 200 µm ≤ d_p ≤ 1000 µm, and thus covering different values of f/d_p.

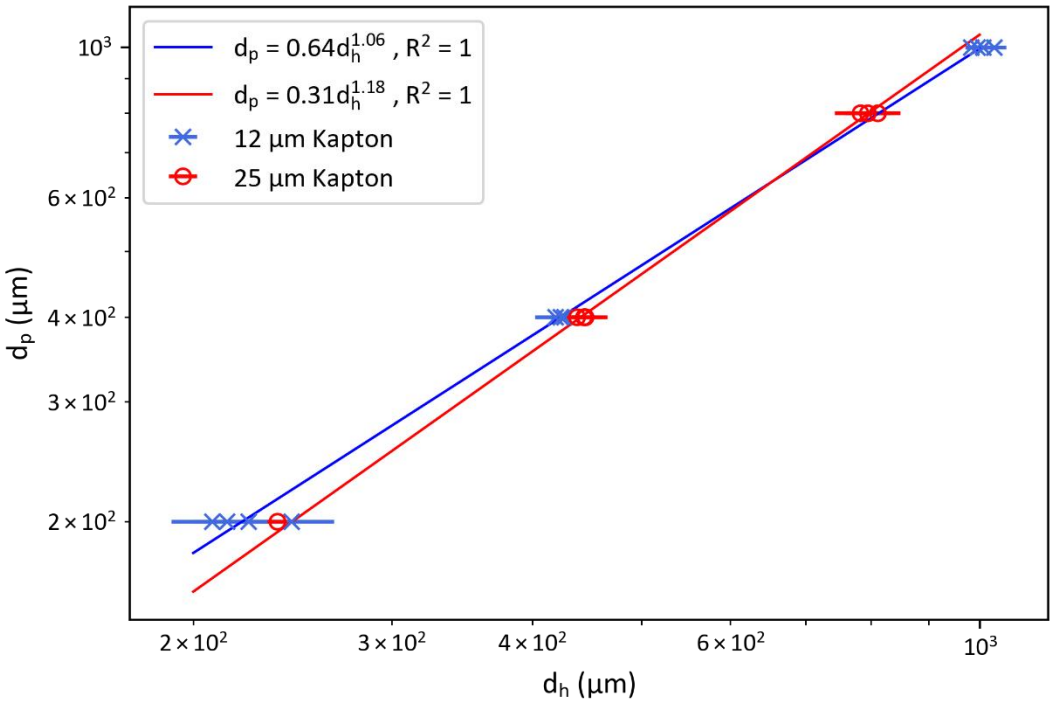

Fig. 5.11: Projectile diameter (d_p) plotted against hole diameter (d_h) for 12.5 µm (blue crosses) and 25 µm (red circles) thickness Kapton films, impacted at ~ 2 km s^{-1} by spherical steel projectiles d_p from 0.2 mm to 0.8 mm. For 12.5 µm films the errors for the fit are 0.64 ± 0.08 and 1.06 ± 0.02, and for 25 µm films the errors for the fit are 0.31 ± 0.04 and the power is 1.18 ± 0.02. Both R^2 = 0.998 to three decimal places.

Plotting d_p/f vs. d_h/f (Fig. 5.12) allows for the comparison of the penetration data collected here with the past results of Neish and Kibe (2001), which considers the ratio between d_p and f, albeit as d_p/f in this instance. A fit with the form:

$$\frac{d_p}{f} = a + \frac{d_h}{f}\left(1 - b^{\left(\frac{d_h}{f} + c\right)}\right) \tag{5.3}$$

was tried, and the constants for the 12.5 µm films found to be a = 1.06 ± 2.5, b = 0.96 ± 0.02, c = 32 ± 15, and for the 25 µm films a = 3.7 ± 1.5, b = 0.93 ± 0.01, c = -1.2 ± 2.7. Neish and Kibe (2001) found a = 0.337, b = 0.89, c = 0.07 (see Section 2.8.1). Although compatible with such a fit here there is a significant discrepancy in *c.* All of the data in Neish and Kibe (2001) for Kapton films of varying thickness were collected at 5 km s^{-1}, however, again it is the studied range, and the fitting process that is likely to cause the most discrepancy. In this work the range of d_p/f studied is $8 \leq d_p/f \leq 80$, whereas the range in Neish and Kibe (2001) was $0.3 \leq d_p/f \leq 80$, and they point out a change in gradient for the slope of Kapton, which is also observed for Teflon, at around d_p/f = 1 to 2. This is supported by the fact that that there is good agreement between the fits derived here and the fit by Neish and Kibe (2001) at larger d_p/f (> approximately 10) but not at smaller d_p/f (< approximately 10). Further to this, various weightings were applied to all data points to produce their fit, which was not the case here.

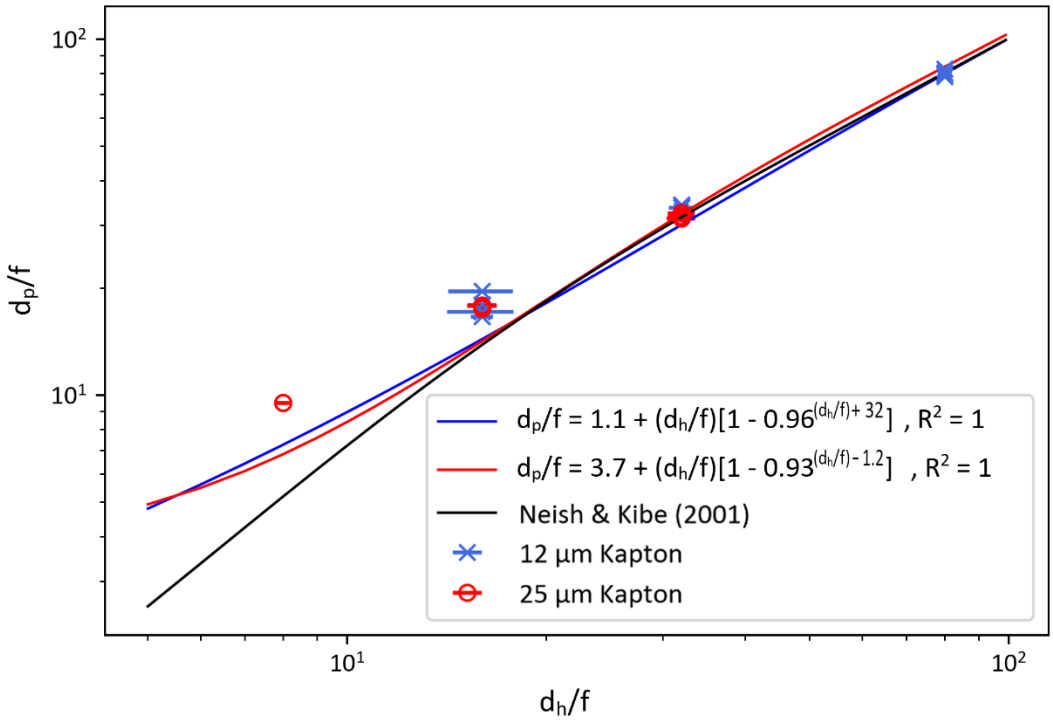

Fig. 5.12: Projectile diameter over film thickness (dp/f) plotted against hole diameter over film thickness (d_h/f) for 12.5 µm (blue crosses) and 25 µm (red circles) thickness Kapton films, impacted at ~ 2 km s^{-1} by spherical steel projectiles d_p from 0.2 mm to 0.8 mm. Both thickness of films are fitted with a fit of the form $\frac{d_p}{f} = a + \frac{d_h}{f}\left(1 - b^{\left(\frac{d_h}{f} + c\right)}\right)$. For 12.5 µm films found to be a = 1.06 ± 2.5, b = 0.96 ± 0.02, c = 32 ± 15, and for the 25 µm films a = 3.7 ± 1.5, b = 0.93 ± 0.01, c = -1.2 ± 2.7. Both R^2 are 0.999 to 3 decimal places. The fit from Neish and Kibe (2001) has been plotted in black for comparison.

5.4.2 Speed Measurement and Deceleration Results

The signal onset determination method (the "manual pick" method) described in Section 3.3.5, and which was applied in Chapter 4, was also applied in the same manor here, with the same assumptions that the projectile is the first thing to impact the films, unless there is reason to believe otherwise. Acoustic traces for each shot can be found in Appendix I. Broadly, the traces shared many features in common with those in Chapter 4, again with some variation between traces (examples are shown in Fig. 5.13 to Fig. 5.15), and showing signs of the same non-acoustic noise (Fig. 5.15). It was the case for shots with larger f:d_p that the three speeds measured by sensor pairs were more varied, giving a larger standard error and thus larger uncertainty in the overall speed. Similarly, wave speeds calculated

from the data suggested that the onset determination was poorer than for those with $d_p >> f$.

For these more difficult shots with a lower success rate, there were more instances of unexpected debris, some of which were seen to impact close in time to the first impact. In the case of Dec. 6 (Fig. 5.16) the unexpected debris contaminated the data of interest and caused misidentification of the projectile impact and onset time, under the previously defined conditions. Dec.6 showed the largest deceleration of all the shots and this is likely the consequence of a smaller, less dense particle being measured. This large deceleration was also accompanied by poor determination of the wave speed, which suggests that the sensor separations to the projectile impact location did not correspond to the acoustic signals, i.e. the signals belong to a piece of debris that hit elsewhere. However, generally speaking the sound speed was less well determined for a significant numbers of these shots, suggesting that as f:d_p increases the acoustic signals become more complicated. More complicated acoustic signals would be well explained by the change in penetration hole morphology. As the penetration holes become more complex, so too could the acoustic signals transmitted into the Kapton by the formation of the penetration hole features at least, if not the impact interaction itself. For these impacts, the first largest peaks in the traces may not always corresponding to the moment in time of the impact, hence poor onset determination and speed measurement.

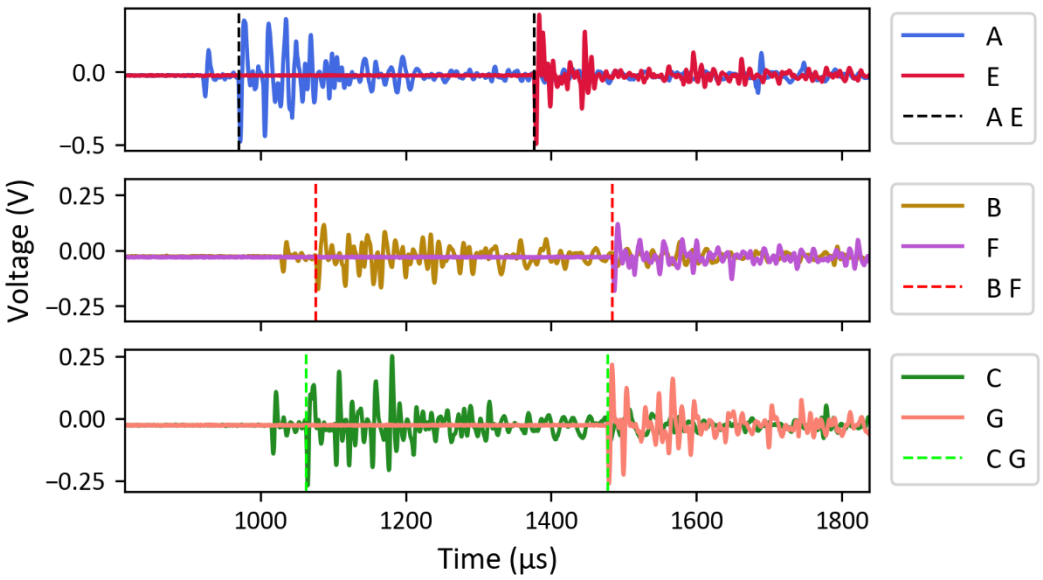

Fig. 5.13: The key time period of acoustic signals in shot Dec.7, for a stainless steel 420 projectile with normal incidence d_p = 0.4 mm, v_{LGG} = 2005 m s^{-1}, f = 25 µm. Vertical dashed lines represent the onset times for each sensor in a pair.

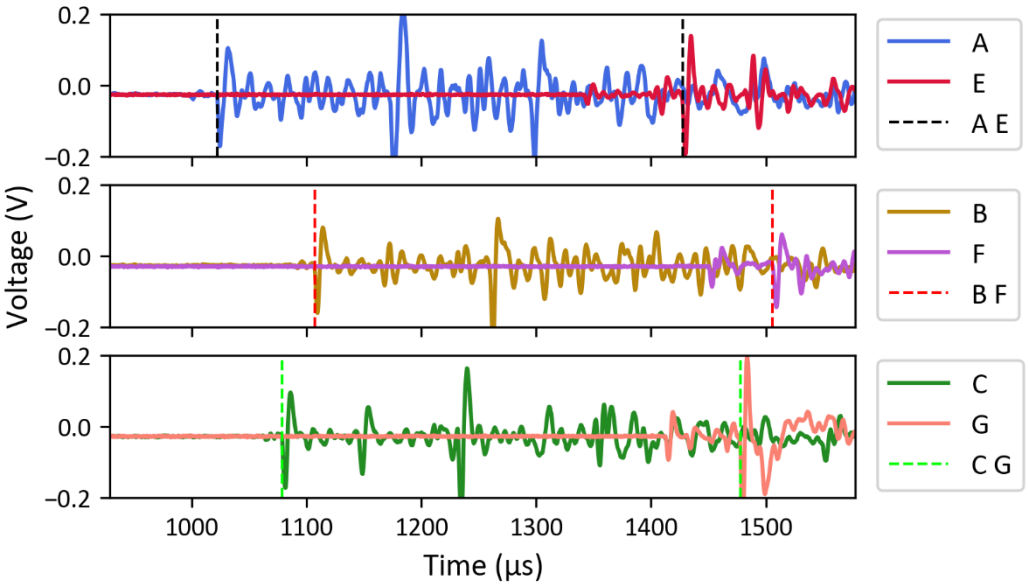

Fig. 5.14: The key time period of acoustic signals in shot Dec.18, for a stainless steel 420 projectile with normal incidence d_p = 0.4 mm, v_{LGG} = 2160 m s^{-1}, f = 12.5 µm. Vertical dashed lines represent the onset times for each sensor in a pair.

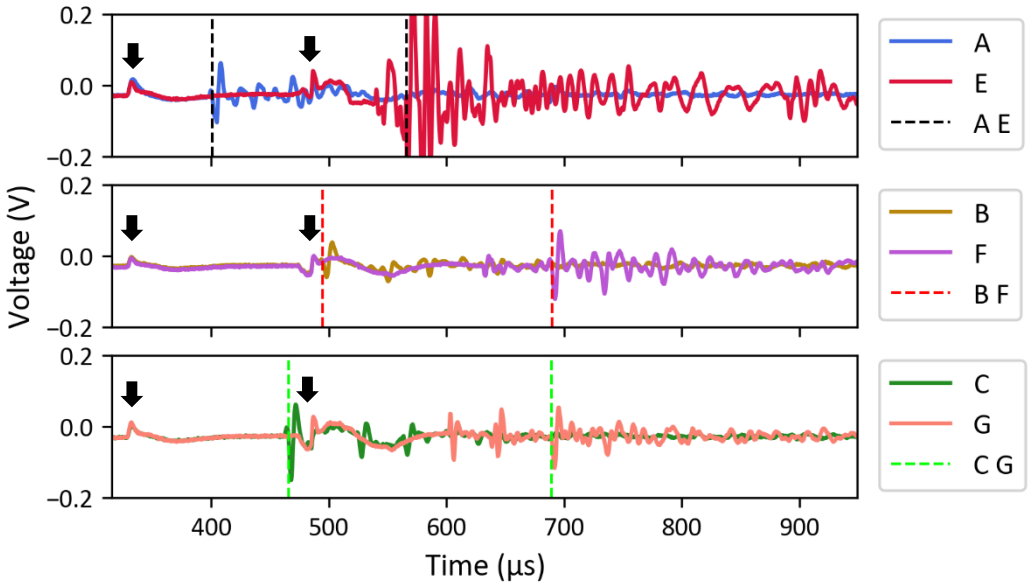

Fig. 5.15: The key time period of acoustic signals in shot Dec.11, for a stainless steel 420 projectile with normal incidence d_p = 0.4 mm, v_{LGG} = 5216 m s^{-1}, f = 25 µm. Vertical dashed lines represent the onset times for each sensor in a pair. Black arrows mark instances of non-acoustic noise.

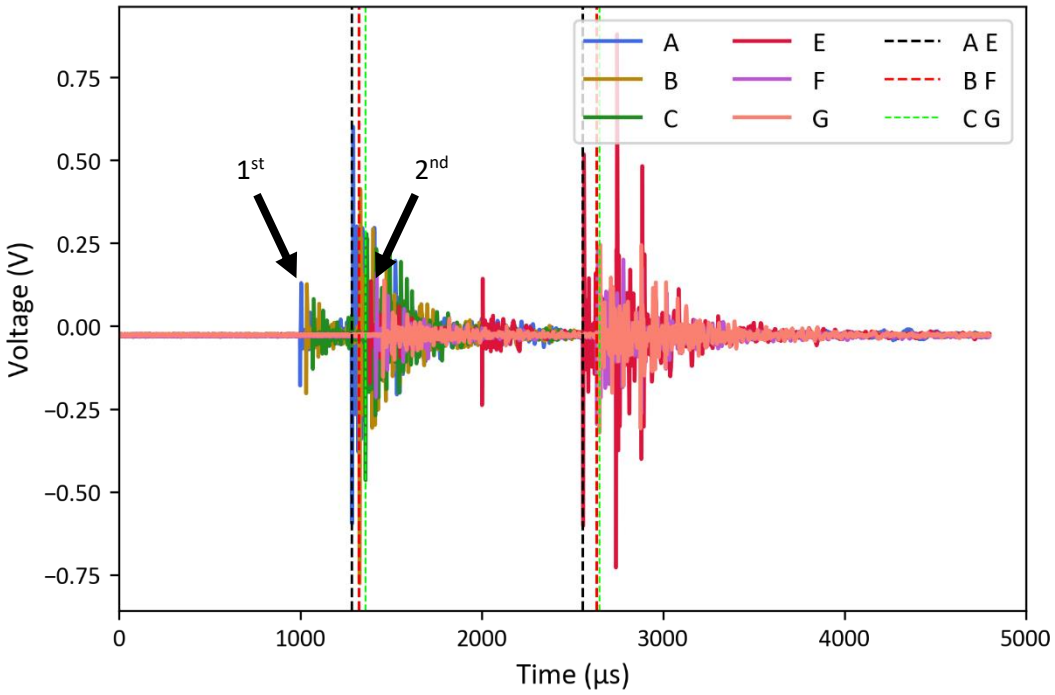

Fig. 5.16: Acoustic signals for shot Dec.6, for a stainless steel 420 projectile with normal incidence d_p = 0.4 mm, v_{LGG} = 1963 m s^{-1}, f = 25 µm. Vertical dashed lines represent the onset times for each sensor in a pair. Unexpected debris arriving close in time to the projectile impact caused misidentification of the projectile impact/onset. The acoustic signals in the first and second film that most likely to correspond to the true projectile impact are marked with black arrows.

Table 5.3: Deceleration results for the shots in the Dec. shot programme, featuring small projectiles with larger $f{:}d_p$. The percent deceleration Δv for measurements made with a manual pick onset determination (Manual) and an autonomous algorithm onset determination (Auto) are shown, with a positive value representing deceleration and a negative value representing a measured speed greater than the incident projectile speed (v_{LGG}). V_{LGG} had an uncertainty of 4% unless explicitly shown otherwise. Average experimentally determined wave speed (WS) for the Manual and Auto onset determinations are shown. A set of data was included in fitting if the onset determination was deemed to be accurate, by comparing WS Manual to the known wave speed in Kapton of 1875 ± 25 m s^{-1}, i.e. the data quality was good, 'Good' or 'Very Good' in the 'Data Quality' column. Note that 4 km s^{-1} data was not fit irrespective of quality as described in the main text. Data for which one of the sensor pairs had a poorly determined onset time and thus a less accurate speed measurement, had that pair excluded during the calculation of Δv and WS, such as C and G in Dec.5 and Dec.10.

Shot ID	v_{LGG} ± 4 % (m s^{-1})	Δv Manual (%)	Δv Auto (%)	WS Manual (m s^{-1})	WS Auto (m s^{-1})	Data Quality
Dec.1	1959	24 ± 4	24 ± 4	2682 ± 327	8733 ± 5944	
Dec.2	1900	42 ± 9	42 ± 4	2113 ± 25	2298 ± 30	
Dec.3	2160	6 ± 20	10 ± 16	5364 ± 4303	4089 ± 2199	
Dec.4	1746	- 4 ± 4	- 4 ± 4	1866 ± 24	1845 ± 62	Very Good
Dec.5	1742	5 ± 4	5 ± 4	1870 ± 72 excluding CG	1988 ± 144	Very Good
Dec.6	1963	70 ± 4	70 ± 4	1386 ± 197	1414 ± 206	
Dec.7	2005	11 ± 4	11 ± 4	1956 ± 31	1995 ± 80	Good
Dec.8	1953	12 ± 4	12 ± 4	1754 ± 37	1759 ± 68	Good
Dec.9	3999	- 6 ± 4	- 18 ± 10	1837 ± 34	1564 ± 187	Good Not fit
Dec.10	4466	- 7 ± 6	- 1.7 ± 7	1811 ± 88 excluding CG	1932 ± 204	Good Not fit
Dec.11	5216	26 ± 8	20 ± 5	1559 ± 217	1777 ± 116	
Dec.12	1920	- 1.0 ± 5	- 3 ± 5	1130 ± 226	1284 ± 278	
Dec.13	2039	0 ± 4	1.0 ± 4	1886 ± 20	1953 ± 35	Very Good
Dec.14	1830 (± 1%)	- 2 ± 1	- 8 ± 40	1888 ± 23	1609 ± 118	Very Good
Dec.15	2013 (± 1%)	0 ± 1	- 8 ± 2	1920 ± 24	1768 ± 95	Very Good
Dec.16	1879 (± 1%)	0 ± 1	- 7 ± 2	1922 ± 27	1734 ± 163	Very Good
Dec.17	2094	- 1.4 ± 4	- 15 ± 4	1951 ± 33	1826 ± 20	Good
Dec.18	2160	- 3 ± 4	- 9 ± 4	1851 ± 34	2430 ± 185	Very Good
Dec.19	1963	- 18 ± 4	- 17 ± 4	1878 ± 13	1820 ± 14	

A full list of deceleration results is presented in Table 5.3. Here the deceleration is presented as a percentage, a positive value represents a deceleration, while a negative value represents a detector measured speed greater than that of v_{LGG}. The average wave speed (WS) calculated from all four pairs of sensors (A and B, A and C, etc.) is shown to give an overall evaluation of onset time, and a 'Note' column is included to provide information on whether debris was present and/or whether identified anomalies are likely produced by inconsistent onset determination. A full table including WS_{mn} for each shot and all other important quantities is available in Appendix I.

Results including the data from the 'Veri.' shot programme that had well determined onset times were plotted in terms of v_i/v_p vs. m_f/m_p. Where v_i is the incident speed as measured by the LGG and v_p the speed of the projectile as measured by the detector, post penetration of the first Kapton film, and m_f is the film mass and m_p the projectile mass. This helps investigate if a fit based on the conservation of momentum, as discussed in Section 2.8.2, was appropriate. Fig. 5.17 shows the 2 km s^{-1} data plotted with a fit described by Eq. 5.1:

$$\frac{v_i}{v_p} = a\frac{m_f}{m_p} + 1, \tag{5.4}$$

where the 1 is a fixed constant to reflect $v_p = v_i$ for infinitesimal m_f/m_p. Only the 2 km s^{-1} data was fitted as there was not enough data to fit a separate 4 km s^{-1} fit and increasing velocity appears to affect deceleration. Similarly, the 15° from normal inclined shots were not included in the fitting.

The results in Fig. 5.17 show that for 12.5 µm films, StSt420 projectiles as small as d_p = 0.4 mm, with $f:d_p$ = 1/32, impacting at ~ 2 km s^{-1} do not experience deceleration. Then at ~ 2 km s^{-1}, 0.2 mm StSt420 projectiles with $f:d_p$ = 1/16 do show signs of starting to decelerate. At the same $f:d_p$ = 1/16 in 25 µm films, 0.4 mm decelerate by as much as 10%. This is a much larger deceleration for the same $f:d_p$ in the thinner film, shown by the steeper gradient of the fit (a = 5.0 ± 1.9 for 25 µm films and a = -0.03 ± 0.83 for 12.5 µm films) and suggests that there are size dependent effects. It is noted that the fit to the 12.5 µm data is poor with an R^2 = -0.008, this is reflective of the spread in the data. Comparison can be made to even thinner films, such as the 5.4 µm and 2.4 µm Mylar film data from Capaccioni and McDonnell (1986). This data is added to Fig. 5.18. Note, however, that as well as using thinner films in Capaccioni and McDonnell (1986), the projectile size was smaller (~ 0.95 µm to 2.5 µm) and speeds ranged from 2.5 km s^{-1} to 5 km s^{-1}. It is indeed the case that deceleration increases with film thickness, coming away from a fit described by

momentum conservation alone. However, the 28 µm PVDF film data from Simpson and Tuzzolino (1989) (produced from the results in Table 1 on page 630 of their work, and taking the incident mass = m_p and the exiting mass = $m_p + m_f$) suggests deceleration may also be dependent on material as well as thickness. It is therefore suggested that as film thickness increases material properties become important, and a constant of the type *a* in Eq. 5.1 must be included for a fit based on consideration of solely the conservation of momentum. Note that this consideration has an intrinsic uncertainty related to the percentage of m_f accelerated to v_p, due to, for example, an amount of material being vaporised upon impact.

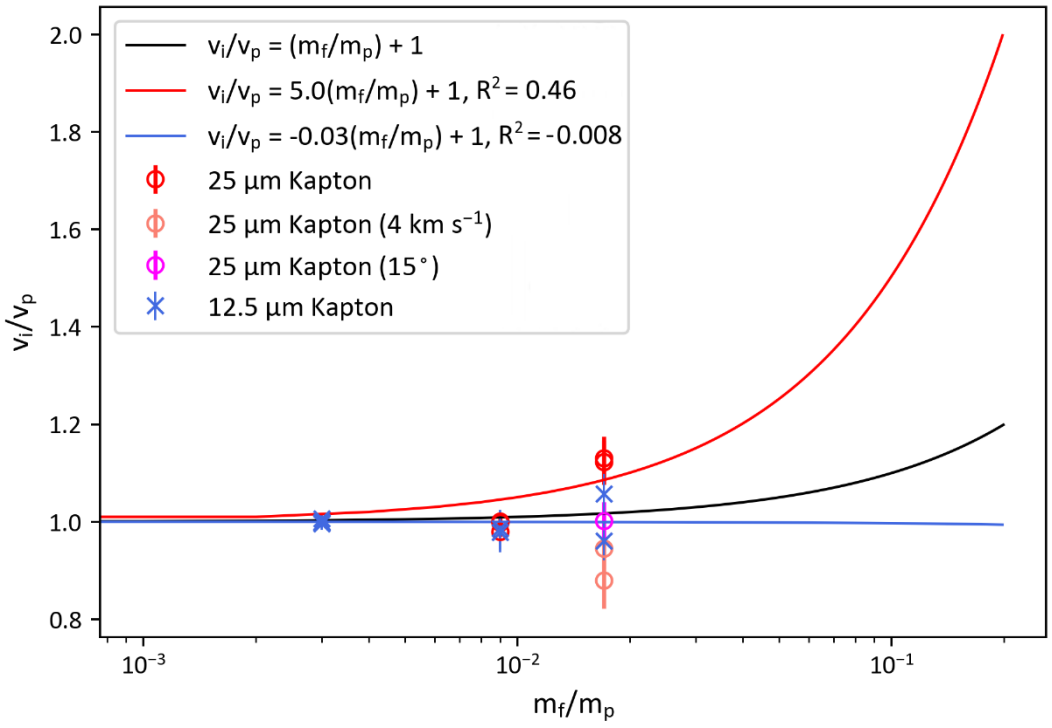

Fig. 5.17: Data with accurately determined onset times (independently verified with wave speed measurements) from the Veri. and Dec. shot programmes, plotted as v_i/v_p vs. m_f/m_p. Here v_i is the incident projectile velocity, v_p the projectile velocity after film penetration, m_f the film mass, and m_p the projectile mass. Deceleration calibration curves were fit to the 2 km s^{-1} data. The + 1 in the fit is a fixed constant to reflect $v_p = v_i$ for infinitesimal m_f/m_p. The red fit for the 25 µm data has a gradient of 5.0 ± 1.9 and R^2 = 0.46. The blue fit for the 12.5 µm data has a gradient of - 0.03 ± 0.83 and R^2 = -0.008. A curve that describes the conservation of momentum in the impact, $\frac{v_i}{v_p} = \frac{m_f}{m_p} + 1$, is included for comparison.

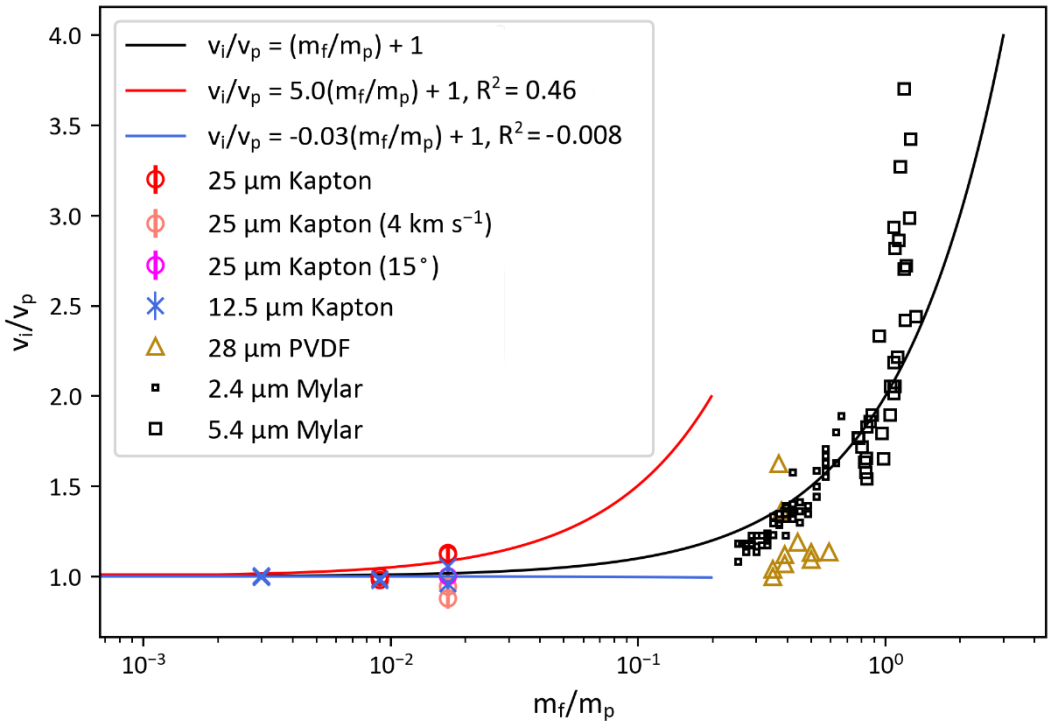

Fig. 5.18: Data with accurately determined onset times (independently verified with wave speed measurements) from the Veri. and Dec. shot programmes, plotted as v_i/v_p vs m_f/m_p showing deceleration, compared to previous research from the literature. Here v_i is the incident projectile velocity, v_p the projectile velocity after film penetration, m_f the film mass, and m_p the projectile mass. Deceleration calibration curves were fit to the 2 km s^{-1} data. The + 1 in the fit is a fixed constant to reflect $v_p = v_i$ for infinitesimal m_f/m_p. The red fit for the 25 µm data has a gradient of 5.0 ± 1.9 and $R^2 = 0.46$. The blue fit for the 12.5 µm data has a gradient of - 0.03 ± 0.83 and $R^2 = -0.008$. The PVDF data is from Simpson and Tuzzolino (1998) and the Mylar data is from Capaccioni and McDonnell (1986). The black curve is not a fit to the previous data, instead it is the curve that describes the conservation of momentum in the impact, $\frac{v_i}{v_p} = \frac{m_f}{m_p} + 1$.

Contrary to the earlier studies by Grün and Rauser (1969) and Capaccioni and McDonnell (1986), here deceleration was observed to depend on the incident speed (see Fig. 5.17 and Fig. 5.18), hence why the 4 km s^{-1} data was excluded from the fits. Similarly, to the penetration hole features suggesting that impact KE affects penetration hole morphology, this could suggest that the impact KE plays a role in deceleration through thicker films. This might be because as the film thickness increases, the internal strength of the material becomes increasingly important. This could require extra KE to wholly remove the material and/or induce hydrodynamic flow. Thus, as film thickness increases, the required KE increases, and as projectile size and speed decrease the ratio between KE required and impactor KE increases, representing a larger percentage loss of KE and hence a slower projectile exit speed.

Another film material property that could play a role in deceleration is the likelihood of the film to produce barrel/tunnel-like penetration hole morphologies at a certain projectile KE. If these tunnel-like features at the back of the film are not the product of flowing material and are instead original non-destroyed material, this would suggest a larger time of acting on the projectile, which could in turn increase deceleration. Fitting v_i/v_p vs $(m_f/m_p)^{0.5}$ which would infer a v^2 dependence indicative of a dependence on KE (Fig. 5.19), did not show as much agreement between data and fit as for m_f/m_p, with 25 µm fits having $R^2 = 0.46$ and $R^2 = 0.25$ for m_f/m_p and $(m_f/m_p)^{0.5}$ respectively. It does, however, show promise for thicker films, with the 25 µm Kapton fit closer to the 28 µm PVDF film data, than for a fit containing m_f/m_p.

A similar penetration hole size to normal incidence shots was observed in the 15° angle of incidence shots. This would suggest that at least the same deceleration would be expected, however, the one 15° inclined angle of incidence shot that had an accurate time of onset determination showed no deceleration (Fig. 5.17). This is likely a consequence of the spread of the data due to inaccuracy of onset determination and velocity measurement for smaller projectiles, and is inconclusive considering there is only one data point.

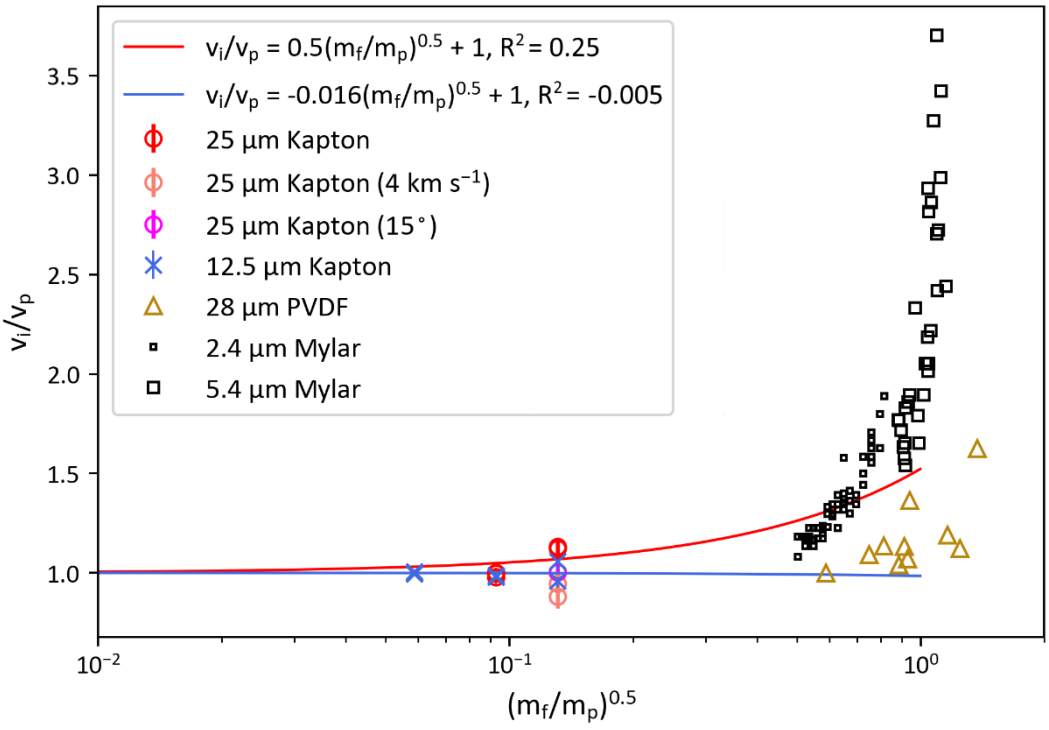

Fig. 5.19: Data with accurately determined onset times (independently verified with wave speed measurements) plotted as v_i/v_p vs $(m_f/m_p)^{0.5}$ showing deceleration. Here v_i is the incident projectile velocity, v_p the projectile velocity after film penetration, m_f the film mass, and m_p the projectile mass. Deceleration calibration curves were fit to the 2 km s^{-1} impact data. The red fit for the 25 µm data has $R^2 = 0.25$, and error of 0.5 ± 0.26. The blue fit for the 12.5 µm data has $R^2 = -0.005$, and error of -0.016 ± 0.09. The PVDF data is from Simpson and Tuzzolino (1998) and the Mylar data is from Capaccioni and McDonnell (1986).

The deceleration measured using the velocity determined by the automatic determination algorithm was mostly in good agreement with that of the manual pick for the 2 km s^{-1} data, with an average deviation of 81 ± 21 m s^{-1}. The 4 km s^{-1} data was in less agreement with an average deviation of 515 ± 14 m s^{-1}. Thus, at 2 km s^{-1} when both automated and manual pick data return similar results, any larger inaccuracy in onset determination (compared to that for 1 mm sized projectiles in Chapter 4) is unlikely to originate from inaccuracy from the manual pick, but instead the underlying behaviour of the acoustic signals observed. Considering all of the data that was accurately determined using a manual pick, collected for large and small projectiles, the average deviation between manual pick and autonomous pick was 75 ± 21 m s^{-1} at 2 km s^{-1}, and 253 ± 109 m s^{-1} at 4 km s^{-1}. This can be considered the accuracy of the rudimentary algorithm.

From the Dec. data set, of the eight shots that showed non-acoustic noise (with a total of 32/114 traces showing noise) only one shot (Dec.10) displayed non-acoustic noise that is likely to have affected the speed determination. Considering all sets of data Veri. and Dec. the probability of non-acoustic noise effecting the velocity measurement from a pair of sensors is 2/26 when considering shots, and as low as 2/156 when considering all individual traces. However, all six shots at speeds $\sim$ 4 km s^{-1}, for which light flash is more likely, showed signs of non-acoustic noise with at least one speed measurement affected. Thus, at the impact speeds expected for a flight model the probability of noise effecting data is more likely to be 2/36 (in terms of all traces) and 2/6 (in terms of impact events). This therefore requires further work to clarify and resolve this issue.

5.5 Conclusions

This chapter started with the consideration of applying automated algorithms to time of onset detection, and their use to potentially produce lower onset determination in-accuracy than a manual pick, for more variable data. An algorithm was developed based on the arrival of a percentage of the total signal in a given window. The algorithm achieved an average speed agreement with the training and verification data of 60 ± 22 m s^{-1} for 2 km s^{-1} shots and a mean deviation of 79 ± 41 m s^{-1} for 4 km s^{-1} shots, considering all of the data that had an accurately determined onset time with a manual pick. This includes the 1 mm projectile data and smaller projectiles, which typically had less accurately determined onset times. The mean deviation between the speed calculated from a manual pick and an

automated pick was found to be 75 ± 21 m s^{-1} at 2 km s^{-1}, and 253 ± 109 m s^{-1} at 4 km s^{-1}. Achieving, good agreement with a rudimentary algorithm suggests that with refinement over a large enough data set, such an algorithm would be applicable to a flight model detector.

Next, the penetration holes in both thickness of film were found to show four morphologies.

- TFL, which were found for f:d_p = 1/32, had penetration holes approaching $d_h = d_p$, with small more individually defined filaments close to the edge of the penetration hole.
- BL, which were observed for f:d_p = 1/16 and 1/8 at ~ 2 km s^{-1}, had a maximum penetration hole size at the film surface with $d_h > d_p$. Front and rear filaments formed continuous lip structures that protrude inwards to create $d_{lip} < d_p$.
- CL, which were seen in shots with f:d_p = 1/16 at ~ 4 km s^{-1}, had larger $d_h > d_p$ than for BL morphologies, and the Kapton filament lips resembled crater lips, curving outwards, creating $d_{lip} > d_h$.
- Di, which were present in the 15° from normal incidence inclined impacts with f:d_p = 1/16, had $d_h > d_p$. Di penetration holes were not significantly elliptical in shape, however, the Kapton filament lips showed directionality downrange of the projectile incidence direction.

Overall, penetration morphology was found to be dependent on KE with respect to film thickness, as well as f:d_p. Normalised hole diameter was found to increase with increasing f/d_p. An expression relating d_p to d_h was determined (Eq. 5.1), and comparison to previous penetration experiments by Nakamura *et al*. (2015), found reasonable agreement. Comparison to the results of Neish and Kibe (2001) also found that a fit of the type in Eq. 5.3 is compatible with the penetration hole diameter results presented here.

The acoustic signals for smaller projectiles showed similar features to those from larger projectiles. Although, signal onset determination tended to be less accurate, returning a larger spread of sensor-pair speed measurements, and less accurate wave speed measurements. It was the case that 6/19 of the data sets were found to have inconsistencies, and thus were deemed unusable. This inaccuracy in the determination of onset time is thought to be a consequence of the complexity of penetration features increasing as f:d_p increases and KE decreases, giving rise to more complex acoustic signals.

Coupling this with the lower accuracy of v_{LGG} for smaller projectiles lead to larger uncertainties and spread in the deceleration data collected. Furthermore, few data points that experienced and thus sampled deceleration were collected.

Non-acoustic noise thought to originate from light flash was again observed in all three shots at $\geq$ 4 km s^{-1}. It is recommended that this be studied further to investigate the possibility and effectiveness of sensor shielding. A further recommendation would be to investigate the use of light flash for impact detection and velocity measurement, as light flash may provide a more consistent signal for onset determination.

For 12.5 µm films only StSt420 projectiles of 200 µm size impacting at $\sim$ 2 km s^{-1} started to show signs of deceleration. In the 25 µm films, projectiles of 400 µm at $\sim$ 2 km s^{-1} showed $\sim$ 10% deceleration. This suggests that at these speeds deceleration is starting at $f{:}d_p$ =1/16. More generally, the data fit a conservation of momentum law, but also show some size dependent effects, with thicker films showing more deceleration at lower m_f/m_p. When considering previous data for different materials there is a clear material dependence. Thus, a final expression describing deceleration would need to include a constant dependent on a material property as well as thickness and the ratio $f{:}d_p$.

As opposed to the findings of previous studies that considered smaller absolute size scales with the use of electrostatic accelerators, here deceleration was found to be dependent on velocity as well as mass. This suggests that deceleration is also linked to the KE of an impactor and not just its momentum. Fitting data to $(m_f/m_p)^{0.5}$ shows promise for thicker films, for which material properties become more important. However, the fits were not of high quality. This could mean that a function of momentum and KE is required (i.e. a power in the fit between 0.5 and 1), however, the data is too scattered to support such an analysis. Thus, it is likely that conservation of momentum explains the data for thin films well, while conservation of energy is required for thicker films that have an appreciable absolute strength.

For StSt420 projectiles ≥ 400 µm, which are the size of interest that pose most threat in space, no deceleration or disruption occurs for impact into 12.5 µm films. Furthermore, due to the apparent dependence on KE, for impacts in space at speeds > 7 km s^{-1}, it is expected that StSt420 projectiles as small as 0.2 mm would not experience deceleration. It is recognised that this study is not comprehensive enough (i.e. with enough deceleration data points) to provide a definitive calibration of the deceleration associated with passage

through 12.5 µm Kapton films. The fits discussed are instead indicative of the features that would appear in such a calibration curve for smaller projectiles. A fit to a fuller range of data should consider both film thickness and material, with a constant in the fit likely to relate to a material property such as yield strength or shear modulus according to:

$$\frac{v_i}{v_p} = \alpha\varepsilon f \frac{m_f}{m_p} + 1\,, \tag{5.5}$$

where α is a constant, ε is the material parameter, and everything else is as defined previously. Different material projectiles that may experience varying deceleration or disruption at smaller f:d_p would be a useful addition to a fuller data set.

Chapter 6: MASTER Model Orbital Environment Simulations

6.1 Introduction

The feasibility of using CubeSat sized impact detectors to measure the dust flux in space has implications for the development of Kapton based thin-film detectors. One such detector called CLOTH, was flown aboard the EQUULUS CubeSat mission (Funase *et al.,* 2020). The CLOTH instrument was a particle impact detector that demonstrated a new technology that the authors refer to as 'smart MLI'. The idea being that a thin-film dust detector (comprised of a thin-PVDF film) is integrated into the multilayer insulation (MLI) of EQUULUS. The CLOTH/smart MLI design was based on the ALADDIN detector flown on the IKAROS solar sail demonstrator mission. In the case of CLOTH, a thin PVDF film that detects the momentum of impacting particle is situated behind the first layer of Kapton film, sandwiched in the MLI. However, Funase *et al*., 2020, make the point that even if technically feasible, "a statistically valid detection of microparticle impacts requires a large sensor area" (Funase *et al.,* 2020).

Another Kapton based thin-film particle detector under development is the thin-film dust sensor flown onboard the ASTERISC CubeSat (Ishimaru *et al.*, 2021). This sensor was a deployable thin-film of Kapton, equipped with equally spaced piezoelectric sensors, that detect elastic waves produced by impacts on the film. True impact signals are distinguished from noise by consideration of the time of arrival, duration, and amplitude of the signals detected by each of the piezoelectric sensors (this is akin to a single layer DRAGONS detector).

More generally, the feasibility of using CubeSats for in-situ orbital debris detection is an important question to investigate, as it has wider implications to the development of detectors with other types of traditional detectors, discussed earlier, being redesigned to fit CubeSats. This carries with it the benefits discussed in Section 2.6 of greatly reducing time to market/launch, and cost of detectors. It is hard to make a comparison between the cost of traditional detector missions and CubeSat detector missions, as this information is usually commercially sensitive. However, an example cost comparison can be attempted. In 2019, a successor to SDS was budgeted at $49m for deployment and 3 years operation (NASA FY2022). A full cost analysis for the impact detector mission flown aboard the 3U CubeSat ARMADILLO was performed (Brumbaugh et al., 2012), and suggested a cost of

$1.5m for design and construction of the detector and CubeSat, and a further $2m for testing, integration, operations, etc., totalling $3.5m in 2011. However, in recent years, COTS components have driven down the costs of CubeSats, and similarly there has been a reduction in launch costs. Thus, if we take a commercially available 3U bus e.g. an Endurosat bus (Endurosat, 2024) ~ $300k (~ 2.5 kg), assume $50k for the design, production, and integration of a detector payload of ≤ 1 kg, take operational costs (staff, ground station access, etc.) for three years to cost ~ $120k, and finally costs for ride-share launches are ~ $70k/kg or less, thus the launch of a 3.5 kg CubeSat would cost ~ $245k. This leads to a total cost for a 3U CubeSat detector mission of ~ $715k today (2023/24). Without considering the inflation that would have to be applied to the values quoted for the earlier CubeSat, and SDS, a large three figure value for a CubeSat mission is a fraction of a traditional mission (~ 1/67 for the above case). However, even if cost benefits suggest that use of CubeSats to host impact detectors is feasible and appropriate detector technologies exist, issues remain: How many detectors do you need to get a valid flux measurement? Does the number simply scale with detector area for example? And most importantly, can a fleet of distributed small sensors deliver a measure of the flux compatible with that from a traditional single, large area detector on a single satellite? All of this is explored using the MASTER modelling tool.

Accordingly, this chapter introduces the theoretical background and the operation of ESA's space environment modelling software MASTER. This is then used to simulate the near-Earth space dust and orbital debris environment. Orbits with higher spatial densities of debris, which are key targets for future debris flux measuring missions, were identified, and the feasibility of using novel small detectors for in-situ flux measurements assessed. This was done with a focus on the mm-sized dust and debris populations and the use of CubeSats as host platforms for particle detectors.

6.2 Basic Functionality and Background of MASTER

The MASTER software (also known as the MASTER model and available at (ESA, 2022)) is designed to characterise the natural space-dust and anthropogenic debris particle environment near the Earth, and provide a simple evaluation of its effects on space missions. MASTER 8.0.3 is the specific version used in this work and outlined herein. The software consists of a spatial density and a flux prediction tool, with analytical capabilities that allow the population to be represented as a function of many variables including, for example, impactor size or mass, impact speed, and impact direction (ESA Space Debris

Office, 2022). The spatial distribution provides a three-dimensional description of the environment up to an altitude of 500,000 km. Incident flux predictions for a body in a user specified orbit can be modelled using one of three surface definitions (target objects):

1. A unit sphere of 1 m^2 cross-section that idealises the spacecraft as a sphere with its centre moving along the specified orbit.
2. A single-sided plate of 1 m^2 surface area randomly tumbling around its centre. The flux incident on such a plate is equivalent to ¼ of the flux for a sphere of 1 m^2 cross-section.
3. An oriented single-sided surface (or plate) of 1 m^2 surface area. Up to ten plates can be assigned, each with its own pointing direction (surface normal vector) specified within the given orientation system. Shielding effects between surfaces are not modelled. The available orientation systems are:
    a) An Earth-oriented surface, for which the spacecraft's nadir points to the Earth and the surface pointing direction is defined by the Azimuth angle (measured from the flight direction of the spacecraft) and the Elevation angle (measured from the local horizontal plane). This is essentially the reference frame of the spacecraft.
    b) A Sun-oriented surface, where the pointing direction is described by the ascension angle (from the direction to the sun), and declination angle (from the Ecliptic).
    c) An inertially fixed surface, with the direction described by an Earth equatorial coordinate system, i.e. the right ascension angle (from the vernal equinox) and the declination angle (from the Ecliptic).

6.2.1 Population Sources and Spatial Distribution

The debris population considered in the MASTER model is comprised of different sources, each with a corresponding generation model in terms of diameter/mass distribution, additional velocity, and directional spreading (André Horstmann *et al.*, 2020). Here, the additional velocity is an added velocity caused by the acceleration of a piece of debris in the creation event, i.e. it is separate to the orbital velocity and would be the velocity of the debris in the reference frame of the initially orbiting parent body. Individual events are simulated in the POEM (Program for Orbital Debris Environment Modelling) tool with the corresponding model, and the resulting debris cloud propagated forward to the MASTER-8 reference epoch (1/10/2016).

Initially, in earlier releases of MASTER, only fragmentation events from explosions and collisions were considered as sources of debris. Indeed, debris particles produced in fragmentation events account for a significant portion of the overall population, especially for the larger diameter regime. Previously, the Battelle model for fragmentation (Fucke and Sdunnus, 1993) was used, which focused on using the mass distribution of the produced particles to determine particle production and key parameters. More recently, the 1998 revision of the NASA breakup model was implemented (Braun *et al*., 2017). This model is based on the diameter distribution of the produced debris and from this the area-to-mass ratio. Other particle characteristics such as mass or additional velocity can be directly derived from the area-to-mass ratio, which in turn can be derived from orbital decay data. Thus, the orbital decay of actual fragments in space can be used to inform and verify the model, as opposed to solely relying on ground testing to determine properties of the produced debris. For the number of objects of a given diameter produced, the Bettelle and revised NASA models do not differ significantly for diameters around 10 cm. However, below 10 cm the NASA model predicts significantly more debris, which is the critical size regime for high performance radar campaigns.

Today, MASTER includes many other debris source including:

- Launch/mission-related objects,
- Fragmentations,
- Dust and slag from solid rocket motor (SRM) firings,
- Sodium Potassium (NaK) droplets, from Radar Ocean Reconnaissance Satellite (RORSAT) core ejection events,
- Surface degradation particles (paint flakes),
- Multi-layer Insulation (MLI),
- Ejecta.

Launch/mission-related objects are in general > 10 cm in size and thus are catalogued, and do not require generation models. For the sources producing debris > 1 mm in size deterministic models are used, considering 258 fragmentation events, 2442 slag creating SRM firings, 16 NaK release events, and 2 NaK leakage events. SRM dust is also modelled deterministically, while the other small particle generations models for ejecta, paint flakes, and MLI degradation are statistical, as no single events are identifiable. A full theoretical description of each generation model used to determine the population spatial density

distribution, and all the other programmes and models described here can be found in Horstmann *et al*. (2020).

Future populations are also generated by the POEM tool, with collision analysis, launch/mission related debris and all event lists required created by simulation with DELTA-4 (the Debris Environment Long-Term Analysis model). Both POEM and DELTA are developer tools used in the 'pre-processing' branch of the MASTER model that produce the probability densities that make up the population database used in the MASTER software user application. The future population depends on somewhat random events that are related to future space activity. Thus, to produce the event lists that are fed into POEM and ultimately produce the population, DELTA-4 uses multiple Monte-Carlo simulations. Three Monte-Carlo scenarios are predicted based on past space activity. These include a 'business as usual', an 'intermediate mitigation', and a 'full mitigation' scenario, essentially a worst, intermediate, and best-case scenario for future space activity and debris production. Each scenario is simulated twenty times with random conditions, and out-put populations from all sixty simulations are averaged to provide a single future population estimate. Unlike the historical population that is simulated up to the reference epoch, and which has quarter yearly epoch populations, future populations are determined for a yearly epoch.

The meteoroid population can be separated into two components - the background population and seasonal streams. In MASTER the background meteoroid population can be modelled with the Divine-Staubach model (Divine, 1993; Staubach, 1996) or the Grün model (Grün *et al*., 1985), and meteoroid streams modelled with the Cour-Palais (Cour-Palais, 1969) or Jenniskens/McBride (Jenniskens, 1994) models. The Grün model is the most recent to be implemented in MASTER-8, and includes an inherent averaging of the seasonal meteoroid streams. This analytical model, which was derived from in-situ measurements, investigation of lunar rocks, and meteor observations, describes an isotropic flux that is dependent on meteoroid mass. The default model uses a constant velocity of 20 km s^{-1}, although the Taylor velocity distribution (with a mean velocity of $\sim$ 17.7 km s^{-1} to 18.1 km s^{-1}) has been added. It is valid for the mass range of 10^{-15} g $\leq$ m $\leq$ 10^{-1} g, equal to a diameter range of 0.9 µm $\leq$ d $\leq$ 4.2 cm, and assumes a constant meteoroid density of ρ = 2.5 g cm^3.

6.2.2 Flux Modelling

Flux predictions for the space debris population are made using a stochastic and probabilistic model. A multi-dimensional probability distribution in terms of size and orbit is created from the population. The individual particles to be considered in the simulation are then randomly produced at the time of simulation, according to this distribution. This population of particles forms the particle Cell Passage Event (CPE) data set used to determine flux.

Firstly, the near-Earth environment is separated into discrete volume elements or 'bins' (Fig. 6.1), each of which is assigned a target CPE data set, comprising of:

- Inertial target velocity of passage (v_t),
- Local azimuth of target passage (A_{lt}),
- Local elevation of target passage (h_{lt}),
- Target residence probability ($p_{t\,bin}$).

While each particle within a bin has a particle CPE data set comprising of:

- Particle ID,
- Inertial particle velocity of passage (v_p),
- Local azimuth of particle passage (A_{lp}),
- Local elevation of particle passage (h_{lp}),
- Particle spatial density contribution ($\varrho_{p\,bin}$).

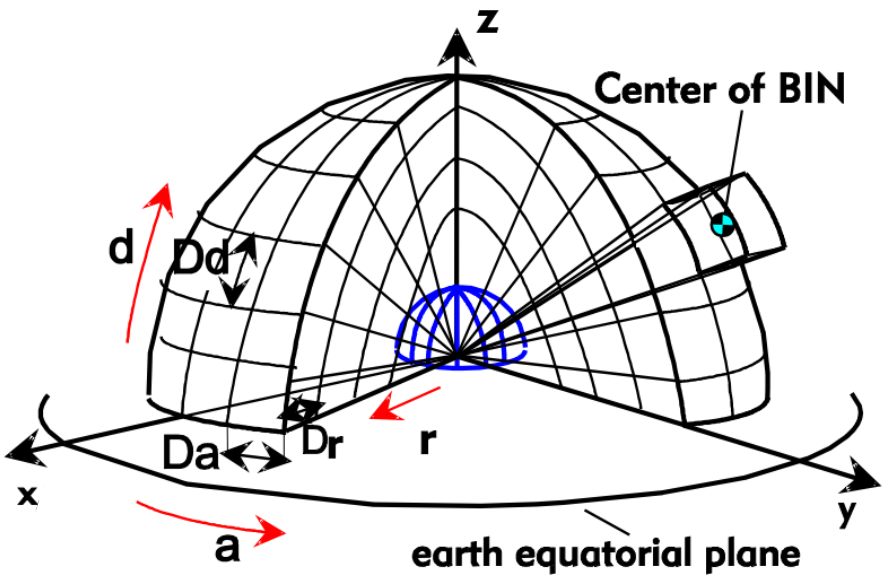

Fig. 6.1: Near-Earth environment volume discretisation scheme implemented by MASTER. Here r is the radius, a the azimuth angle, d the declination angle, and D stands for delta (Δ). Modified from Horstmann *et al.* (2020).

The spacecraft's passage through the space environment filled with particles is considered equivalent to a surface sweeping through a series of bins filled with static particles (albeit each assigned a particle velocity v_p that is not yet considered). All particles in the path of the surface, and thus intersected, are considered to impact. Thus, the impact probability for a single particle in a bin is expressed as per Eq. 6.1 (Horstmann *et al.*, 2020):

$$p_i = \Phi_{p\,bin}\, A_t\, \Delta t = p_{p\,bin}\, p_{t\,bin}\, p_{p\,V}\,, \tag{6.1}$$

where:

p_i = Impact probability,

$\Phi_{p\,bin}$ = Object flux encountered in a bin from a single particle,

A_t = Target surface area,

Δt = Residence time of target in bin,

$p_{p\,bin}$ = Probability of particle residence within bin,

$p_{t\,bin}$ = Probability of target residence within bin,

$p_{p\,V}$ = Probability of particle within swept volume.

Eq. 6.1 describes the simple conditions for an impact to occur within a volume element: that both target and particle must be in the same bin and the particle must occupy the volume swept out by the target surface. The latter condition can be described by Eq. 6.2:

$$p_{p\,V} = \frac{V_t}{V_{bin}} = \frac{A_t\,\Delta v_{p_{rel}}\,\Delta t}{V_{bin}}. \tag{6.2}$$

Here:

V_t = Bin volume swept by the target surface in Δt

V_{bin} = Total volume of bin

$\Delta v_{p_{rel}}$ = Particle relative velocity = v_t for a static particle.

Reformulating the particle residence probability in terms of its spatial density contribution

$$p_{p\,bin} = \varrho_{p\,bin} V_{bin}\,, \tag{6.3}$$

and considering the residence probability of the target, which is the fraction of time spent in the bin of its total orbital period ($\Delta\tau_t$):

$$p_{t\,bin} = \frac{\Delta t}{\tau_t}\,, \tag{6.4}$$

leads to the flux produced by a single particle as Eq. 6.5:

$$\Phi_{p\,bin} = \varrho_{p\,bin}\, p_{t\,bin}\, \Delta v_{p_{rel}}\,. \tag{6.5}$$

Here $\varrho_{p\ bin}$ is the object density contribution of the particle within the volume segment. Most of these terms, are functions of the volume element e.g. V_{bin}, $\varrho_{p\ bin,}$ and Δt. Whereas, some other terms that are not wholly described in terms of a volume element, such as Δv_{prel}, are assigned a mean value over the bin crossing period, equal to the value at the centre of the bin. The total flux encountered by a target (Φ) can then be calculated by a summation over all i bins crossed, and all j particles in each bin:

$$\Phi = \sum_i \Phi_{bin} = \sum_i \left(\sum_j \Phi_{p\,bin}\right) = \sum_i \left(p_{t\,bin} \sum_j \varrho_{p\,bin}\, \Delta v_{p_{rel}}\right). \tag{6.6}$$

All that is left to do is apply the fact that the particles are not stationary, thus the impact velocity ($\Delta\vec{v}_{imp}$) will be the difference vector of $\vec{v}_t$ and $\vec{v}_p$, given by Eq. 6.7:

$$\Delta\vec{v}_{imp} = \vec{v}_p - \vec{v}_t. \tag{6.7}$$

Hence, by replacing $\Delta v_{p_{rel}}$ in Eq. 6.6 with $\Delta\vec{v}_{imp}$, the final vector expression for the flux incident on the target surface is given by Eq. 6.8:

$$\overrightarrow{\Phi} = -\sum_i \left(p_{t\ bin} \sum_j \varrho_{p\ bin}\, \Delta\vec{v}_{imp}\right). \tag{6.8}$$

To better fit the general definition of flux, a minus sign is added to make the direction of impact towards the target surface, as the resultant difference vector will point away.

Here we can see that the flux determination process has to loop over each bin crossed by the target and each particle within those bins. While this is computationally expensive, it allows the individual flux geometry to be resolved. This provides information not only on the object flux, but also on its distribution in terms of impact velocity, impact angle, and impact location (in orbit), as well as orbit and impacting object characteristics. This knowledge of impact directionality is critical for the comparison of space returned surfaces that have specific on-orbit pointing directions.

6.2.3 Uncertainties in MASTER

In MASTER the uncertainties for the historic reference population in LEO (up until the reference epoch of 1/10/2016) are based on comparisons between simulation outputs and measured/validation data. The source of validation data for large objects ≥ 10 cm that can be readily tracked form Earth, is the direct measurements of the population using telescopes and radar, such as the ESA-Space Debris Telescope (ESA-SDT), European Infrared Scattering Radar (EISCAT), and the Tracking and Imaging Radar (TIRA). Radar measurements are also used to produce validation data for down to centimetre-sized objects (Horstmann *et al*., 2017). The Program for Radar and Optical Observation Forecast (PROOF) tool is then used to estimate a detection probability for a specific (and parameterised) sensor, based on the MASTER population, for comparison to the observation data (Braun *et al.*, 2021). Small object validation < 1 cm, is made through indirect observation data collected from the LDEF, HST-SM1, HST-SM3B, and EuReCa missions. These data use impact features from returned surfaces to provide flux values to which MASTER results are compared. There are almost no sources of validation data for medium Earth orbit (MEO), thus LEO uncertainties are projected to MEO. For geostationary equatorial orbit (GEO) a group uncertainty for the population > 1cm is produced from ESA-SDT data. The low size resolution in this uncertainty

is the product of this instrument measuring magnitude, as opposed to size. Again, in absence of any data on the small size regime, the LEO uncertainties are applied to GEO.

Both methods, direct and in-direct, provide uncertainties in a similar way, by means of the error ratio (Horstmann *et al*., 2020). The error ratio defines the difference between the MASTER predicted data and the measurement data, normalised by the model value:

$$\text{Error ratio} = \frac{\text{Measurment} - \text{MASTER}}{\text{MASTER}}. \tag{6.9}$$

Sigma error values for the cumulative MASTER data are calculated by the summation of the variance of all the uncertainty bins crossed (considered), each weighted by their flux contribution. Weightings (ω) are applied to mitigate large uncertainties from low flux values affecting the total uncertainty, whereas larger flux contributions have smaller uncertainties. The general form for cumulative sigma values is given by:

$$\sigma_{cum} = \sqrt{\frac{\sum_{i=1}^{n}(\omega_i \cdot {\sigma_i}^2)}{\sum_{i=1}^{n}(\omega_i)}}. \tag{6.10}$$

In the absence of measurement data to compare the results to, future population uncertainties are calculated slightly differently. Delta-4 outputs a symmetric standard deviation based on the Monte Carlo simulations that produced the populations. This uncertainty can be expressed in a similar way to the error ratio, as the '1σ uncertainty evolution', ε(t):

$$\varepsilon(t) = \frac{N_{\sigma_{+/-}} - \bar{N}_{nom.}}{\bar{N}_{nom.}}. \tag{6.11}$$

Here $N_{\sigma_{+/-}}$ is the upper or lower 1σ number of objects and $\bar{N}_{nom.}$ is the nominal mean number of objects.

6.3 ESABase2/Debris

ESABase2 is a modelling software package produced by FEV etamax GmbH, under contract for ESA (available at Etamax (2023), website last accessed 09/06/2023). The software is a space engineering analysis tool akin to the more mission-oriented of ESA's space debris software tool-kit, such as the Debris Risk Assessment and Mitigation Analysis (DRAMA) tool. ESABase2/Debris is a module/application that builds upon the '/Framework' module to provide incident flux calculations for a user defined three-dimensional geometric model.

An example of a 6U CubeSat geometry in the geometry window is shown in Fig. 6.2. ESABase2/Debris can be considered a front-end to a MASTER backend (although other models such as ORDEM 3.0 are available), that allows the implementation of a particular geometric model for subsequent flux analysis. In this work, the MASTER-8 model was used and so the population and particle flux derivation method is the same as that described for MASTER.

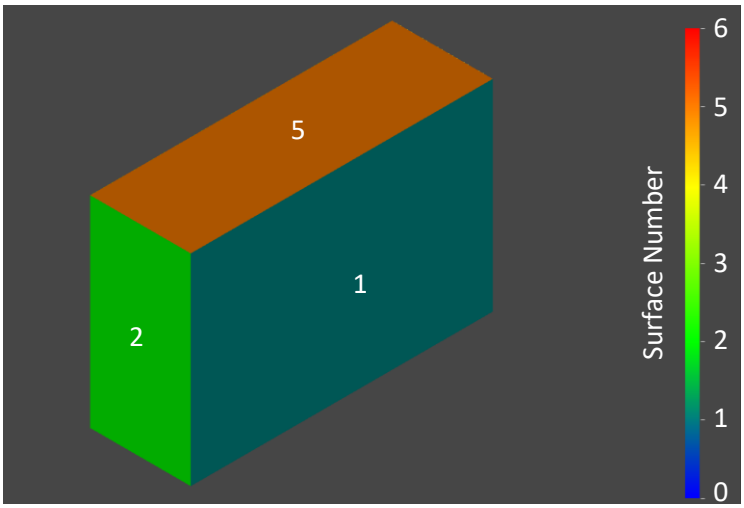

Fig. 6.2: Geometric model of a 6U CubeSat in the ESABase2 geometry window. Each individual surface is given a number, surfaces 1, 2 and 5 can be seen here.

6.4 Validation of MASTER

When using third party software there is the possibility that it may be incorrectly implemented, even when the appropriate measures have been taken to familiarise oneself with the software. To ensure that MASTER was correctly implemented (i.e. correct variables specified, appropriate surface definition logic used, etc.) and that the results collected had real world validity, validation data for comparison to known results was generated before running simulations for the data investigated in this chapter.

6.4.1 Validation on the Implementation of MASTER

After familiarising myself with the variables used within MASTER, and the operation/workflow, a test was carried out to reproduce a set of data given in Wozniakiewicz and Burchell (2019), produced using MASTER-8 by V. Braun (a space debris

engineer at ESA's Space Debris Office, responsible for the development of MASTER). The data being simulated was that of the time expected before an impact of a given sized object (debris or meteoroid) on a spacecraft with a surface area of 30 m^2 at different altitude Earth orbits. To do this, impact flux (m^{-2} $year^{-1}$) predictions were computed using MASTER's flux prediction tool, and converted to a time for impact by multiplying by the spacecraft surface area, and taking the inverse. The only parameters known from the original simulations by V. Braun were the altitude, inclination, and epoch, all other parameters were left as their default values. Only the total flux incident on a 30 m^2 surface area spacecraft, irrespective of direction, was presented. Thus, the unit sphere surface definition was used during my simulation (henceforth known as 'simulation' or 'this simulation', the original will be specified as 'past simulation'). For the LEO orbits (altitudes of 400 km and 800 km) the inclination was set to 98.7°, for the geostationary orbit (GEO) the altitude was set to 35,786 km and inclination 0°. The epoch used for all three simulations was the 2016 reference epoch. This was set as the start and end epoch, to provide a so called 'snapshot' of the population at this time.

A comparison between the data from the simulation and the past simulation is shown in Table 6.1. Considering the deviations from all altitude data points (both combined and debris only) the mean absolute deviation is 19%, mode = 6%, and median = 6%. If we consider only the data for the > 0.1 mm and > 1mm columns, of most relevance to this chapter, the mean value is 7.5%, mode = 3%, and median = 5%. These results show good agreement, with an average deviation of $\sim$ 6%. This deviation is likely to arise from a difference in starting conditions (e.g. a differently selected population or model), or from updates in the software. For example, improvements made in only the most recent revision (MASTER 8.0.3, released 18/03/2022) include a "fix in Earth shielding modelling for oriented surfaces when using the Grün meteoroid model" and "minor improvements" (ESA's Space Debris Office, 2022). This suggests that the MASTER software was implemented correctly, thus providing results consistent with the current MASTER model.

Table 6.1: Comparison between data generated for the time before an impact occurs for a given sized object (debris or meteoroid) on a spacecraft with a surface area of 30 m^2, from this simulation and data from a past simulation (Wozniakiewicz & Burchell, 2019). The spacecraft surface area and orbit altitudes used are the same as those used for the past simulation. In each cell the past results are shown at the top followed in successive rows by the results from this simulation, and the percent difference between the two values. The values and percentages included in parentheses for the > 0.1 mm and > 1mm results are the time before an impact when considering only debris objects.

Altitude (km)	> **0.1 mm**	> **1 mm**	> **1 cm**	> **10 cm**
400				
Past	0.92 (2.2) days	7.9 (40) years	1,700 years	21,600 years
This	0.89 (1.8) days	9.6 (39) years	1,800 years	21,100 years
Δ%	3% (18%)	17% (3%)	6%	2%
800				
Past	0.17 (0.19) days	2.6 (3.4) years	101 years	1,510 years
This	0.16 (0.18) days	2.7 (3.5) years	40 years	1,749 years
Δ%	6% (5%)	4% (3%)	60%	16%
35,786				
Past	1.8 (23) days	12 (660) years	71,000 years	1,020,000 years
This	1.8 (21) days	14 (628) years	75,000 years	2,690,000 years
Δ%	0% (9%)	17% (5%)	6%	163%

6.4.2 Validation of the Real World Applicability of MASTER

Another important aspect to verify is that the simulations being produced are applicable to the real world, i.e. were the simulations providing results that accurately modelled the real world environment? For this, two simulations were conducted for comparison to results from previous studies of space-based measurements: One from the LDEF mission (Humes, 1993), and the other from a returned HST solar array wing (Drolshagen *et al*., 1997).

6.4.2.1 Validation against LDEF Data

The LDEF was a cylindrical twelve sided spacecraft, 4.27 m in diameter, comprising of a 9.14 m long aluminium grid frame (O'Neal & Burton Lightner, 1991). There were seventy-two equal-size openings on the sides, six openings on the Earth-facing end, and eight openings on the space-facing end. Each of these openings held experiment trays (Fig. 6.3).

LDEF's scientific objective was to host a series of fifty-seven experiments, mostly containing materials, to probe the effects of space exposure on materials and to investigate the space environment (see O'Neal and Burton Lightner, 1991 for an overview of the LDEF mission). The space shuttle Challenger deployed LDEF in a near-circular orbit (apogee of 480 km and a perigee of 474 km) with an inclination of 28.5°, in April 1984, and it was retrieved 69 months later on January 1990. LDEF was three-axis gravity-gradient stabilised, allowing for a known, and maintained, pointing direction. Post-flight the LDEF Meteoroid and Debris Special Investigation Group conducted a survey on a number of the space exposed aluminium plates to determine the flux. One such set of flux data was generated for the space-facing end of LDEF and is the source for comparison in this validation (Humes, 1993).

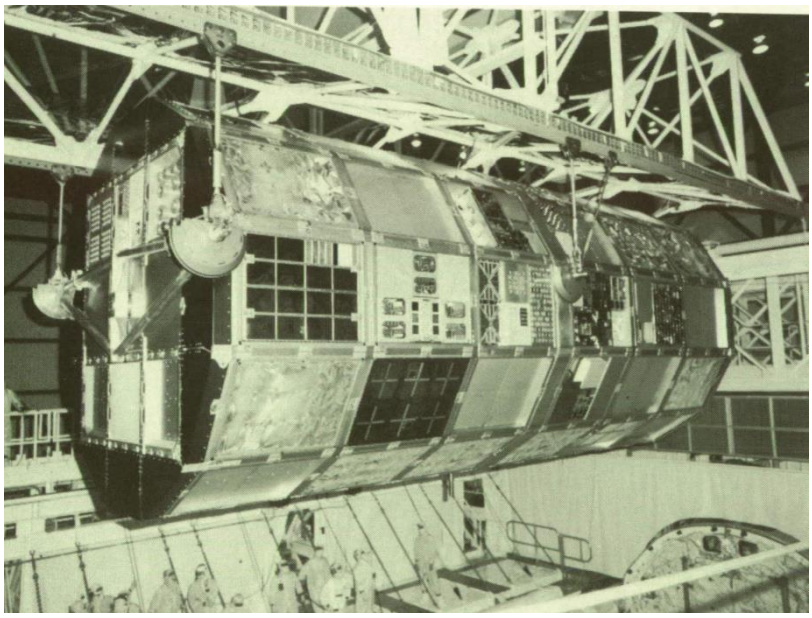

Fig. 6.3: LDEF lifted from the cargo bay of the space shuttle Columbia after retrieval (O'Neal & Burton Lightner, 1991). The LDEF spacecraft was 9.14 m long and 4.27 m in diameter.

The simulation for the flux expected on the space-facing end of LDEF employed an oriented target surface in an Earth-oriented coordinate system. The Azimuth angle was set to 0° and the Elevation set to 90° to orientate the defined surface in the space facing direction. For the population sources, only objects in the range 10^{-6} m ≤ d_p ≤ 3 x10^{-1} m were considered, as anything greater than 30 cm was not of relevance here. This led to a reduction in computation time. The 'Grün (constant velocity 20 km/s)' source was selected for the 'Meteoroid Sources' and the 'Condensed' source for the 'Debris Sources'. A circular orbit with eccentricity = 1 x10^{-4}, inclination of 28.5°, and an altitude of 476 km was assumed (the altitude at which LDEF spent most of its mission according to Tylka *et al*. (1991). Full target

orbit parameters input into the 'Target Orbit Settings' are shown in Table 6.2. Both the right ascension of the ascending node (RAAN) and the argument of perigee (AoP) of LDEF at orbit insertion were unknown. Having assumed a circular orbit the AoP was not applicable and set to 'AoP = 0.0', and the RAAN was equally set to 'RAAN = 0'. To gauge the effect that this lack of information would have on the results, a simulation with identical parameters to a control simulation, only with the RAAN set to 90°, was conducted. Differing the RAAN by 90° led to a difference in the cumulative flux value of 0.6% for > 100 µm, 0.9% for > 1 mm, and 0.4% for > 1 cm, thus having a relatively insignificant effect on the results. In corroboration with this, MASTER's historic population reference spatial densities are only considered in terms of altitude and declination, to reduce the complexity for probability coding (Horstmann *et al*., 2020), with the right ascension assumed to be uniformly distributed, with a single class value applied to all right ascension. It is, however, possible to include right ascension for more detailed analyses of new debris clouds. Future orbit propagation was activated, and the 'satellite properties' (which were based on the information in O'Neal and Burton Lightner, 1991) and the coefficients (which were defaults) used are shown in Table 6.3. The solar incident angle was assumed to have an average value of 45°, thus the solar radiation pressure (SRP) cross section was cos(45°) of the drag cross section. The full rectangular cross-section from the cylindrical body was used for the drag cross section.

Table 6.2: 'Target Orbit Settings' for the simulation of LDEF data. SMA stands for semi-major axis (MASTER assumes an equatorial radius for Earth), ECC for eccentricity, Inc for Inclination, RAAN for right ascension of the ascending node, and AoP for the argument of perigee.

Start epoch (YYYY/MM/DD/HH)	End epoch (YYYY/MM/DD/HH)	SMA (km)	ECC	INC (°)	RAAN (°)	AoP (°)
1984 04 07 12	1990 01 12 12	6854	1×10^{-4}	28.5	0.0	0.0

Table 6.3: Input parameters for MASTER's 'Satellite Properties' used for LDEF. SRP stands for solar radiation pressure.

Mass (kg)	Cross Section (drag) (m^2)	Cross Section (SRP) (m^2)	Drag Coefficient	Drag Coefficient Rate (1/d)	Reflection Coefficient
9710.0	39.13	27.7	2.2	0.0	1.3

Results for the particle flux for the space facing end of LDEF predicted by MASTER were generated (Fig. 6.4). However, the crater survey of Al6061-T6 plates aboard LDEF caried out in Humes (1993) reported the results and flux in terms of crater-lip diameter (D_r) not impacting particle diameter. Thus, to allow the comparison between the predicted flux and the d_r flux reported, a conversion from d_p to d_r is required. The best crater scaling relationship to do this was identified from Hörz *et al.* (1995). In Hörz *et al*. (1995) hypervelocity impact experiments into Al1100 and Al6061 were compared to the existing damage equations of the time. This found E. Christiansen's damage equation (modified from the Cour-Palais equation (Cour-Palais, 1987)) to best predict the experimental data in Al6061. These are given here as Eq. 6.12 to Eq.6.14 (Hörz *et al*., 1991; Christiansen, 1993; Hörz *et al*., 1995):

$$P_d = 5.24 d_p^{\frac{19}{18}} H^{-0.25} \left(\frac{\rho_p}{\rho_t}\right)^{0.5} \left(\frac{v}{v_c}\right)^{\frac{2}{3}}, \tag{6.12}$$

$$d_c = 2P_d\ , \tag{6.13}$$

$$d_r = 1.28 d_c\ . \tag{6.14}$$

Firstly, the particle penetration depth (P_d) is calculated from Eq. 6.12, as a function of the density of the particle (ρ_p) and target (ρ_t), impact speed (v), sound speed in the target material (v_c), and the Brinell hardness of the target material (H). For laboratory experiment impacts into aluminium at LGG speeds of ~ 7 km s^{-1} craters are typically hemispherical, thus the crater diameter at the original surface (d_c) relates to P_d as per Eq. 6.13. This is quantified in Humes (1993) where P_d/d_C ratios for the LDEF craters of 0.50 for 500 µm craters and 0.56 for 100 µm craters were reported. Later it was reported from a wider range of crater sizes that the LDEF craters in general typically had P_d/d_C ratios ~ 0.56 (Love et al., 1995). Lastly a conversion between d_c and the diameter at the crater rim (d_r) is applied (Eq. 6.14).

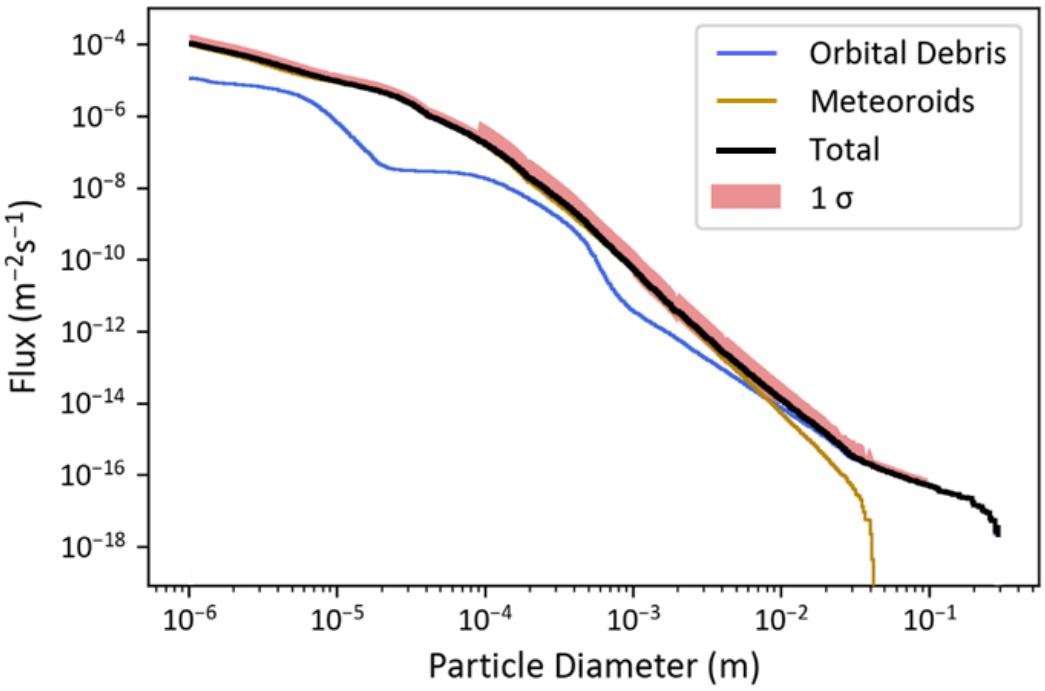

Fig. 6.4: MASTER 8.0.3 predicted cumulative particle flux for the space-facing end of LDEF. Orbital debris is represented by blue, meteoroids by gold, the combined total is in black, and the 1 σ error condition is shaded in red.

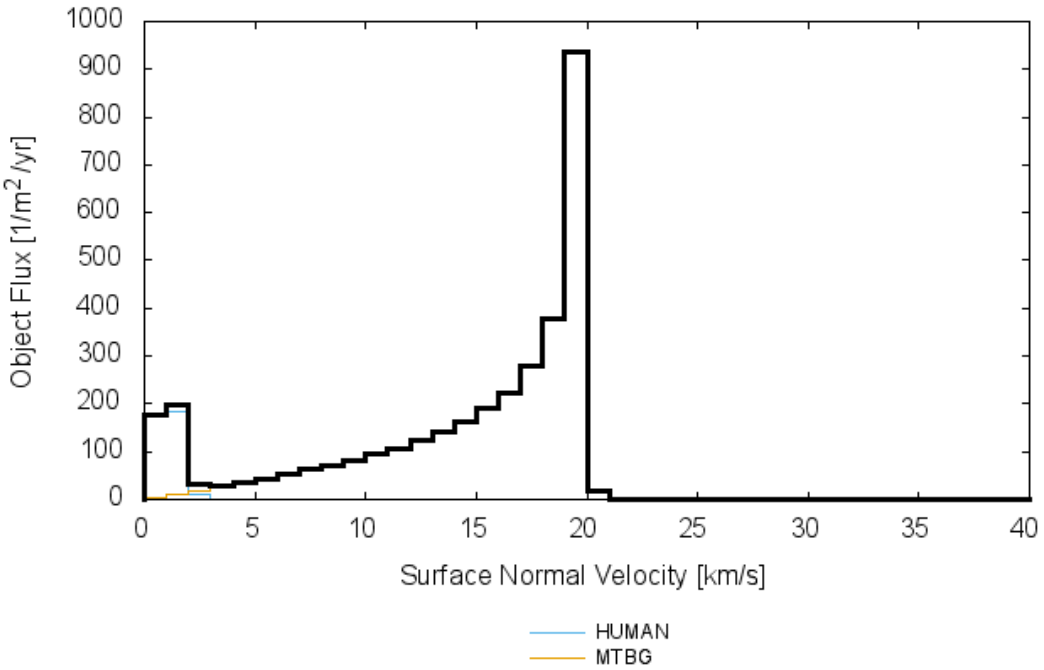

Fig. 6.5: Flux vs. surface normal impact velocity, for human made debris (HUMAN blue), meteoroid background (MTBG gold), and combined total (black) impacts on an orientated surface modelling the space-facing end of LDEF, as simulated and output by MASTER 8.0.3. The flux shown is for the object population in the range 10^{-6} m ≤ d_p ≤ 3 x10^{-1} m. Full target orbit settings are given in Table 6.2.

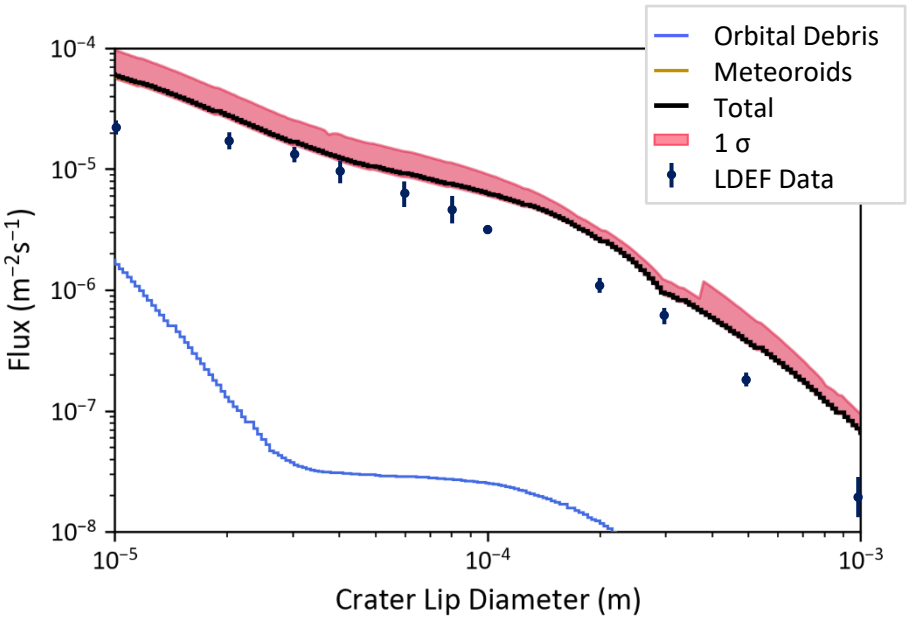

Fig. 6.6: Comparison between MASTER 8.0.3 predicted crater lip diameter flux and the measured crater lip diameter flux for the space-facing end of LDEF. Orbital debris flux is shown in light blue, meteoroid flux in gold, total flux in black, the 1 σ error in red, and the total flux measured from LDEF, taken from Humes (1993) as dark blue circles with error bars. The 1 σ error is that taken from the MASTER particle flux shifted to the corresponding population, and does not include consideration of the damage equation applied to convert particle diameter to crater lip diameter and should be treated as a minimum uncertainty. Note: the gold meteoroid data lies beneath the black total data.

To apply the Christiansen equation to the particle flux in Fig. 6.4 the density of Al6061-T6 was taken as ρ_t = 2.7 g cm^{-3} from Hörz *et al*. (1995), as was H = 90 and v_c = 5.1 km s^{-1}. Averaging of ρ_p and v was required to apply the equations to the entire contents of each diameter bin, and across all bins. However, the equations were applied to the meteoroid and debris populations separately using the differential data, and then accumulated into cumulative values and totals, to avoid the error associated with applying a single parameter value to two populations that can have significantly different parameter values, e.g. for v. A density of ρ_p = 2.7 g cm^{-3} was assumed for orbital debris, and ρ_p = 2.5 g cm^{-3} was assumed for the meteoroid population. The average density for debris was assumed from the density of aluminium (ρ_p = 2.7 g cm^{-3}) one of the most abundant spacecraft and debris materials. For the meteoroid population ρ_p = 2.5 g cm^{-3} was assumed as this is the constant density assumed by the Grün model implemented in MASTER (Grün *et al*., 1985; Horstmann *et al*., 2020). Further to this, Humes (1993) found that a meteoroid density of 2.5 g cm^{-3} was required to make the predictions from the Watts equation, used in their study, resemble the meteoroid impacts observed on LDEF more closely. The average impact speed for the

debris population was assigned as 1.5 km s^{-1}, and the meteoroid population assigned an average impact speed of 18 km s^{-1}. These velocities were estimated from the surface normal impact velocity data for the defined surface, output by MASTER (Fig. 6.5). The resulting flux vs. crater diameter is shown in Fig. 6.6.

The 1 σ error shown in Fig. 6.6 are the uncertainties output by MASTER associated with the total flux in Fig. 6.4, shifted to the corresponding size population in Fig. 6.6. This shift corresponds to the minimum crater size produced by a 1 μm meteoroid particle impacting at 18 km s^{-1}. Hence, this represents a minimum uncertainty that does not take into consideration uncertainties related to the scaling law used, the use of an average value for v and ρ_p, and the disparity between the crater-lip diameter shift for the meteoroid and debris populations and hence a different total.

The comparison between the simulated and LDEF data in Fig. 6.6 shows relatively good agreement, with a similar overall shape to the flux evolution with diameter. One LDEF data point lies within combined uncertainties of the simulated data, and considering that the simulated 1 σ is a minimum, more points are likely to overlap in reality. However, on the whole the simulated data has an elevated flux. This is likely to be a consequence of the average meteoroid impact velocity slightly overestimating the crater diameter for the relatively large population of particles with v < 18 km s^{-1} in Fig. 6.5. Another source that would contribute to the overall uncertainty (not included in the 1 σ) and the disparity between the two set of data is the effect of impact angle on crater size/morphology. For the defined oriented surface, orbital debris has highly oblique impact angles ~ 75° – 90° from normal incidence, whereas the meteoroid population impact angle is widely spread with a modal value of 20°. Fig. 6.7 of the flux against surface impact angle for each population and combined total shows the impact angle distribution, with 0° representing normal incidence. Humes (1993) reported that the crater flux for the space-facing end of LDEF was 30 to 60 times the flux incident on the Earth-facing end, for craters in the size range 0.1 mm ≤ d_r ≤ 1 mm. This suggests that essentially all of the craters on the space-facing end for this size regime were from meteoroid impacts, with as few as 2% to 3% of impacts caused by debris. The simulation data agrees with this observation, with the meteoroid population heavily dominating the total impacts.

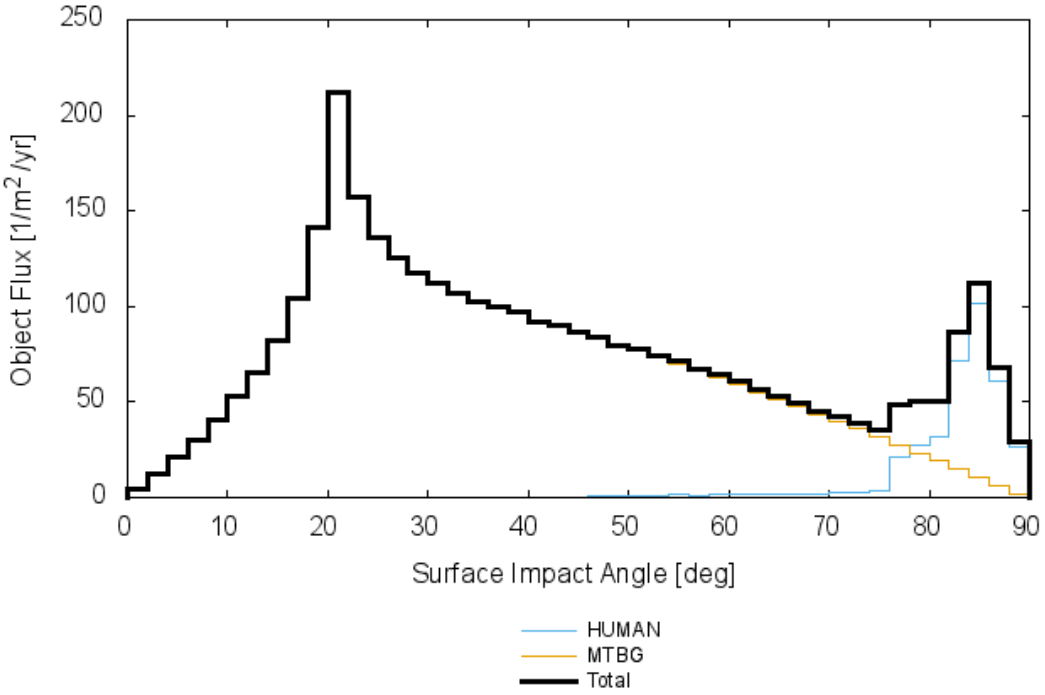

Fig. 6.7: Flux vs. surface impact angle (measured from normal incidence), for human made debris (blue), meteoroid background (MTBG gold), and combined total (black) impacts on an orientated surface modelling the space-facing end of LDEF, as simulated and output by MASTER 8.0.3. The flux shown is for the object population in the range 10^{-6} m ≤ d_p ≤ 3 x10^{-1} m. Full target orbit settings are given in Table 6.2.

6.4.2.2 Validation against HST Data

On 3rd December 1993 one of the HST solar array wings was replaced in a servicing mission and returned to Earth, providing a valuable data set of space exposed surface impacts. Results from an impact survey of this array were presented in Drolshagen *et al*. (1997) and have been used here as the second set of validation data.

HST was launched on 24th April 1990 and inserted into a very nearly circular orbit, at 614.2 km altitude with an inclination of 28.5°. Unlike the fixed pointing direction of LDEF, HST's solar arrays were in sun-pointing mode, thus different surfaces were aligned with the velocity vector during orbit. To model this pointing direction in MASTER, an oriented surface in a sun-oriented coordinate system (orientation system) was used, with azimuth and elevation angles set to 0°, i.e. the surface facing the sun. A circular orbit was assumed, and the appropriate target orbit parameters used, see Table 6.4 for full parameters. Orbit propagation was enabled and the 'satellite properties' used (Table 6.5) were calculated

from the data in Drolshagen *et al*. (1997). This time it was the solar array area aligned to the velocity direction (drag cross section) that required averaging, with an average angle of 45° assumed. The full rectangular cross-section from the cylindrical body was assumed to face the velocity direction and the sun facing direction at all times. The debris and meteoroid populations were again set to the 'condensed' and 'Grün (constant velocity 20 km/s)' sources respectively, and considered over the object size range 10^{-6} m ≤ d_p ≤ 3 x10^{-1} m.

Unlike crater diameter, a flux spectrum for the impact features, conchoidal diameter (d_{co}), and ballistic limit can be generated with MASTER. For this, MASTER applies a damage law (the exact damage law for d_{co} used in MASTER could not be found in the documentation) to the relevant particle CPE data set, at the time of simulation. Drolshagen *et al*., 1997 present results for the d_{co} of impacts on the front side of the solar array. Accordingly, a comparison between this set of d_{co} data and a simulated d_{co} flux spectrum for the HST solar array (Fig. 6.8) were considered for the HST comparison. The MASTER predicted flux for the HST solar array closely matches the HST measured data, with significant overlap between the two sets of data.

Table 6.4: 'Target Orbit Settings' for the simulation of HST data. SMA stands for semi-major axis (MASTER assumes an equatorial radius for earth), ECC for eccentricity, Inc for Inclination, RAAN for right ascension of the ascending node, and AoP for the argument of perigee.

Start epoch (YYYY/MM/DD/HH)	End epoch (YYYY/MM/DD/HH)	SMA (km)	ECC	INC (°)	RAAN (°)	AoP (°)
1990 04 24 12	1993 12 03 12	6992.2	1 x10^{-4}	28.5	0.0	0.0

Table 6.5: Input parameters for MASTER's 'Satellite Properties' used for HST. SRP stands for solar radiation pressure.

Mass (kg)	Cross Section (drag) (m^2)	Cross Section (SRP) (m^2)	Drag Coefficient	Drag Coefficient Rate (1/d)	Reflection Coefficient
12246.0	86.2	113.28	2.2	0.0	1.3

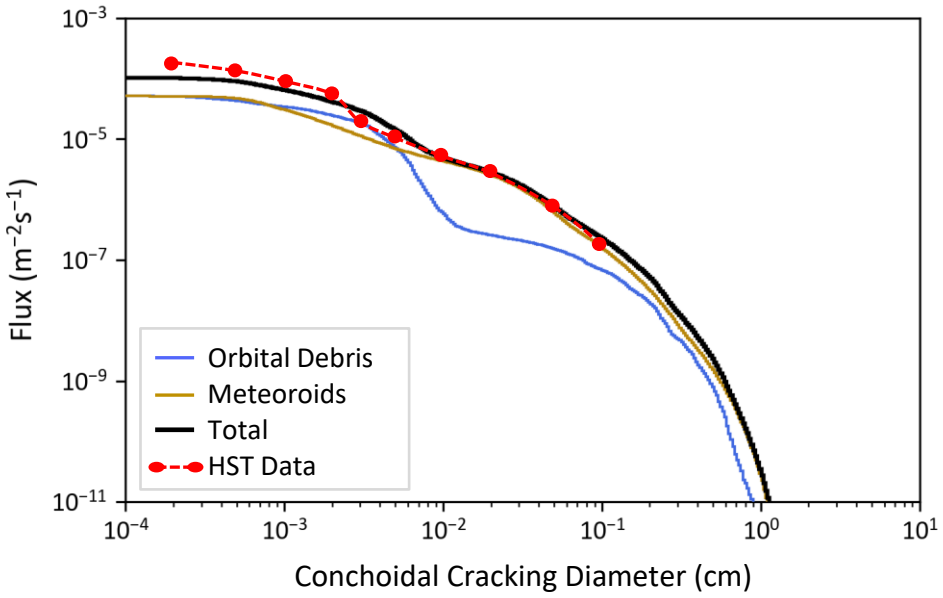

Fig. 6.8: Comparison of MASTER 8.0.3 predicted conchoidal cracking diameter flux for the HST solar arrays (between 04/1990 – 12/1993) and data measured from a returned solar array wing. Orbital debris flux is shown in blue, meteoroid flux in gold, total flux in black, and the total flux measured from the HST solar array, taken from Drolshagen *et al.*, 1997, in red.

6.4.2.3 Summary

Considering an increased uncertainty in the predicted crater-lip diameter flux for LDEF, due to the global averages assumed in its calculation, both LDEF and HST simulated data sets are in close agreement with the flux measured from the corresponding spacecraft. This suggest that the MASTER simulations run used a realistic scenario logic (target orbit settings and pointing direction) and provide results that are reflective of the orbital environment. Of course, it is expected that the model would describe these sets of data well, as they were used to inform, develop, and reweight the MASTER model and its uncertainties. The main objective here was to ascertain that the software was implemented and run correctly.

6.5 Results from MASTER

Once the operation and real-world applicability of MASTER simulations had been confirmed, the investigation of two of the questions posed in the introduction could begin. Those questions were: What does the current orbital environment look like at the time of writing this thesis in 2023? And can small area detectors that could be flown on nanosatellite/CubeSat missions provide meaningful statistical data?

6.5.1 Current Particle Environment in Earth-orbit

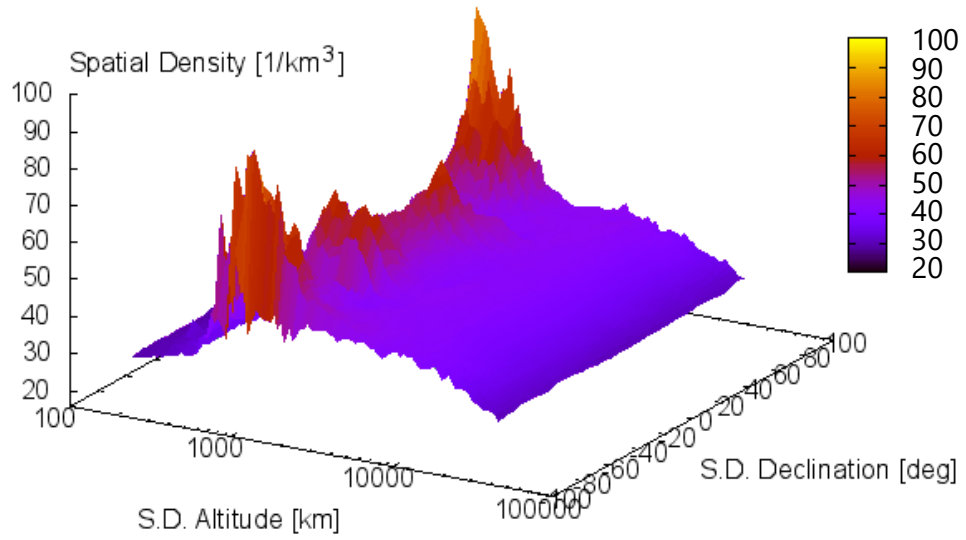

Fig. 6.9: 3D spatial density (S.D.) distribution of dust and debris vs. altitude and declination, output by MASTER 8.0.3. The increased density at -90° and 90° is a result of a greater residence probability for near-polar orbiting objects. There are also two peaks in density at altitudes of 900 km and 1400 km.

Particle environment modelling was carried out using the spatial density prediction tool in MASTER. The spatial density of the 10^{-6} m ≤ d_p ≤ 3 x10^{-1} m object population was modelled for a time snapshot of 31/10/2023 (corresponding to the 10/2023 reference population), for an altitude of 186 km to 36786 km, over a full (-90° to 90°) declination and a full (-180° to 180°) right ascension. The Grün model (the only model allowed in the spatial density tool) was used for the meteoroid population and the individual debris source populations were used. Results showing the spatial density (S.D.) with respect to altitude against declination are presented in Fig. 6.9. The increase in density at the two poles (-90° and 90°) is an artefact of how the simulation computes this value, and is a consequence of all near-polar orbiting objects having to occupy the same small volume element at high declinations,

(this is not the case approaching the equator where all polar orbiting objects will be spread out according to their RAAN). Each declination is represented by a small circle at the given declination. For declinations near ± 90° small circle occupies the more populated volume elements and thus have an increased density. Furthermore, at these points the flight path is parallel to the small circle of latitude, which results in a larger time spent at this latitude and an increased residence probability. There are two peaks in density at altitudes of 900 km and 1400 km, a result of a larger number of satellites launched to and operated around these altitudes. There may also be some contribution from the larger fragmentation events (see Table 2.1 in Section 2.3.1 for the altitude of the top ten on orbit breakup events that occurred before 2016), such as the Fengyun-1C ASAT test that occurred at ~ 850 km altitude, and the Iridium 33 – Cosmos 2251 collision that occurred at ~ 790 km altitude. In these fragmentation events, debris tended to be produced with a velocity that puts it into a range of different orbits. The debris cloud from Fengyun-1C ranged from a perigee of 167 km to an apogee of 3921 km (Kelso, 2007), thus the debris was somewhat spread out.

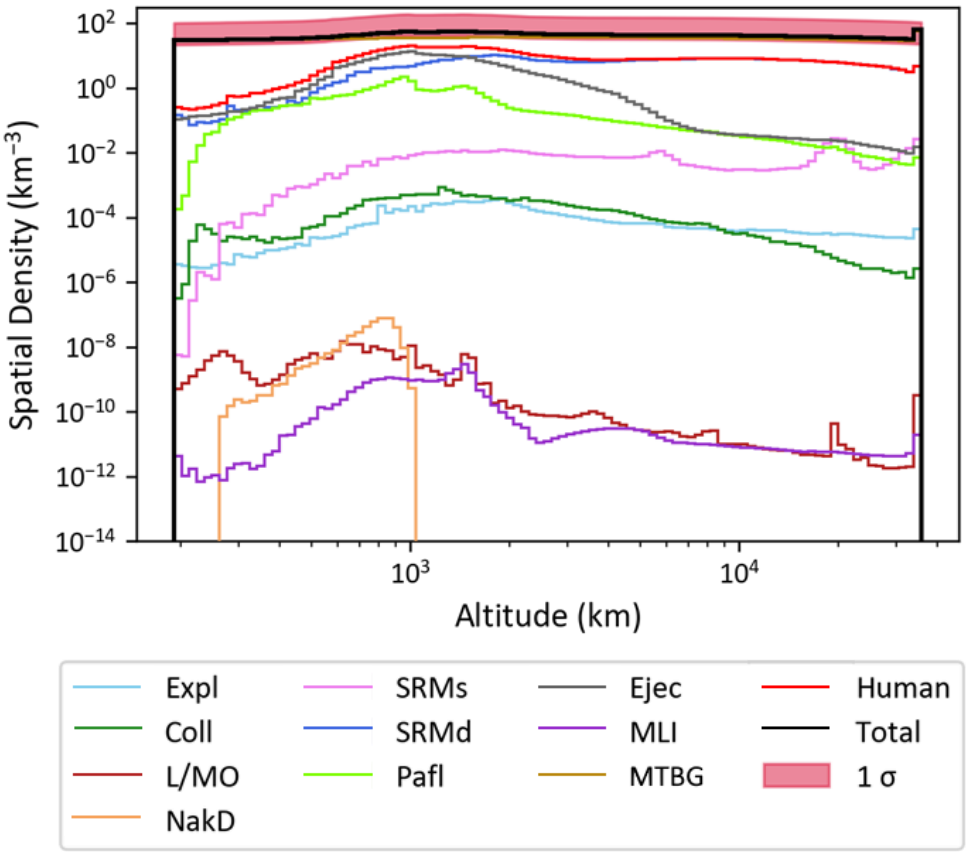

Fig. 6.10: Spatial density of the different space debris (Human) and the meteoroid background (MTBG) populations as a function of altitude, as predicted by MASTER 8.0.3. Expl represents explosion related fragments, Coll – collision fragments, L/MO – launch and mission related objects, NakD – sodium potassium droplets, SRMs – solid rocket motor slag, SRMd – solid rocket motor dust, Pafl – paint flakes, Ejec – impact ejecta, MLI – multilayer insulation. The 1 σ error (red shaded region) is associated with the combined total.

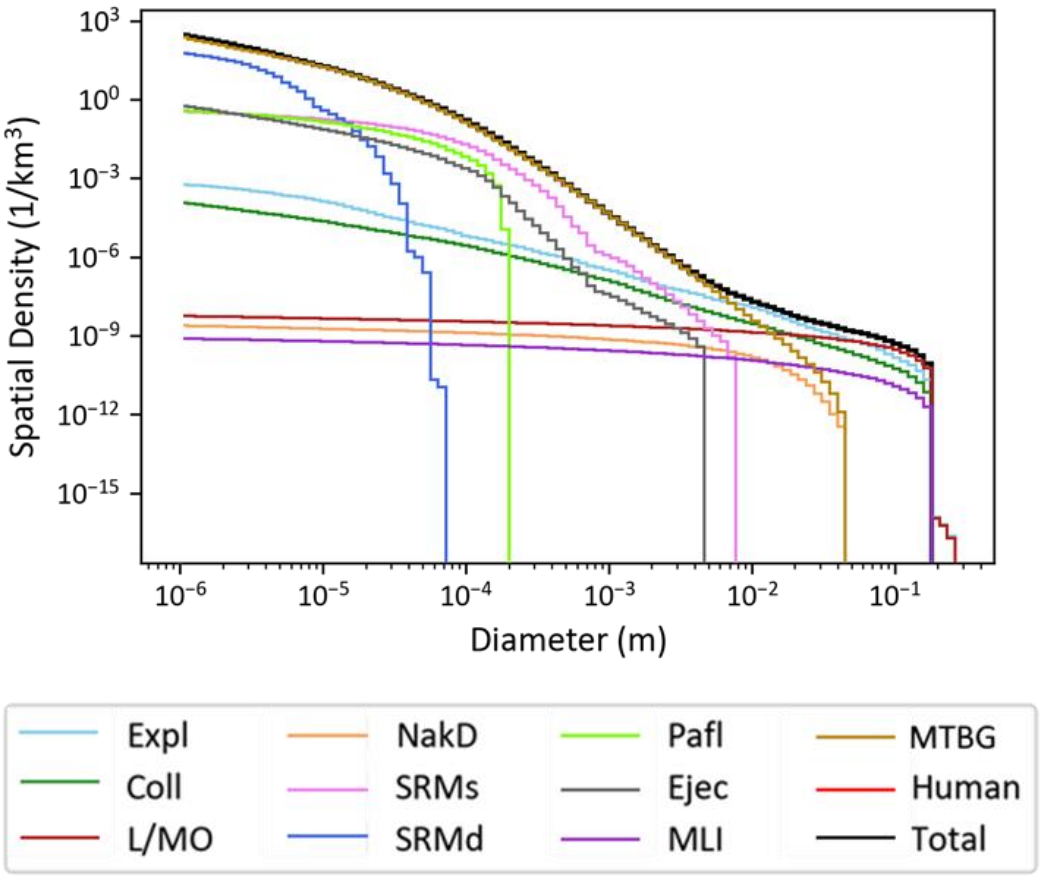

Fig. 6.11: Spatial density of the different space debris (Human) and the meteoroid background (MTBG) populations as a function of diameter, as predicted by MASTER 8.0.3. Expl represents explosion related fragments, Coll – collision fragments, L/MO – launch and mission related objects, NakD – sodium potassium droplets, SRMs – solid rocket motor slag, SRMd – solid rocket motor dust, Pafl – paint flakes, Eject – ejecta, MLI – multilayer insulation.

Fig. 6.10 shows the spatial density of different populations against altitude. We see that the meteoroid population is dominant, followed by the smaller sized debris such as SRM dust, impact ejecta, and paint flakes. A fuller description of the size distribution of the spatial density can be ascertained by considering the spatial density against diameter plot in Fig. 6.11, and comparing the relative component populations. Here we see that the smaller size regime (< 0.001 m) is dominated by SRM dust (and to a lesser degree slag), impact ejecta, and paint flakes. Whereas the larger size regime (> 0.001 m) is dominated by explosion and collision fragments.

6.5.2 Small-Area Detectors

To assess the feasibility of combining detection area from many small area sensors to provide meaningful flux data, analysis of data from past small and finite space exposed surfaces was conducted and compared to predictions from MASTER. The space exposed

surfaces used for this investigation were flown aboard LDEF, and the data taken from the crater study performed in Humes (1993). The plates under investigation here were donated to the LDEF Meteoroid and Debris Special Investigation Group by Wayne Slemp from the peripheral tray at location B9 (Tray B9) with dimensions 1.35 m x 1.07 m. For relevance to CubeSat sized detectors, only plates with a surface area smaller than the largest face of a 6U CubeSat (0.06 m^2) were considered here. These small plates and small strip-like plates used to fix samples to the tray (called clamps), were made of aluminium Al6061-T6 and are shown in Fig. 6.12. In this work the ID numbers used for plates are the same as those assigned to them in the original study in Humes (1993).

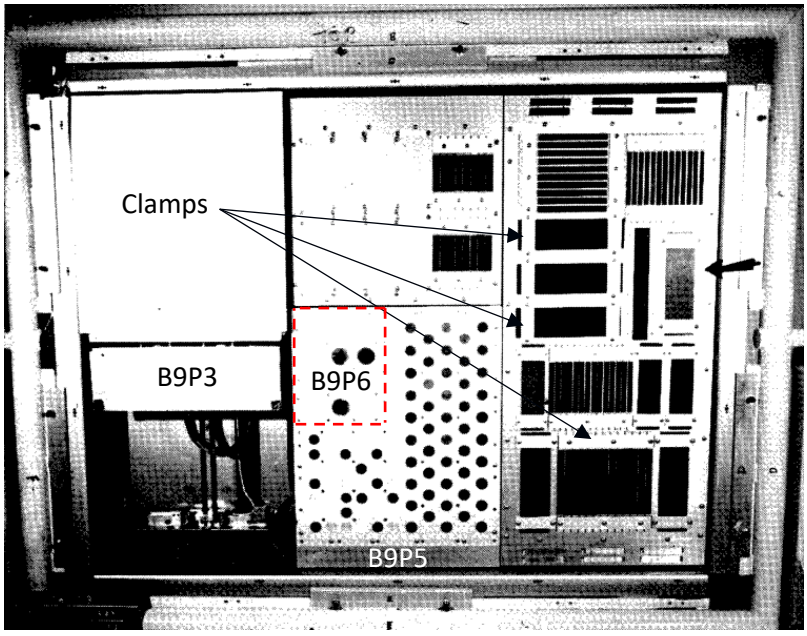

Fig. 6.12: Tray B9 (dimensions 1.35 m x 1.07 m) post de-integration from LDEF. The three small plates used for this investigation are shown labelled with the ID numbers (B9P…) assigned to them in the study by Humes (1993). The outer edge of plate B9P6 has been marked with a red dashed line for visibility. Three examples of the strip like plates used as 'clamps' are shown labelled. Modified from See. *et al*. 1990.

For these small plates, data for craters with a $d_r \geq 500$ µm were collected and presented in Humes (1993). Only a few plates in the study were scanned with the more time consuming higher magnification lenses necessary to detector smaller craters (Humes, 1993). Individual fluxes for the size range $d_r \geq 500$ µm and $d_r \geq 1000$ µm were calculated for each plate using the plate area and exposure time of 5.75 years (Table 6.6). An accumulated flux was calculated by combining the total area of all the plates and the total number of craters for each size regime over the 5.75 year exposure. Note that clamps were assigned ID numbers

of B9P7 and higher, and only one clamp (B9P7) received an impact with a crater ≥ 500 µm. Hence, the other twenty-eight clamps that did not receive any impacts were combined into a single row in Table 6.6. It is coincidence that the total area of the considered plates 0.174 m^2 almost exactly cancels out the 5.75 years in the flux calculation, to give a combined area flux of the same value as the total number of craters in the final row.

Table 6.6: Data from a crater survey on Al6061-T6 plates from Tray B9 of the LDEF mission, with an area less than the largest face of a 6U CubeSat (0.06 m^2). The surface area of each plate, number of craters with a crater lip diameter ≥ 500 µm and ≥ 1000 µm, and their corresponding flux are shown. The final row represents a total over all rows in that column. The accumulated flux was calculated using the total area, relevant total number of impacts, and the duration of space exposure of 5.75 years. Note that a single column represents 28 small plates used as clamps ('clamps') that did not receive any impacts. Modified from Humes (1993). Note that the combined area and exposure time cancel to give a flux equal to the number of craters.

Plate ID	Area (m^2)	Number of Craters		Flux (m^{-2} y^{-1})	
		≥ 500 µm	≥ 1000 µm	≥ 500 µm	≥ 1000 µm
B9P3	0.04	4	1	15.8	4.0
B9P6	0.04	2	1	9.0	4.5
B9P5	0.02	0	0	0.0	0.0
B9P7	1.8 x10^{-3}	1	0	96.6	0.0
x 28 clamps	1.4 to 4.5 x10^{-3}	0	0	0.00	0.00
Total/accumulated flux from 32 Plates	0.174	7 ± 3	2 ± 1.4	7 ± 3	2 ± 1.4

Particle flux modelling was carried out in a similar manner to the LDEF validation work described in section 6.4.2.1, with the only difference being the pointing direction. The target orbit settings and satellite properties used for LDEF were again those presented in Tables 6.2 and Table 6.3 respectively, and the same source populations used as before. Tray B9 was effectively on the ram face of LDEF and had a pointing direction of 8 degrees from the velocity vector (Humes, 1993). To model this in MASTER, an oriented surface in an Earth-oriented system was used with the azimuth angle set to 8°, i.e. pointing 8° from the velocity vector. Particle flux predictions for a surface pointing 8° from the velocity vector in an LDEF like orbit are presented in Fig. 6.13.

To enable the comparison between the particle flux from MASTER and crater-lip flux from the data in Humes (1993), the Christensen scaling relationship Eq. 6.13 to Eq.6.15 was applied to the data in Fig. 6.13 (in an analogous way to previously for the space facing edge of LDEF). This time the same material parameters for Al6061-T6 were assumed (ρ_t = 2.7 g cm^{-3}, H = 90, and v_c = 5.1 km s^{-1}, taken from Hörz *et al.*, 1995), and the same average particle density for orbital debris and meteoroids, ρ_p = 2.7 g cm^{-3} and 2.5 g cm^{-3}, respectively. However, due to the new pointing direction the surface normal impact velocity required new average impact velocities. The average debris impact speed was taken as v = 10 km s^{-1} and the average meteoroid impact speed v = 18 km s^{-1}. These were estimated from the surface normal impact velocity distribution from master (Fig. 6.14) and are in good agreement with the accepted average impact speeds for these populations. The expected crater-lip flux for Tray B9 is presented in Fig. 6.15, along with the flux measurements calculated from the accumulated flux of the small plates in Table 6.6 (green crosses 'x').

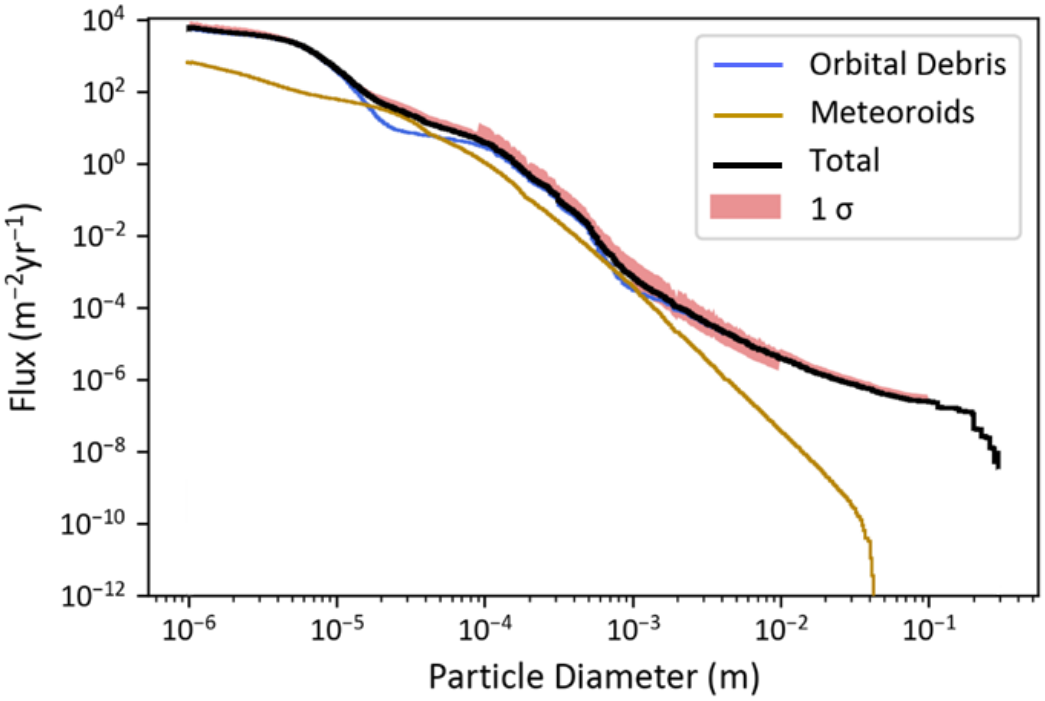

Fig. 6.13: Cumulative particle flux data for particle diameter (d_p) in the range 10^{-6} m ≤ d_p ≤ 3 x10^{-1} m, for a surface pointing 8° from the velocity vector in a LDEF-like orbit as predicted by MASTER 8.0.3 (full orbit parameters are given in Table 6.2). The contributions from the debris and natural particles are shown separately, along with a combined total flux. The estimated 1 σ variation in the total flux is also shown. There is an increase in the relative uncertainty between 10^{-4} m and 10^{-2} m, as a result of the poorly constrained flux for this population.

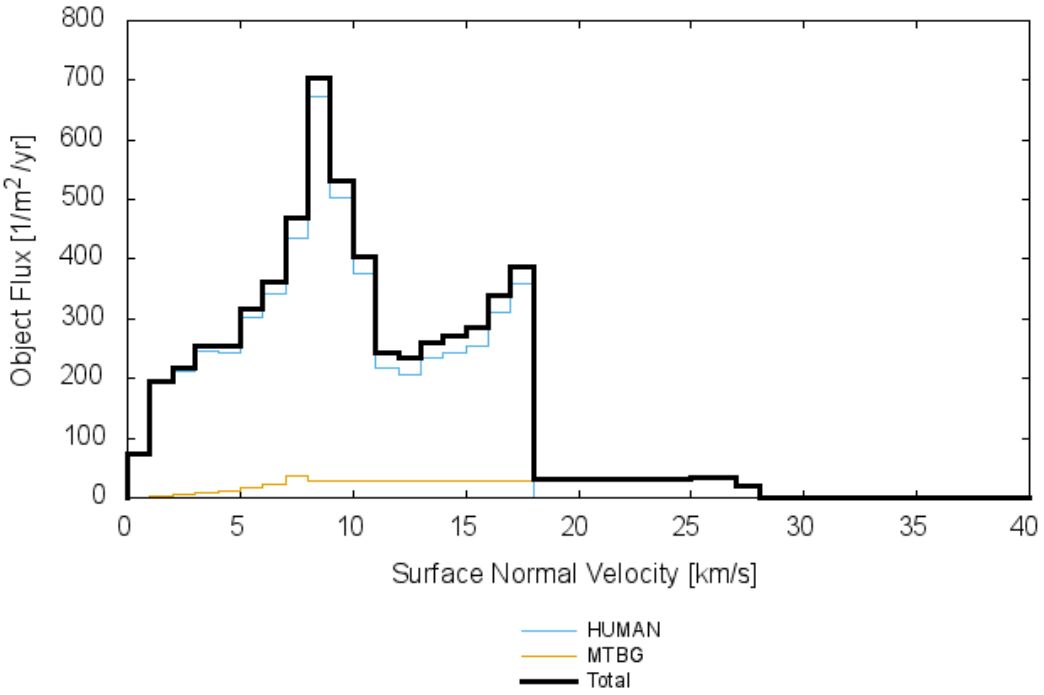

Fig. 6.14: Flux vs. surface normal impact velocity, for human made debris (blue), meteoroids (gold), and combined total (black) impacts on an orientated surface modelling the LDEF Tray B9 pointing direction of 8° from the velocity vector, as simulated and output by MASTER 8.0.3. The flux shown is for the object population in the range 10^{-6} m ≤ d_p ≤ 3 x10^{-1} m. Full target orbit settings are given in Table 6.2.

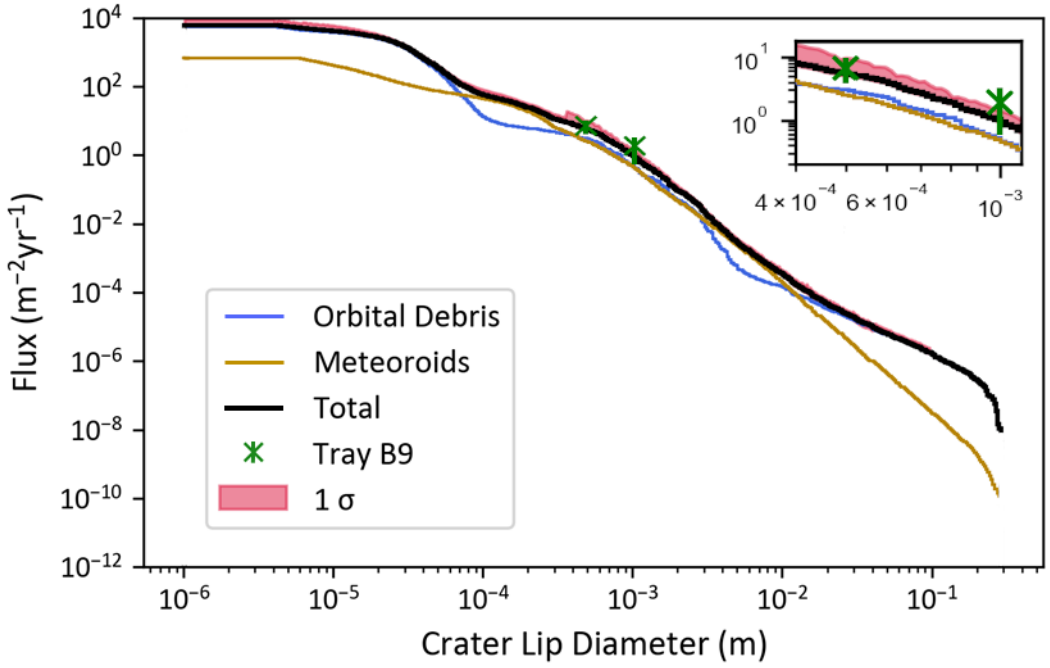

Fig. 6.15: Cumulative flux data for crater-lip diameter (d_r) for impacts into Al6061-T6, for a surface pointing 8° from the velocity vector in a LDEF like orbit as predicted by MASTER (full orbit parameters are given in Table 6.2). Fluxes were derived from particle diameter flux data for particles in the range 10^{-6} m ≤ d_p ≤ 3 x10^{-1} m (Fig.3), using the crater scaling relationship given in eq. 1 to eq. 3. The flux data obtained from the small plates from Tray B9 of LDEF ('x') is also shown and in good agreement with the predicted flux.

The 1 σ uncertainties in Fig. 6.15 were obtained in the same way as for the space-facing end of LDEF (Fig. 6.5) and should be considered a minimum uncertainty. This time the shift in population to which the 1 σ error applies is based on the minimum crater size produced by a 1 µm debris particle impacting at 10 km s^{-1}. The errors in the Tray B9 values were calculated using Poisson statistics of small numbers.

There is good agreement between the flux accumulated over the small plates and the flux predicted by MASTER, with both Tray B9 data points within estimated minimum uncertainty. This agreement suggests that accumulating detection area over several small CubeSat sized surfaces leads to statistically meaningful data. Here the investigation assumes that combining area over small plates with separations no more than tens of centimetres covering an area of no more than 1.35 m x 1.07 m, is comparable to small detection surfaces separated within an orbit. This in turn relies on the assumption that the dominant contribution to impacts comes from the average background population, which would be relatively homogeneous within an orbit i.e. the same for surfaces separated by a small or large distances. This latter assumption is based on the tendency of debris particles to distribute over the entire orbit, over time (Kelso, 2007).

6.5.2.1 Time Scales for Small Area Detectors and CubeSats

To consider the time scales before an impact on a small area detector in a key target orbit, a flux analysis was carried out for a circular, polar orbit (inclination of 98.7°) with an altitude of 800 km, for the epoch 2023/11/01 to 2026/11/01. MASTER was used to determine the flux on a ram facing surface (pointing direction aligned with the velocity vector), and this was converted to the impact flux on the leading edge of a 1U, 1.5U, 3U and 6U CubeSat (where the CubeSat's largest face was set as the leading edge, thus maximizing the encountered debris flux). The condensed debris population and the Grün meteoroid population, with an object size ranging from 10^{-6} m ≤ d_p ≤ 1 x10^0 m, were used. An oriented surface target object, aligned with the velocity vector (Azimuth and Elevation angles set to 0° in the Earth-oriented scheme), with the target orbit parameters in Table 6.7 were applied to model the orbit and pointing direction. Propagation was activated and the satellite properties for a 6U CubeSat in Table 6.8 were assumed.

Table 6.7 'Target Orbit Settings' used for a circular polar orbit of 98.7° inclination (INC) and altitude of 800 km. SMA stands for semi-major axis (MASTER assumes an equatorial radius for earth), ECC for eccentricity, RAAN for right ascension of the ascending node, and AoP for the argument of perigee.

Start epoch (YYYY/MM/DD/HH)	End epoch (YYYY/MM/DD/HH)	SMA (km)	ECC	INC (°)	RAAN (°)	AoP (°)
2023 11 01 00	2026 11 01 00	7178.0	1×10^{-4}	98.7	0.0	0.0

Table 6.8: Input parameters for MASTER's 'Satellite Properties' used for the propagation of future CubeSat missions. SRP stands for solar radiation pressure.

Mass (kg)	Cross Section (drag) (m^2)	Cross Section (SRP) (m^2)	Drag Coefficient	Drag Coefficient Rate (1/d)	Reflection Coefficient
6	0.06	0.042	2.2	0.0	1.3

Flux predictions were extended to the entire area (from all six faces) of the sizes of CubeSats considered here, using geometric analysis in ESABase2/Debris. ESABase2 requires the definition of the spacecraft geometry, in this case separate 1U, 1.5U, 3U, and 6U geometries as shown in Fig. 6.2. All geometries were aligned such that their largest face was pointing along the velocity vector, the next largest/equal face pointing towards space, and the smallest face pointing orthogonal to the velocity vector direction. Mission parameters used the same orbit and epoch as defined in Table 6.7 (note that the corresponding future MASTER population files needed adding to the ESABase2 library folder), with the exception that ESABase2 requires altitude (800 km) instead of SMA, and the eccentricity was specified as 0.0 (unlike MASTER which does not except a value of zero). The number of orbital points was set to 4.03, with a corresponding time interval between orbital points of 1500 s. These points are used for later analysis of a given point in the orbit if desired. The analysis type used was the debris and meteoroid analysis, with a MASTER 8 debris model and the Grün meteoroid model, over an object diameter range of 10^{-6} m ≤ d_p ≤ 10^{0} m. The fluxes for the ram face and entire surface area for each size CubeSat, were then converted into a time before impact for a given sized object.

One could consider making total area flux predictions for these CubeSats using the unit sphere target model in MASTER. However, with the relatively large difference between surface areas pointing in different directions a different overall average spacecraft flux would be expected. Comparison between the average spacecraft flux for a 6U CubeSat as

predicted by ESABase2 and the flux for a unit Sphere in the same 800 km orbit (Fig. 6.15), shows that there is indeed a difference between the two flux predictions. Overall, there is an average difference of ~ 50%, with varying agreement between the data for the central region (see Fig. 6.15). The flux difference due to the unit sphere model assuming the same area pointing in all directions, is most easily seen for 1 µm, for which MASTER predicts a flux of ~ 15000 m^{-2} yr^{-1}, whereas ESABase2 predicts ~ 9000 m^{-2} yr^{-1}, with a difference of 65% (considering the un-rounded values). At 1 µm MASTER predicts the meteoroid flux to be ~ 5400 m^{-2} yr^{-1}, which represents 94% of the total difference between the two totals. This would suggest that there is an over-estimation in flux due to the sphere model appropriating too large an area to the space-facing direction, from which the flux is dominated by meteoroids and would contribute a larger meteoroid flux than for a spacecraft with the majority of its surface area pointing in the forward direction. This, suggests that geometric considerations are important for spacecraft that do not have relatively equal surface areas in all directions.

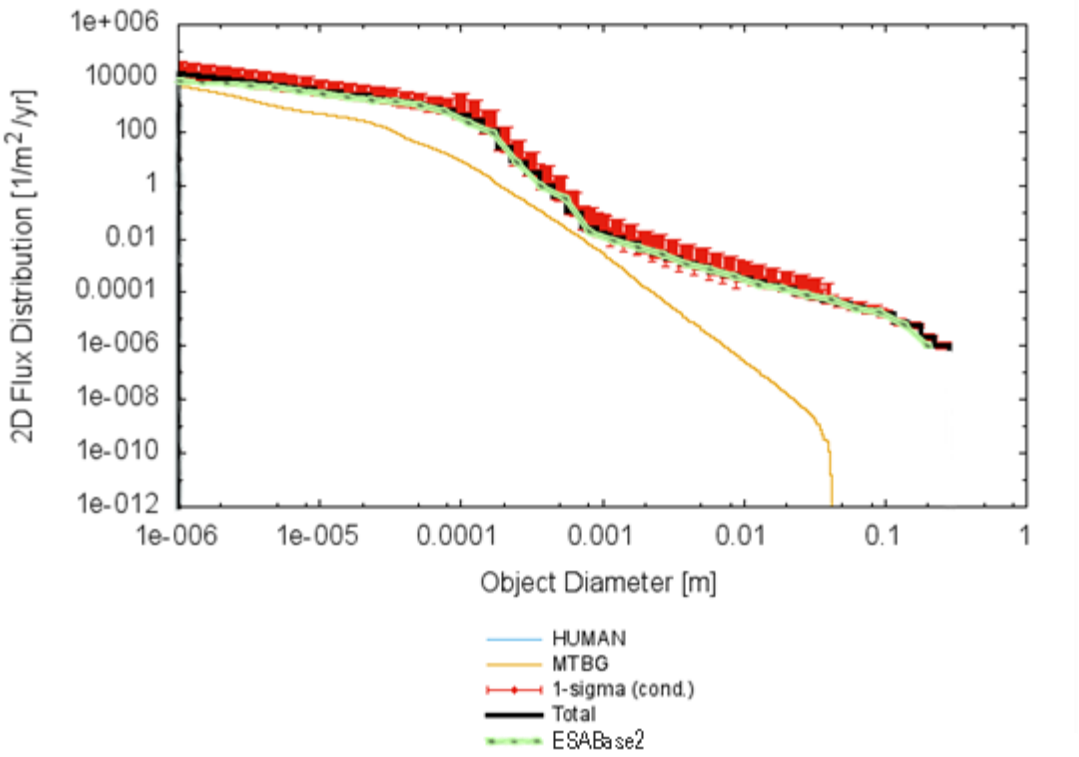

Fig. 6.16: Comparison between the output predicted cumulative flux from MASTER 3.0.8 for a 1 m^2 cross-section sphere and the cumulative flux for a 6U CubeSat (flying its largest face in the ram direction) predicted by ESABase2/Debris (Green), with the same orbital parameters. There is varying agreement between the data for the central region, ranging from a difference of ~ 26% at 0.1 mm, and 19% at 0.5 mm, to 59% at 1mm. There is a 65% difference at 1 µm which is likely dominated by a difference in meteoroid flux, with the meteoroid flux for the sphere (5373 m^{-2} yr^{-1}) accounting for 94% of the difference between the two totals. Note the blue 'Human' flux data lies beneath the back total flux data.

The three-dimensional flux results for a 6U CubeSat are presented in Fig. 6.17, and the time before impacts of a given size particle, in the range 10^{-6} m ≤ d_p ≤ 10^{-2} m, on the leading surface and entire CubeSat, is shown plotted in Fig. 6.18. There is a significant difference in the power law that can be fit to the time before impact data above and below 10^{-3} mm, which is reflective of the change in the underlying population from mm to cm. Fig. 6.13 shows a decrease in the gradient of the decreasing flux around the 10^{-3} m mark, even though the meteoroid population begins to decrease rapidly after this point. This is likely due to a combination of the different production sources, and processes governing the evolution, of the different populations. Above 10^{-3} m the difference in production quantities of different sized particles will reduce, likely as a result of the dominant sources being rarer and tending to produce relatively fewer larger particles. Conversely the dominant sources below 10^{-3} m are more frequent and tending to produce more smaller particles. Furthermore, as particle size increases the processes governing their evolution become more important. Where atmospheric drag and solar radiation pressure related drag, such as Poynting-Robertson drag (Robertson, 1937), have less effect on larger particles resulting in larger orbital lifetimes. Accordingly, it can be considered that the steeper regions of the graph at smaller d_p are characteristic of the production rates of these particles (this is supported by the meteoroid population, which is a larger portion of the overall flux at this d_p, being constantly replenished/transient). In contrast, the shallower regions at larger d_p are characteristic of the evolution of these particles.

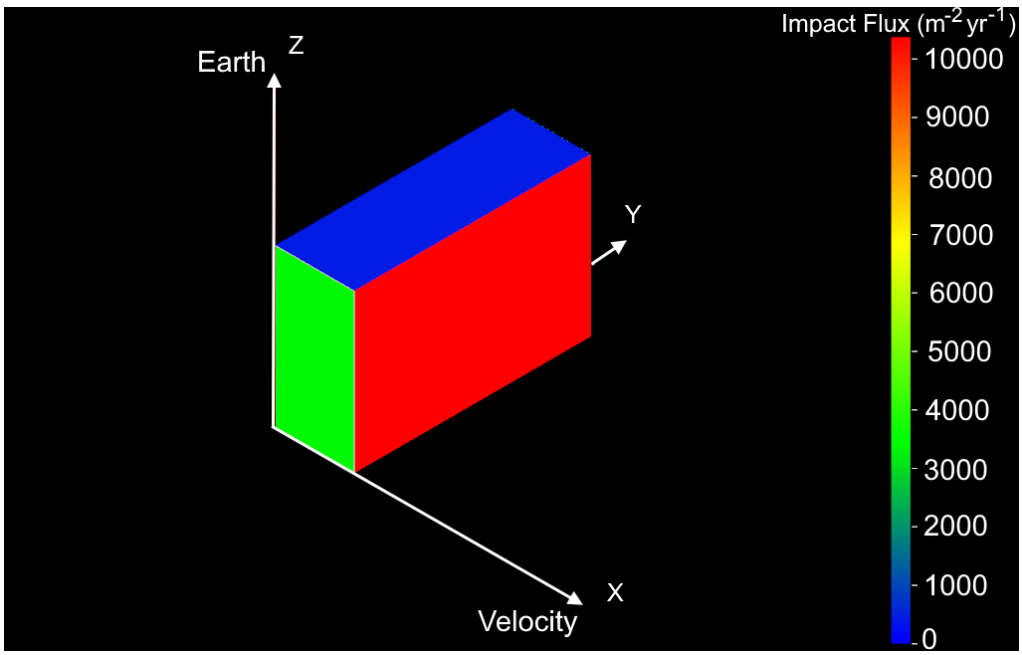

Fig. 6.17: Three-dimensional flux results for a 6U CubeSat with its largest face poinitng along the velocity vector, showing the different flux incident on each face of the spacecraft. The velocity vector (which is aligned with the x-axis) and the Earth-pointing vector (which is aligned with the Z-axis) are shown.

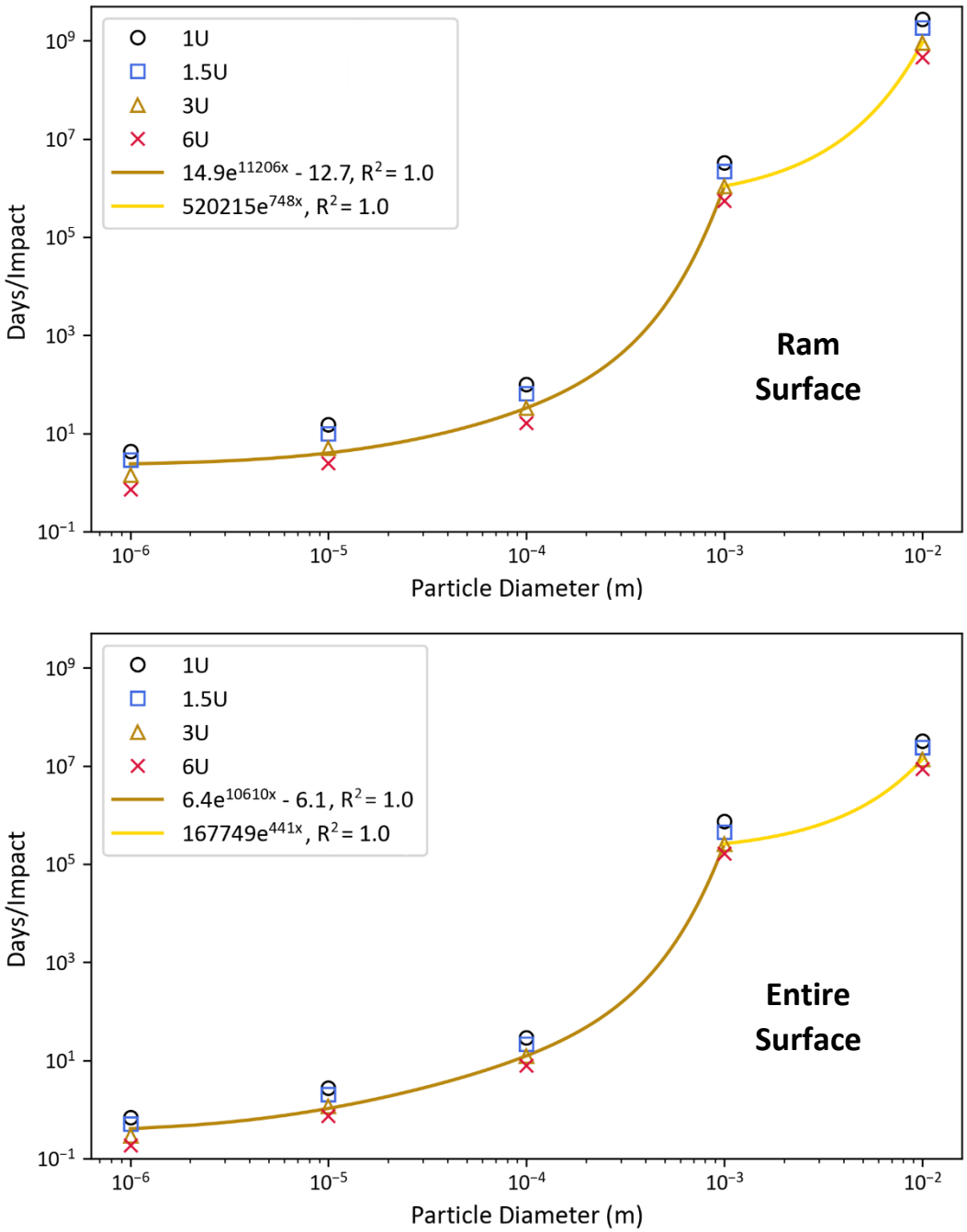

Fig. 6.18: The time in days expected for a particle (debris or meteoroid) ≥ a given size will impact the ram face (top) and entire surface area (bottom) of a 1U, 1.5U, 3U, and 6U CubeSat in a circular orbit, with an inclination of 98.7°, and altitude of 800 km (where the largest surface area face is pointing in the ram direction). The 3U data is shown fitted. A single power law function does not fit the full data range, thus two fits are shown (one above and one below a particle diameter of 1 mm). This change in slope is a result of the rate of change of flux between the 1 mm and 1 cm-sized populations. Both gold fits in each plot had an R^2 = 0.9999 (to many d.p.), and the yellow fits for the > 1 mm populations had an R^2 = exactly 1.0. For the gold fits (particle diameter up to 10^{-3} m), the errors on the fit coefficient in the top plot are 14.9 ± 1.0, 11206 ± 67, and –(12.7 ± 1.8) and in the bottom plot are 6.4 ± 0.13, 10610 ± 20, and - 6.1 ± 0.2 for the gold fit. Errors in the yellow fits (particle diameter from 10^{-3} m upwards) could not be determined due to the small number of data points used (two points). These spline fits are intended to give a sense of the gradient and estimate the time before impact within the given range, and it is not clear how far they can be extrapolated to a wider range of particle diameters.

The 0.174 m^2 area of small plates investigated from LDEF would suggest that the area of seventeen 1U CubeSat faces, be it seventeen 1U or three 6U CubeSats, could lead to statistically significant data. On the other hand, considering the time for an impact of a given size, a minimum of the entire surface area of one-hundred 6U CubeSats would be required to reduce the observation time for a 1 mm impactor to the order of 5 years, a time scale more in-line with the operational lifetime for a typical CubeSat. Employing the entire surface area of a CubeSat as the detection area could be achieved using smart MLI, as flown on EQUULEUS (Funase *et al*., 2020), via use of telemetry anomaly data for impact detection (Bennett *et al*., 2021), or via multiple sensors such as the resistive wire based detector built into solar panel substrate SOLID (Bauer *et al*., 2016). Many larger CubeSats ≥ 12U are being proposed and developed for missions that require greater payload power and space (e.g. Yu *et al*., 2018; Chafetz *et al*., 2021; Blue Skies Space, 2022). Hosting small (< 6U) sized detectors on larger CubeSats or more traditional satellites, that can accommodate the extra mass and power, would be a sustainable and efficient way of accumulating detection area.

The greatest appeal of CubeSats is their relatively cheap cost and quick time to launch and service. For example, ADLER-1 went from idea to in orbit in 1 year (Austrain Space Forum, 2023). With such improved launch availability for small CubeSats, it could be possible to launch debris monitoring CubeSats in response to a specific event, such as a fragmentation or collision. This would be ideal for monitoring the small particle population produced in such an event, before it has time to evolve significantly. However, for such short timescales it is unlikely that deploying enough CubeSats, to produce the required area, would be possible. Thus, responsive CubeSats missions would benefit from employing novel detection area increasing technologies developed for CubeSat debris monitoring missions. Current detectors in use and under development include:

- In-situ radar (Ahmed *et al*., 2019) or bistatic radar, such as ADLER-1 and ADLER-2 (Austrain Space Forum, 2023), and STRATHcube (Creed *et al*., 2021), respectively.
- Optical systems, that could include the use of CubeSat star trackers (Dave & Lee, 2022).
- Laser based optical systems (Englert *et al*., 2014).
- Deployable larger area detectors such as APID and APID-2 flown aboard ADLER-1 and ADLER-2, and the Polyimide thin-film detector flown aboard ASTERISC (Ishimaru *et al*., 2021).
- Use of telemetry data (Bennett *et al*., 2021), or other entire surface techniques described above.

The deployment of large area detectors will affect the area to mass ratio of the CubeSat, thus effecting its orbital lifetime. However, this can be taken into consideration in the concept of operations (CONOPS) for the mission. Given small numbers of CubeSats in such a mission, and the non-randomly distributed nature of the debris cloud, careful targeting of the CubeSat trajectory through the predicted cloud could be required to fully characterise it.

6.6 Conclusions

The basic theoretical background and functionality of ESA's space environment modelling software MASTER were introduced, with specific reference to the simulations performed in this chapter. Simulation scenarios and parameters used to produce the discussed results were described, as was the use of ESABase2 to apply this model to specific spacecraft geometries. Validation of the correct operation of the software, and applicability of the simulations run to the real world, was conducted. Good agreement between data simulated here, past simulation data, and analytical data collected from space-exposed surfaces, suggest that the software was implemented correctly, and that the results were reflective of the actual space environment.

Using MASTER, the current orbital environment was investigated. Orbital altitudes with high densities of debris and the predominant constituents of the population were identified and presented. However, the main focus of this chapter was to investigate the feasibility of accumulating detection area over numerous small area detectors, such as those applicable to nanosatellites, with an emphasis on less frequent large (mm-sized) impacts which pose a threat to vulnerable space exposed surfaces. Accumulated flux from small space exposed surfaces (smaller than those of a 6U CubeSat) was compared to environment predictions from MASTER. Substantial agreement between the flux data and predictions suggests that accumulating area over many small area detectors does lead to statistically meaningful results. This assumes that impacts are dominated by the average background population, which would be relatively homogeneous over an orbit.

Investigating the timescales expected for impacts, geometric analysis of CubeSats showed that the entire surface area of one-hundred CubeSats would be required to bring the time before impact for a 1 mm sized particle down to 5 years (for 6U CubeSats) to 20 years (for 1U CubeSats), more in line with the operational lifetime of a CubeSat. Their quick time to service would also suggest that CubeSats could be used for responsive debris monitoring of sudden debris creating events, such as fragmentations and collision, sampling the small

particle debris cloud before it has significant time to evolve. For the short time scales required for responsive debris monitoring, it is unlikely that enough CubeSats would be deployed, thus fewer CubeSats equipped with area increasing detection technologies may be required.

Future work that could be undertaken in this line of investigation could include, outputting CPE dump files (data dump files up to GB in size) from MASTER, so that analysis and processing can be applied to individual particles, as opposed to entire bins, as was the case in the above. Modelling of results that start to become available from the current dust and debris flux measuring CubeSat missions could also be undertaken. These values could be compared to simulations in MASTER to access the quality of the data being produced, and further inform on the feasibility of combining detection area of small detectors to produce statistically meaningful data.

Chapter 7: Conclusions and Future Work

7.1 Conclusions

This thesis aimed to develop new techniques and methods for in-situ orbital debris detection. This focused on the development of acoustic, thin film TOF detectors, specifically the DRAGONS detector concept under development by NASA and my industrial partners AstroAcoustics (through a NASA contract). In light of the current move towards small spacecraft for space missions, the feasibility of using small area dust and debris flux detectors was also explored as an associated piece of research, with a focus on CubeSats.

The three main objectives were:

1. To determine the speed measurement accuracy achievable with the DRAGONS concept, for mm-sized debris that poses the greatest threat to space missions in LEO (NASA, Office of Inspector General, Office of Audit, 2021).
2. To determine the effects of film penetration on particles, and the subsequent effect on detector measurements. Here the focus was on the deceleration and/or disruption of an impactor during passage through the film. This is required to determine accurate information about the incident particles.
3. Use the latest space environment modelling software (MASTER 8.0.3) to assess the feasibility of using multiple small CubeSat sized detectors for orbital debris detection, and flux measurements.

Objective 1 was addressed in Chapter 4. A prototype of the DRAGONS detector concept, which was optimised for speed determination, was impacted with 1 mm stainless steel projectiles at $\sim$ 2 km s^{-1} and $\sim$ 4 km s^{-1}. To measure the speed of an impactor the onset time of the signals of interest that correspond to the time of impact had to be identified. For these shots the first of the largest peaks was found to be the signal of interest, from which speed measurements should be taken (see Chapter 3 for details). At least some of the pre-signal (which arrived before the signals of interest) was found to be non-acoustic in origin and coincided in time with the production of impact light flash, observed with photodiodes, and is likely noise caused by photons/EM waves incident on the PVDF sensors. The non-acoustic noise had a single peak followed by a recovery tail, which is characteristic of the signals identified as “flash” and hypothesised to originate from light flash in the results from the space flight test of DRAGONS (the SDS detector) (Anz-Meador *et al.*, 2019).

For 1 mm stainless steel projectile impacts into 12.5 µm Kapton films at 2 km s^{-1} with a ratio of f/d_p = 1/80, the penetration holes were relatively simple. The holes had circular rims lined with a few small filaments of melted Kapton, and a hole diameter $d_h = d_p$ (which is the thin film limit (Hörz, 2012)), and are categorised as TFL morphologies. As speed increased to 4 km s^{-1}, there was a slight increase in hole diameter and more of the filaments were removed leaving cleaner penetration holes. Acoustic signals for these impacts were equally relatively simple and time of onset determination was accurate, unless contaminated by non-acoustic noise that was characteristic of impact light flash and which, as already stated, may originate from either impact light flash, or impacts by charged particles such as ions produced in impact plasma. Hence, speed measurements for particles of this size were found to be accurate, matching the independently measured impactor incident speed within ±1%. Thus, in ideal laboratory conditions acoustic thin film TOF detectors such as the DRAGONS concept can accurately measure incident speed for mm-sized particles to within ±1%. No deceleration or disruption of the relatively strong projectiles was observed at this ratio of f/d_p = 1/80.

Chapter 5 concerned Objective 2 and investigated impacts for smaller particles from 200 µm to 800 µm into separately investigated Kapton films of 12.5 µm and 25 µm thicknesses, with f/d_p in the range $1/32 \leq f/d_p \leq 1/8$, for which deceleration and disruption is more likely to occur. At this size range, four morphologies of penetration hole were observed in both thicknesses of films. These were:

- TFL, which were observed for impacts with $f:d_p$ = 1/32, had penetration holes approaching $d_h = d_p$, and had few small individually defined filaments at the edge of the penetration hole.
- BL, which were found for impacts with $f:d_p$ = 1/16 and 1/8 at ~ 2 km s^{-1}, and which had a maximum penetration hole size at the film surface with $d_h > d_p$. The front and rear Kapton filaments formed continuous lip structures that protrude inwards to create $d_{lip} < d_p$.
- CL, which were present for impacts with $f:d_p$ = 1/16 at ~ 4 km s^{-1}, had larger $d_h > d_p$ at the film surface than for BL morphologies, and the Kapton filament lips resembled crater lips, which curve outwards creating $d_{lip} > d_h$.
- Di, was present in inclined impacts that had an angle of incidence of 15° from normal incidence, with $f:d_p$ = 1/16, and showed $d_h > d_p$ at the film surface. Despite the non-normal incidence, these penetration holes were not significantly elliptical

in shape, however, the Kapton filament lips showed directionality downrange of the projectile incidence direction.

As f/d_p increased the normalised hole diameter d_h/d_p was also found to increase, and a relationship relating incident particle diameter to penetration hole diameter was determined as per Eq. 5.1, which is shown again below:

$$d_p = 0.64 \pm 0.08\, {d_h}^{1.064 \pm 0.019}.$$

For the relatively strong steel projectiles used here, no disruption of the projectiles was observed over the entire range of f/d_p, $1/32 \leq f/d_p \leq 1/8$.

Time of signal onset determination was found to decrease in accuracy as hole penetration morphologies became more complex, which occurred at larger values of f/d_p. This may suggest that the acoustic signals became more complex with more complex penetration morphologies, ultimately resulting in less accurate speed determination for projectiles with $f/d_p > 1/32$. Indeed, the data for the deceleration of smaller particles was variable and spread. It was found that no deceleration was observed for steel projectiles ≥ 400 µm impacting 12.5 µm films at 2 km s^{-1} with $f{:}d_p \geq 1/32$, which is the size range of greatest interest to DRAGONS. In contrast, in the 12.5 µm films, 200 µm projectiles impacting at 2 km s^{-1} started to show signs of deceleration, and in the 25 µm films, 400 µm projectiles impacting at 2 km s^{-1} showed a deceleration of $\sim$ 10%. This suggests that at 2 km s^{-1} deceleration is starting to occur at $f{:}d_p = 1/16$. Generally, fitting the data to a conservation of momentum law showed size dependent effects, as above, with thicker films producing more deceleration at smaller m_f/m_p. Comparing this to previous data for different materials (Capaccioni & McDonnell, 1986; Simpson & Tuzzolino, 1989), also suggests that there is a material dependence.

When considering 400 µm projectile impacts into 25 µm films at 4 km s^{-1}, which showed no deceleration, the deceleration thus also appears to be dependent upon impactor energy. Accordingly, a fit that is a function of both momentum and kinetic energy may be required, with the film mass to projectile mass ratio (m_f/m_p) raised to a power between 0.5 and 1. However, the data collected here was too scattered to support such analysis. It is, however, recommended that 12.5 µm films be used (in preference to 25 µm films) to reduce the effects of particle deceleration.

Admittedly this study is not comprehensive, with enough deceleration data to provide a definitive deceleration calibration curve for Kapton films at all thicknesses, incident speeds and particle sizes. Instead, the fit functions discussed contain terms and dependences indicative of those that would appear in such a calibration curve. It is likely that a fit to a fuller range of data should include film thickness, and material, which is likely relatable to a material property such as yield strength or shear modulus. This would result in a fit, which is a more general form of Eq. 5.5 shown earlier, for incident velocity over exit velocity (v_i/v_p) of the kind:

$$\frac{v_i}{v_p} = \alpha\varepsilon f\left(\frac{m_f}{m_p}\right)^b + 1\,, \tag{7.1}$$

where α is a constant, b is a constant likely to be between 0.5 and 1, and ε is a material parameter.

Finally Objective 3 is treated in Chapter 6. The increase in availability for small satellite launches has seen an increase in the opportunities for using small satellites as science platforms in space missions. Accordingly, there has been an increase in research into nanosatellite missions for flux measurements, with various CubeSat sized detectors having already been used, and more undergoing development (see Table 2.3 in Section 6 for a review of some examples). To investigate whether the accumulation of detection area over multiple CubeSat-sized small area detectors would lead to statistically meaningful data, historic small space exposed surfaces from the LDEF mission were compared with flux predictions from MASTER. Comparison between the accumulated flux from multiple small CubeSat-sized plates from Tray B9 of LDEF and the MASTER predicted flux for the Tray B9 pointing direction in an LDEF like orbit showed good agreement, with the fluxes for crater diameters > 500 um and > 1000 um within or very close to the estimated minimum uncertainties. Considering the timescales before an impact, geometric analysis using ESABase2/Debris suggests that the entire area of one hundred CubeSats would be required to bring the time before a 1 mm particle impact down to 5 years for 6U satellites and 20 years for 1U satellites, which is closer to the operational life-time for a CubeSat.

7.2 Future Work

Taking into consideration all of the data collected for 0.2 mm to 1 mm projectiles, the probability of non-acoustic noise affecting the speed measurement from a pair of sensors

in a shot was 2/26, when considering the total number of shots. If the total number of individual traces is taken into account, the probability of a speed measurement being affected is 2/156. However, for the shots at 4 km s^{-1} all six shots showed signs of non-acoustic noise, with two speed measurements affected. Thus, at the higher average speeds expected in space impacts, for which impact light flash and impact plasma are more likely, the probability of noise affecting a speed measurement is 2/6 (in terms of shots) and 2/36 (in terms of individual traces). Therefore, future work should investigate this further to understand and solve this issue, potentially with shielding. It is recommended that the detection of impact light flash for time of impact determination also be investigated, as this may provide a more consistent signal that produces a higher accuracy for time of impact determination.

The study herein did not sample enough data points with large enough f/d_p that experienced deceleration, to determine a full and accurate calibration curve for the deceleration of small projectiles penetrating Kapton films. Therefore, future work is suggested to extend the projectile size range to lower d_p and allow a fit (such as that described in Section 7.1) to a fuller range of data. The inaccuracy in onset determination that occurs for projectiles with $f/d_p > 1/32$, likely caused by the increasing complexity of acoustic signals as penetration holes and their features become more complex, would suggest that a different mechanism for detecting time of impact is required for the speed determination of smaller impactors. This would be beneficial for a fuller study into the deceleration of projectiles penetrating Kapton films, and for the design of future versions of DRAGONS. Another useful addition to a future study would be use of fragile projectiles to investigate the disruption of such impactors and irregularly shaped projectiles (more realistic of debris). Further to this, simulations of impacts into Kapton films and the acoustic signals produced, using software such as Ansys Autodyn, would be useful to try and determine the origin of the small acoustic signals (distinct for non-acoustic noise) that are sometimes observed to precede the signals of interest in each film.

There are also improvements possible regarding the analysis of the feasibility of using small area detectors for flux measurements. Future work could be carried out to reanalyse the expected crater flux for Tray B9 of LDEF using CPE dump files, so that the crater scaling equation used in Section 6.4.2.1 can be applied to individual impacting particles piecewise, rather than in discrete size populations. This would determine the validity of applying average values for impact speed and impactor density to entire diameter classes, as

implemented in Chapter 6. Also, as data from recent flux measuring CubeSat missions becomes available, this could be compared to expected fluxes from MASTER to further investigate the effectiveness of accumulating detection area over many small area detectors in space.

Overall, this work has shown that the basic ideas of measuring speed in TOF detectors, and of using multiple small area instruments in place of a single large area one, are sound. However, as indicated above, there is more work needed on some of the finer details to fully understand the physics of the various phenomena involved.

References

Adams, N. G., & Smith, D. (1971). Studies of microparticle impact phenomena leading to the development of a highly sensitive micrometeoroid detector. *Planetary and Space Science*, **19**(2), 195–204. https://doi.org/https://doi.org/10.1016/0032-0633(71)90199-1.

Agu, H. O., Hameed, A., & Appleby-Thomas, G. J. (2019). Comparison of the Microstructure of Machined and Laser Sintered Shaped Charge Liner in the Hydrodynamic Regime. *Journal of Dynamic Behavior of Materials*, **5**(4), 484–494. https://doi.org/10.1007/s40870-019-00213-y.

Ahmed, R., Majurec, N. & De Bleser, J. (2019). A CubeSat-based radar for characterization of millimetric orbital debris. *1st Int. Orbital Debris Conf.* https://www.hou.usra.edu/meetings/orbitaldebris2019/orbital2019paper/pdf/6079.pdf.

Ahrens, T. J. (1993). Equation of State. In J. R. Asay & M. Shahinpoor (Eds.), *High-Pressure Shock Compression of Solids* (pp. 75–113). Springer New York. https://doi.org/10.1007/978-1-4612-0911-9_4.

Ahrens, T. J., & Johnson, M. L. (1994). *Shock Wave Data for Minerals*. NASA-CR-199490 https://doi.org/10.1029/rf002p0143.

Alby, F., Lansard, E., & Michal, T. (1997). Collision of Cerise with Space Debris. *Proceedings of the Second European Conference on Space Debris*, *ESA SP-393*, 1–14. https://conference.sdo.esoc.esa.int/proceedings/sdc2/paper/30/SDC2-paper30.pdf.

Anz-Meador, P., Ward, M., Manis, A., Nornoo, K., Dolan, B., Claunch, C., & Rivera, J. (2019). The Space Debris Sensor Experiment. *First Int'l Orbital Debris Conf.*, 1–10. https://spacelaws.com/articles/laws-relating-to-space-situational-awareness-ssa/.

Atkins W. W. (1955). Flash Associated with High-Velocity Impact on Aluminum. J. Appl. Phys. **26**, 126–127 (1955) https://doi.org/10.1063/1.1721850.

Auer, A., & Sitte, K. (1968). Detection technique for micrometeoroids using impact ionization. *Earth and Planetary Science Letters*, **4**(2), 178–183. https://doi.org/https://doi.org/10.1016/0012-821X(68)90013-7

Austrian Space Forum. ADLER-1-2. https://adler.oewf.org/.

Banks, B. A. (1990). Atomic oxygen interaction with materials on LDEF. In B. A. Stain & P. R. young (Eds.), *In Proc. LDEF Materials Data Analysis Workshop* (pp. 191–216). NASA Conference Publication 10046.

Banks, B. A., Snyder, A., Miller, S. K., & Demko, R. (2002). Issues and Consequences of Atomic Oxygen Undercutting of Protected Polymers in Low Eerth Orbit. *Sixth International Conference on Protection of Materials and Structures from Space Environment*, 9 pages. https://doi.org/10.1007/1-4020-2595-5_18.

Barker, L. M., Shahinpoor, M., & Chhabildas, L. C. (1993). Experimental and Diagnostic Techniques. In J. R. Asay & M. Shahinpoor (Eds.), *High-Pressure Shock Compression of Solids* (pp. 43–73). Springer New York. https://doi.org/10.1007/978-1-4612-0911-9_3.

Bauer, W. Romberg, O., Krag, H., Visser, G. H., Digirolamo, D., Barschke, M. F., & Montenegro, S. (2016). DEBRIS IN-SITU IMPACT DETECTION BY UTILIZATION OF CUBE-SAT SOLAR PANELS. in *4S Symposium* 1–11. doi:10.13045/acupunct.2016045.

Bauer, W., Romberg, O., Wiedemann, C., Drolshagen, G., & Vörsmann, P. (2014). Development of in-situ Space Debris Detector. *Adv. in Space Res.* **54**(9), 1858–1869. https://doi.org/10.1016/j.asr.2014.07.035.

Bauer, W. (2021). SOLID-A solar panel based impact detector. In: From Measurements to Understanding: MASTER Modelling Workshop, https://indico.esa.int/event/370/timetable/?view=standard (Accessed 10/05/2023).

Bell, E. V.. NSSDCA Photo Gallery Comets. https://nssdc.gsfc.nasa.gov/photo_gallery/photogallery-comets.html#halley (Date unknown) (Last accessed 08/01/2024)

Bennett, A. A., Schaub, H. & Carpenter, R. Assessing debris strikes in spacecraft telemetry: Development and comparison of various techniques. *Acta Astronaut.* **181**, 516–529 (2021).

Berkebile, D. H., & Stevenson, D. L. (1981). The use of “kapton” polyimide film in aerospace applications. *SAE Technical Papers*, **90**, 3562–3568. https://doi.org/10.4271/811091.

Berthoud, L., & Mandeville, J. C. (1993). Empirical Impact Equation and Marginal Perforation. *Proceedings of the First European Conference on Space Debris*, 459–464. ESA

SD-01. https://conference.sdo.esoc.esa.int/proceedings/sdc1/paper/74/SDC1-paper74.pdf.

Blue Skies Space. MAUVE. https://bssl.space/blue-skies-space-announces-new-satellite-to-monitor-how-energy-released-by-stars-can-affect-the-habitability-of-distant-planets/. (2022) (Last accessed 23/06/2023)

Boslough, M. B., & Asay, J. R. (1993). Basic Principles of Shock Compression. In J. R. Asay & M. Shahinpoor (Eds.), *High-Pressure Shock Compression of Solids* (pp. 7–42). Springer New York. https://doi.org/10.1007/978-1-4612-0911-9_2.

Bourne, N. K., & Bourne, F. L. (2022). On the transition from weak to strong shock response. *Journal of Applied Physics*, **131**(14). https://doi.org/10.1063/5.0084553.

Braun, V., Horstmann, A., Lemmens, S., & Wiedemann, C. (2021). *Recent Developments in Space Debris Environment Modelling , Verification and Validation With Master*. In: *8th European Conference on Space Debris* (ed. T. Flohrer, S. Lemmens & F. Schmitz) (ESA Space Debris Office, 2021). https://conference.sdo.esoc.esa.int/proceedings/sdc8/paper/28/SDC8-paper28.pdf.

Braun, Vitali, Lemmens, S., Reihs, B., Krag, H., & Horstmann, A. (2017). Analysis of breakup events. *7th European Conference on Space Debris*, *April*, 18–21, Darmstadt, Germany. https://conference.sdo.esoc.esa.int/proceedings/sdc7/paper/1005/SDC7-paper1005.pdf.

Brumbaugh, K. M., Kjellberg, H. C., Glenn Lightsey, E., Wolf, A. & Laufer, R. (2012). In-situ sub-millimeter space debris detection using cubesats. *Adv. Astronaut. Sci.* **144**, 789–803.

Burchell, M. J., Cole, M. J., & McDonnell, J. A. M. (1998). Role of particle charge in impact ionization by charged microparticles. *Nuclear Instruments and Methods in Physics Research, Section B: Beam Interactions with Materials and Atoms* **143**(3), 311–318. https://doi.org/10.1016/S0168-583X(98)00371-1.

Burchell, M. J., Cole, M. J., McDonnell, J. A. M., & Zarnecki J. C. (1999). Hypervelocity impact studies using the 2 MV Van de Graaff accelerator and two-stage light gas gun of the University of Kent at Canterbury. *Meas. Sci. Technol.*, **10**, 41–50.

Burchell, M. J., Cole, M. J., & Ratcliff, P. R. (1996). Light flash and ionization from hypervelocity impacts on ice. *Icarus* **122**(2), 359–365. https://doi.org/10.1006/icar.1996.0129.

Burchell, M. J., Corsaro, R., Giovane, F., Cole, M., Sadilek, A., Price, M. C., & Liou, J. C. (2013). A new cosmic dust detector with a novel method using a resistive grid sensitive to hypervelocity impacts. *Procedia Engineering* **58**, 68–76. https://doi.org/10.1016/j.proeng.2013.05.010.

Burchell, M. J., Standen, S., Cole, M. J., Corsaro, R. D., Giovane, F., Liou, J. C., Pisacane, V., Sadilek, A., & Stansbery, E. (2011). Acoustic response of aluminium and duroid plates to hypervelocity impacts. *International Journal of Impact Engineering* **38**(6), 426–433. https://doi.org/10.1016/j.ijimpeng.2010.10.012.

Burns, J. A., Lamy, P. L., & Soter, S. (1979). Radiation forces on small particles in the solar system. *Icarus* **40**(1), 1–48. https://doi.org/https://doi.org/10.1016/0019-1035(79)90050-2.

California Polytechnic State University. (2017). CubeSat 101 Basic Concepts and Processes for First-Time CubeSat Developers. https://www.nasa.gov/sites/default/files/atoms/files/nasa_csli_cubesat_101_508.pdf.

California Polytechnic State University. Cubesat Design Specification Rev 14.1. 34 (2022).

Capaccioni, F., & McDonnell, J. A. M. (1986). Experimental measurement of particle deceleration and survival in multiple thin foil targets. *Adv. Space Res.* **6**(7), 17–20. https://doi.org/10.1016/0273-1177(86)90205-X.

Carey, W. C., McDonnell, J. A. M., & Dixon, D. G. (1985). An Empirical Penetration Equation for Thin Metallic Films Used in Capture Cell Techniques. *International Astronomical Union Colloquium* **85**, 131–136. https://doi.org/10.1017/s0252921100084499.

Chafetz, D., Fleming, B. T., Williams, J., Fotherby, R. L., Tompkins, A., Anderson, N. K., Kohnert, R., France, K., Vorobiev, D., & Siegmund, O. (2021). Mechanical design and development of SPRITE: a 12U CubeSat with a Far-ultraviolet imaging spectrograph. In O. H. Siegmund (Ed.), *UV, X-RAY, AND GAMMA-RAY SPACE INSTRUMENTATION FOR ASTRONOMY XXII* (Vol. 11821). https://doi.org/10.1117/12.2594006.

Christiansen, E. L. (1993). Design and performance equations for advanced meteoroid and debris shields. *Int. J. Impact Eng.* **14**, 145–156. https://doi.org/10.1016/0734-743X(93)90016-Z.

Collins, G. S., Melosh, H. J., & Osinski, G. R. (2012). The impact-cratering process. *Elements* **8**(1), 25–30. https://doi.org/10.2113/gselements.8.1.25.

Colombo, C., Trisolini, M., Scala, F. & and et al. E . CUBE MISSION : THE ENVIRONMENTAL CUBESAT. in *8th European Conference on Space Debris* (ed. T. Flohrer, S. L. & F. S.) (ESA Space Debris Office, 2021). https://conference.sdo.esoc.esa.int/proceedings/sdc8/paper/309/SDC8-paper309.pdf.

Cooper, R., Upadhyaya, H. P., Minton, T. K., Berman, M. R., Du, X., & George, S. M. (2008). Protection of polymer from atomic-oxygen erosion using Al2O3 atomic layer deposition coatings. *Thin Solid Films*, **516**(12), 4036–4039. https://doi.org/10.1016/j.tsf.2007.07.150.

Cornwell, L. T., Wozniakiewicz, P. J., Burchell, M. J., Alesbrook, L. S., Corsaro, R. D., Giovane, F., & Liou, J.-C. (2023). A study on the capabilities and accuracy of Kapton based TOF space dust and debris detectors. *Advances in Space Research*, **72**(7), 2959–2970. https://doi.org/10.1016/j.asr.2022.07.022.

Corsaro, R. D., Giovane, F., Liou, J.-C., Burchell, M. J., Cole, M. J., Williams, E. G., Lagakos, N., Sadilek, A., & Anderson, C. R. (2016). Characterization of space dust using acoustic impact detection. *The Journal of the Acoustical Society of America* **140**(2), 1429–1438. https://doi.org/10.1121/1.4960782.

Corsaro, R. D., Liou, J.-C., Giovane, F., Burchell, M., Pisacane, V., Lagakos, N., Williams, E., & Stansbery, E. (2010). Micrometeoroid and lunar secondary ejecta flux measurement: Comparison of three acoustic systems. *41st Lunar and Planetary Science Conference (Houston Tx.)*, abstract #1108.

Cour-Palais, B. G. (1969). *Meteorid Environment Model - 1969 (Near Earth to Lunar Surface) NASA SP-8013*.

Cour-Palais, B. G. Hypervelocity impact in metals, glass and composites. *Int. J. Impact Eng.* **5**, 221–237 (1987).

Cowardin, H., Anz-Meador, P., Murray, J., Liou, J. C., Christiansen, E., Sorge, M., Fitz-Coy, N., & Huynh, T. (2021). Updates to the DebriSat project in support of improving breakup models and orbital debris risk assessments. *2019 15th Hypervelocity Impact Symposium, HVIS 2019*, 572–580. https://doi.org/10.1115/HVIS2019-066.

Creed, L. *et al.* (2021). STRATHcube: The Design of a CubeSat for Space Debris Detection Using In-Orbit Passive Bistatic Radar. in *International Astronautical Congress (IAC)*, Dubai, United Arab Emirates. 1–8 https://pureportal.strath.ac.uk/files/130341788/Creed_etal_IAC_2021_STRATHcube_the_design_of_a_CubeSat_for_space_debris_detection.pdf.

Crozier, W. D., & Hume, W. (1957). High-velocity, Light-gas gun. *Journal of Applied Physics* **28**(8), 892–894. https://doi.org/10.1063/1.1722882.

Dave, S. & Lee, R. S. K. (2022). Feasibility of a Virtual Constellation using Small Aperture , Wide Field of View Optical Systems for Space Domain Awareness and Applications. in *AMOS 2022 Technical Papers*. https://www.google.co.uk/url?sa=t&rct=j&q=&esrc=s&source=web&cd=&cad=rja&uact=8&ved=2ahUKEwiL77m5wq-BAxVCX0EAHeh0AHAQFnoECBcQAQ&url=https%3A%2F%2Famostech.com%2FTechnicalPapers%2F2022%2FPoster%2FDave.pdf&usg=AOvVaw0vmLWB0Q1_ehhjwL5XlNcW&opi=89978449.

Della Corte, V. *et al.* (2021). Dust Impact Sensors for small spacecrafts. in *Europlanet Science Congress 2020* vol. 14 1–4.

De Simone, M. E., Andreades, C., Meo, M., & Ciampa, F. (2019). Smart composite detector of orbital debris and micrometeoroids particles. *Materials Today: Proceedings* **34**, 202–209. https://doi.org/10.1016/j.matpr.2020.02.796.

Della Corte, V., Ferretti, S., Piccirillo, A. M., Zakharov, V., Di Paolo, F., Rotundi, A., Ammannito, E., Amoroso, M., Bertini, I., Di Donato, P., Ferraioli, G., Fiscale, S., Fulle, M., Inno, L., Longobardo, A., Mazzotta-Epifani, E., Muscari Tomajoli, M. T., Sindoni, G., Tonietti, L., Rothkaehl, H., Wozniakiewicz, P.J., Burchell, M.J., Alesbrook, L.A., Sylvest, M.E., Patel, M. R. (2023).. DISC - the Dust Impact Sensor and Counter on-board Comet Interceptor: characterization of the dust coma of a dynamically new comet. *Adv. Sp. Res.* **71**, 3457–3467 (2023).

Della Corte, V., Rotundi, A., Bertini, I., Zakharov, V., Inno, L., Longobardo, A., Aboudan, A., Bettanini, C., Colombatti, G., Martellato, E., Ivanovski, S., Ferraioli, G., Dirri, F., Ammanito, E., Amoroso, M., & Sindoni, G. (2021). Dust Impact Sensors for small spacecrafts. *Europlanet Science Congress 2020* **14***, 1–4.*

Dietzel, H., Eichhorn, G., Fechtig, H., Grun, E., -J.Hoffmann, H., & Kissel, J. (1973). The HEOS 2 and HELIOS micrometeoroid experiments. *Journal of Physics E: Scientific Instruments* **6**, 209–217. https://doi.org/10.1088/0022-3735/6/3/008.

Dignam, A., Wozniakiewicz, P. J., Burchell, M. J., Alesbrook, L. S., Tighe, A., Suliga, A., Wessing, J., Kearsley, A., Bridges, J., Holt, J., Howie, S., Peatman, L., & Fitzpatrick, D. (2022). Palladium-coated kapton for use on dust detectors in low earth orbit : Performance under hypervelocity impact and atomic oxygen exposure. *Frontiers in Space Technologies*, *September*, 1–14. https://doi.org/10.3389/frspt.2022.933664.

Divine, N. (1993). Five populations of interplanetary meteoroids. *Journal of Geophysical Research* **98**, 17029–17048.

Dorschner, J. (2001). Interstellar dust and circumstellar dust disks. In E. Grün, B. A. S. Gustafson, S. Dermott, & H. Fechtig (Eds.), *Interplanetary Dust* (pp. 727–786). Springer.

Draine, B. T. (2003). Interstellar Dust Grains. *Annual Review of Astronomy and Astrophysics* **41**, 241–289. https://doi.org/10.1146/annurev.astro.41.011802.094840.

Drolshagen, G., Carey, W. C., McDonnell, J. A. M., Stevenson, T. J., Mandeville, J. C., & Berthoud, L. (1997). HST solar array impact survey: Revised damage laws and residue analysis. *Advances in Space Research* **19**(2), 239–251. https://doi.org/10.1016/S0273-1177(97)00007-0.

Drolshagen, G., McDonnell, J. A. M., Stevenson, T. J., Deshpande, S., Kay, L., Tanner, W. G., Mandeville, J. C., Carey, W. C., Maag, C. R., Griffiths, A. D., Shrine, N. G., & Aceti, R. (1996). Optical survey of micrometeoroid and space debris impact features on EURECA. *Planetary and Space Science* **44**(4), 317–340. https://doi.org/10.1016/0032-0633(95)00140-9.

DuPont. (2021). *DuPont Kapton Summary of Properties* (20 Pages).

Duvall, G. E., and Fowles, G. R. Shock waves, in High Pressure Physics and Chemistry, vol. 2, R. S. Bradley (eds)., pp. 209- 292, Academic Press, New York, 1963.

Eichhorn, G. (1975). Measurements of the light flash produced by high velocity particle impact. *Planetary and Space Science* **23**(11), 1519–1525. https://doi.org/https://doi.org/10.1016/0032-0633(75)90005-7.

Eichhorn, G. (1976). Analysis of the hypervelocity impact process from impact flash measurements. *Planetary and Space Science* **24**(8), 771–781. https://doi.org/https://doi.org/10.1016/0032-0633(76)90114-8.

Endurosat. (2024). 3U CUBESAT PLATFORM. https://www.endurosat.com/cubesat-store/cubesat-platforms/3u-cubesat-platform/. Website last accessed 17/01/2024.

Englert, C. R. *et al.* (2014). Optical orbital debris spotter. *Acta Astronaut.* **104**, 99–105.

ESA. (2016). Copernicus Sentinel-1A satellite hit by space particle. https://www.esa.int/Applications/Observing_the_Earth/Copernicus/Sentinel-1/Copernicus_Sentinel-1A_satellite_hit_by_space_particle last accessed 20/01/2024.

ESA. (2022). Space Debris User Portal. https://sdup.esoc.esa.int/ accessed 1/10/2022.

ESA's Space Debris Office. (2022). *Master 8.0.3 Release Note* (p. 6). European Space Agency.

ESA Space Debris Office. (2023). *ESA's Annual Space Environment Report*. https://www.sdo.esoc.esa.int/environment_report/Space_Environment_Report_latest.pdf.

ESA Space Debris Office (2023b). Space debris by the numbers. www.esa.int/Space_Safety/Space_Debris/Space_debris_by_the_numbers.

Etamax (2023). ESABase2. https://esabase2.net.

Faure, P., Masuyama, S., Nakamoto, H., Akahoshi, Y., Kitazawa, Y., & Koura, T. (2013). Space dust impacts detector development for the evaluation of ejecta. *Procedia Eng.* **58**, 594–600.

Fechtig, H., Grün, E., & Kissel, J. (1978). Laboratory Simulation. In J. A. M. McDonnell (Ed.), *Cosmic Dust* (pp. 607–669). John Wiley & Sons. ISBN: 0471995126

Finckenor, M. M., & Dooling, D. (1999). Multilayer Insulation Material Guidelines. NASA TP-1999-209263. https://ntrs.nasa.gov/api/citations/19990047691/downloads/19990047691.pdf.

Fish, R. H., & Summers, J. L. (1965). The effect of material properties on threshold perforation. *Proceedings of the Seventh Hypervelocity Impact Symposium,Vol. 6*.

Friichtenicht, J. F. (1964). Micrometeroid simulation using nuclear accelerator techniques. *Nuclear Instruments and Methods* **28**(1), 70–78. https://doi.org/https://doi.org/10.1016/0029-554X(64)90351-9.

Fucke W., Sdunnus H., Population Model of Small Size Space Debris, Final Report of ESOC contract no. 9266/90/D/MD, Battelle-Institut, Frankfurt am Main, Germany, June 1993

Funase, R., Ikari, S., Miyoshi, K., Kawabata, Y., Nakajima, S., Nomura, S., Funabiki, N., Ishikawa, A., Kakihara, K., Matsushita, S., Takahashi, R., Yanagida, K., Mori, D., Murata, Y., Shibukawa, T., Suzumoto, R., Fujiwara, M., Tomita, K., Aohama, H., … Hashimoto, T. (2020). Mission to Earth-Moon Lagrange Point by a 6U CubeSat: EQUULEUS. *IEEE Aerospace and Electronic Systems Magazine* vol. 35 30–44.

Gardner, D. J., McDonnell, J. A. M., & Collier, I. (1997). Hole growth characterisation for hypervelocity impacts in thin targets. *International Journal of Impact Engineering* **19**(7), 589–602. https://doi.org/10.1016./s0734-743x(96)00047-4.

Gault, D. E., Shoemaker, E. M., & Moore, H. J. (1963). *Spray Ejected from the Lunar Surface by Meteoroid Impact* (NASA Technical Note). National Aeronautics and Space Administration. https://ntrs.nasa.gov/api/citations/19630004711/downloads/19630004711.pdf.

Graham, R. A. (1993). Introduction to High-Pressure Shock Compression of Solids. In J. R. Asay & M. Shahinpoor (Eds.), *High-Pressure Shock Compression of Solids* (pp. 1–6). Springer New York. https://doi.org/10.1007/978-1-4612-0911-9_1.

Graham, G. A., Kearsley, A. T., Drolshagen, G., McBride, N., Green, S. F., & Wright, I. P. (2001). Microparticle impacts upon HST solar cells. *Advances in Space Research*, **28**(9), 1341–1346. https://doi.org/10.1016/S0273-1177(01)00408-2.

Gouzman, I., Grossman, E., Verker, R., Atar, N., Bolker, A., & Eliaz, N. (2019). Advances in Polyimide-Based Materials for Space Applications. *Advanced Materials 31*(18), 1–15. https://doi.org/10.1002/adma.201807738.

Griseri, V. (2016). Polyimide Used in Space Applicaitons. In *Intech* (Issue Polymide for Electronic and Electrical Engineering Applcations, pp. 1–19). https://www.intechopen.com/books/advanced-biometric-technologies/liveness-detection-in-biometrics.

Groemer, G. & Stumptner, W. ADLER-1 Austrian Debris Detection Low Earth (orbit) Reconnoiter. in From Measurement to understanding: MASTER Modeling Workshop, https://indico.esa.int/event/370/timetable/?view=standard. (Accessed 10/05/2023).

Grün, E. (2001). *Interplanetary Dust* (E. Grün, B. Gustafson, S. Dermott, & H. Fechtig (eds.)). Springer.

Grün E., Gustafson B.Å.S, Dermott S.F., Fechtig H. (eds). Interplanetary Dust. Pub. Springer 2001. ISBN 3-350-42067-3.

Grün, E., Krüger, H., & Srama, R. (2019). The Dawn of Dust Astronomy. The Dawn of Dust Astronomy. *Space Sci. Rev.* 215. https://doi.org/10.1007/s11214-019-0610-1.

Grün, E., & Rauser, P. (1969). Penetration Studies of Iron Dust Particles in Thin Foils. *Space Research* **9**, 147–154.

Grün, E., Zook, H. A., Fechtig, H., & Giese, R. H. (1985). Collisional balance of the meteoritic complex. *Icarus* **62**(2), 244–272. https://doi.org/https://doi.org/10.1016/0019-1035(85)90121-6.

Gouzman, I., Grossman, E., Verker, R., Atar, N., Bolker, A., & Eliaz, N. (2019). Advances in Polyimide-Based Materials for Space Applications. *Advanced Materials* **31**(18), 1–15. https://doi.org/10.1002/adma.201807738.

Gusarov, B. (2015). PVDF piezoelectric polymers: characterization and application to thermal energy harvesting. Electric power. Université Grenoble Alpes. English. NNT : 2015GREAT091

Gwynn, D. W., Horz, F., Bernhard, R. P., & See, T. H. (1997). The Dispersion of Molten Soda-Lime Glass Projectiles Following Penetration of Thin Aluminum Membranes. *Int. J. Impact Engng.* **20**, 325–336.

Hamilton, J., Liou, J.-C., Anz-Meador, P. D., Corsaro, B., Giovane, F., Matney, M., & Christiansen, E. (2017). Development of The Space Debris Sensor. In T. Schmitz & F. Flohrer (Eds.), *7th European Conference on Space Debris*. ESA Space Debris Office. https://conference.sdo.esoc.esa.int/proceedings/sdc7/paper/965.

He, Q.-G., & Chen, X. (2023). Simulation method of debris cloud from fiber-reinforced composite shield under hypervelocity impact. *Acta Astronautica*, **204**, 402–417. https://doi.org/10.1016/j.actaastro.2023.01.008.

Henderson, R. A. (1989). Thermal Control of Spacecraft. In P. Fortescue & J. Stark (Eds.), *Spacecraft Systems Engineering* (Second ed., pp. 337–364). Pub: John Wiley & Sons.

Hibbert, R., Cole, M. J., Price, M. C., & Burchell, M. J. (2017). The Hypervelocity Impact Facility at the University of Kent: Recent Upgrades and Specialized Capabilities. *Procedia Engineering* **204**, 208–214. https://doi.org/10.1016/j.proeng.2017.09.775.

Higashide, M., Kusano, T., Takayanagi, Y., Arai, K., & Hasegawa, S. (2015). Comparison of aluminum alloy and CFRP bumpers for space debris protection. *Procedia Engineering* **103**, 189–196. https://doi.org/10.1016/j.proeng.2015.04.026.

Hirai, T., Cole, M. J. Fujii, M.Hasegawa, S., Iwai, T., Kobayashi, M., Srama, R., and Yano, H. (2014). Microparticle impact calibration of the Arrayed Large-Area Dust Detectors in INterplanetary space (ALADDIN) onboard the solar power sail demonstrator IKAROS. *Planetary and Space Science* **100**, 87–97. https://doi.org/10.1016/j.pss.2014.05.009.

Hirayama, K. (1923). Families of asteroids. *Jap. J. Astron. Geophys.* **1**, 55–93.

Horányi, M., Sternovsky, Z., Lankton, M., Dumont, C., Gagnard, S., Gathright, D., Grün, E., Hansen, D., James, D., Kempf, S., Lamprecht, B., Srama, R., Szalay, J. R., & Wright, G. (2014). The Lunar Dust Experiment (LDEX) Onboard the Lunar Atmosphere and Dust Environment Explorer (LADEE) Mission. *Space Science Reviews* **185**(1–4), 93–113. https://doi.org/10.1007/s11214-014-0118-7.

Horstmann, A, Manis, A., Braun, V., Matney, M., & et al. (2021). Flux Comparison of MASTER-8 and ORDEM 3.1 Modelled Space Debris Population. in *8th European Conference on Space Debris* (ed. T. Flohrer, S. Lemmens & F. Schmitz) (ESA Space Debris Office, 2021). https://conference.sdo.esoc.esa.int/proceedings/sdc8/paper/11/SDC8-paper11.pdf.

Horstmann, A., Hesselbach, S., Kebschull, C., Lorenz, J., & Wiedemann, C. (2022). Software User Manual - MASTER. In *Issue 1.3*. https://sdup.esoc.esa.int.

Horstmann, A., Hesselbach, S., & Wiedemann, C. (2020). Enhancement of S/C Fragmentation and Environment Evolution Models. In *ESOC Contract No. 4000115979/15/D/SR*.

Horstmann, A, Stoll, E., & Krag, H. (2017). A Validation Method of ESA ' s MASTER 1 cm Population in Low Earth Orbit. *AMOS Conference 2017*. https://amostech.com/TechnicalPapers/2017/Poster/Horstmann.pdf.

Hörz, F. (2012). Cratering and penetration experiments in aluminum and teflon: Implications for space-exposed surfaces. *Meteoritics and Planetary Science* **47**(4), 763–797. https://doi.org/10.1111/j.1945-5100.2012.01354.x.

Hörz, F., Bernhard, R. P., Warren, J., See, T. H., Brownlee, D. E., Laurance, M. R., Messener, S., Peterson, R. B. Preliminary Analysis of LDEF Instrument A0187-1 "Chemistry of Micrometeoroids Experiment. in *LDEF-69 Months in Space First Post-retrieval Symposium Part-1* (ed. Levine, A. S.) 487–501 (NASA Conference Publication 3134, 1991).

Hörz, F., Bernhard, R. P. & See, T. H. Hypervelocity penetration in aluminum 6061 and 1100 alloys. in *Metallurgical and materials applications of shock-wave and high-strain-rate phenomena* (eds. Murr, L. E., Staudhammer, K. P. & Meyers, M. A.) 273–283 (Elsevier Science B.V., 1995).

Hörz, F., Cintala, M., Bernhard, R. P., & See, T. H. (1994). Dimensionality scaled penetration experiments: Aluminum targets and glass projectiles 50 µm to 3.2 MM in diameter. *International Journal of Impact Engineering* **15**(3), 257–280. https://doi.org/10.1016/S0734-743X(05)80017-X.

Hörz, F., Cintala, M. J., Bernhard, R. P., Cardenas, F., Davidson, W. E., Haynes, G., See, T. H., & Winkler, J. L. (1995). *Penetration experiments in aluminum 1100 targets using soda-lime glass projectiles* NASA-TM-104813. 228. https://ntrs.nasa.gov/search.jsp?R=19960008824.

Humes, D. H. Small Craters on The Meteoroid and Space Debris Impact Experiment. in *LDEF - 69 Months in Space Third Post-Retrieval Symposium Part 1* (ed. Levine, A. S.) 287–322 (NASA Conference Publication 3275, 1993).

Ishimaru, R. *et al.* (2021). ASTERISC Project: CubeSat Mission for Observation of Cosmic Dust with a New Large Film Type Dust Sensor. in *52nd Lunar and Planetary Science Conference 2021,* abstract#1712.

Jenniskens, P. (1994). Meteor stream activity I. The annual streams. *Astronomy and Astrophysics* **287**, 990–1013.

Jones, D. R., Chapman, D. J., & Eakins, D. E. (2014). Gas gun driven dynamic fracture and fragmentation of Ti-6Al-4V cylinders. In W. Buttler, M. Furlanetto, & W. Evans (Eds.), *18TH APS-SCCM AND 24TH AIRAPT, PTS 1-19* (Vol. 500). https://doi.org/10.1088/1742-6596/500/11/112037.

Kelso, T. S. (2007). Analysis of the 2007 Chinese ASAT Test and the Impact of its Debris on the Space Environment. *AMOS 2007 Tech. Pap.* 10 Pages. http://celestrak.org/publications/AMOS/2007/AMOS-2007.pdf.

Kessler, D. J., Reynolds, R. C. & Anz-meador, P. D. (1989). Orbital Debris Environment for Spacecraft Designed to Operate in Low Earth Orbit. NASA Technical Memorandum 100 471, 22 pages. https://ntrs.nasa.gov/api/citations/19890013267/downloads/19890013267.pdf.

Kirkup, L. (2019). *Experimental Methods for Science and Engineering Students: An Introduction to the Analysis and Presentation of Data* (2nd ed.). Cambridge University Press. https://doi.org/10.1017/9781108290104.

Koschny, D., Soja, R. H., Engrand, C., Flynn, G. J., Lasue, J., Levasseur-Regourd, A. C., Malaspina, D., Nakamura, T., Poppe, A. R., Sterken, V. J., & Trigo-Rodríguez, J. M. (2019). Interplanetary Dust, Meteoroids, Meteors and Meteorites. *Space Science Reviews* **215**(4). https://doi.org/10.1007/s11214-019-0597-7.

Krag, H., Serrano, M., Braun, V., Kuchynka, P., Catania, M., Siminski, J., Schimmerohn, M., Marc, X., Kuijper, D., Shurmer, I., O'Connell, A., Otten, M., Muñoz, I., Morales, J., Wermuth, M., & McKissock, D. (2017). A 1 cm space debris impact onto the Sentinel-1A solar array. *Acta Astronautica* **137**, 434–443. https://doi.org/10.1016/j.actaastro.2017.05.010.

Krisko, P. H., Flegel, S., Matney, M. J., Jarkey, D. R., & Braun, V. (2015). ORDEM 3.0 and MASTER-2009 modeled debris population comparison. *Acta Astronautica* **113**, 204–211. https://doi.org/10.1016/j.actaastro.2015.03.024.

Lamberson, L. E., & Boettcher, P. A. (2018). Compressed gas combined single- and two-stage light-gas gun. *Review of Scientific Instruments* **89**(2), 1–7. https://doi.org/10.1063/1.5000912.

Lamontagne, C. G., Manuelpillai G. N., Keer, Taylor, E. A., Tennyson, R. C. and Burchell, M. J. Projectile Density, Impact Angle and Energy Effects on Hypervelocity Impact Damage to Carbon Fibre/PEEK Composites, *International Journal of Impact Engineering* **26**, 381-398, 2001.

Leinert, C., Bowyer, S., Haikala, L. K., Hanner, M. S., Hauser, M. G., Levasseur-Regourd, A.-C., Mann, I., Mattila, K., Reach, W. T., Schlosser, W., Staude, H. J., Toller, G. . N., Weiland, J. L., Weinberg, J. L., & Witt, A. N. (1998). The 1997 reference of diffuse night sky brightness. *Astron. Astrophys. Suppl. Ser.* **127***,* 1–99.

Leitner, J., & Hoppe, P. (2019). A new population of dust from stellar explosions among meteoritic stardust. *Nature Astronomy* **3**, 725-729.

Liou, J.-C., Corsaro, R., Giovane, F., Anderson, C., Sadilek, A., Burchell, M., & Hamilton, J. (2015). DRAGONS – A Micrometeoroid and Orbital Debris Impact Sensor. NSAT Symposium, Kobe 2015, 6 pages. https://ntrs.nasa.gov/archive/nasa/casi.ntrs.nasa.gov/20150019424.pdf.

Liou, J., Giovane, F. J., Corsaro, R. D., Burchell, M. J., Drolshagen, G., Kawai, H., Stansbery, E. G., Tabata, M., Westphal, A. J., & Yano, H. LAD-C : A large area debris collector on the ISS. COSPAR 36th General Assembly, Beijing 2006. https://ntrs.nasa.gov/api/citations/20060028448/downloads/20060028448.pdf. (2006).

Liou, J.-C., & Johnson, N. L. (2006). Risks in Space from orbiting Debris. *Science* **311**(5759), 340–341. https://doi.org/10.1016/j.asr.2005.06.021.

Love, S. G., & Brownlee, D. E. (1993). A Direct Measurement of the Terrestrial Mass Accretion Rate of Cosmic Dust. *Science* **262**(5133), 550–553.

Love, S. G., Brownlee, D. E., King, N. L. & Hörz, F. (1995). Morphology Of Meteoroid And Debris Impact Craters Formed In Soft Metal Targets On The LDEF Satellite. *Int. J. Impact Engng.* **16**, 405–418.

Marsh, S. P. (1980). LASL shock Hugoniot data. Univ of California Press. ISBN: O-520-04008-2. http://large.stanford.edu/publications/coal/references/docs/shd.pdf.

McDonald, D. (2022). Recovery of a Lost Satellite : The ARMADILLO Mission. in *36th Annual Small Satellite Conference*, https://digitalcommons.usu.edu/cgi/viewcontent.cgi?article=5163&context=smallsat. , 9 pages.

McDonnell, J. A. M. (1970). Factors affecting the choice of foils for penetration experiments in space. *Space Research* **10**, 214–325.

McDonnell, J. A. M. (1987). The Giotto dust impact detection system. *J. Phys. E.* **20**, 741–758. https://doi.org/10.1088/0022-3735/20/6/033.

McDonnell, J. A. M. (1999). HVI phenomena: Applications to space missions. *International Journal of Impact Engineering*, **23**(1 PART II), 597–619. https://doi.org/10.1016/s0734-743x(99)00107-4.

McDonnell, J. A. M. (2006). The Open University planetary impact facility: A compact two-stage light gas gun for all impact angles. *International Journal of Impact Engineering* **33**(1–12), 410–418. https://doi.org/10.1016/j.ijimpeng.2006.09.038.

McDonnell, J. A. M., & Sullivan, K. (1992). Hypervelocity impacts on space detectors: decoding the projectile parameters. In *Hypervelocity Impacts in Space* (J. A. M. M). University of Kent at Canterbury.

Measurement Specialties Inc. (1999). *Piezo Film Sensors Technical Manual*. https://doi.org/10.1148/100.2.415.

Melosh, H. Jay. (2011). Impact cratering. In *Planetary Surface Processes* (Issue 5810, pp. 222–275). Cambridge University Press.

Melosh, H.J. (1989). *Impact cratering : a geologic process*. Oxford University Press, 1989.

Ménard, B., Kilbinger, M., & Scranton, R. (2010). On the impact of intergalactic dust on cosmology with type Ia supernovae. *Monthly Notices of the Royal Astronomical Society* **406**(3), 1815–1820. https://doi.org/10.1111/j.1365-2966.2010.16464.x.

Mizutani, H., Takagi, Y., & Kawakami, S. I. (1990). New scaling laws on impact fragmentation. *Icarus* **87**(2), 307–326. https://doi.org/10.1016/0019-1035(90)90136-W.

Moussi, A., Drolshagen, G., McDonnell, J. A. M., Mandeville, J. C., Kearsley, A. T., & Ludwig, H. (2005). Hypervelocity impacts on HST solar arrays and the debris and meteoroids population. *Advances in Space Research*, **35**(7), 1243–1253. https://doi.org/10.1016/j.asr.2005.03.060.

Nakamura, M., Kitazawa, Y., Matsumoto, H., Okudaira, O., Hanada, T., Sakurai, A., Funakoshi, K., Yasaka, T., Hasegawa, S., & Kobayashi, M. (2015). Development of in-situ micro-debris measurement system. *Advances in Space Research* **56**(3), 436–448. https://doi.org/10.1016/j.asr.2015.04.009.

NASA. (2016). Monthly Number of Objects in Earth Orbit by Object Type. *Orbital Debris Quarterly News*, **20**, 14 pages. https://www.orbitaldebris.jsc.nasa.gov/quarterly-news/pdfs/odqnv20i1-2.pdf.

NASA, Orbital Debris Program Office (2020). *Orbital Debris Quarterly News* **24**, 1-14.

NASA, Orbital Debris Program Office (2021). *Orbital Debris Quarterly News* **25**(1), 1–12. https://doi.org/10.1016/0094-5765(93)90151-L.

NASA FY2022, NASA Congressional Budget Justification, 2022. https://www.nasa.gov/sites/default/files/atoms/files/fy2022_congressional_justification_nasa_budget_request.pdf. Website accessed Sept. 2023.

Neish, M. J., & Kibe, S. (2001). Hypervelocity Impact Damage Equations for Kapton Multi-. *Proceedings of the 3rd European Conference on Space Debris*, *ESA SP-473*, 1–6.

Office of the Inspector General, NASA Office of Audit, US, (2021). NASA'S EFFORTS TO MITIGATE THE RISKS POSED BY ORBITAL DEBRIS, Report No. IG-21-011. https://oig.nasa.gov/docs/IG-21-011.pdf..

O'Neal, R. L. & Burton Lightner, E. Long Duration Exposure Facility-A General Overview.. in *LDEF-69 Months in Space First Post-retrieval Symposium Part 1* (ed. Levine, A.) 3–48 (NASA Conference Publication 3134, 1991).

Oikonomidou, X., Karagiannis, E., Still, D., Strasser, F., Firmbach, F. S., Hettwer, J., Schweinfurth, A. G., Pucknus, P., Menekay, D., You, T., Vovk, M., Weber, S., & Zhu, Z. (2022). MOVE-III : A CubeSat for the detection of sub-millimetre space debris and meteoroids in Low Earth Orbit. *Front. Sp. Technol.* 1–18. doi:10.3389/frspt.2022.933988.

Pailer, N., & grün, E. (1980). The penetration limit of thin films. *Planetary and Space Science 28*(3), 321–331. https://doi.org/10.1016/0032-0633(80)90021-5

Parnell, J., Bowden, S., Lindgren, P., Burchell, M. J., Milner, D., Price, M., Baldwin, E. C., & Crawford, I. A. (2010). The preservation of fossil biomarkers during meteorite impact events: Experimental evidence from biomarker-rich projectiles and target rocks. *Meteoritics and Planetary Science* **45**(8), 1340–1358. https://doi.org/10.1111/j.1945-5100.2010.01100.x.

Pearson, M. R., Eaton, M., Featherston, C., Pullin, R., & Holford, K. (2017). Improved acoustic emission source location during fatigue and impact events in metallic and composite structures. *Structural Health Monitoring 16*(4), 382–399. https://doi.org/10.1177/1475921716672206

Pierazzo, E., Vickery, A. M., & Melosh, H. J. (1997). A re-evaluation of impact melt production. *Icarus* **127**(2), 408–423. https://doi.org/10.1006/icar.1997.5713.

Pierrazzo, E., & Melosh, H. J. (2000). Understanding Oblique Impacts From Experiments, Observations, And Modeling. *Annu. Rev. of Earth Planet. Sci.* **28**, 141–167.

Qi, H., Shi, Q., Qian, Y., Li, Y., Xu, J., Xu, C., Zhang, Z., & Xie, X. (2022). The Atomic Oxygen Erosion Resistance Effect and Mechanism of the Perhydropolysilazane-Derived SiOx Coating Used on Polymeric Materials in Space Environment. *Polymers 14*(2). https://doi.org/10.3390/polym14020322.

Ringrose, T. J., Doyle, H. W., Foster, P. S., Betney, M., Skidmore, J. W., Edwards, T., Tully, B., Parkin, J. R., & Hawker, N. (2017). A hypervelocity impact facility optimised for the dynamic study of high pressure shock compression. *Procedia Engineering*, **204**, 344–351. https://doi.org/10.1016/j.proeng.2017.09.756.

Rivkin, A. S., & Cheng, A. F. (2023). Planetary defense with the Double Asteroid Redirection Test (DART) mission and prospects. *Nature Communications* **14**(1), 2–4. https://doi.org/10.1038/s41467-022-35561-2.

Robertson, H. P. (1937). Dynamical Effects of Radiation in the Solar System. *Monthly Notices of the Royal Astronomical Society* **97**(6), 423–437.

Rogers, J. A., Bass, N., Mead, P. T., Rogers, J. A., Bass, N., Mead, P. T., Mote, A., Lukasik, G. D., & Intardonato, M. (2022). The Texas A & M University Hypervelocity Impact Laboratory : A modern aeroballistic range facility The Texas A & M University Hypervelocity Impact Laboratory : A modern aeroballistic range facility. *Rev. Sci. Instrum.* **93**(8), 085106-1–26. https://doi.org/10.1063/5.0088994

Schafer, F., & Schneider, E. (1997). An Experimental Study to Investigate Hypervelocity Impacts on Pressure Vessels. *ESA SP-393*, *May*, 435–443.

Schimmerohn, M. *et al* (2021). LARID: CONCEPT OF A LARGE AREA LOW RESOURCE INTEGRATED IMPACT DETECTOR. in *19th IAA SYMPOSIUM ON SPACE DEBRIS (A6) Space Debris Detection, Tracking and Characterization - SST (1)* 2 pages.

Schneider, E., & Schäfer, F. (2001). Hypervelocity impact research- Acceleration technology and applications. *Adv. Space Res.* **28**(9), 1417–1424. https://doi.org/10.1016/S0273-1177(01)00448-3.

Schwanethal, J. P., McBride, N., Green, S. F., McDonnell, J. A. M. & Drolshagen, G. Analysis of impact data from the Debie (Debris In-Orbit Evaluator) sensor in polar low earth orbit. Proceedings of the Fourth European Conference on Space Debris, Darmstadt, Germany, 18-20 April 2005 (ESA SP-587, August 2005).

See, T., Allbrooks, M., Atkinson, D., Simon, C. & Zolensky, M. (1990). *Meteoroid and Debris Impact Features Documented on the Long Duration Exposure Facility*. https://apps.dtic.mil/sti/pdfs/ADA337849.pdf.

Seigel, A. E. (1965). *The Theory of High Speed Guns* (Nelson W. C. (ed.); Issue 91). NATO-AGARD Fluid Dynamics Panel. http://handle.dtic.mil/100.2/AD475660.

Shu, A., Collette, A., Drake, K., Gruen, E., Horany, M., Kempf, S., Mocker, A., Munsat, T., Northway, P., Srama, R., Sternovsky, Z., & Thomas, E. (2012). 3 MV hypervelocity dust

accelerator at the Colorado Center for Lunar Dust and Atmospheric Studies. *Review of Scientific Instruments* **83**(7). https://doi.org/10.1063/1.4732820.

Silverman, E. M. (1995). Space Environmental Effects on Spacecraft: LEO Materials Selection Guide. In *Nasa Contractor Report 4661 Part 2*.

Simpson, J. A., & Tuzzolino, A. J. (1985). Polarized polymer films as electronic pulse detectors of cosmic dust particles. *Nucl. Inst. and Meths. A236*, 187–202.

Simpson, J. A., Rabinowitz, D., & Tuzzolino, A. J. (1989). Cosmic Dust Investigations I.PVDF detector signal dependence on mass and velocity for penetrating particles. *Nucl. Inst. and Meths.* **279**, 611–624.

Simpson, J. A., & Tuzzolino, A. J. (1989). Cosmic dust investigations. II. Instruments for measurement of particle trajectory, velocity and mass. *Nuclear Inst. and Methods in Physics Research A* **279**(3), 625–639. https://doi.org/10.1016/0168-9002(89)91312-0.

Simpson, J. A., Sagdeev, R. Z., Tuzzolino, A. J., Perkins, M. A., Ksanfomality, L. V., Rabinowitz, D., Lentz, G. A., Afonin, V. V., Erö, J., Keppler, E., Kosorokov, J., Petrova, E., Szabó, L., & Umlauft, G. (1986). Dust counter and mass analyser (DUCMA) measurements of comet Halley's coma from vega spacecraft. *Nature* **321**(6067), 278–280. https://doi.org/10.1038/321278a0.

Smith, C. H., Mckinley, I. M., Ramsey, P. G., & Rodriguez, J. I. (2016). Performance of Multi-Layer Insulation for Spacecraft Instruments at Cryogenic Temperatures. *46th International Conference on Environmental Systems*, 1–20.

Sordini, R. *et al.* (2018). GIADA performance during Rosetta mission scientific operations at comet 67P. *Adv. Sp. Res.* **62**, 1987–1997.

Srama, R., Ahrens, T. J., Altobelli, N., Auer, S., Bradley, J. G., Burton, M., Dikarev, V. V., Economu, T., Fechtig, H., Gorlich, M., Grande, M., Graps, A., Grun, E., Havnes, O., Helfert, S., Horanyi, M., Igenbergs, E., Jessberger, E. K., Johnson, T. V., … and et al. (2004). THE CASSINI COSMIC DUST ANALYZER. *Space Science Reviews* **114**, 465–518.

Staubach, P. (1996). *Numerische Modellierung von Mikrometeoriden und ihre Be_deutung für interplanetare Raumsonden und geozentrische Satelliten*. PhD thesis, University of Heidelberg.

Strub, P., Sterken, V. J., Soja, R., Krüger, H., Grün, E., & Srama, R. (2019). Heliospheric modulation of the interstellar dust flow on to Earth. *Astronomy and Astrophysics* 621, 1–16. https://doi.org/10.1051/0004-6361/201832644.

Sweeting, M. N., Hashida, Y., Bean, N. P., Hodgart, M. S., & Steyn, H. (2004). CERISE microsatellite recovery from first detected collision in low Earth orbit. *Acta Astronautica* **55**(2), 139–147. https://doi.org/10.1016/S0094-5765(03)00062-6.

Tang, W., Wang, Q., Wei, B., Li, J., Li, J., Shang, J., Zhang, K., & Zhao, W. (2020). Performance and modeling of a two-stage light gas gun driven by gaseous detonation. *Applied Sciences (Switzerland)* **10**, 4383. https://doi.org/10.3390/app10124383.

Taylor, E., Herbert, M. K., Gardner, D. J., Kay, L., Thomson, R. and Burchell, *M. J.* Hypervelocity Impact on Spacecraft Carbon Fibre Reinforced Plastic/Aluminium Honeycomb, *Proc. Instn. Mech. Engrs. G* **211**, 355-363, 1997.

Todd I. SpaceX Starship launch fails due to "rapid unscheduled disassembly", BBC Sky at Night Magazine, 20th April 2023. https://www.skyatnightmagazine.com/news/spacex-starship-integrated-flight-test (Accessed 25/08/2023).

Trümpler, R. J. (1930). Absorption of light in the galactic system. *Publ. Astron. Soc. Pac.* **42**(248), 214–226.

Tsembelis K., Burchell M. J., Cole M. J., and Margaritis N., Residual Temperature Measurements of Light Flash Under Hypervelocity Impact, N. *Int. J. Impact Engng*. **35**, 1368 – 1373, 2008.

Tuzzolino, A. J. (1996). Applications of PVDF dust sensor systems in space. *Advances in Space Research* **17**(12), 123–132. https://doi.org/10.1016/0273-1177(95)00769-B.

Tuzzolino, A. J., Economou, T. E., McKibben, R. B., Simpson, J. A., McDonnell, J. A. M., Burchell, M. J., Vaughan, B. A. M., Tsou, P., Hanner, M. S., Clark, B. C., & Brownlee, D. E. (2003). Dust Flux Monitor Instrument for the Stardust mission to comet Wild 2. *Journal of Geophysical Research E: Planets* **108**(10). https://doi.org/10.1029/2003je002086.

Tuzzolino, A. J., McKibben, R. B., Simpson, J. A., BenZvi, S., Voss, H. D., & Gursky, H. (2001). The Space Dust (SPADUS) instrument aboard the Earth-orbiting ARGOS spacecraft: I - Instrument description. *Planetary and Space Science* **49**(7), 689–703. https://doi.org/10.1016/S0032-0633(01)00012-5.

Tylka, A. J., Boberg, P. R., Adams, J. H. J., Beahm, L. P. & Kleis, T. Results from the Heavy Ions in Space (HIIS) Experiment on the Ionic Charge State of Solar Energetic Particles. in *LDEF-69 Months in Space First Post-retrieval Symposium Part 1* (ed. Levine, A. S.) 113–127 (NASA Conference Publication 3134, 1991).

University of Manchester, Impact and explosion facility. (Accessed 27/06/2023) https://www.mace.manchester.ac.uk/research/facilities/impact-and-explosion/.

Vavrin, A., Manis, A., Seago, J., Gates, D., Anz-Meador, P., Xu, Y.-L., Barahona, R., Malachi, A., Bigger Jacobs, I., Matney, M., & Liou, J.-C. (2019). *NASA Orbital Debris Engineering Model ORDEM 3.0 - User's Guide Orbital Debris Program Office* (Issue NASA/TP-2019-220448). https://ntrs.nasa.gov/api/citations/20190033393/downloads/20190033393.pdf.

VOAnews. NASA's New Horizons Is on New Post-Pluto Mission (2015). https://www.voanews.com/a/nasa-new-horizons-is-on-new-post-pluto-mission/3018989.html accessed 26/08/2022

Walsh, J. M., Johnson, W. N., Dienes, J. K., Tillotson, J. H., & Yates, D. R. (1964). Summary report on the theory of hypervelocity impact. https://apps.dtic.mil/sti/pdfs/AD0436251.pdf.

NASA, NASA SP-8024 (1970) Meteoroid damage assessment.

Watts, A., Atkinson, D. & Rieco, S. (1993). *Dimensional scaling for impact cratering and perforation*. NASA-CR-188259. https://ntrs.nasa.gov/api/citations/19940006210.

Warren, J., Cole, M., Offenberger, S., Kota, K. R., Lacy, T. E., Toghiani, H., Burchell, M. J., Kundu, S., & Pittman, C. U. (2021). Hypervelocity Impacts on Honeycomb Core Sandwich Panels Filled with Shear Thickening Fluid. *International Journal of Impact Engineering* **150**, 103803. h

Weinberg, J. L., & Sparrow, J. G. (1978). Zodiacal Light as an Indicator of Interplanetary Dust. In J. A. M. McDonnell (Ed.), *Cosmic Dust* (pp. 75–122). Pub. John Wiley & Sons. ISBN: 0471995126.

Whipple, F. L. (1947). Meteorites and space travel. *Astronomical Journal* **52**, 131. https://doi.org/10.1086/106009.

Willis, P. B., & Hsieh, C. H. (2000). Space Applications of Polymeric Materials. *Kobunshi*, **49**(2), 52–56. https://doi.org/10.1295/kobunshi.49.52.

Wood, D. C., Appleby-Thomas, G. J., Fitzmaurice, B. C., Hameed, A., Millett, J. C. F., & Hazell, P. J. (2017). On the shock response of PCTFE (Kel-F 81 ®). *AIP Conference Proceedings*, *1793*(January 2017). https://doi.org/10.1063/1.4971539.

Wozniakiewicz, P. (2017). Cosmic dust in space and on Earth. *Astron. and Geophys.* **58**, 1.35-1.40. https://doi.org/10.1093/astrogeo/atx027

Wozniakiewicz, P. J. & Burchell, M. J. (2019) Space dust and debris near the Earth. *Astron. Geophys.* **60**, 38–42. https://doi.org/10.1093/astrogeo/atz150.

Xin, Y., Sun, H., Tian, H., Guo, C., Li, X., Wang, S., & Wang, C. (2016). The use of polyvinylidene fluoride (PVDF) films as sensors for vibration measurement: A brief review. *Ferroelectrics* **502**(1), 28–42. https://doi.org/10.1080/00150193.2016.1232582.

Yu, X., Zhou, J., Zhu, P. & Guo, J. (2018). Star of AOXiang: An innovative 12U CubeSat to demonstrate polarized light navigation and microgravity measurement. *Acta Astronaut.* **147**, 97–106. https://doi.org/10.1016/j.actaastro.2018.03.014.

Appendix I

This Appendix contains tables of all of the recorded data necessary for speed determination from the detector, for each shot. Followed by tables of all of the calculated detector measured projectile speeds, and measured wave speeds in the Kapton films, for the Dec. shot programme that were not presented in the main text. Also included is a table relating the shots ID's in this thesis to the shot date and number (first, second, third shot of the day) for cross referencing with Kent's LGG data archive.

All full acoustic signal traces, key time periods of signal traces, and penetration features in the first and second film for each shot, as imaged from the incident direction of the projectile, that were not included in the main text are presented.

Table A1 The recorded data used for speed determination. 209
Table A2 Projectile speed, and the wave speed in Kapton calculated for the Dec. shot programme. 211
Table A3 Shot date reference table for cross referencing thesis shot ID's with the Kent's LGG facility archives. 213
Fig. A1 Full acoustic signals for shot Veri.2. 214
Fig. A2 Full acoustic signals for shot Veri.4. 214
Fig. A3 Full acoustic signals for shot Veri.5. 215
Fig. A4 Full acoustic signals for shot Veri.6. 215
Fig. A5 Full acoustic signals for shot Veri.7. 216
Fig. A6 Full acoustic signals for shot Dec.1. 216
Fig. A7 The key time period of acoustic signals in shot Dec.1. 217
Fig. A8 Full acoustic signals for shot Dec.2. 217
Fig. A9 The key time period of acoustic signals in shot Dec.2. 218
Fig. A10 Full acoustic signals for shot Dec.3. 218
Fig. A11 The key time period of acoustic signals in shot Dec.3. 219
Fig. A12 Full acoustic signals for shot Dec.4. 219
Fig. A13 The key time period of acoustic signals in shot Dec.4. 220
Fig. A14 Full acoustic signals for shot Dec.5. 220
Fig. A15 The key time period of acoustic signals in shot Dec.5. 221
Fig. A16 The key time period of acoustic signals in shot Dec.6. 221
Fig. A17 Full acoustic signals for shot Dec.7. 222

Fig. A18 Full acoustic signals for shot Dec.8. 222
Fig. A19 The key time period of acoustic signals in shot Dec.8. 223
Fig. A20 Full acoustic signals for shot Dec.9. 223
Fig. A21 The key time period of acoustic signals in shot Dec.9. 224
Fig. A22 Full acoustic signals for shot Dec.10. 224
Fig. A23 The key time period of acoustic signals in shot Dec.10. 225
Fig. A24 Full acoustic signals for shot Dec.11. 225
Fig. A25 Full acoustic signals for shot Dec.12. 226
Fig. A26 The key time period of acoustic signals in shot Dec.12. 226
Fig. A27 Full acoustic signals for shot Dec.13. 227
Fig. A28 The key time period of acoustic signals in shot Dec.13. 227
Fig. A29 Full acoustic signals for shot Dec.14. 228
Fig. A30 The key time period of acoustic signals in shot Dec.14. 228
Fig. A31 Full acoustic signals for shot Dec.15. 229
Fig. A32 The key time period of acoustic signals in shot Dec.15. 229
Fig. A33 Full acoustic signals for shot Dec.16. 230
Fig. A34 The key time period of acoustic signals in shot Dec.16. 230
Fig. A35 Full acoustic signals for shot Dec.17. 231
Fig. A36 The key time period of acoustic signals in shot Dec.17. 231
Fig. A37 Full acoustic signals for shot Dec.18. 232
Fig. A38 Full acoustic signals for shot Dec.19. 232
Fig. A39 The key time period of acoustic signals in shot Dec.19. 233
Fig. A40 Penetration holes in both films from shot Veri.1. 233
Fig. A41 Penetration holes in both films from shot Veri.3. 233
Fig. A42 Penetration holes in both films from shot Veri.5. 234
Fig. A43 Penetration holes in both films from shot Veri.6. 234
Fig. A44 Penetration holes in both films from shot Veri.7. 234
Fig. A45 Penetration holes in both films from shot Dec.1. 235
Fig. A46 Penetration holes in both films from shot Dec.2. 235
Fig. A47 Penetration holes in both films from shot Dec.3. 235
Fig. A48 Penetration holes in both films from shot Dec.4. 236
Fig. A49 Rear view of the penetration hole in the second film from shot Dec.4. 236
Fig. A50 Penetration holes in both films from shot Dec.5. 236
Fig. A51 Penetration holes in both films from shot Dec.6. 237

Fig. A52 Penetration holes in both films from shot Dec.7. 237
Fig. A53 Penetration holes in both films from shot Dec.8. 237
Fig. A54 Penetration holes in both films from shot Dec.9. 238
Fig. A55 Penetration holes in both films from shot Dec.10. 238
Fig. A56 Penetration holes in the second film from shot Dec.11. 238
Fig. A57 Penetration holes in both films from shot Dec.12. 239
Fig. A58 Penetration holes in both films from shot Dec.13, focused at the top of the rim. 239
Fig. A59 Penetration holes in both films from shot Dec.14. 239
Fig. A60 Penetration holes in both films from shot Dec.15. 240
Fig. A61 Penetration holes in both films from shot Dec.16. 240
Fig. A62 Penetration holes in both films from shot Dec.17. 240
Fig. A63 Penetration holes in both films from shot Dec.18. 241
Fig. A64 Penetration holes in both films from shot Dec.19. 241
Fig. A65 Photodiode and PVDF signals recorded for shot Light.2. 242
Fig. A66 Key time period of photodiode and PVDF signals recorded for shot Light.2. 242
Fig. A67 Photodiode and PVDF signals recorded for shot Light.3. 243
Fig. A68 Key time period of photodiode and PVDF signals recorded for shot Light.3. 243
Fig. A69 Photodiode and PVDF signals recorded for shot Light.4. 244
Fig. A70 Key time period of photodiode and PVDF signals recorded for shot Light.4. 244
Fig. A71 Photodiode and PVDF signals recorded for shot Light.5. 245
Fig. A72 Key time period of photodiode and PVDF signals recorded for shot Light.5. 245
Fig. A73 Photodiode and PVDF signals recorded for shot Light.6. 246
Fig. A74 Key time period of photodiode and PVDF signals recorded for shot Light.6. 246
Fig. A75 Photodiode and PVDF signals recorded for shot Light.7. 247
Fig. A76 Key time period of photodiode and PVDF signals recorded for shot Light.7. 247

Table A1: The recorded data used for speed determination. S_n is the impact to sensor separation, and t_n is the onset time for a given sensor, determined using the manual pick method. v_{LGG} is the incident projectile speed measured by the LGG. Shots Veri.1 to Veri.7, and Dec.14 to Dec.15 have an uncertainty in v_{LGG} of 1% and all other shots an uncertainty of 4%. Where a data point is missing '-' this is due to a faulty sensor not recording any data.

Shot ID	v_{LGG}	S_A (±1.0 mm)	t_A (±1.0 µs)	S_B (±1.0 mm)	t_B (±1.0 µs)	S_C (±1.0 mm)	t_C (±1.0 µs)	S_E (±1.0 mm)	t_E (±1.0 µs)	S_F (±1.0 mm)	t_F (±1.0 µs)	S_G (±1.0 mm)	t_G (±1.0 µs)
Veri.1	2084	145.0	964.4	349.0	1070.8	287.0	1040.4	145.0	1326.8	338.0	1426.8	278.0	1397.2
Veri.2	2192	31.0	867.6	280.5	998.0	277.5	999.2	34.5	1213.6	277.5	1340.4	276.0	1339.6
Veri.3	2132	113.5	945.6	281.5	1035.2	325.5	1061.6	119.5	1303.8	280.0	1389.2	328.0	1409.8
Veri.4	3900	247.0	603.8	205.0	579.0	100.0	524.8	237.0	790.0	201.5	745.8	105.0	722.2
Veri.5	3779	228.0	611.0	97.0	543.4	181.0	588.0	231.0	812.6	98.0	743.4	183.0	787.4
Veri.6	3740	208.0	601.4	119.5	553.6	111.0	552.8	208.0	803.0	120.5	756.8	110.00	751.6
Veri.7	2097	74.5	930.0	207.5	999.2	197.5	996	94.5	1300.8	203.5	1358.8	190.0	1350.0
Dec.1	1959	145.5	1051.5	263.0	1108.0	198.5	1071.2	145.4	1562.4	263.0	1612.0	198.5	1577.2
Dec.2	2094	127.5	1628.8	269.0	1706.0	314.0	1730.0	134.5	2268.8	257.5	2318.8	311.5	2345.2
Dec.3	2160	56.0	764.0	243.5	690.0	256.0	775.0	208.0	1109.0	232.5	1199.0	253.5	1206.0
Dec.4	1746	88.0	1051.0	288.5	1155.2	233.0	1128.0	90.0	1464.8	275.5	1565.6	226.5	1540.0
Dec.5	1742	137.0	1359.4	286.5	1436.8	209.0	1398.0	144.0	1816.4	279.0	1890.8	204.5	1856.4
Dec.6	1963	146.0	1283.8	208.0	1326.0	275.5	1358.0	149.0	2557.0	212.5	2634.0	284.0	2646.8

Table A1 Continued

Shot ID	v_{LGG}	S_A (±1.0 mm)	t_A (±1.0 μs)	S_B (±1.0 mm)	t_B (±1.0 μs)	S_C (±1.0 mm)	t_C (±1.0 μs)	S_E (±1.0 mm)	t_E (±1.0 μs)	S_F (±1.0 mm)	t_F (±1.0 μs)	S_G (±1.0 mm)	t_G (±1.0 μs)
Dec.7	2005	59.0	970.0	271.0	1076.4	247.5	1063.2	53.0	1376.8	259.5	1484.4	243.5	1477.6
Dec.8	1953	75.0	932.0	257.0	1034.4	292.5	1049.8	88.5	1371.2	248.5	1466.4	290.0	1489.0
Dec.9	3999	132.5	456.0	266.0	532.0	325.5	562.8	149.0	646.4	266.5	708.4	333.5	744.0
Dec.10	4466	72.5	413.2	254.5	507.2	288.0	552.4	83.0	575.6	252.5	665.2	288.5	685.6
Dec.11	5216	139.0	400.8	319.5	494.8	259.5	465.6	130.5	565.8	314.0	689.8	251.0	689.2
Dec.12	1920	150.5	1018.4	211.0	1064.4	279.0	1099.6	165.5	1389.6	207.5	1470.8	284.0	1496.8
Dec.13	2039	86.5	934.4	298.5	1046.8	260.0	1029.2	83.0	1304.8	287.0	1411.0	247.5	1391.0
Dec.14	1830	100.0	1043.2	218.0	-	260.0	1128.4	102.5	1448.8	220.5	1511.2	270.5	1537.4
Dec.15	2013	93.0	973.0	217.5	1038.0	202.5	1030.0	82.5	1342.4	215.0	1411.2	201.5	1404.4
Dec.16	1879	114.5	1054.8	246.0	1122.8	203.0	1100.4	97.0	1446.0	239.0	1520.0	201.5	1501.2
Dec.17	2094	50.5	816.2	272.5	928.8	234.5	909.6	59.5	1179.6	258.5	1278.8	229.5	1271.2
Dec.18	2160	96.0	1022.4	259.0	1107.0	202.5	1078.8	108.5	1427.4	251.0	1506.0	198.0	1477.8
Dec.19	1963	21.0	846.0	262.0	973.6	245.5	966.4	41.0	1240.6	252.0	1354.0	241.0	1346.0

Table A2: Projectile speed, and the wave speed in Kapton calculated for the Dec. shot programme to investigate deceleration of small projectiles penetrating thin Kapton films. Projectile speed measurements from pairs of sensors are denoted v_{AE}, v_{BF}, v_{CG}, and the average speed from all pairs denoted TOF Avg.. Wave speeds calculated from pairs of sensors on the same film are shown as WS_{AB}, WS_{AC}, WS_{EF}, WS_{EG}, with the average wave speed from all WS_{mn} labelled WS. Where a data point is missing '-' this is due to a faulty sensor not recording any data.

Shot ID	v_{LGG} (m s^{-1})	v_{AE} (m s^{-1})	v_{BF} (m s^{-1})	v_{CG} (m s^{-1})	TOF Avg. (m s^{-1})	WS_{AB} (m s^{-1})	WS_{AC} (m s^{-1})	WS_{EF} (m s^{-1})	WS_{EG} (m s^{-1})	WS (m s^{-1})
Dec.1	1959	1476 ± 5	1496 ± 5	1490 ± 5	1487 ± 6	2079 ± 58	2690 ± 206	2370 ± 73	3588 ± 356	2682 ± 327
Dec.2	2094	1185 ± 3	1218 ± 4	1223 ± 4	1209 ± 12	1833 ± 38	1843 ± 29	2460 ± 75	2317 ± 47	2113 ± 162
Dec.3	2160	2857 ± 21	1464 ± 5	1744 ± 7	2022 ± 425	2534 ± 52	18181 ± 2341	272 ± 16	469 ± 16	5364 ± 4303
Dec.4	1746	1827 ± 7	1807 ± 7	1814 ± 7	1816 ± 6	1924 ± 29	1883 ± 39	1840 ± 29	1815 ± 39	1866 ±24
Dec.5	1742	1663 ± 6	1646 ± 6	1636 ± 6	1649 ± 8	1932 ± 40	1865 ± 78	1815 ± 39	1512 ± 64	1780 ± 93
Dec.6	1963	592 ± 1	578 ± 1	587 ± 1	586 ± 5	1469 ± 60	1745 ± 38	825 ± 24	1503 ± 28	1386 ± 197
Dec.7	2005	1839 ± 8	1821 ± 7	1810 ± 7	1823 ± 4	1992 ± 30	2022 ± 34	1919 ± 28	1890 ± 30	1956 ± 31
Dec.8	1953	1745 ± 7	1727 ± 7	1712 ± 7	1728 ± 4	1777 ± 28	1846 ± 25	1681 ± 29	1711 ± 24	1754 ± 37
Dec.9	3999	4152 ± 37	4281 ± 39	4262 ± 39	4231 ± 40	1757 ± 38	1807 ± 27	1895 ± 49	1890 ± 31	1837 ± 34
Dec.10	4466	4809 ± 50	4740 ± 48	5672 ± 69	5074 ± 300	1936 ± 33	1548 ± 19	1891 ± 34	1868 ± 27	1811 ± 89
Dec.11	5216	4448 ± 42	3809 ± 31	3305 ± 24	8354 ± 330	1920 ± 32	1860 ± 46	1480 ± 20	977 ± 16	1559 ± 217

Table A2 Continued

Shot ID	v_{LGG} (m s^{-1})	v_{AE} (m s^{-1})	v_{BF} (m s^{-1})	v_{CG} (m s^{-1})	TOF Avg. (m s^{-1})	WS_{AB} (m s^{-1})	WS_{AC} (m s^{-1})	WS_{EF} (m s^{-1})	WS_{EG} (m s^{-1})	WS (m s^{-1})
Dec.12	1920	2070 ± 10	1841 ± 8	1905 ± 8	1939 ± 68	1315 ± 51	1583 ± 33	517 ± 20	1105 ± 20	1130 ± 226
Dec.13	2039	2025 ± 9	2036 ± 9	2046 ± 9	2036 ± 6	1886 ± 27	1830 ± 31	1921 ± 29	1908 ± 35	1886 ± 20
Dec.14	1830	1865 ± 8	-	1869 ±8	1867 ± 6	-	1878 ± 35	1891 ± 48	1896 ± 34	1888 ± 23
Dec.15	2013	2011 ± 9	2013 ± 9	2011 ± 9	2012 ± 5	1915 ± 47	1921 ± 54	1926 ± 45	1919 ± 49	1920 ± 24
Dec.16	1879	1883 ± 8	1881 ± 8	1878 ± 8	1880 ± 5	1934 ± 45	1941 ± 68	1919 ± 41	1893 ± 55	1922 ± 27
Dec.17	2094	2103 ± 10	2109 ± 10	2070 ± 10	2093 ± 12	1972 ± 28	1970 ± 33	2006 ± 32	1856 ± 33	1951 ± 33
Dec.18	2160	1893 ± 8	1870 ± 8	1878 ± 8	1880 ± 7	1927 ± 36	1888 ± 54	1813 ± 37	1776 ± 57	1851 ± 34
Dec.19	1963	1964 ± 9	1955 ± 9	1974 ± 9	1964 ± 6	1889 ± 24	1865 ± 25	1861 ± 26	1898 ± 29	1878 ± 13

Table A3: Shot date reference table for cross referencing thesis shot ID's with the Kent's LGG facility archives. Date format is the shot number (#n) performed for myself for that day, followed by the date (DD/MM/YY).

Shot ID	Date (# DD/MM/YY)	Shot ID	Date (# DD/MM/YY)	Shot ID	Date (# DD/MM/YY)
Veri.1	#1 11/06/21	**Dec.3**	#1 25/01/22	**Dec.12**	#1 18/05/22
Veri.2	#1 28/06/21	**Dec.4**	#1 22/02/22	**Dec.13**	#2 12/05/22
Veri.3	#1 19/07/21	**Dec.5**	#1 03/03/22	**Dec.14**	#1 03/12/21
Veri.4	#1 11/10/21	**Dec.6**	#1 22/11/21	**Dec.15**	#1 11/01/22
Veri.5	#2 11/10/21	**Dec.7**	#2 01/11/21	**Dec.16**	#2 11/01/22
Veri.6	#3 11/10/21	**Dec.8**	#1 25/11/21	**Dec.17**	#3 25/01/22
Veri.7	#1 24/05/22	**Dec.9**	#1 09/05/22	**Dec.18**	#1 03/03/22
Dec.1	#1 17/01/22	**Dec.10**	#2 09/05/22	**Dec.19**	#2 25/01/22
Dec.2	#1 20/01/22	**Dec.11**	#3 12/05/22	-	-

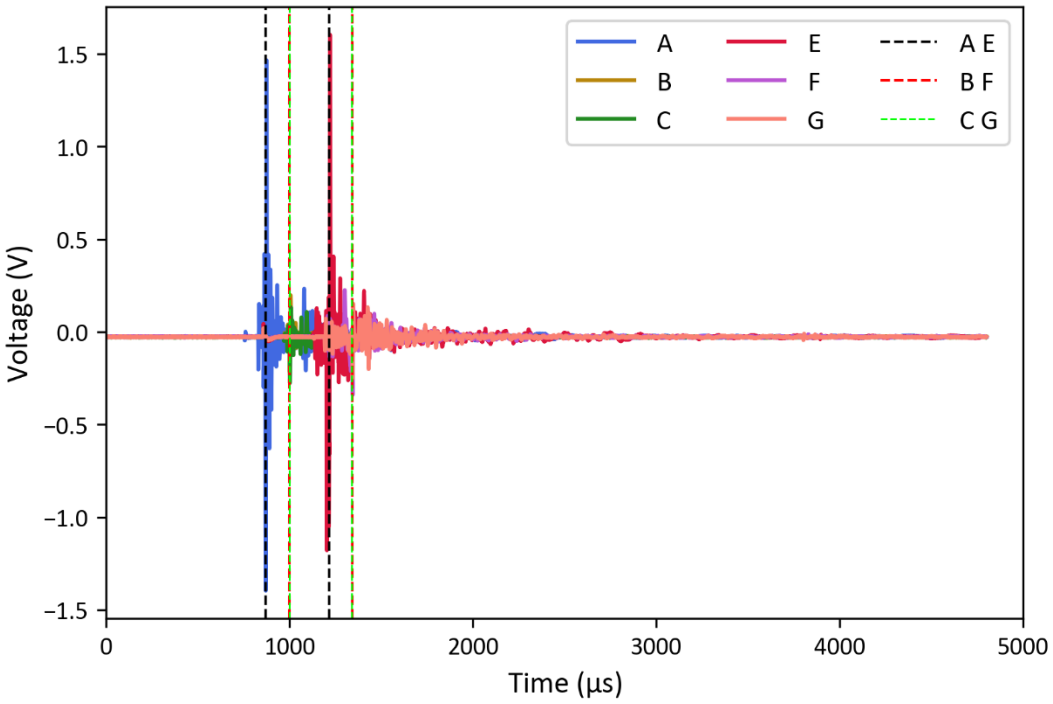

Fig. A1: Full acoustic signals for shot Veri.2. The incident projectile speed was ~ 2 km s^{-1}.

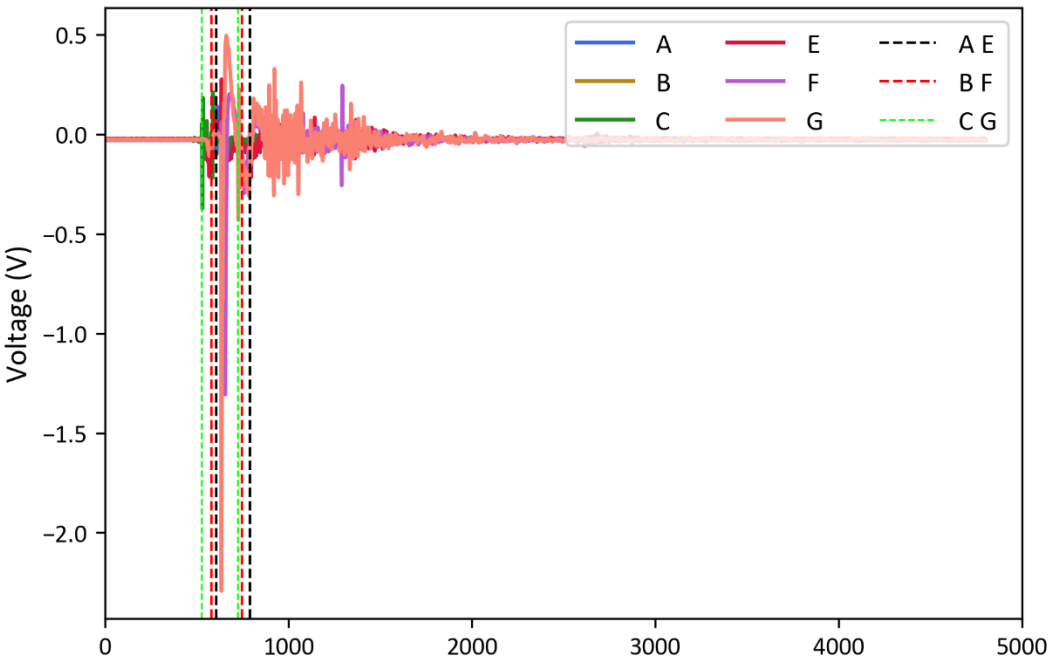

Fig. A2: Full acoustic signals for shot Veri.4. The incident projectile speed was ~ 4 km s^{-1}.

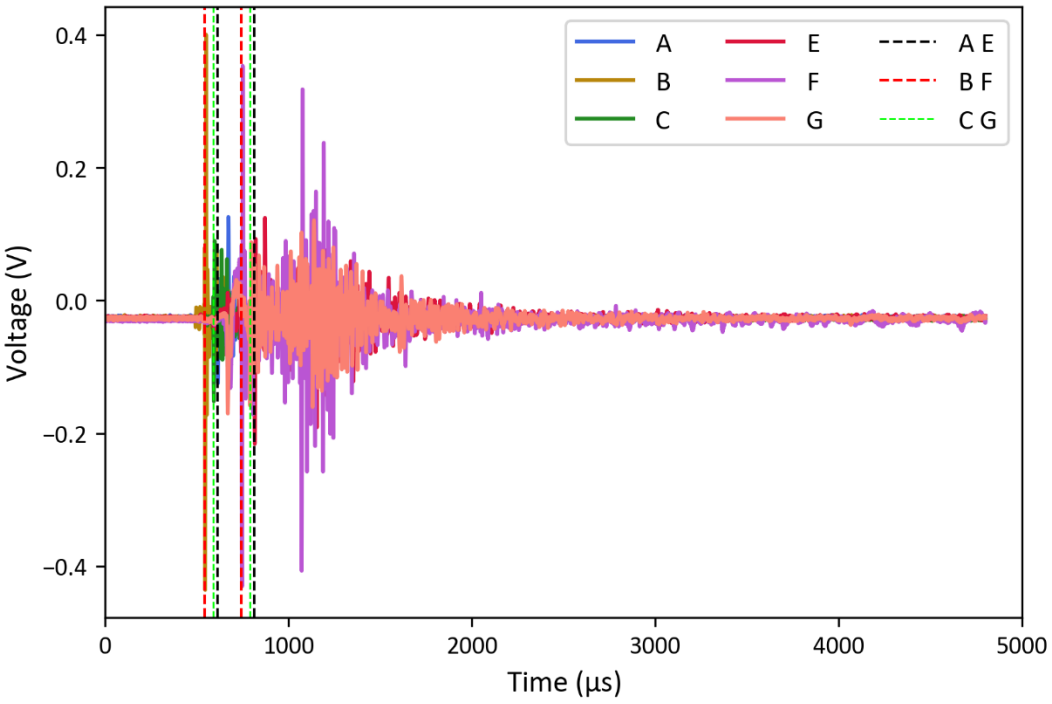

Fig. A3: Full acoustic signals for shot Veri.5. The incident projectile speed was ~ 4 km s^{-1}.

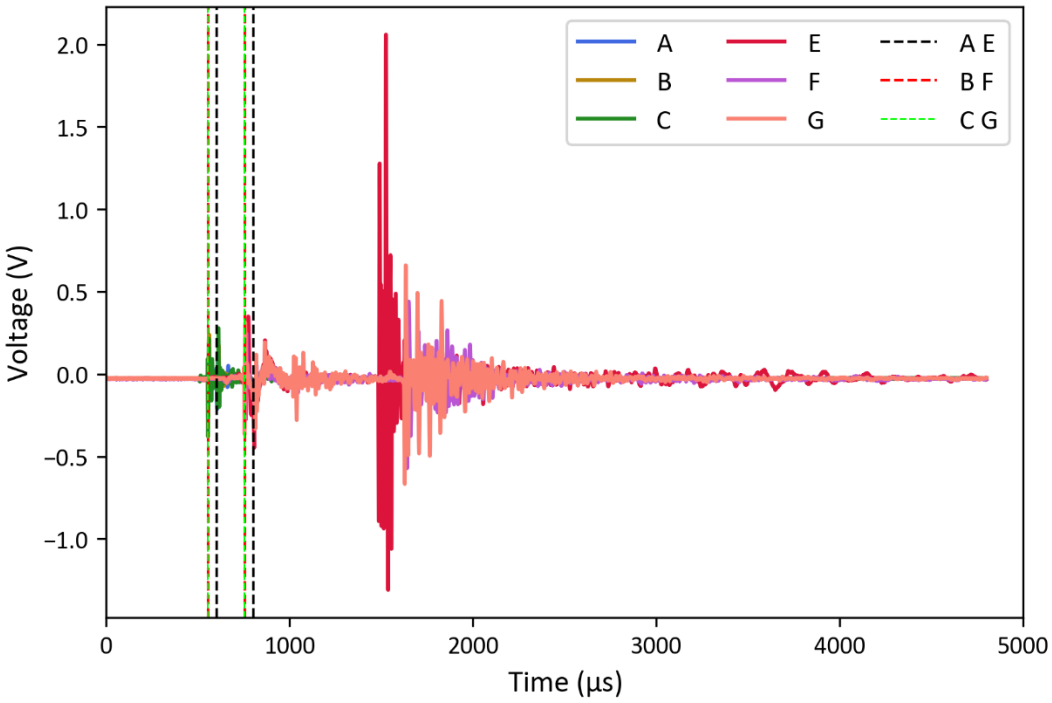

Fig. A4: Full acoustic signals for shot Veri.6. The incident projectile speed was ~ 4 km s^{-1}.

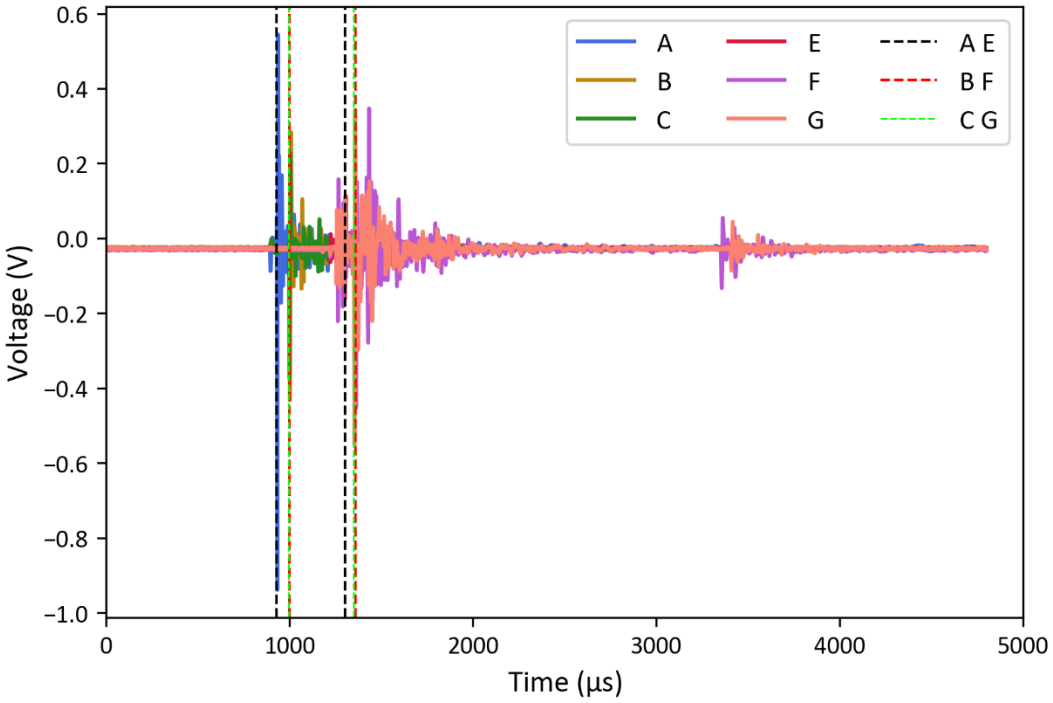

Fig. A5: Full acoustic signals for shot Veri.7. The incident projectile speed was ~ 2 km s^{-1}. Note the first and second films were mounted in the chamber separately with no adjoining trusses.

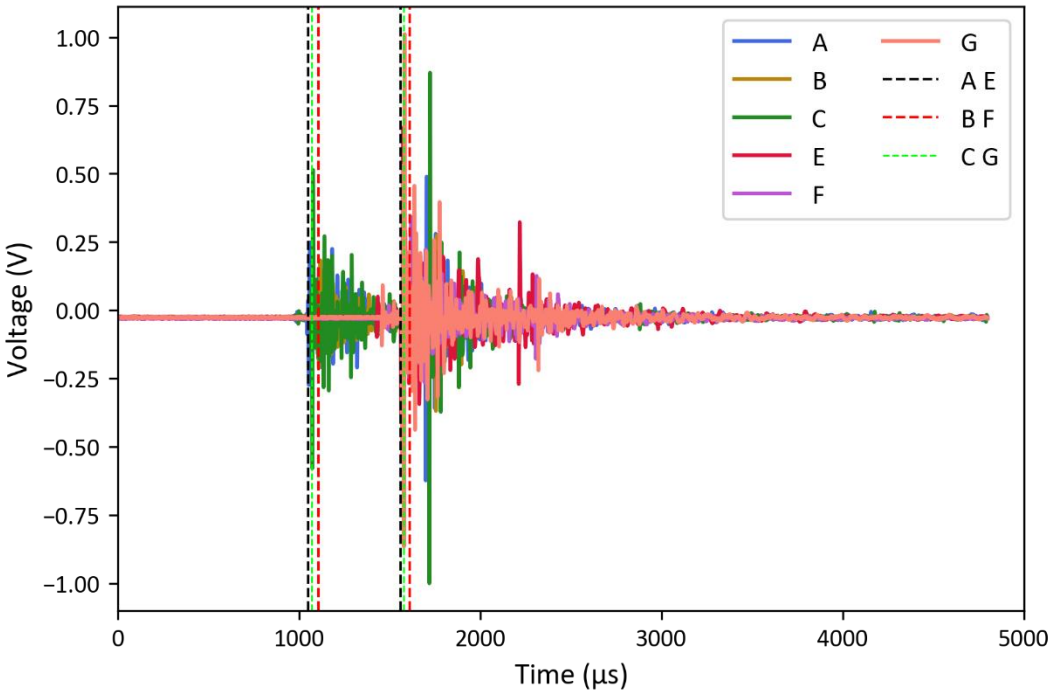

Fig. A6: Full acoustic signals for shot Dec.1. The incident projectile speed was ~ 2 km s^{-1}.

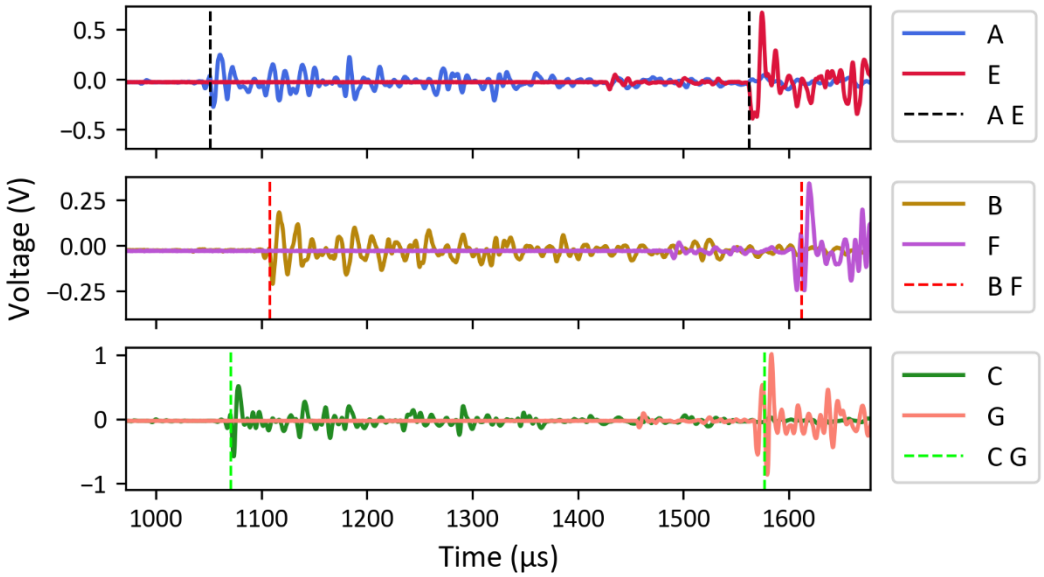

Fig. A7: The key time period of acoustic signals in shot Dec.1. The incident projectile speed was ~ 2 km s^{-1}.

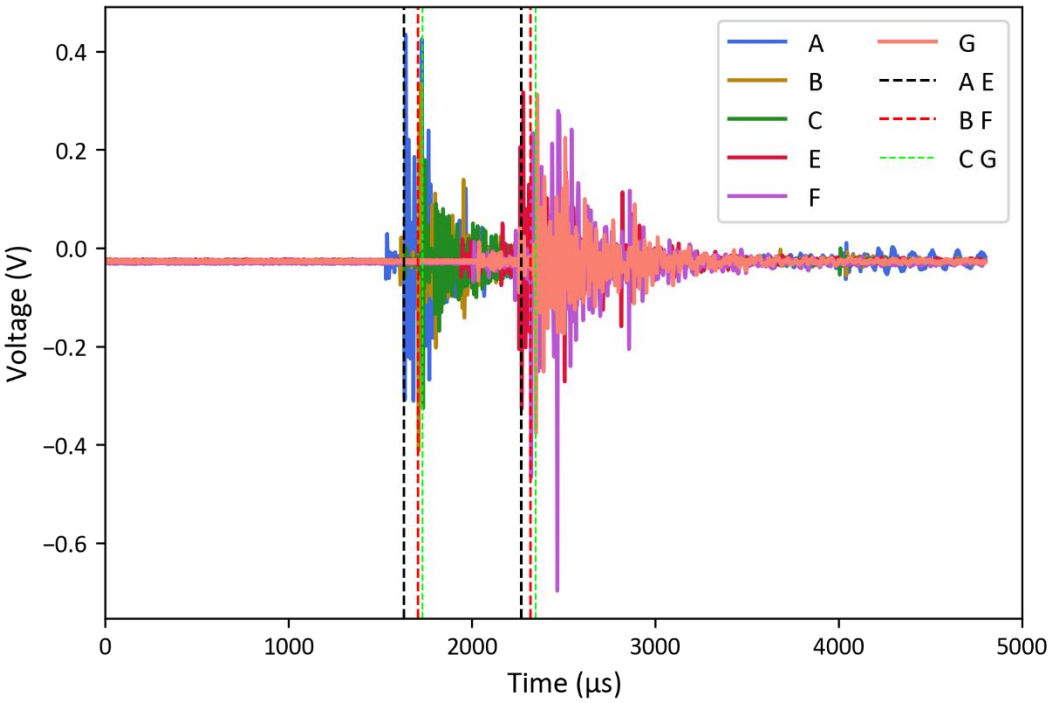

Fig. A8: Full acoustic signals for shot Dec.2. The incident projectile speed was ~ 2 km s^{-1}.

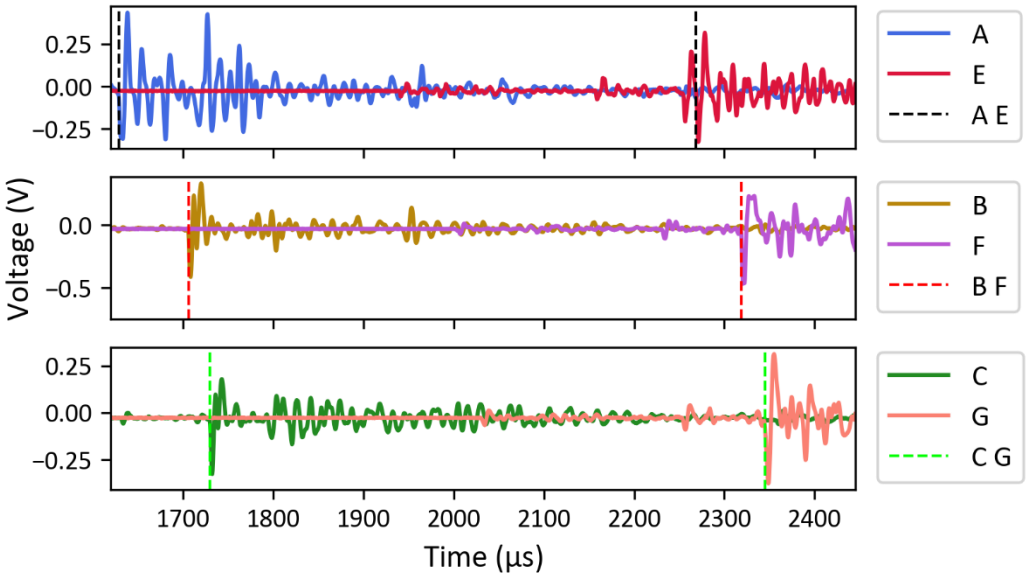

Fig. A9: The key time period of acoustic signals in shot Dec.2. The incident projectile speed was ~ 2 km s^{-1}.

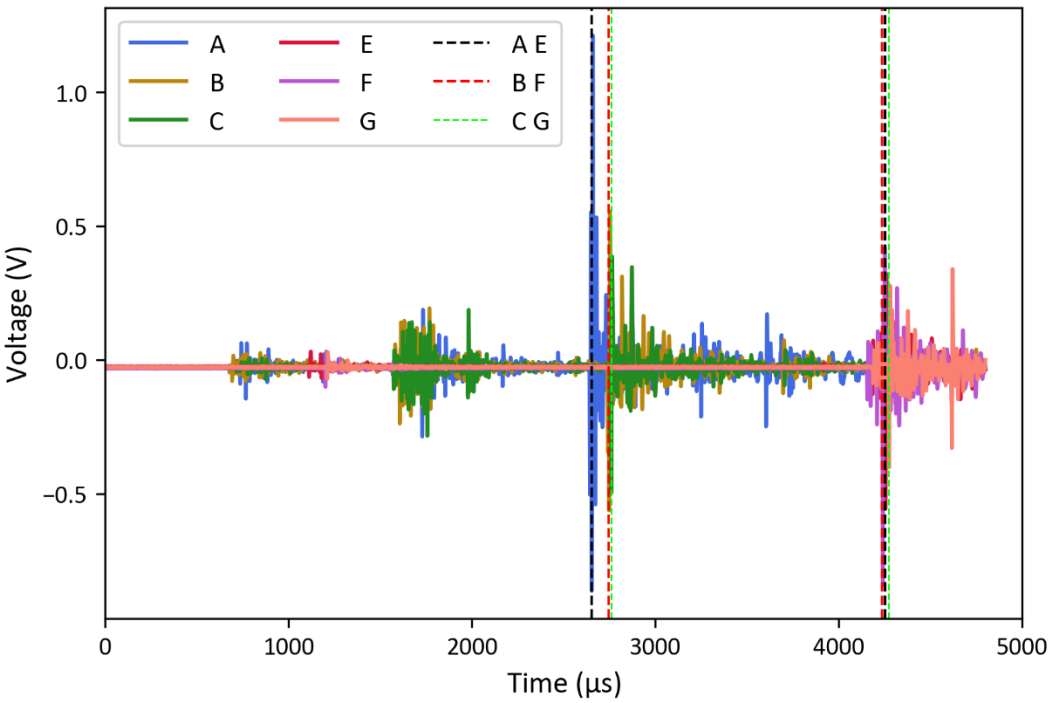

Fig. A10: Full acoustic signals for shot Dec.3. The incident projectile speed was ~ 2 km s^{-1}.

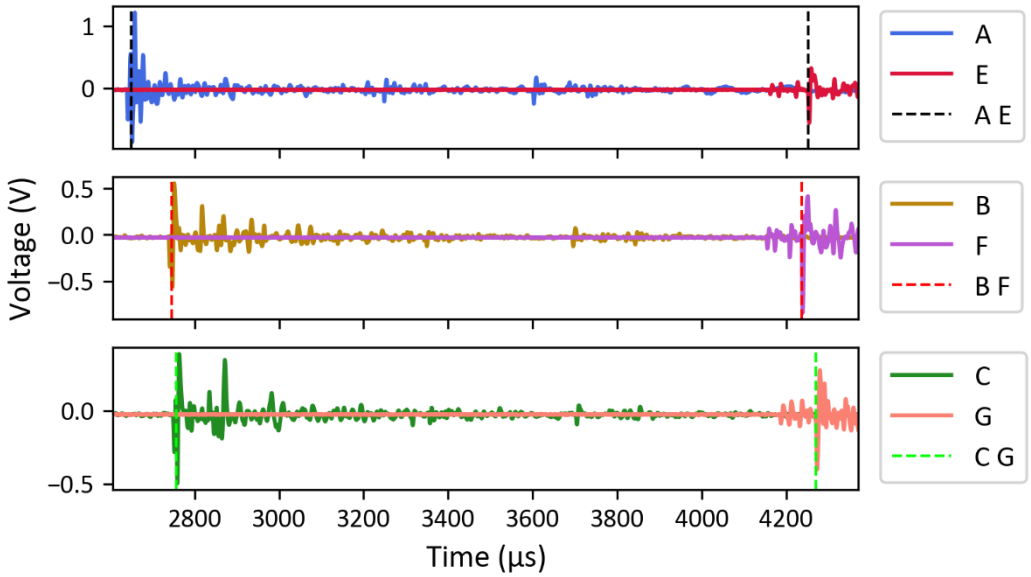

Fig. A11: The key time period of acoustic signals in shot Dec.3. The incident projectile speed was ~ 2 km s^{-1}.

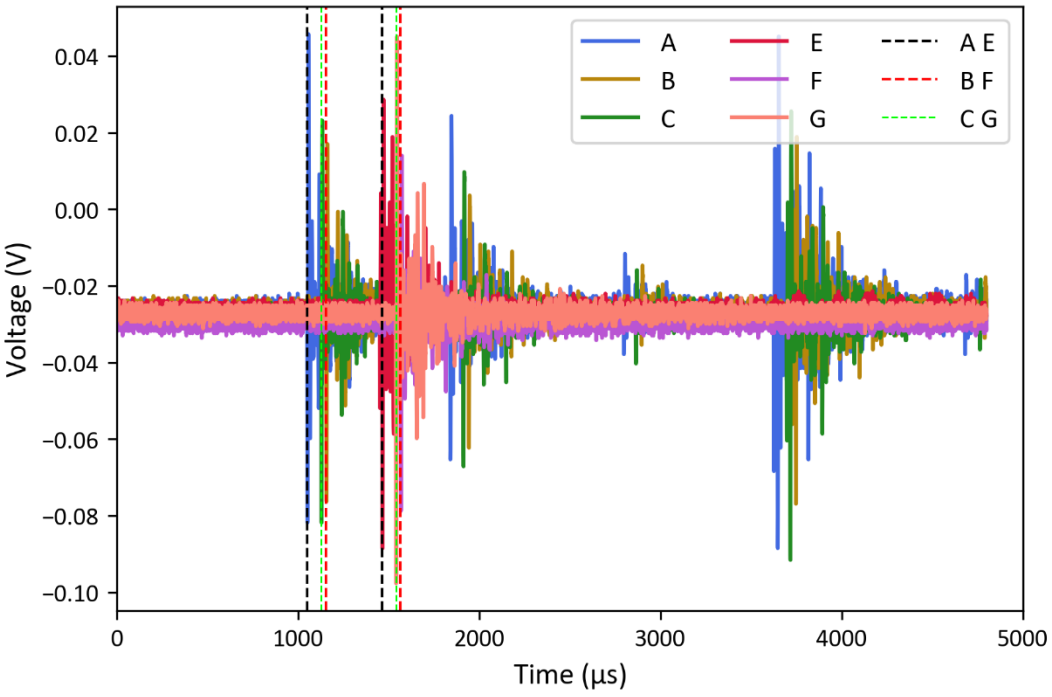

Fig. A12: Full acoustic signals for shot Dec.4. The incident projectile speed was ~ 2 km s^{-1}.

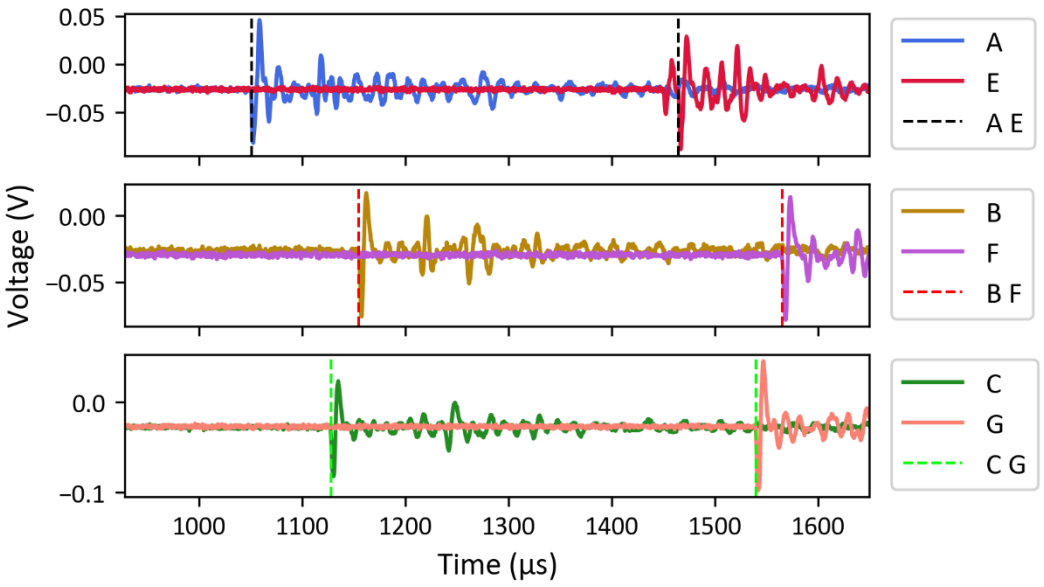

Fig. A13: The key time period of acoustic signals in shot Dec.4. The incident projectile speed was ~ 2 km s^{-1}.

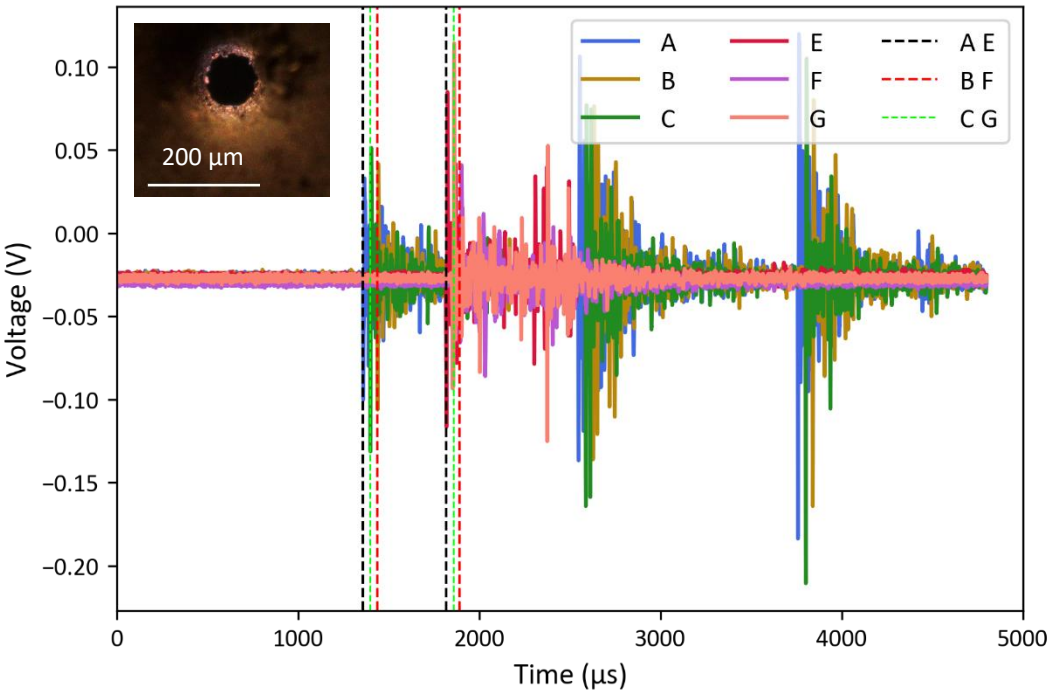

Fig. A14: Full acoustic signals for shot Dec.5. The incident projectile speed was ~ 2 km s^{-1}. An image of a piece of debris likely to have caused some of the later arriving peaks is included top left.

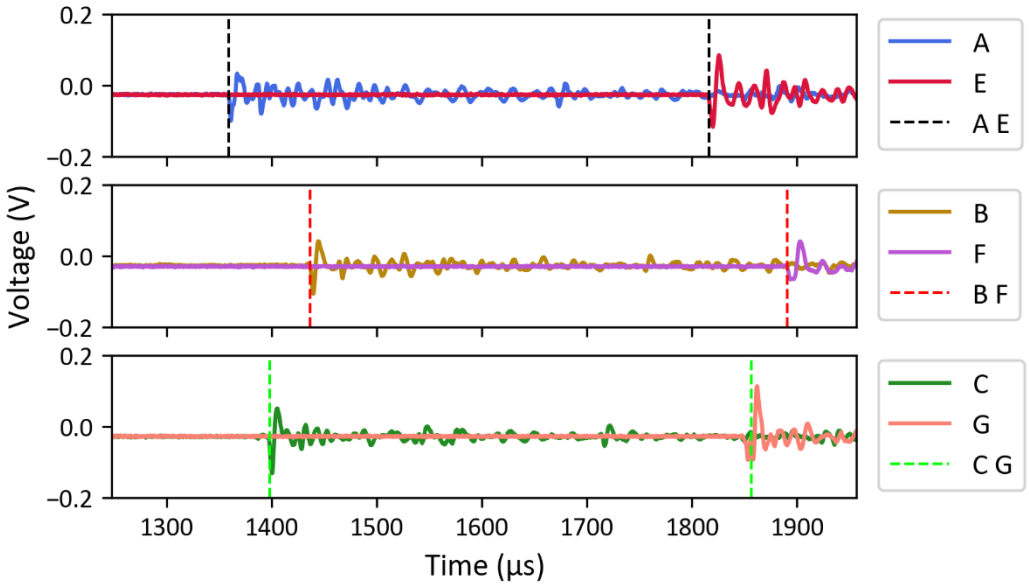

Fig. A15: The key time period of acoustic signals in shot Dec.5. The incident projectile speed was ~ 2 km s^{-1}.

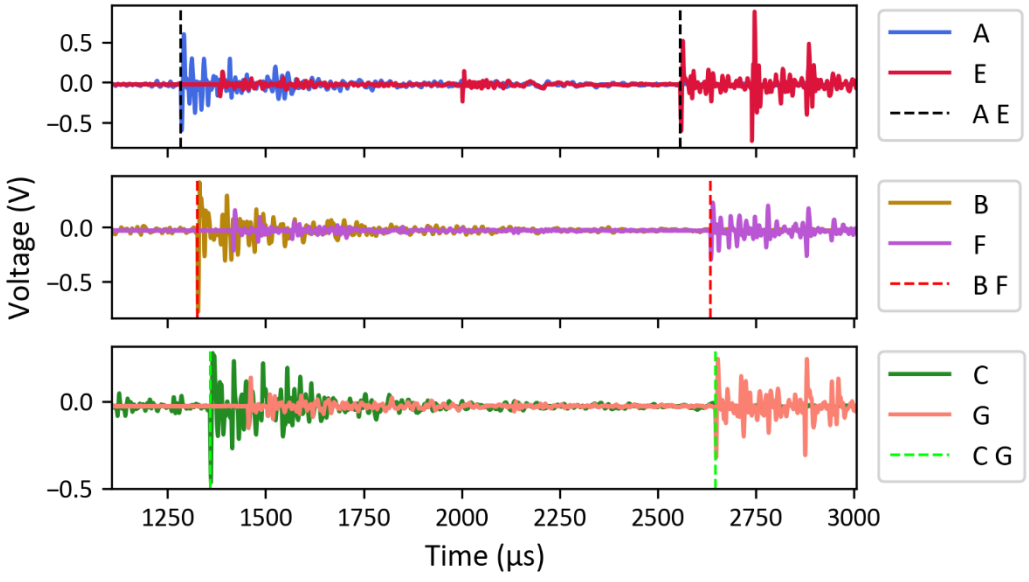

Fig. A16: The key time period of acoustic signals in shot Dec.6. The incident projectile speed was ~ 2 km s^{-1}.

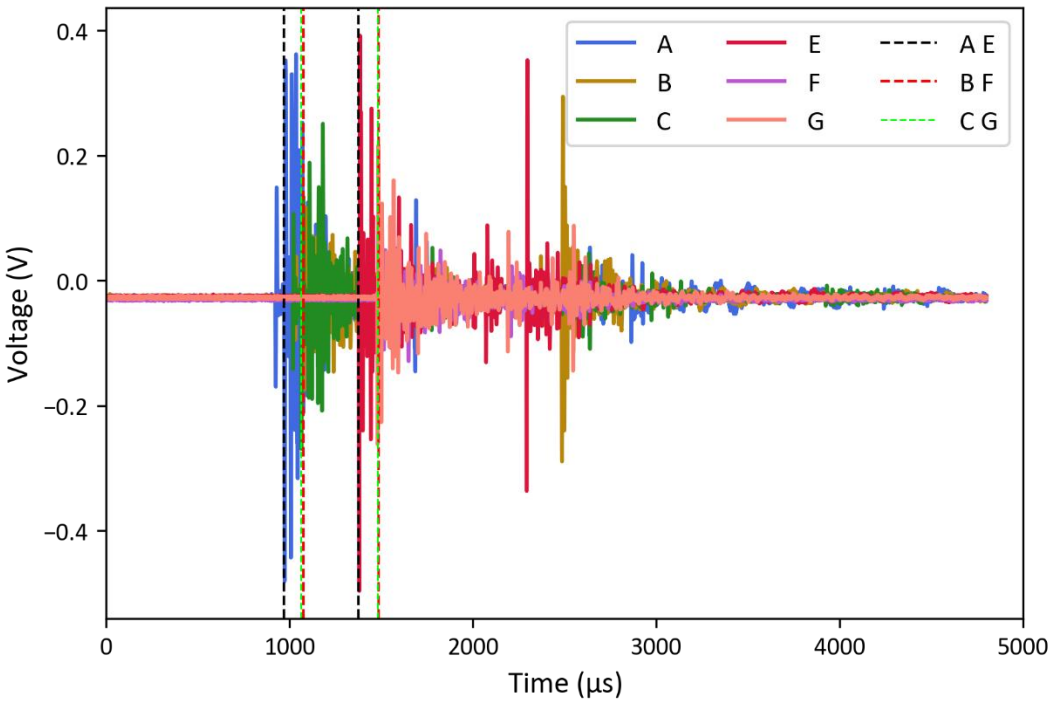

Fig. A17: Full acoustic signals in shot Dec.7. The incident projectile speed was ~ 2 km s^{-1}.

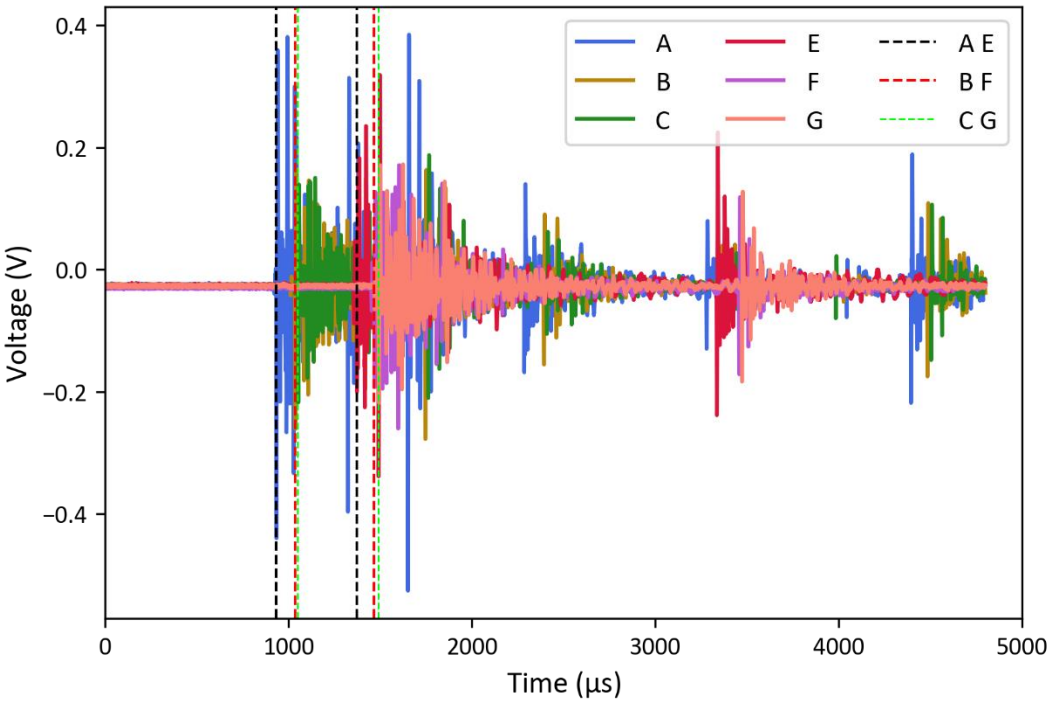

Fig. A18: Full acoustic signals for shot Dec.8. The incident projectile speed was ~ 2 km s^{-1}.

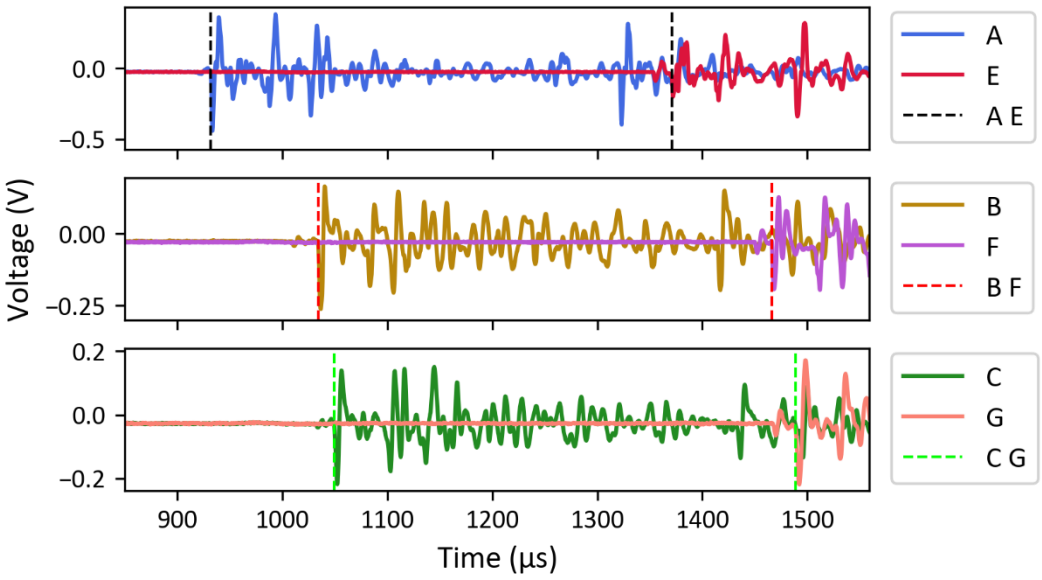

Fig. A19: The key time period of acoustic signals in shot Dec.8. The incident projectile speed was ~ 2 km s^{-1}.

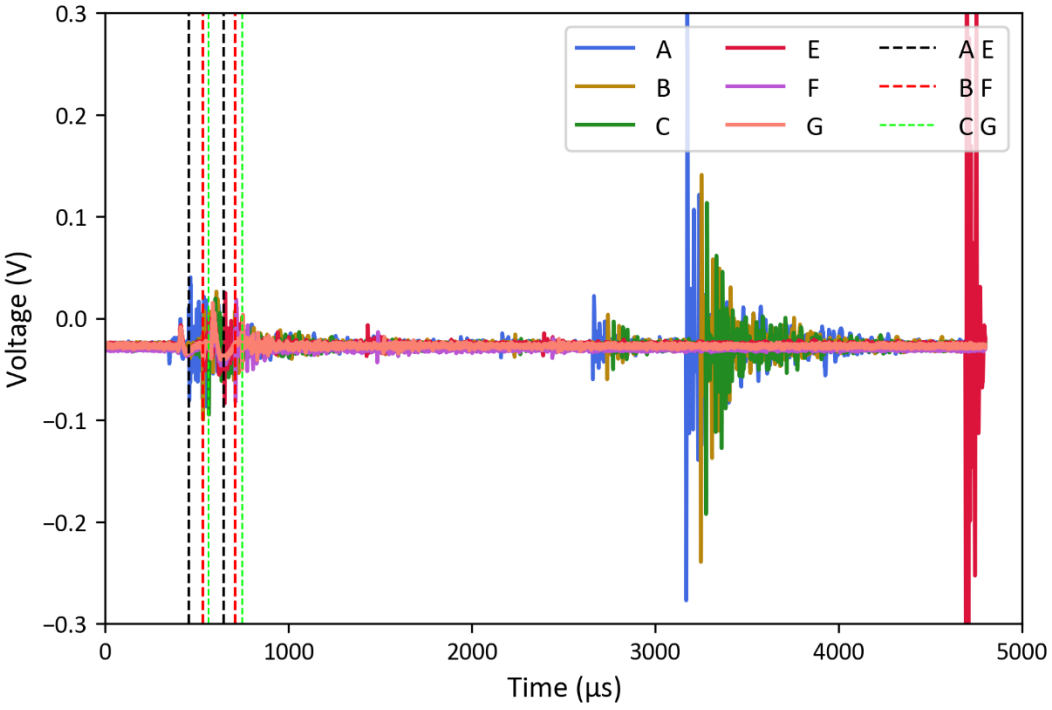

Fig. A20: Full acoustic signals for shot Dec.9. The incident projectile speed was ~ 4 km s^{-1}.

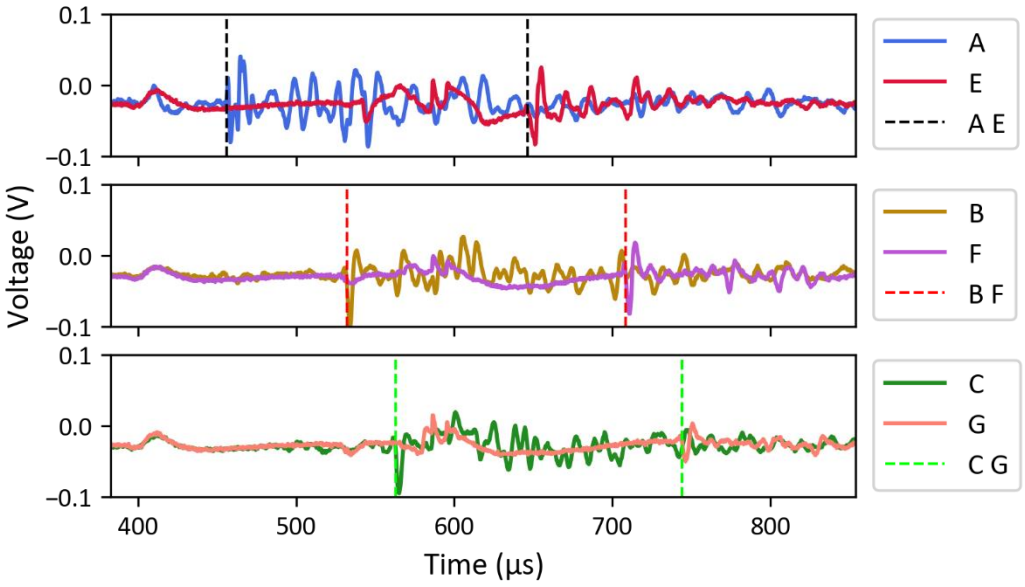

Fig. A21: The key time period of acoustic signals in shot Dec.9. The incident projectile speed was ~ 4 km s^{-1}.

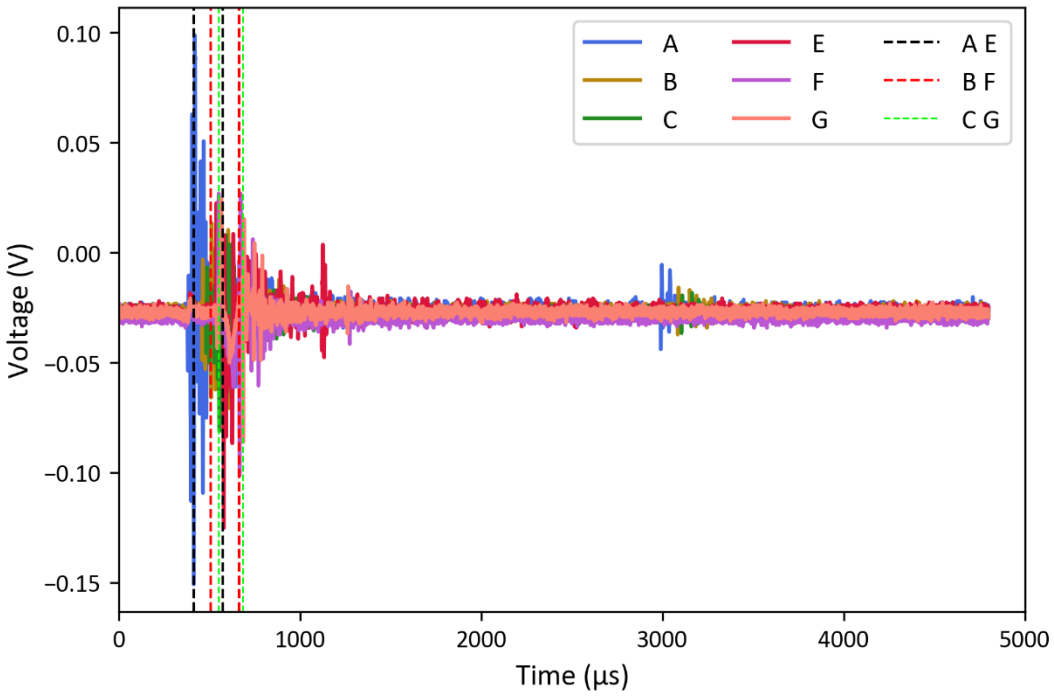

Fig. A22: Full acoustic signals for shot Dec.10. The incident projectile speed was ~ 4 km s^{-1}.

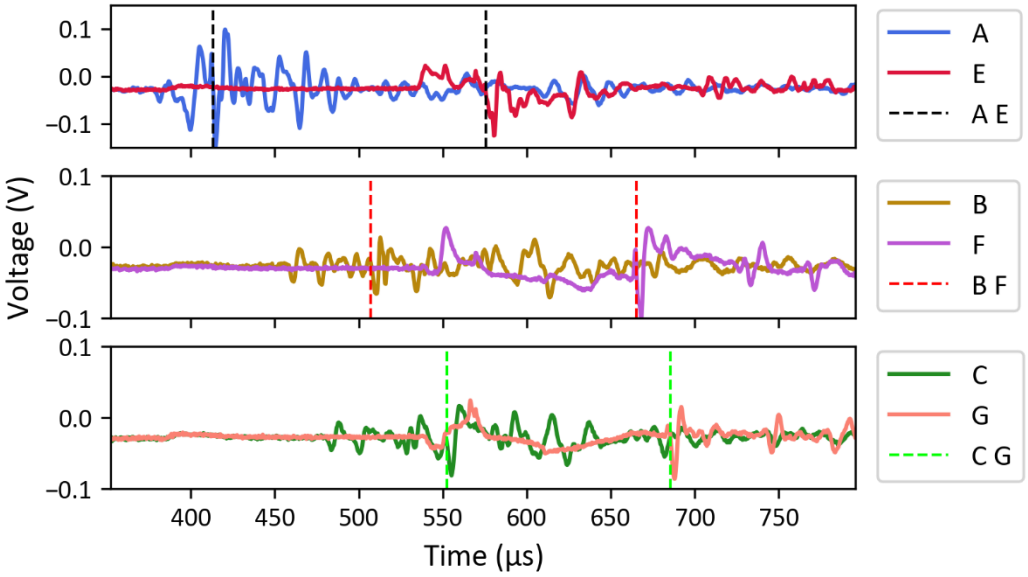

Fig. A23: The key time period of acoustic signals in shot Dec.10. The incident projectile speed was ~ 4 km s^{-1}.

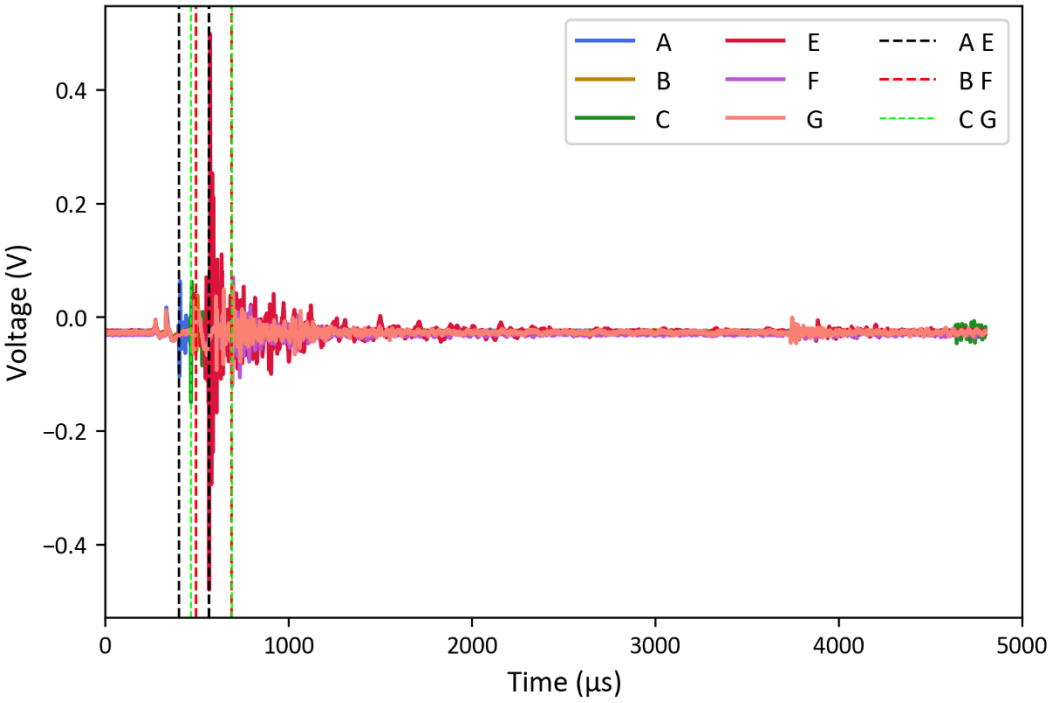

Fig. A24: Full acoustic signals for shot Dec.11. The incident projectile speed was ~ 4 km s^{-1}.

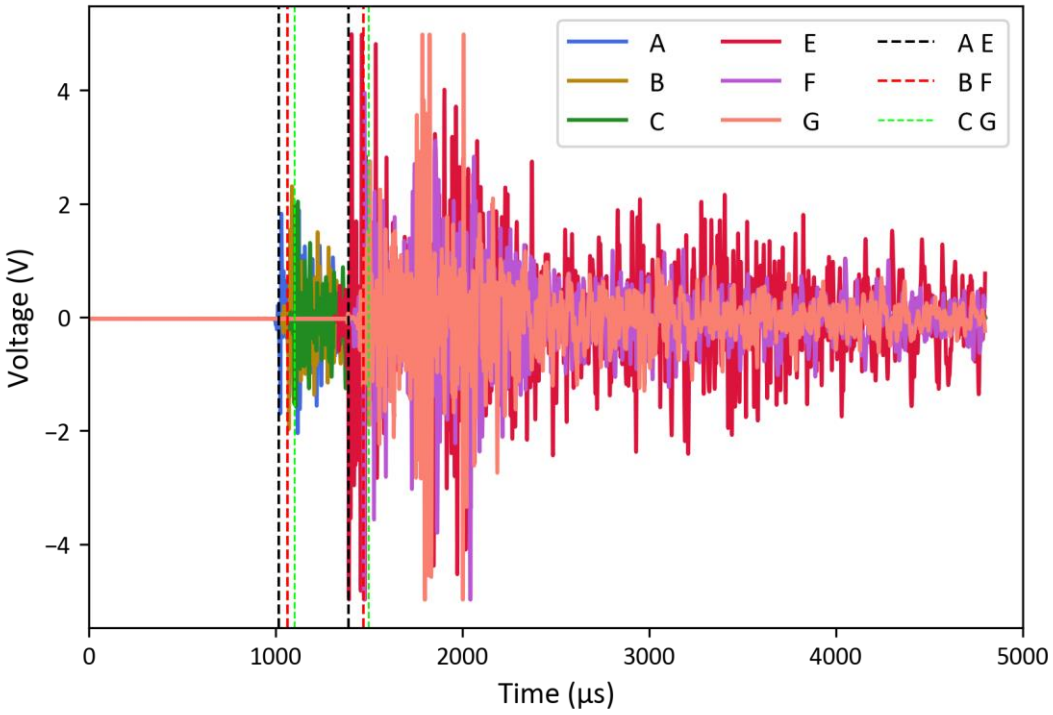

Fig. A25: Full acoustic signals for shot Dec.12. The incident projectile speed was ~ 2 km s^{-1}.

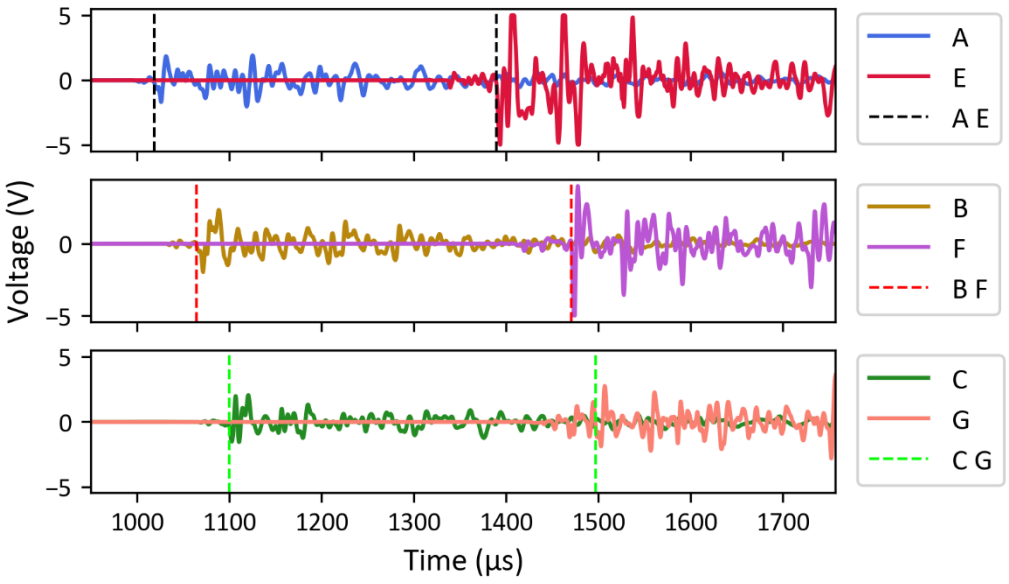

Fig. A26: The key time period of acoustic signals in shot Dec.12. The incident projectile speed was ~ 2 km s^{-1}.

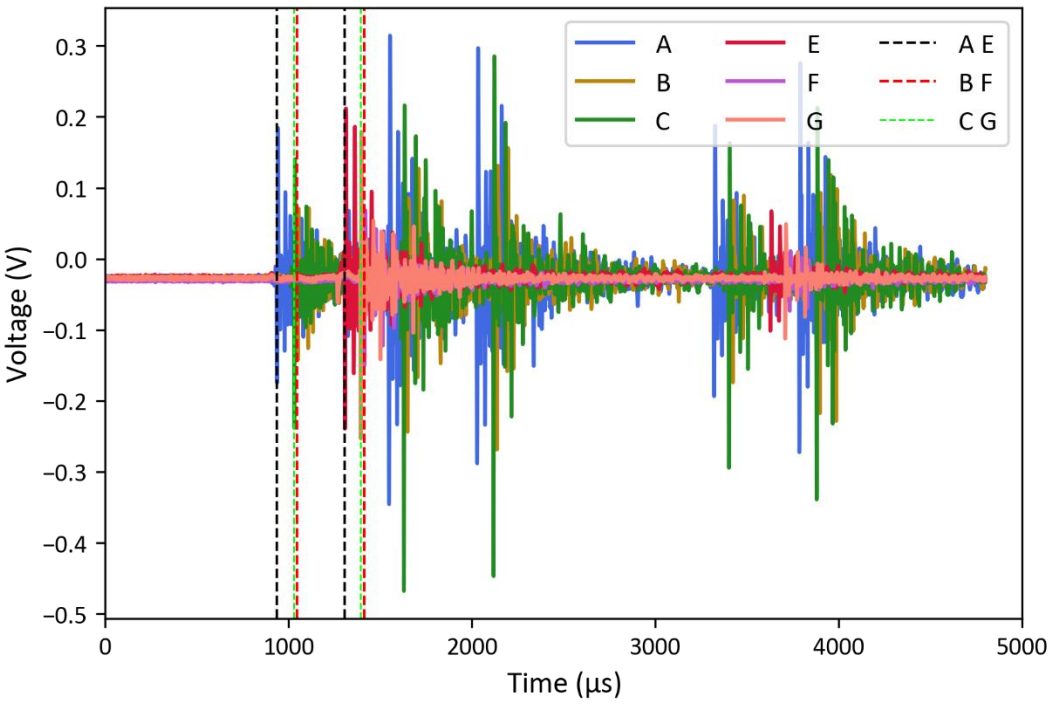

Fig. A27: Full acoustic signals for shot Dec.13. The incident projectile speed was ~ 2 km s^{-1}.

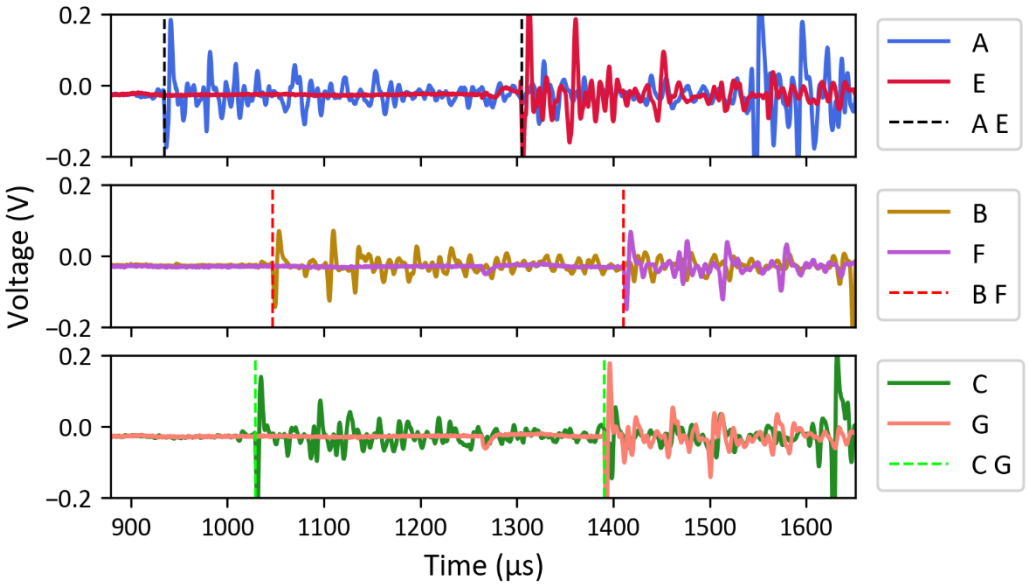

Fig. A28: The key time period of acoustic signals in shot Dec.13. The incident projectile speed was ~ 2 km s^{-1}.

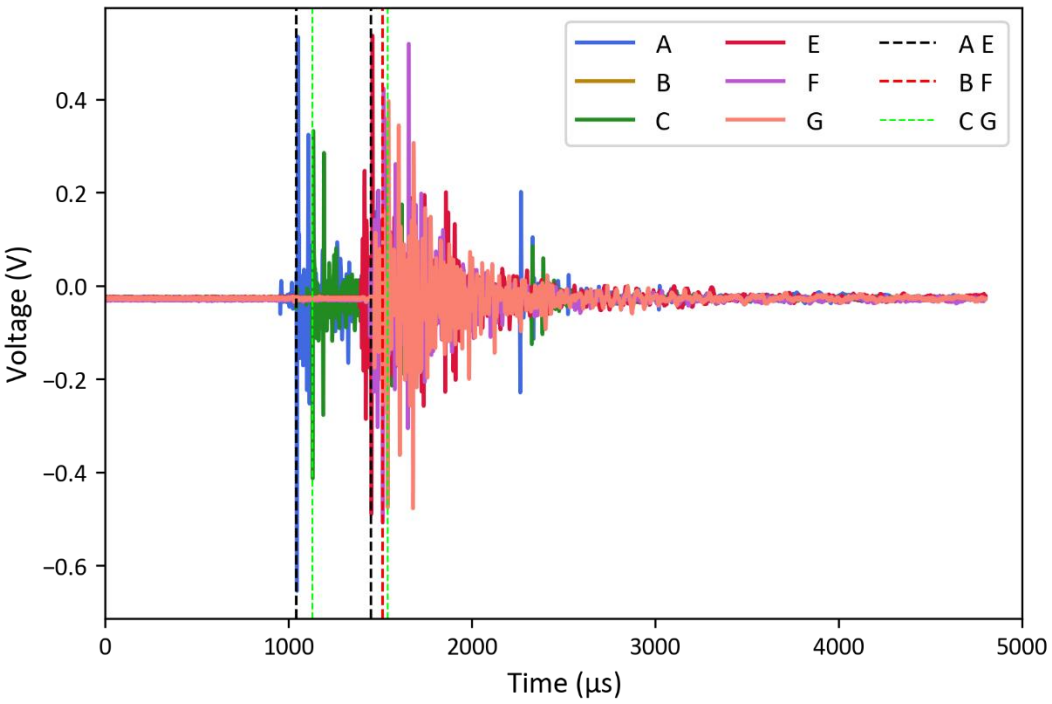

Fig. A29: Full acoustic signals for shot Dec.14. The incident projectile speed was ~ 2 km s^{-1}.

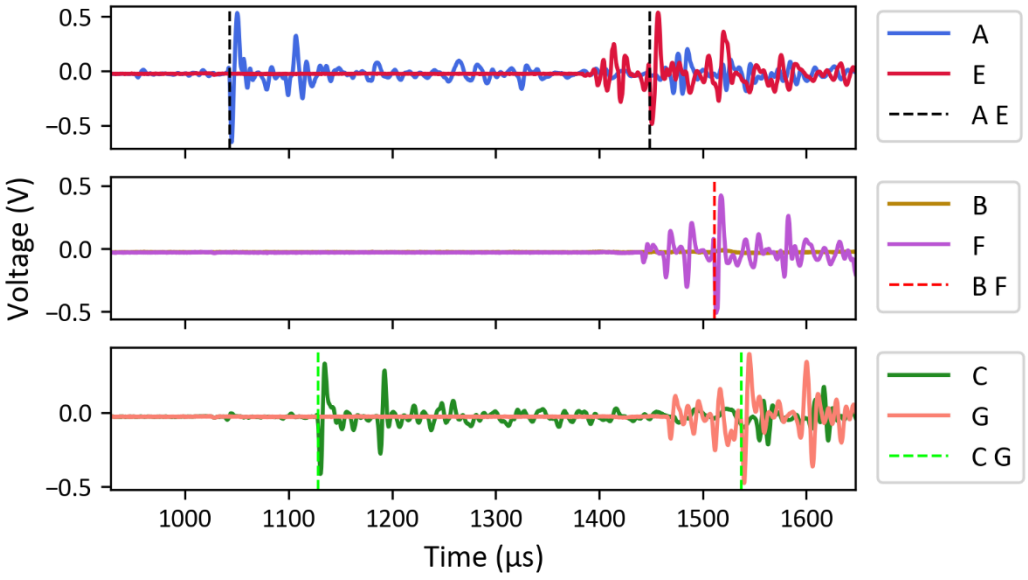

Fig. A30: Full acoustic signals for shot Dec.14. The incident projectile speed was ~ 2 km s^{-1}.

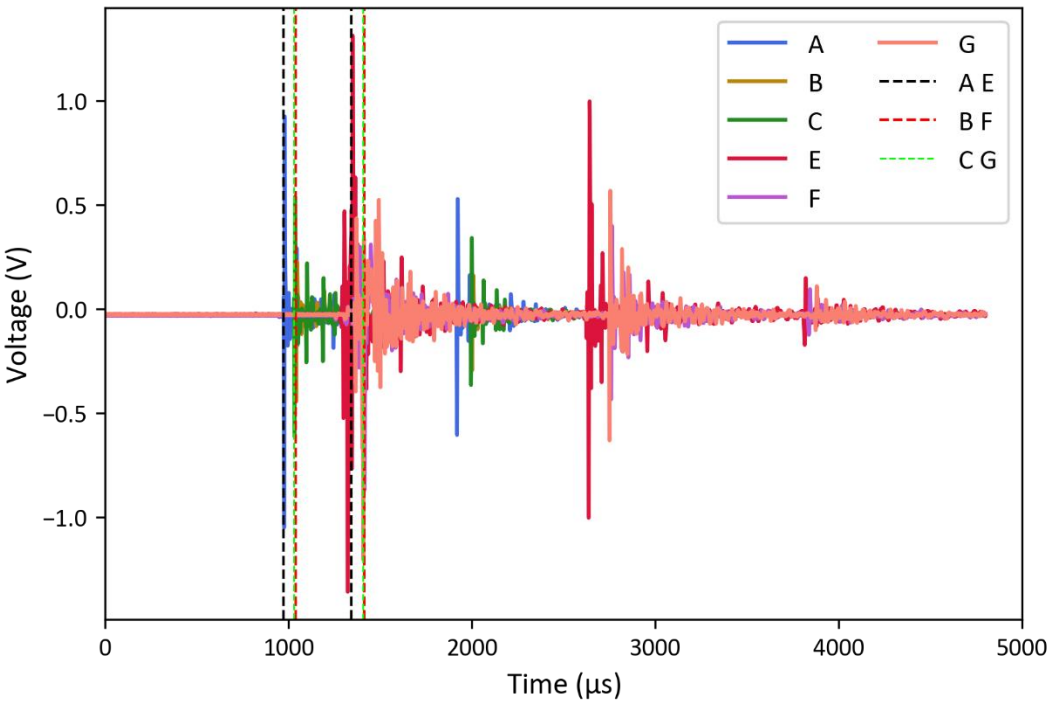

Fig. A31: Full acoustic signals for shot Dec.15. The incident projectile speed was ~ 2 km s^{-1}.

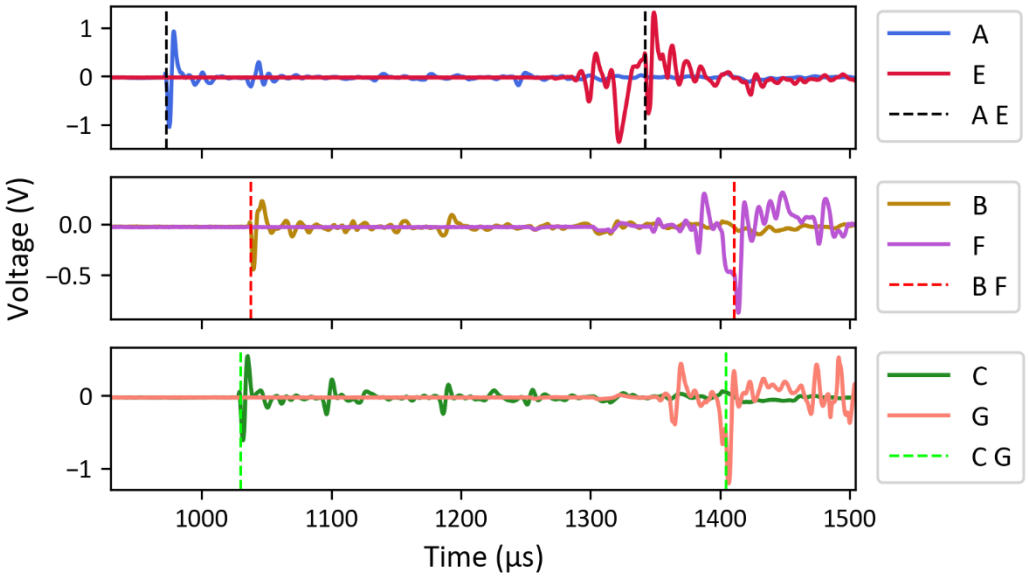

Fig. A32: The key time period of acoustic signals in shot Dec.15. The incident projectile speed was ~ 2 km s^{-1}.

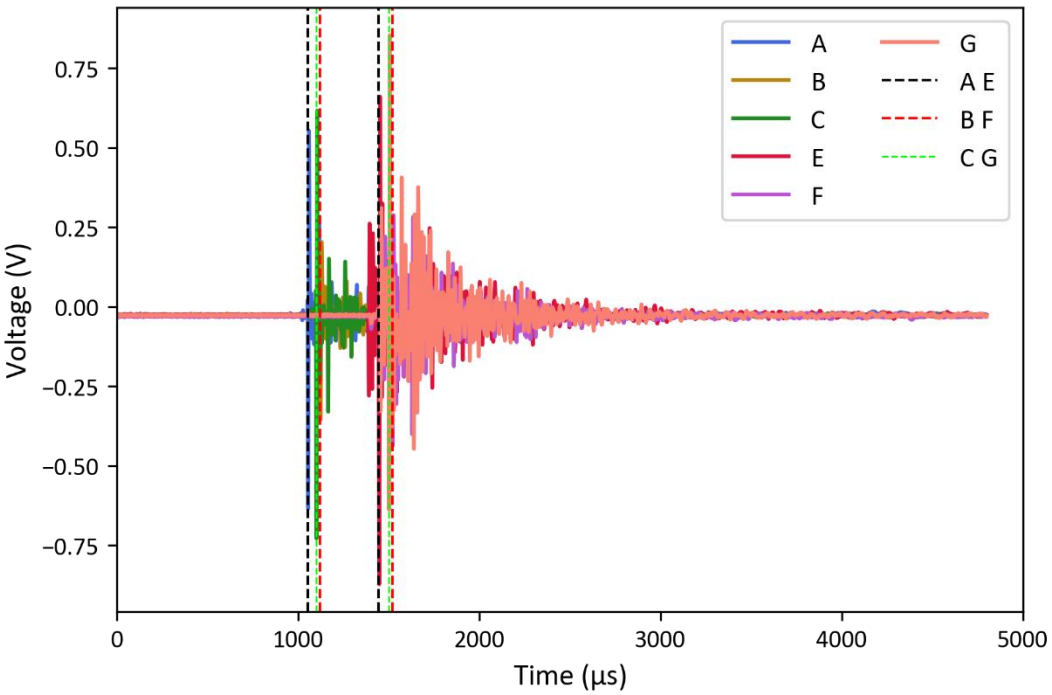

Fig. A33: Full acoustic signals for shot Dec.16. The incident projectile speed was ~ 2 km s^{-1}.

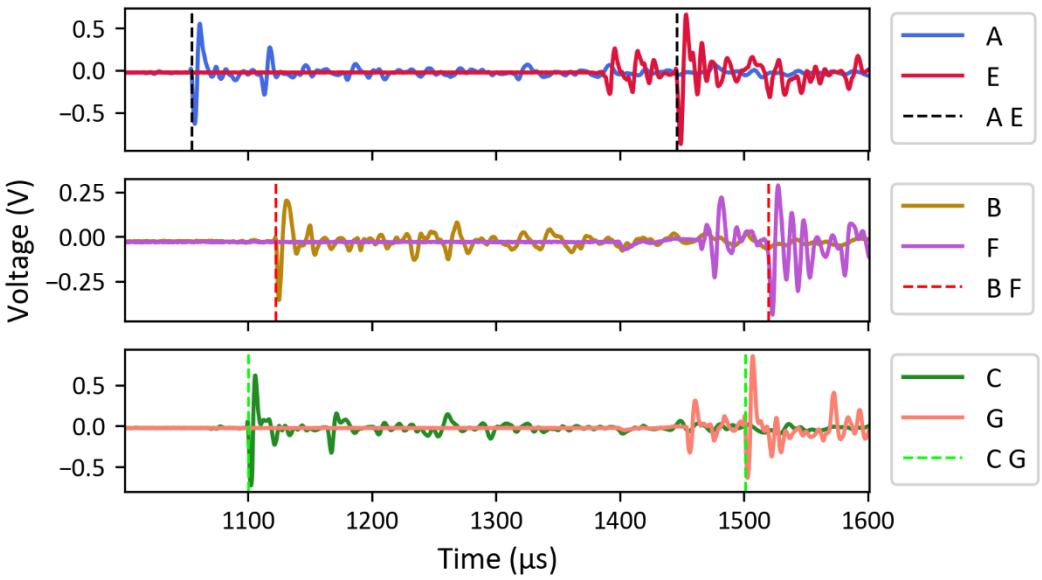

Fig. A34: The key time period of acoustic signals in shot Dec.16. The incident projectile speed was ~ 2 km s^{-1}.

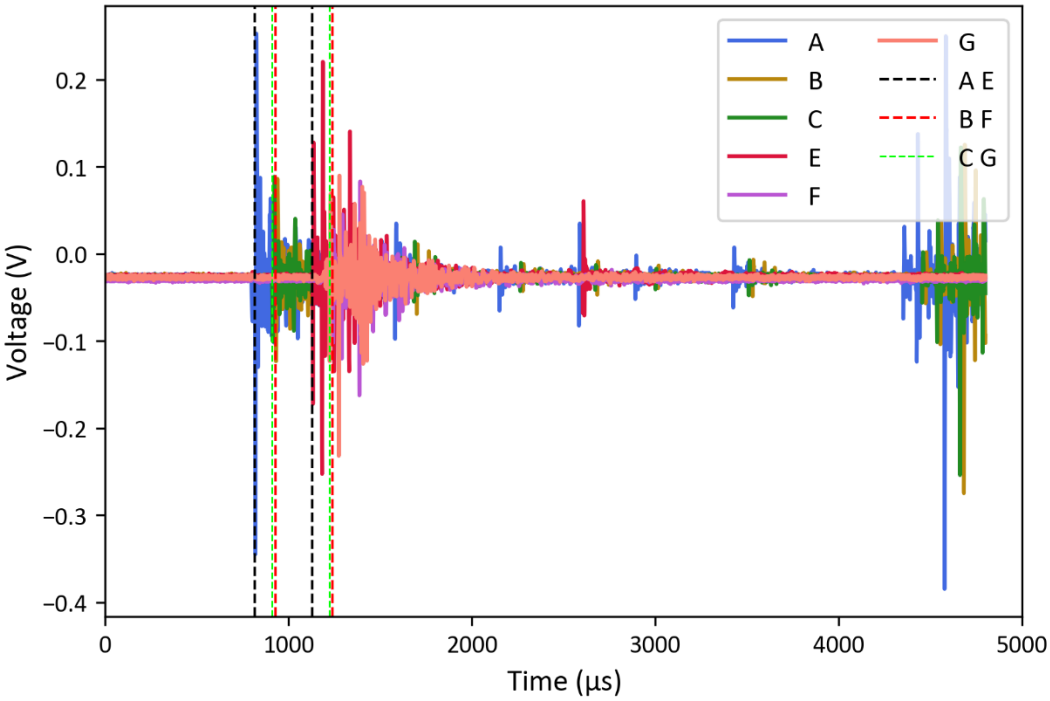

Fig. A35: Full acoustic signals for shot Dec.17. The incident projectile speed was ~ 2 km s^{-1}.

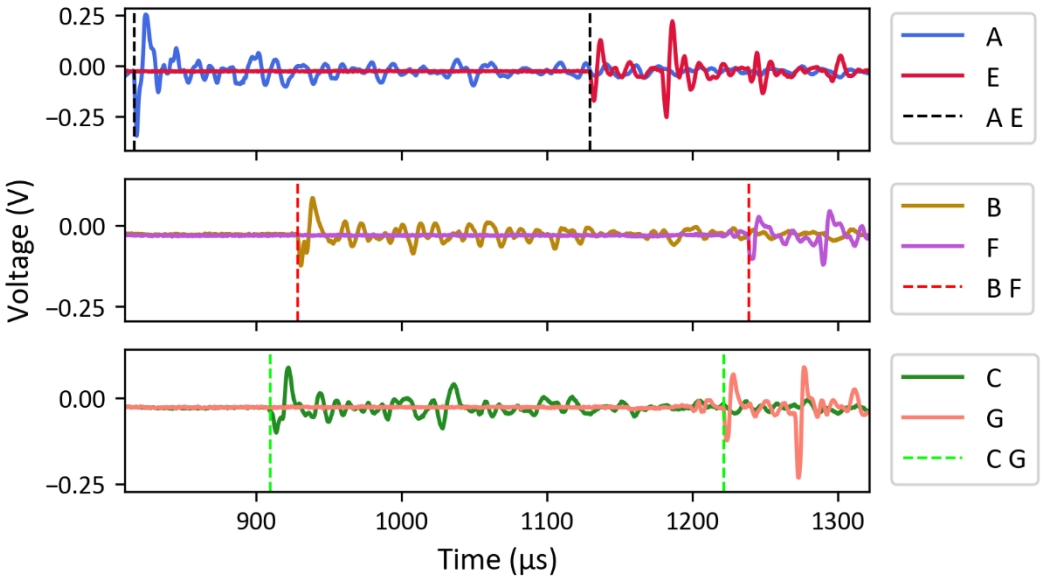

Fig. A36: The key time period of acoustic signals in shot Dec.17. The incident projectile speed was ~ 2 km s^{-1}.

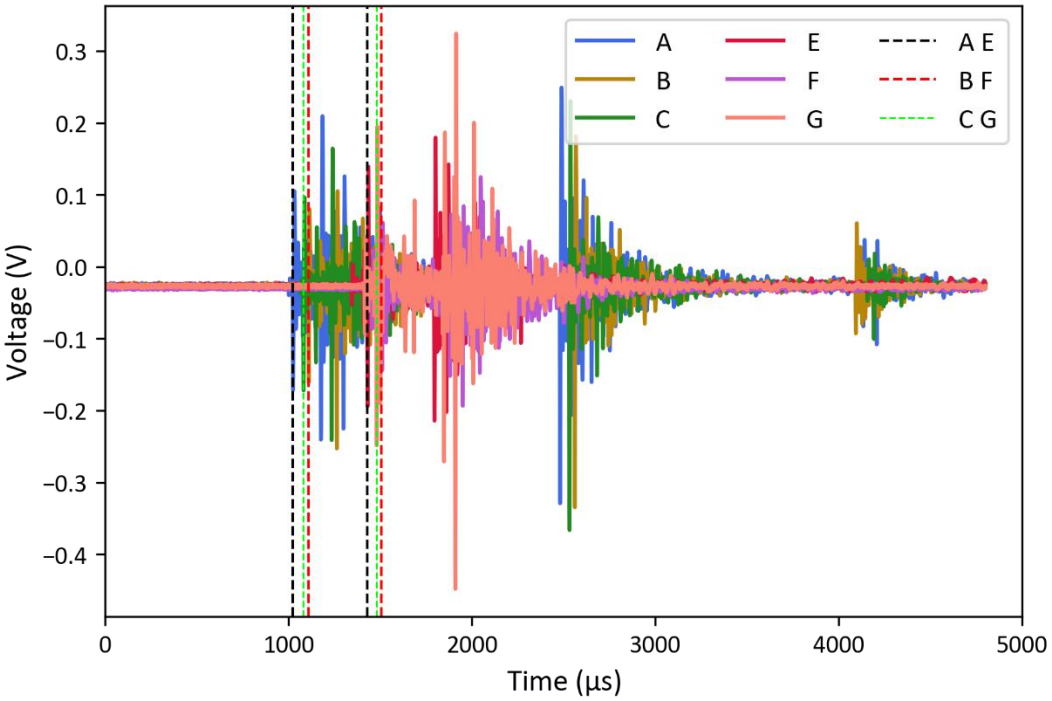

Fig. A37: Full acoustic signals for shot Dec.18. The incident projectile speed was ~ 2 km s^{-1}.

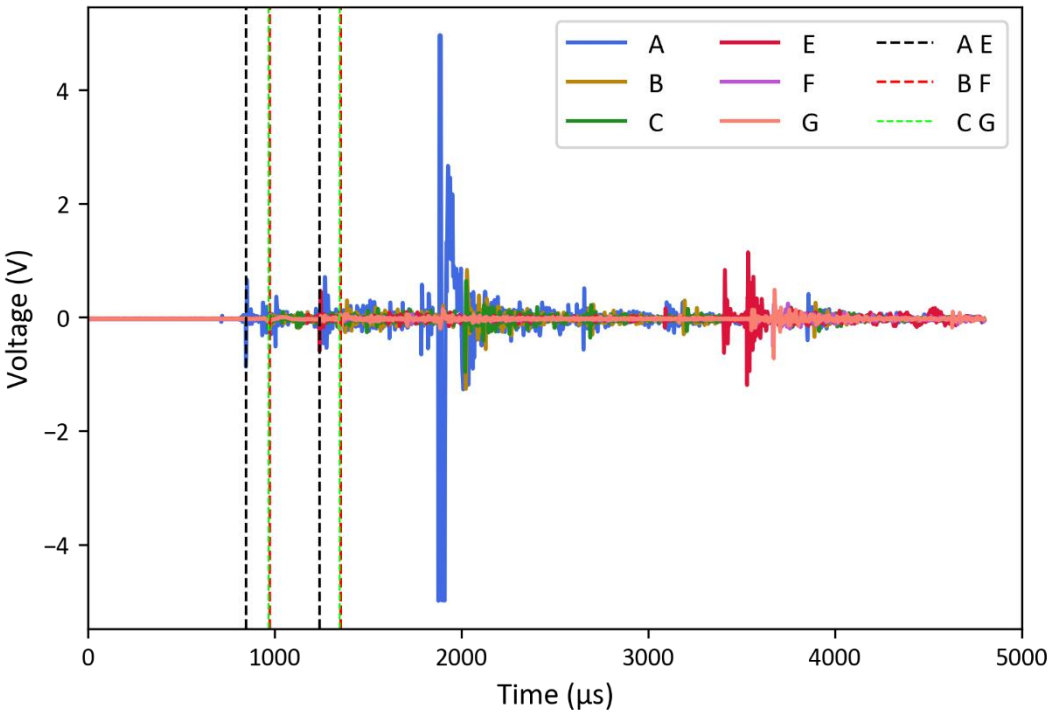

Fig. A38: Full acoustic signals for shot Dec.19. The incident projectile speed was ~ 2 km s^{-1}.

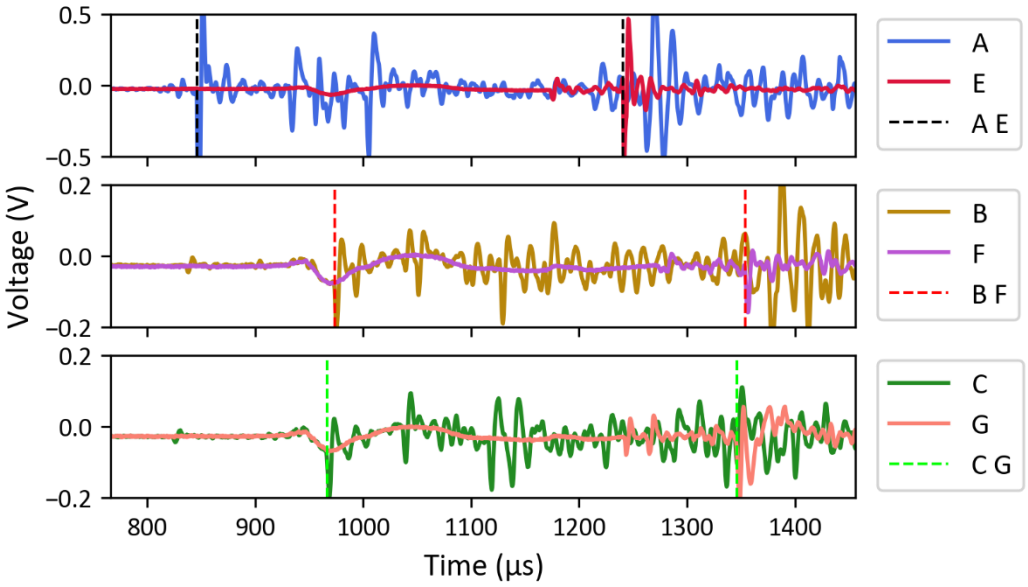

Fig. A39: The key time period of acoustic signals in shot Dec.19. The incident projectile speed was ~ 2 km s^{-1}.

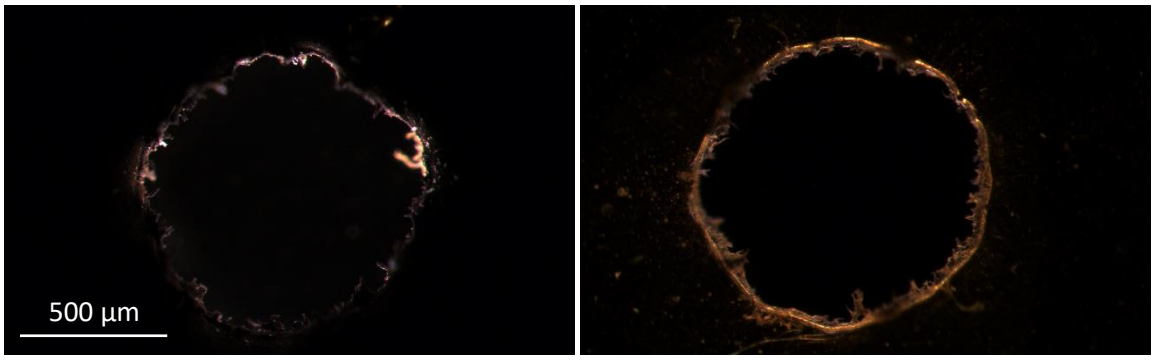

Fig. A40: Penetration holes in the first film (left) and second film (right) from shot Veri.1. The scale bar applies to both microscopy images.

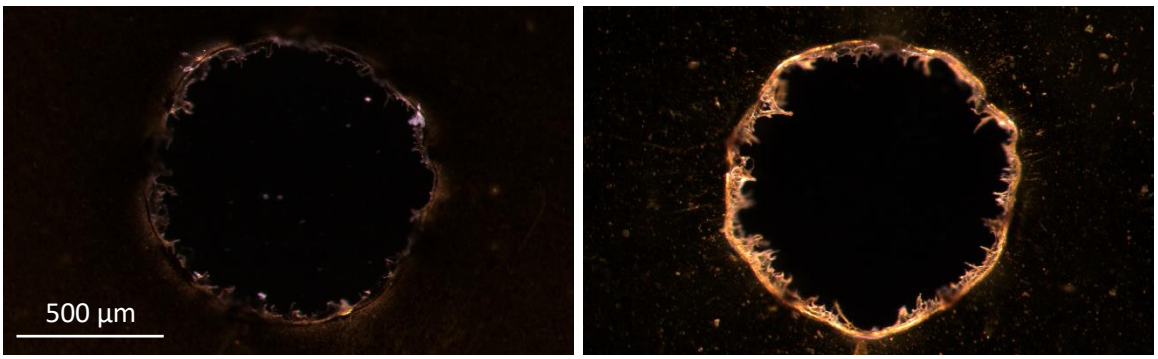

Fig. A41: Penetration holes in the first film (left) and second film (right) from shot Veri.3. The scale bar applies to both microscopy images.

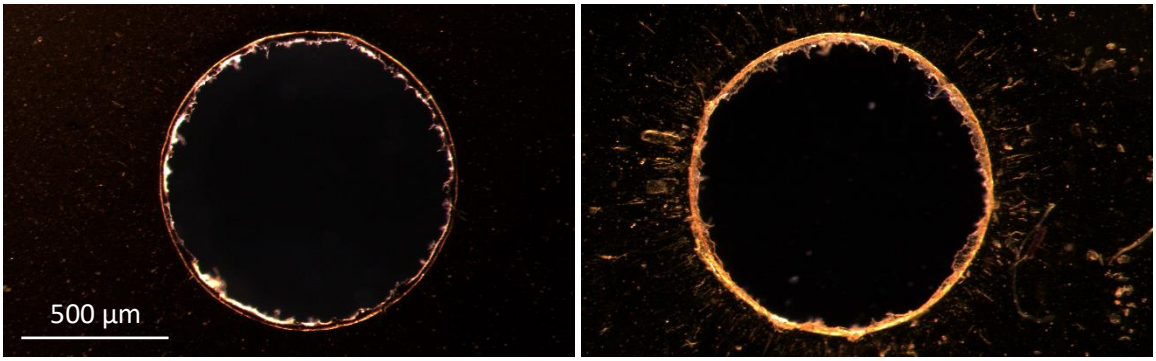

Fig. A42: Penetration holes in the first film (left) and second film (right) from shot Veri.5. The scale bar applies to both microscopy images.

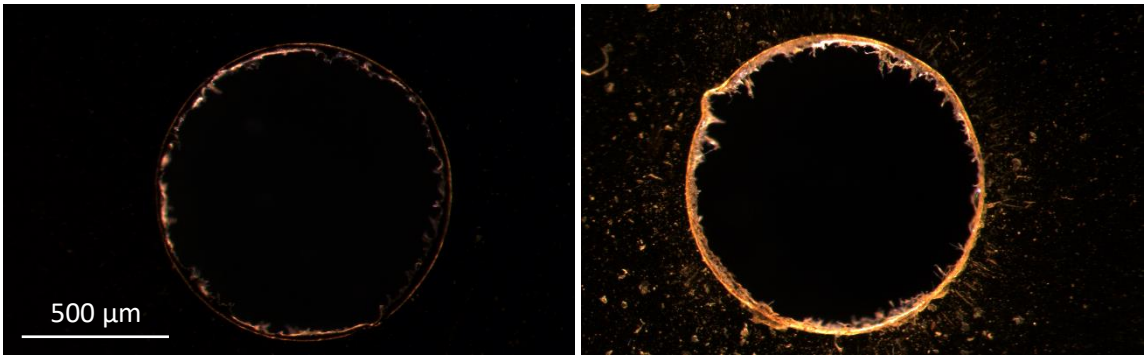

Fig. A43: Penetration holes in the first film (left) and second film (right) from shot Veri.6. The scale bar applies to both microscopy images.

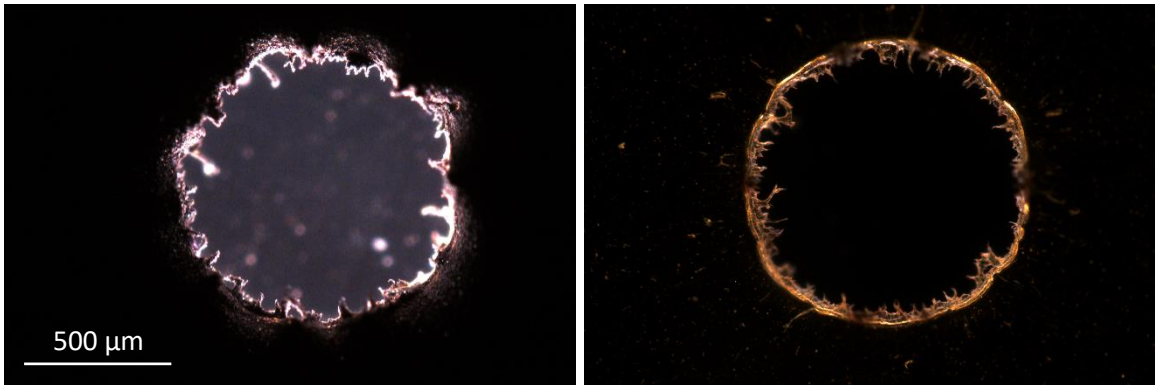

Fig. A44: Penetration holes in the first film (left) and second film (right) from shot Veri.7. The scale bar applies to both microscopy images.

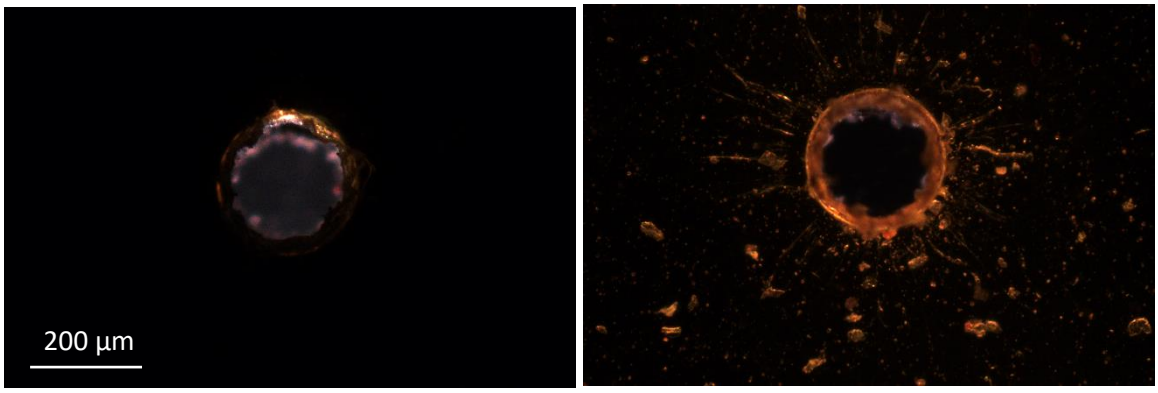

Fig. A45: Penetration holes in the first film (left) and second film (right) from shot Dec.1. The scale bar applies to both microscopy images.

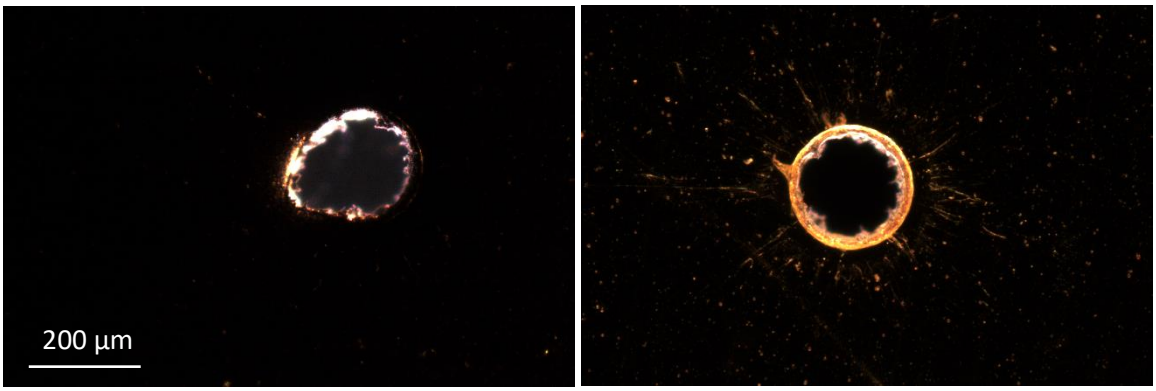

Fig. A46: Penetration holes in the first film (left) and second film (right) from shot Dec.2. The scale bar applies to both microscopy images.

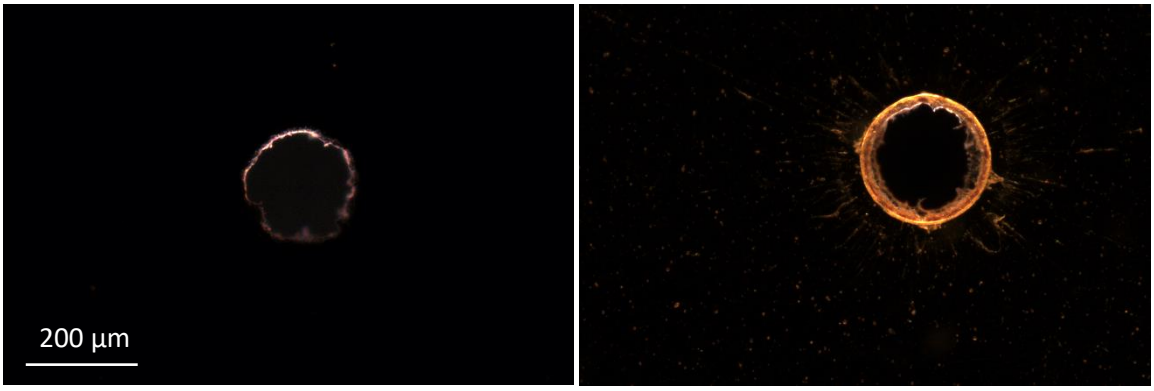

Fig. A47: Penetration holes in the first film (left) and second film (right) from shot Dec.3. The scale bar applies to both microscopy images.

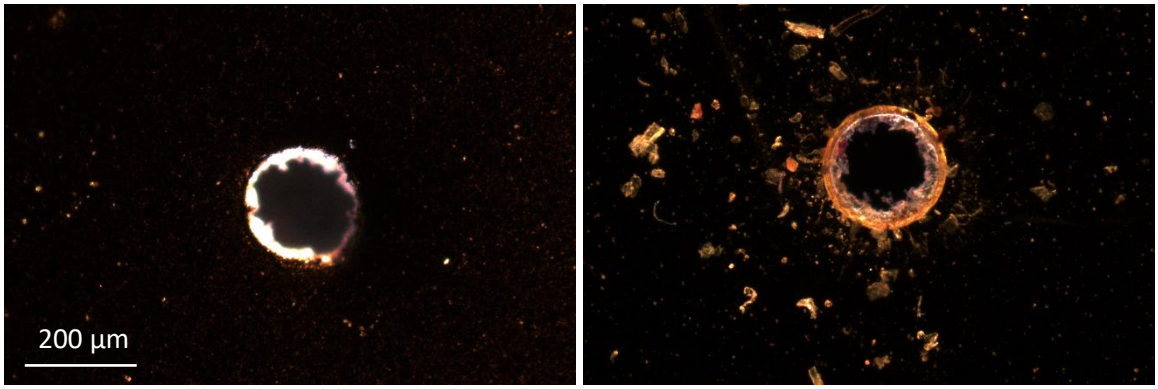

Fig. A48: Penetration holes in the first film (left) and second film (right) from shot Dec.4. The scale bar applies to both microscopy images. Note that the second film picked up significant contaminant residue from around the lab, on the front of the film. This did not significantly affect the measurement of penetration feature measurements, however the rear view of the penetration hole has been included in Fig. A48 for reference.

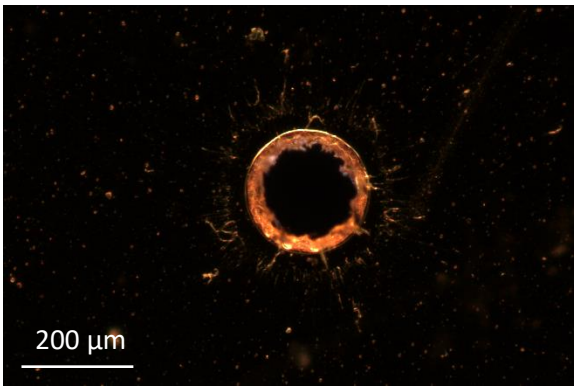

Fig. A49: Penetration hole in the second film from shot Dec.4, viewed from the rear of the film.

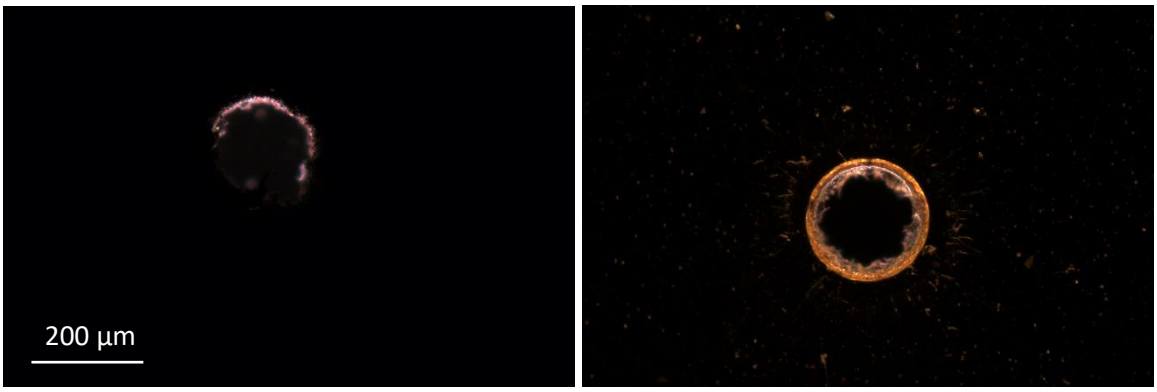

Fig. A50: Penetration holes in the first film (left) and second film (right) from shot Dec.5. The scale bar applies to both microscopy images.

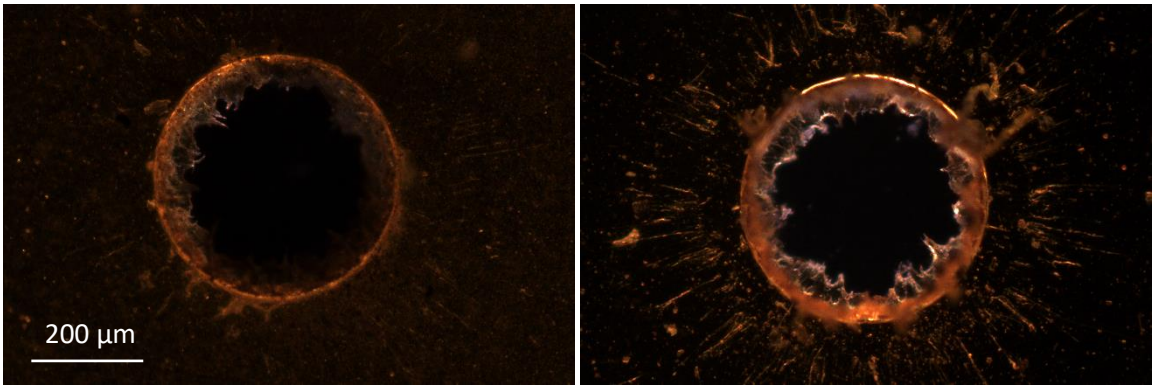

Fig. A51: Penetration holes in the first film (left) and second film (right) from shot Dec.6. The scale bar applies to both microscopy images.

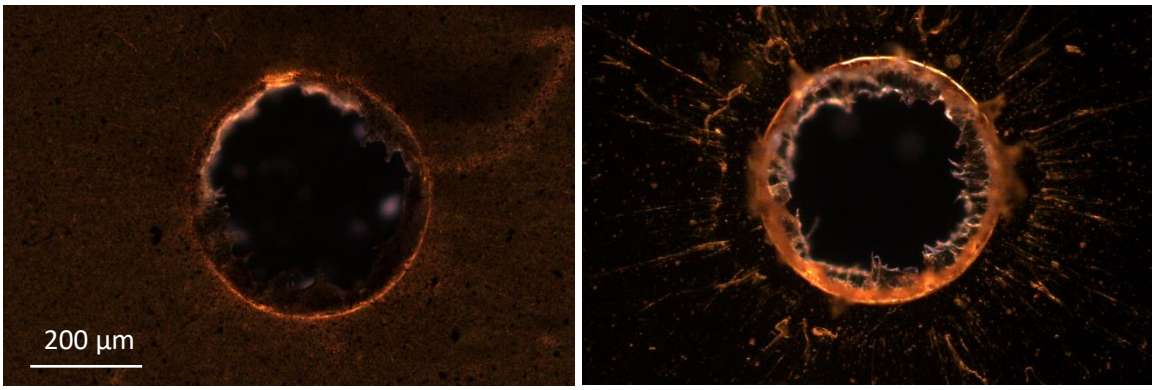

Fig. A52: Penetration holes in the first film (left) and second film (right) from shot Dec.7. The scale bar applies to both microscopy images.

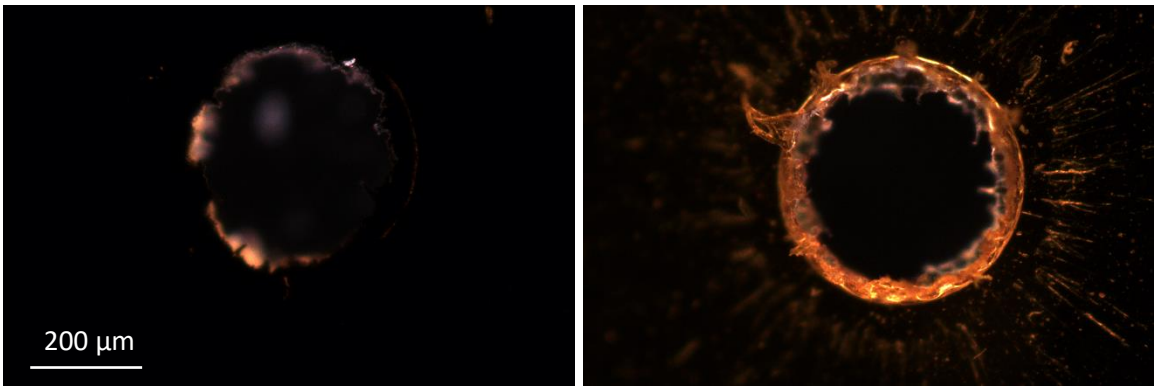

Fig. A53: Penetration holes in the first film (left) and second film (right) from shot Dec.8. The scale bar applies to both microscopy images.

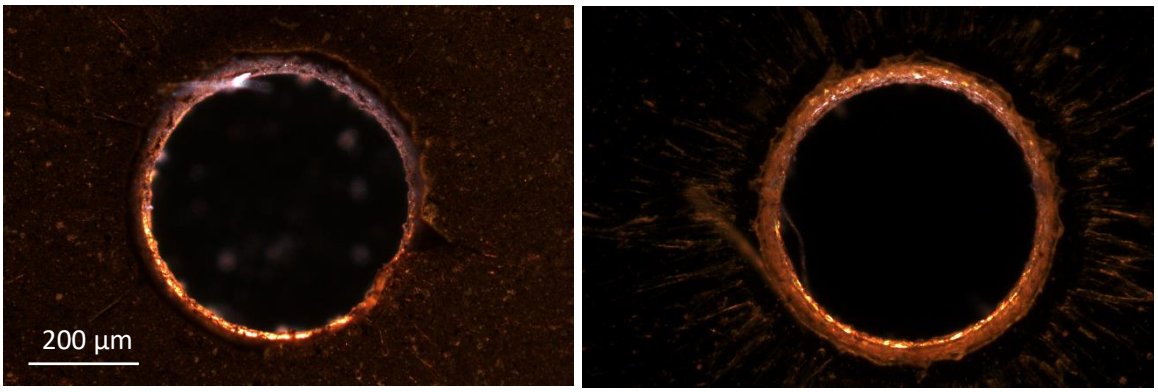

Fig. A54: Penetration holes in the first film (left) and second film (right) from shot Dec.9. The scale bar applies to both microscopy images.

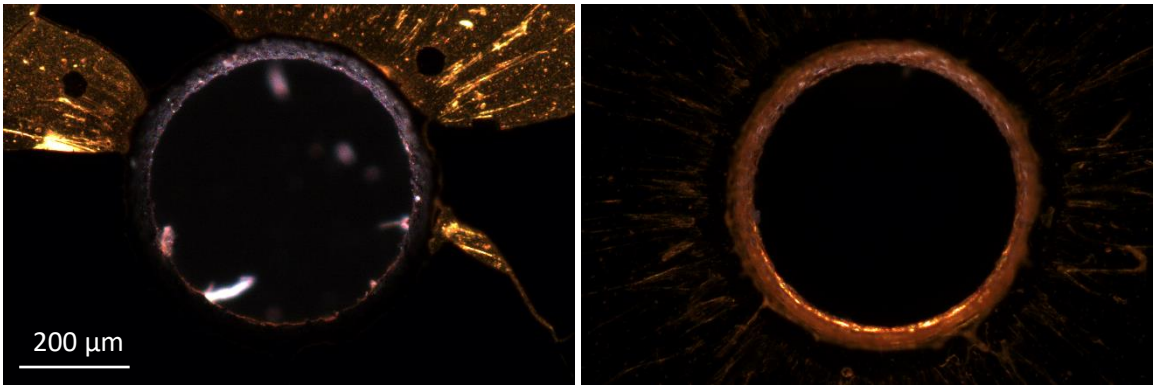

Fig. A55: Penetration holes in the first film (left) and second film (right) from shot Dec.10. The scale bar applies to both microscopy images. Note some of the powder deposited on the first film flaked off, exposing the Kapton below.

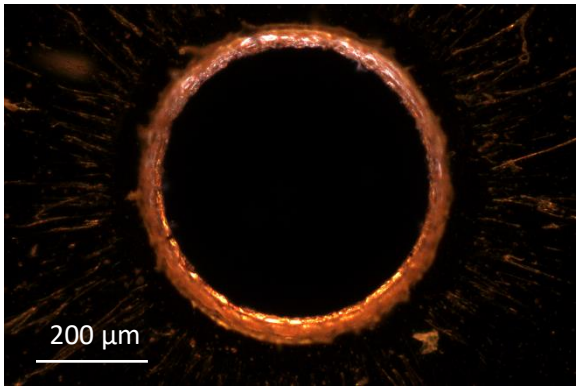

Fig. A56: Penetration hole in the second film from shot Dec.11.

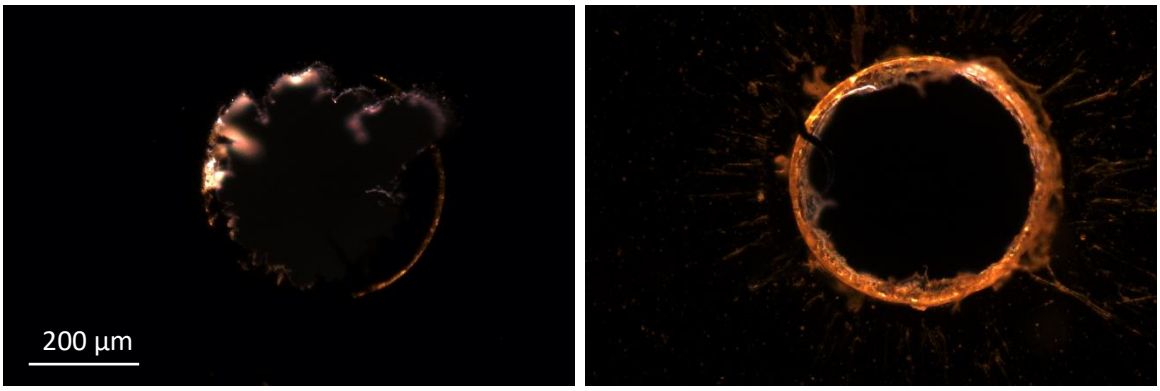

Fig. A57: Penetration holes in the first film (left) and second film (right) from shot Dec.12. The scale bar applies to both microscopy images.

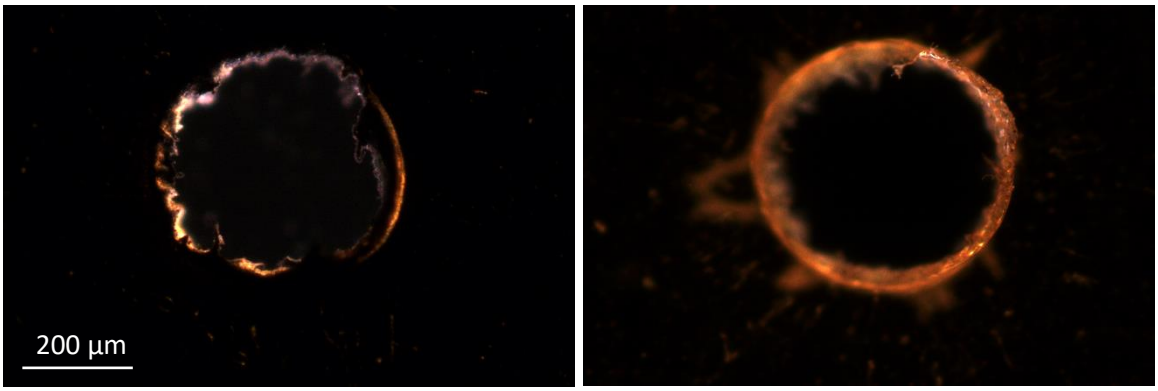

Fig. A58: Penetration holes in the first film (left) and second film (right) from shot Dec.13, with the image focused on the top lip. The scale bar applies to both microscopy images.

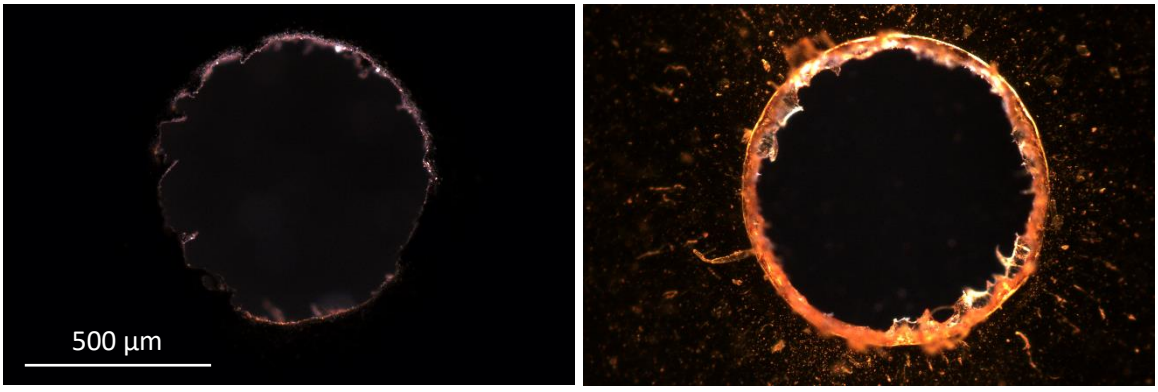

Fig. A59: Penetration holes in the first film (left) and second film (right) from shot Dec.14. The scale bar applies to both microscopy images.

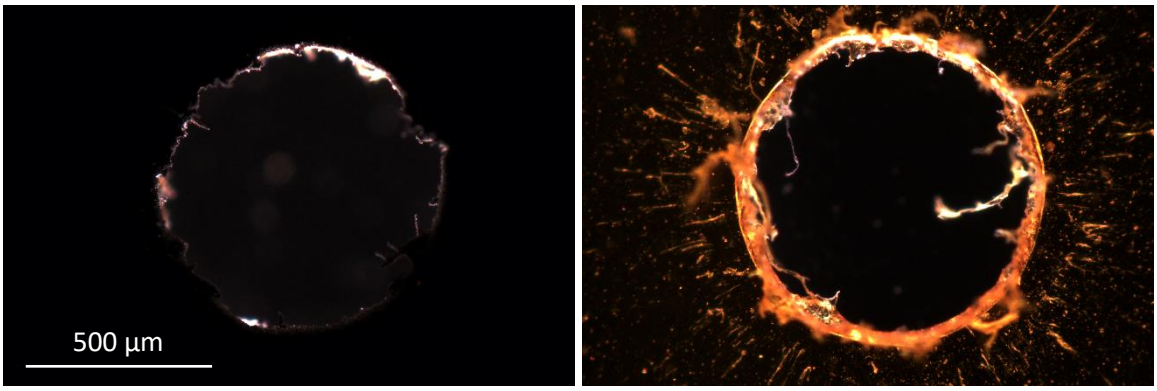

Fig. A60: Penetration holes in the first film (left) and second film (right) from shot Dec.15. The scale bar applies to both microscopy images. Note the strand greatly extending into the centre of the penetration hole is thought to be a contaminant fibre caught on the edge of the penetration hole.

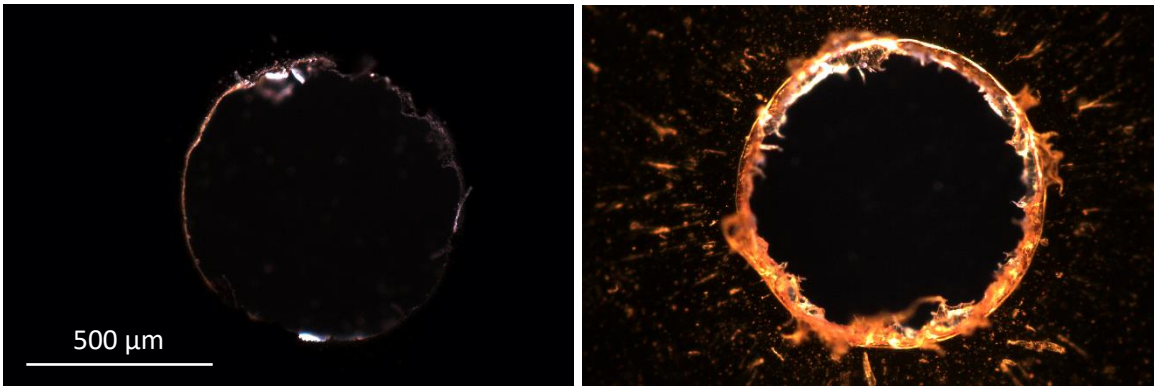

Fig. A61: Penetration holes in the first film (left) and second film (right) from shot Dec.16. The scale bar applies to both microscopy images.

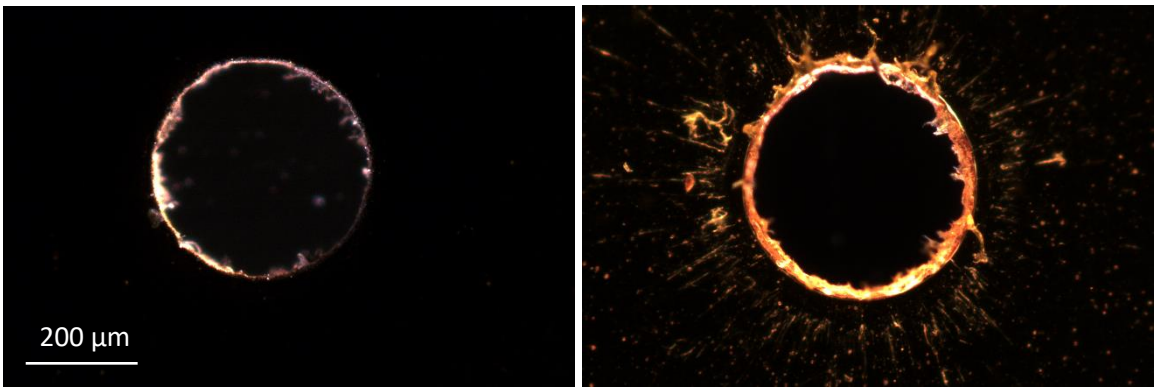

Fig. A62: Penetration holes in the first film (left) and second film (right) from shot Dec.17. The scale bar applies to both microscopy images.

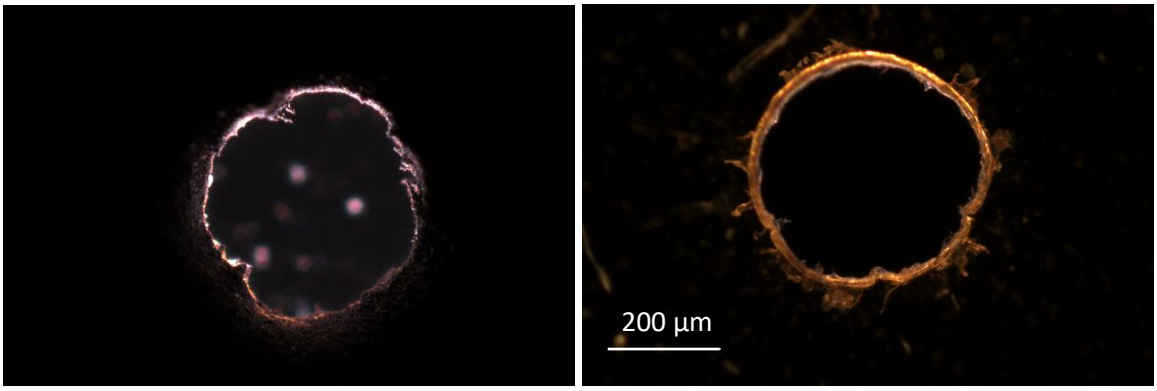

Fig. A63: Penetration holes in the first film (left) and second film (right) from shot Dec.18. The scale bar applies to both microscopy images.

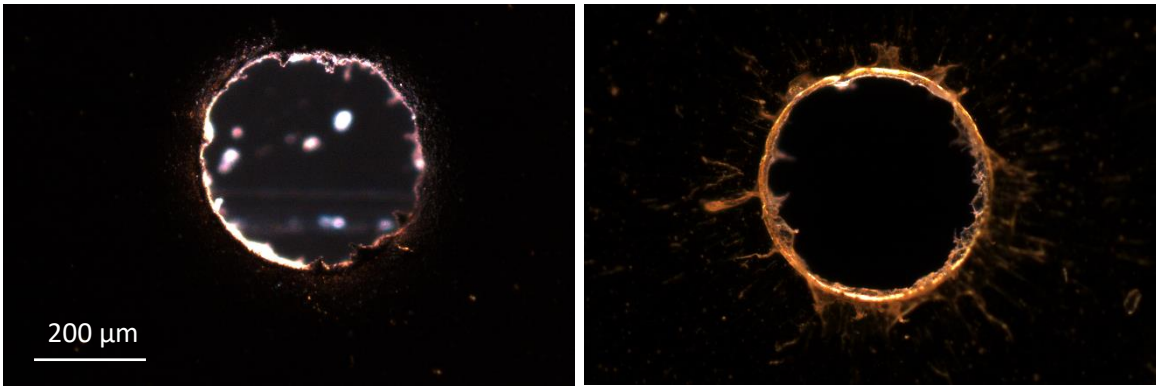

Fig. A64: Penetration holes in the first film (left) and second film (right) from shot Dec.19. The scale bar applies to both microscopy images.

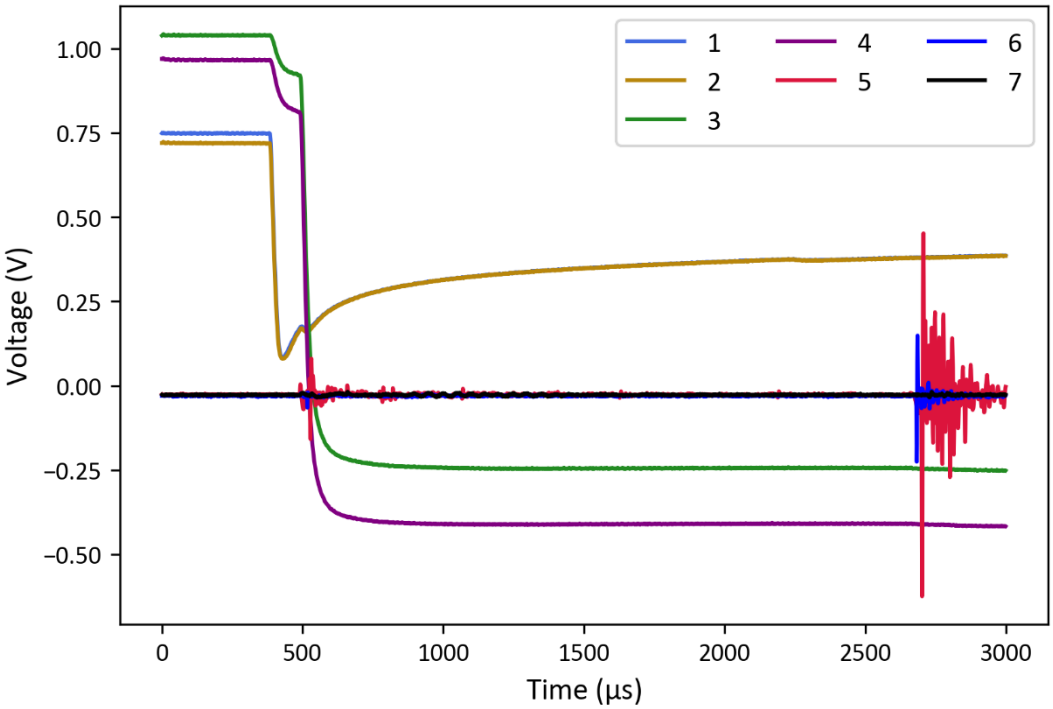

Fig. A65: Photodiode (1 – 4) and PVDF (5 – 7) signals recorded for shot Light.2. The shot speed was ~ 5 km s^{-1}.

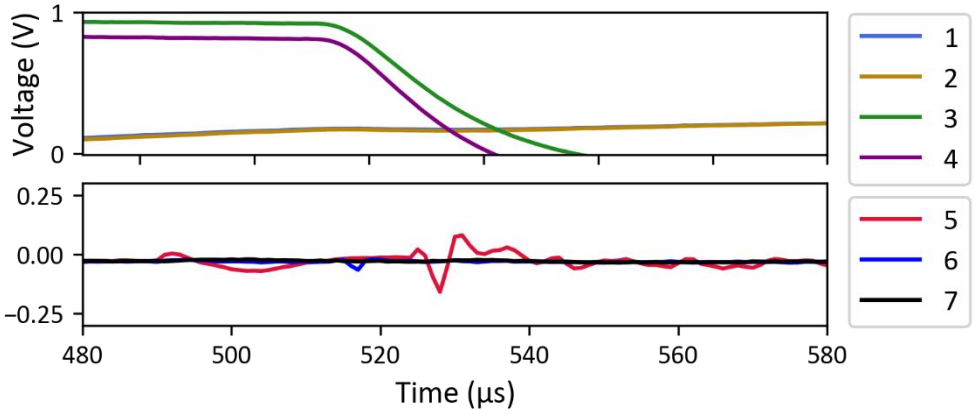

Fig. A66: Key time period of photodiode (1 – 4) and PVDF (5 – 7) signals recorded for shot Light.2. The shot speed was ~ 5 km s^{-1}.

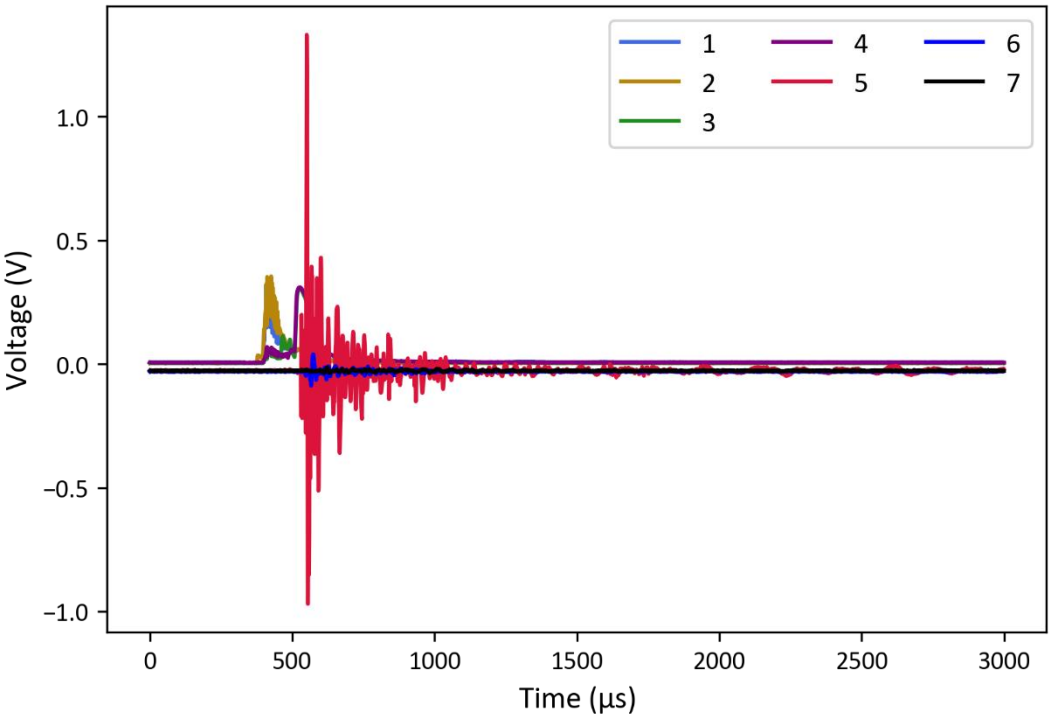

Fig. A67: Photodiode (1 – 4) and PVDF (5 – 7) signals recorded for shot Light.3. The shot speed was ~ 5 km s^{-1}. Note PVDF sensor 6 started to fail.

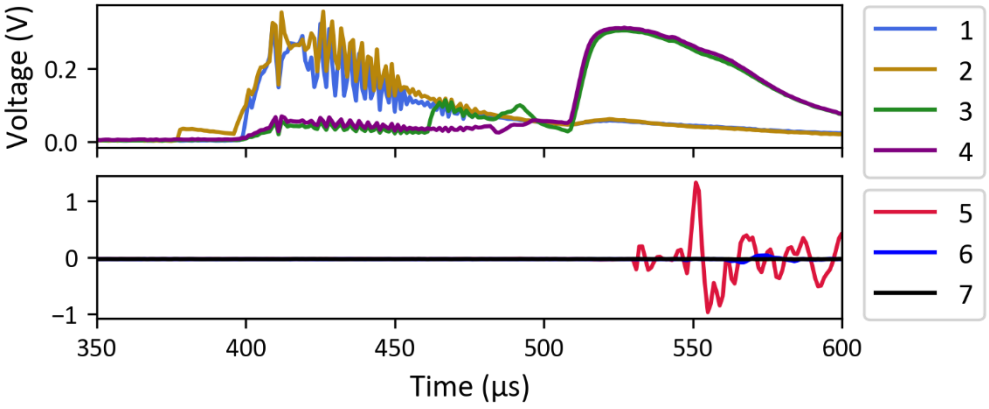

Fig. A68: Key time period of photodiode (1 – 4) and PVDF (5 – 7) signals recorded for shot Light.3. The shot speed was ~ 5 km s^{-1}. Note PVDF sensor 6 started to fail.

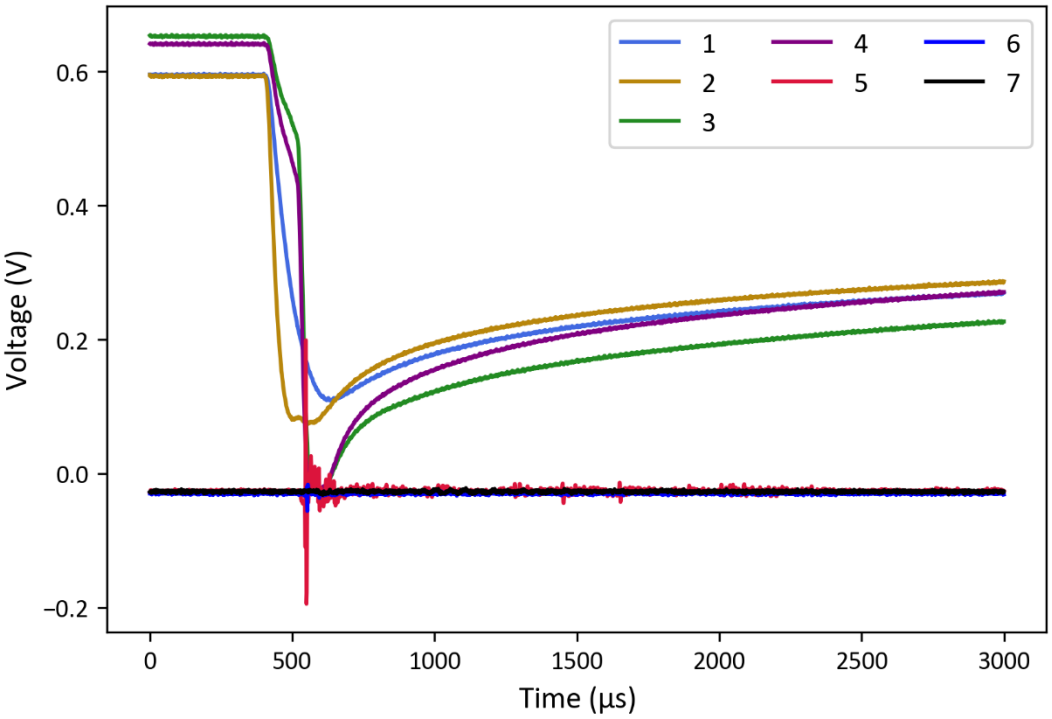

Fig. A69: Photodiode (1 – 4) and PVDF (5 – 7) signals recorded for shot Light.4. The shot speed was ~ 5 km s^{-1}. Note PVDF sensor 6 started to fail.

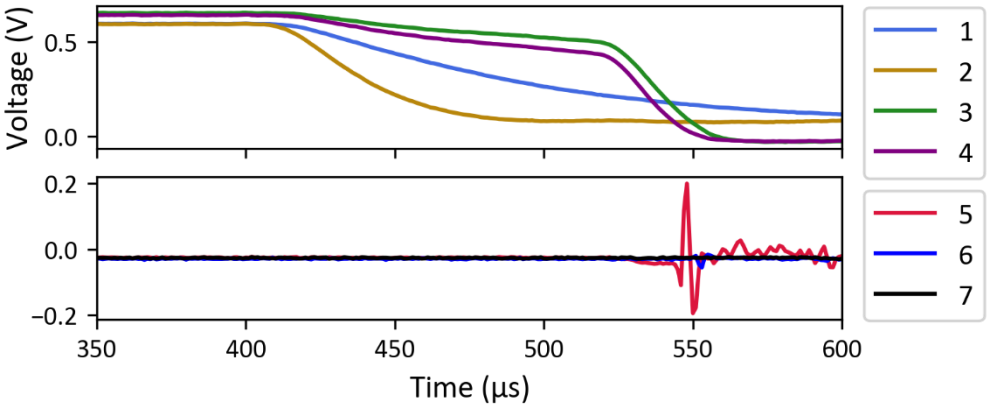

Fig. A70: Key time period of photodiode (1 – 4) and PVDF (5 – 7) signals recorded for shot Light.4. The shot speed was ~ 5 km s^{-1}. Note PVDF sensor 6 started to fail.

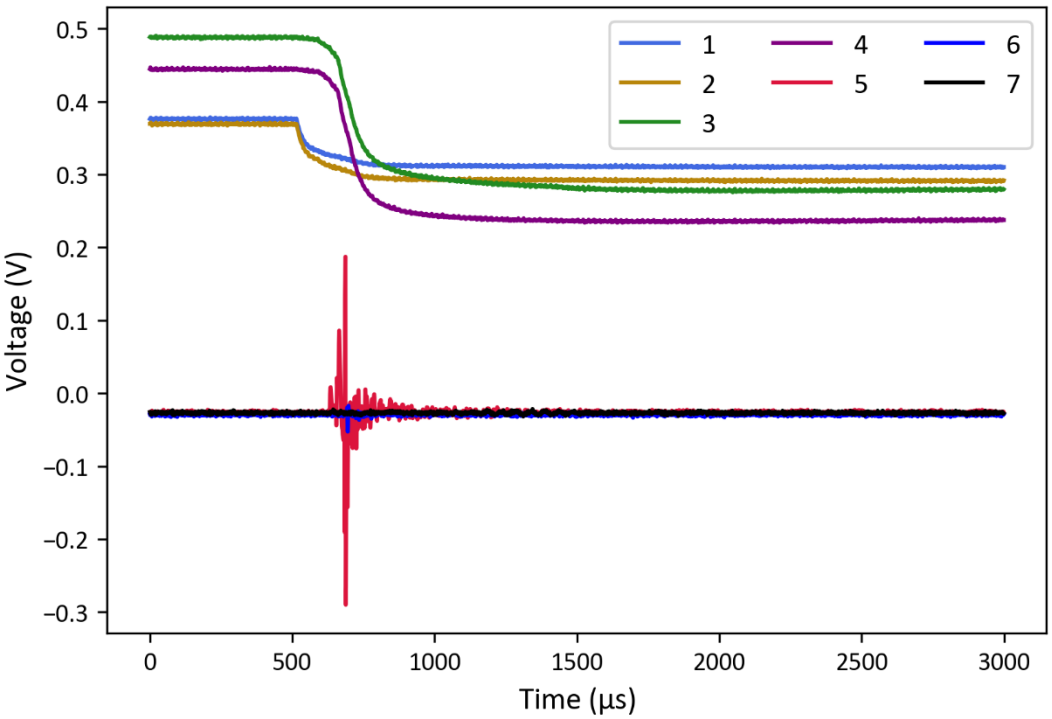

Fig. A71: Photodiode (1 – 4) and PVDF (5 – 7) signals recorded for shot Light.5. The shot speed was ~ 4 km s^{-1}. Note PVDF sensor 6 started to fail.

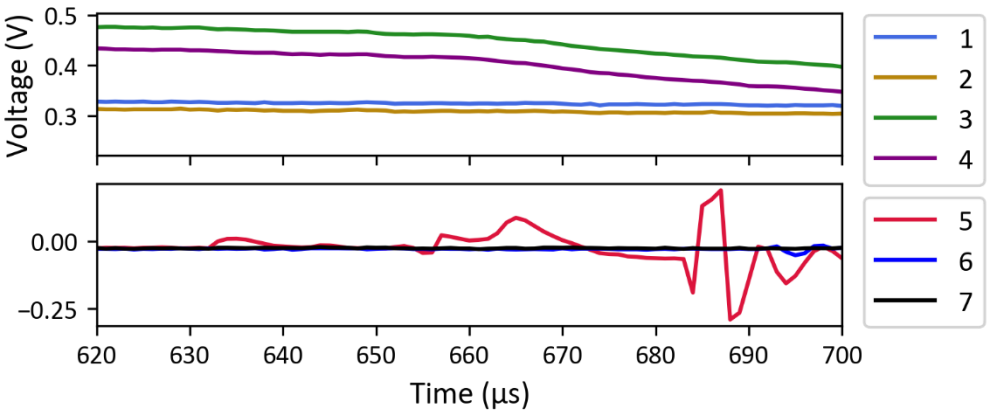

Fig. A72: Key time period of photodiode (1 – 4) and PVDF (5 – 7) signals recorded for shot Light.5. The shot speed was ~ 4 km s^{-1}. Note PVDF sensor 6 started to fail.

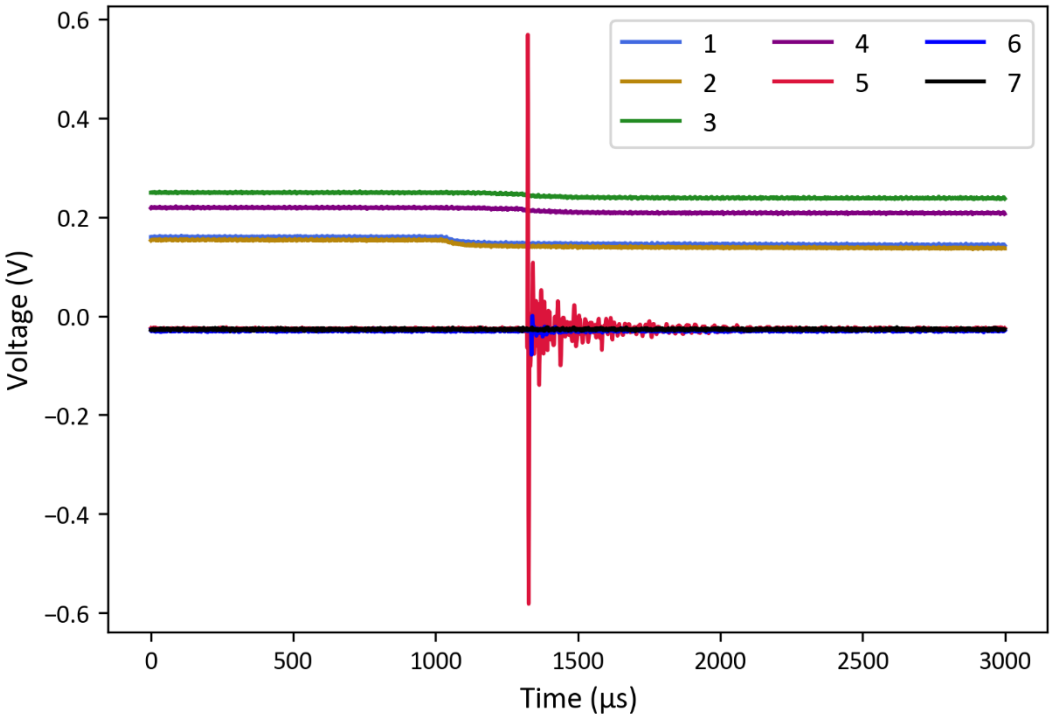

Fig. A73: Photodiode (1 – 4) and PVDF (5 – 7) signals recorded for shot Light.6. The shot speed was ~ 2 km s^{-1}. Note PVDF sensor 6 started to fail.

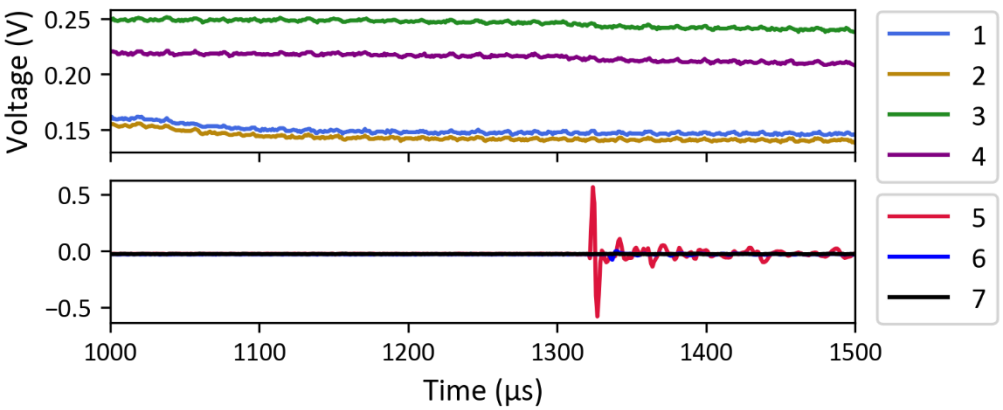

Fig. A74: Key time period of photodiode (1 – 4) and PVDF (5 – 7) signals recorded for shot Light.6. The shot speed was ~ 2 km s^{-1}. Note PVDF sensor 6 started to fail.

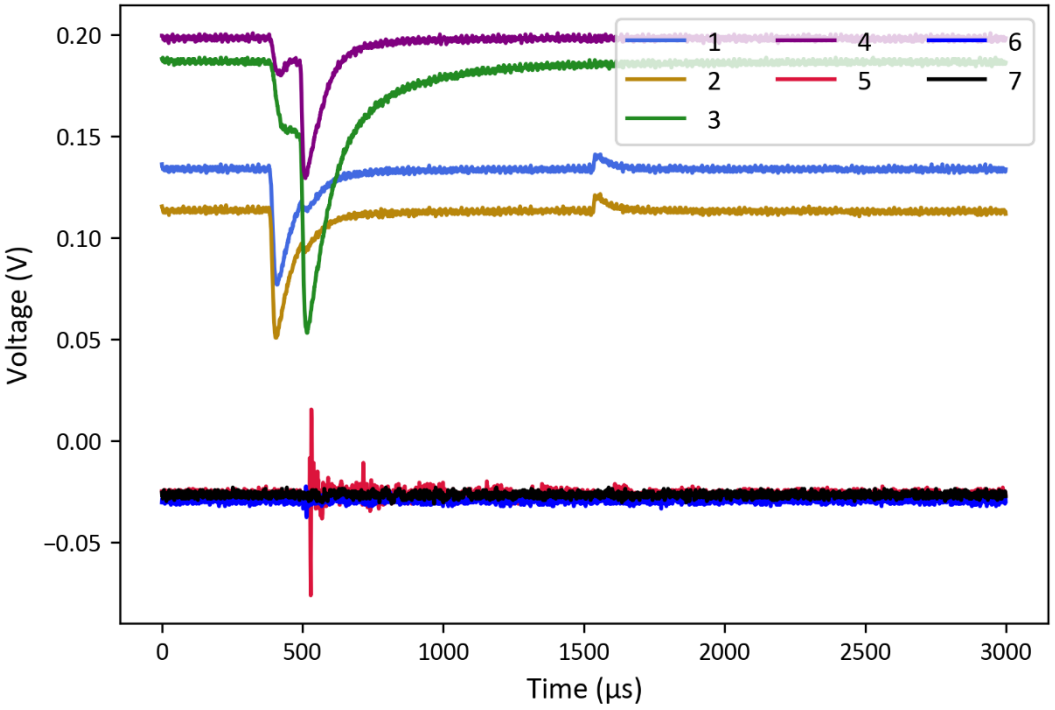

Fig. A75: Photodiode (1 – 4) and PVDF (5 – 7) signals recorded for shot Light.7. The shot speed was ~ 5 km s^{-1}. Note PVDF sensor 6 started to fail.

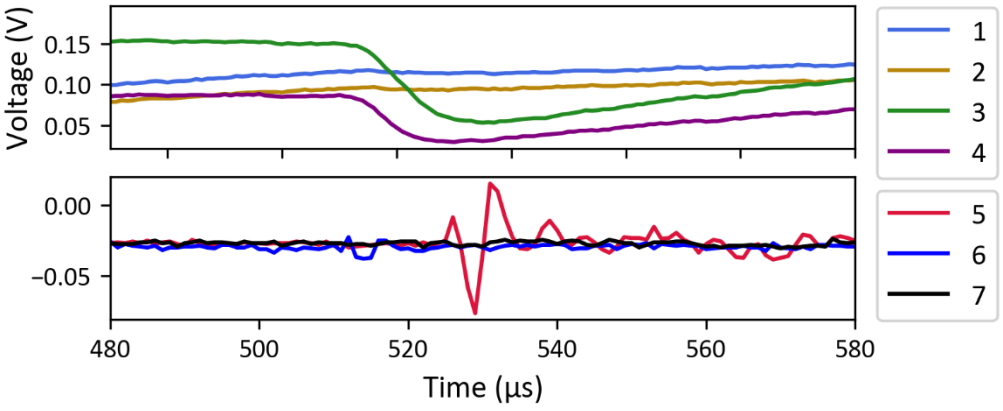

Fig. A76: Key time period of photodiode (1 – 4) and PVDF (5 – 7) signals recorded for shot Light.7. The shot speed was ~ 5 km s^{-1}. Note PVDF sensor 6 started to fail.

Appendix II

This appendix contains supplementary information, including the derivation of the scaling equality for projectile mass (m_p) and film mass (m_f) when scaling film thickness (f) and projectile diameter (d_p) by a factor of two, the python code used to implement the autonomous signal onset algorithm described in Chapter 5, the average flux (averaged over all faces) vs. diameter data for the different sizes of CubeSat discussed in Chapter 6.

Equality of m_f/m_p When Scaling d_p and f by a Factor of Two 249

Python Code to Implement the Autonomous Signal Onset Detection Algorithm 250

Fig. A77 Average flux (averaged over all faces) vs. diameter for a 1U CubeSat. 253

Fig. A78 Average flux (averaged over all faces) vs. diameter for a 1.5U CubeSat. 253

Fig. A79 Average flux (averaged over all faces) vs. diameter for a 3U CubeSat. 254

Fig. A80 Average flux (averaged over all faces) vs. diameter for a 6U CubeSat. 254

Equality of m_f/m_p When Scaling d_p and f by a Factor of Two

The projectile mass is given by:

$$m_p = \frac{4}{3}\pi r^3 \rho_P, \tag{A1}$$

and the mass of the Kapton film removed during an impact is given by:

$$m_f = \pi r^2 \rho_{kap} \times f, \tag{A2}$$

where, ρ_p is the projectile density, ρ_{kap} is the density of Kapton, r is the radius of the projectile, and everything else is as defined above. Now if the projectile diameter and the film thickness are increased by a factor of two we get m_{2p}:

$$m_{2p} = \frac{4}{3}\pi (2r)^3 \rho_p, \tag{A3}$$

and m_{2f}:

$$m_{2f} = \pi (2r)^2 \rho_{kap} \times 2f. \tag{A4}$$

The ration m_f/m_p is thus:

$$\frac{m_f}{m_p} = \frac{\pi r^2 \rho_{kap} \times f}{\frac{4}{3}\pi r^3 \rho_p}, \tag{A5}$$

and the ration m_{2f}/m_{2p} is:

$$\frac{m_{2f}}{m_{2p}} = \frac{\pi (2r)^2 \rho_{kap} \times 2f}{\frac{4}{3}\pi (2r)^3 \rho_p} = \frac{8}{8}\frac{\pi r^2 \rho_{kap} \times f}{\frac{4}{3}\pi r^3 \rho_p} = \frac{\pi r^2 \rho_{kap} \times f}{\frac{4}{3}\pi r^3 \rho_p}. \tag{A6}$$

The equivalence of Eq. A5 and Eq. A6 shows that scaling the d_p and f by a factor of two leads to the same ratio of m_f/m_p and thus a direct scaling of m_f to m_p.

Python Code to Implement the Autonomous Signal Onset Detection Algorithm

Below is the Python code to implement the autonomous signal onset detection algorithm described in Chapter 5. Were the peak search and the running integral is applied to a sensor trace, only one trace (sensor A) is shown as an example. The same code is applied to each of the traces in the full algorithm.

Raw signal data acquisition:

```
import numpy as np
#Extracts data from the .lvm file
mydtype = np.dtype([("X",float),("Dev2_ai0",float),("Dev2_ai1",float),("Dev2_ai2",float),("Dev2_ai3",float),
                    ("Dev2_ai4",float),("Dev2_ai5",float),("Dev2_ai6",float),("Dev2_ai7",float)])
#!!!!!ai7 changed to 5 becasue output H was used instead of F.
def readcsv_np(filename):
    a = np.genfromtxt(filename,skip_header=20,dtype=mydtype,usecols=[0,1,2,3,4,5,6,7,8])
    return a

A = readcsv_np('Veri.1.lvm') # place cvs file name in the '  ' here.
def createlist(r1,r2,s): # list has to be a function of time steps associated with each trace.
    return np.arange(r1, r2, s)

X = createlist(0, 4.7996e-3, 0.4e-6  ) #X = createlist(0 , 4.7996e-3, 0.4e-6) #X cordinates
#print(X)
XuS = createlist(0, 4.7996e3, 0.4  ) #XP = createlist(0, 4.7996e3, 0.4  )
```

Begin processing, find the zero point and centre:

```
#Calculate estimated time of impact
vi = vi = df.at[0,"Speed"]
Xstop = 1.90 # ~ Distance from stop plate to first film
#Use time of impact to slice list 200 us before estimated impact due to delay in triggering syste
texp = Xstop/vi
Slice = round(((texp/1e-6) - 200)*0.4)

#Use first part of trace to calculate a mean zero point, 199 becomes 200 due to :a not including c
import statistics as stats
MeanA = stats.mean(A['Dev2_ai0'][:Slice]); MeanB = stats.mean(A['Dev2_ai1'][:Slice]);
MeanC = stats.mean(A['Dev2_ai2'][:Slice]); MeanE = stats.mean(A['Dev2_ai4'][:Slice]);
MeanF = stats.mean(A['Dev2_ai5'][:Slice]); MeanG = stats.mean(A['Dev2_ai6'][:Slice])

AZero = MeanA; BZero = MeanB; CZero = MeanC; EZero = MeanE; FZero = MeanF; GZero = MeanG;

#Convert to an array
SigA = np.array(A['Dev2_ai0']); SigB = np.array(A['Dev2_ai1']); SigC = np.array(A['Dev2_ai2']);
SigE = np.array(A['Dev2_ai4']); SigF = np.array(A['Dev2_ai5']); SigG = np.array(A['Dev2_ai6']);

# Subtract zero value to centre zero value at 0
SigA = SigA - AZero; SigB = SigB - BZero; SigC = SigC - CZero;
SigE = SigE - EZero; SigF = SigF - FZero; SigG = SigG - GZero
```

Automated search for the time of the largest peak:

```
#Find the time step with the maximum amplitudes of each trace.
## Sensor A ##
MaxA_0ed_Positive = (max(A["Dev2_ai0"])-AZero) ; MaxA_0ed_Negative = (min(A["Dev2_ai0"])-AZero)

if np.abs(MaxA_0ed_Positive) >= np.abs(MaxA_0ed_Negative):
    MaxA_0ed = MaxA_0ed_Positive
    s = np.where(A["Dev2_ai0"]== max(A["Dev2_ai0"])) ; spass = s[0] ;
    whereA = float(XuS[spass[0]])
else :
    MaxA_0ed = MaxA_0ed_Negative
    s = np.where(A["Dev2_ai0"]== min(A["Dev2_ai0"])) ; spass = s[0] ;
    whereA = float(XuS[spass[0]])
```

Apply the band pass filter:

```
from scipy import signal
sos1 = signal.butter(6, 100e3, btype = 'highpass', fs = 2.5e6 ,output='sos')
sos2 = signal.butter(6, 200e3, btype = 'lowpass', fs = 2.5e6 ,output='sos')

SigA = signal.sosfilt(sos1, SigA)
SigB = signal.sosfilt(sos1, SigB)
SigC = signal.sosfilt(sos1, SigC)
SigE = signal.sosfilt(sos1, SigE)
SigF = signal.sosfilt(sos1, SigF)
SigG = signal.sosfilt(sos1, SigG)

SigA = signal.sosfilt(sos2, SigA)
SigB = signal.sosfilt(sos2, SigB)
SigC = signal.sosfilt(sos2, SigC)
SigE = signal.sosfilt(sos2, SigE)
SigF = signal.sosfilt(sos2, SigF)
SigG = signal.sosfilt(sos2, SigG)
```

Apply the Hibert transform and find the signal envelope:

```
from scipy.signal import hilbert

SigA_Env1 = hilbert(SigA)
SigA_Env = np.abs(SigA_Env1)
SigB_Env1 = hilbert(SigB)
SigB_Env = np.abs(SigB_Env1)
SigC_Env1 = hilbert(SigC)
SigC_Env = np.abs(SigC_Env1)
SigE_Env1 = hilbert(SigE)
SigE_Env = np.abs(SigE_Env1)
SigF_Env1 = hilbert(SigF)
SigF_Env = np.abs(SigF_Env1)
SigG_Env1 = hilbert(SigG)
SigG_Env = np.abs(SigG_Env1)
```

Perform running integral for onset determination:

```
#Create window and determine signal arrival time from the percentage of signal
#that has arrived.

import scipy.integrate
SelPent = 0.1 # Selection criteria: % of total signal arrival within window.
Wind_low = 125 # 125 time steps is = 50 us
Wind_up =  750


####
#A
####
low = int(df.at[0,"PA"]/0.4) - Wind_low     #/0.4 converts time to time steps
up = int(df.at[0,"PA"]/0.4) + Wind_up

integ = scipy.integrate.trapezoid(y = SigA_Env[low : up], dx = 1)
cuminteg = 0
i = 0
while cuminteg < (integ*SelPent):
    i += 1
    low = int(low)
    up = int(low) + i

    cuminteg =(scipy.integrate.trapezoid(y = SigA_Env[low : up], dx = 1))

Upper_limit = XuS[up]; ArrA = Upper_limit      # Signal onset for A
```

Average flux vs. diameter for a 1U CubeSat:

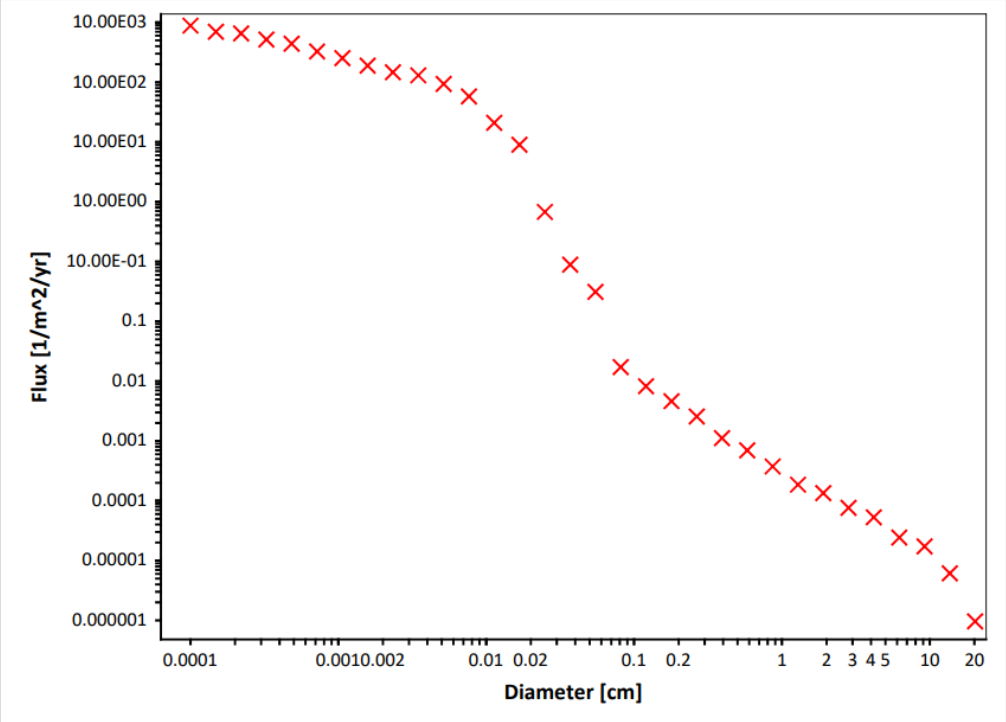

Fig. A77: Average flux (averaged over all faces) vs. diameter for a 1U CubeSat in the orbit described in Chapter 6.

Average flux vs. diameter for a 1.5U CubeSat:

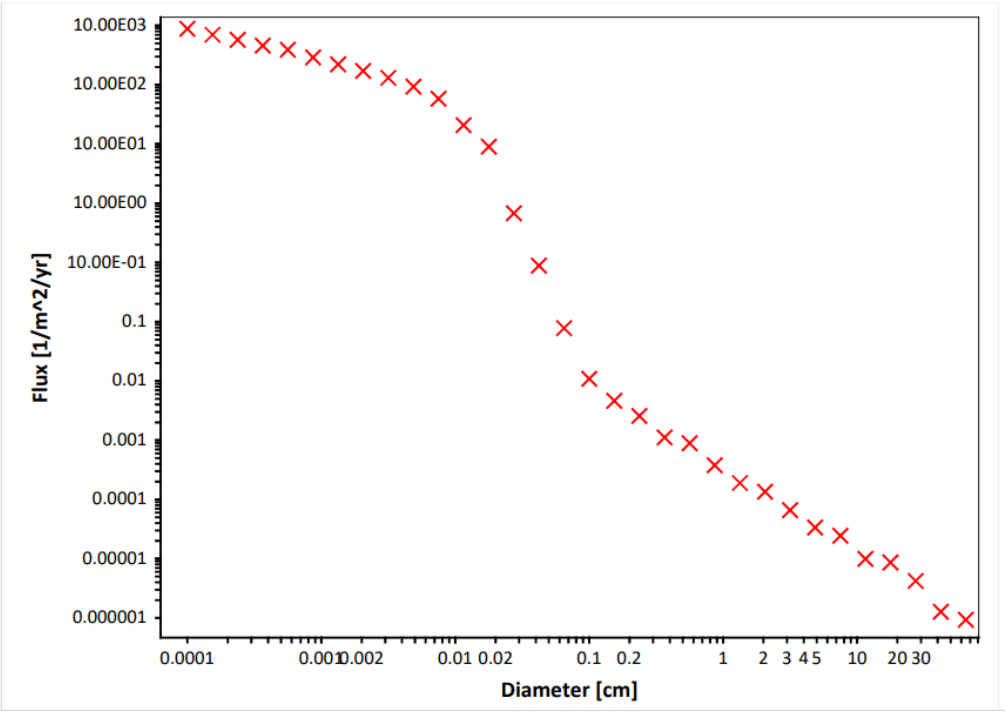

Fig. A78: Average flux (averaged over all faces) vs. diameter for a 1.5U CubeSat in the orbit described in Chapter 6.

Average flux vs. diameter for a 3U CubeSat:

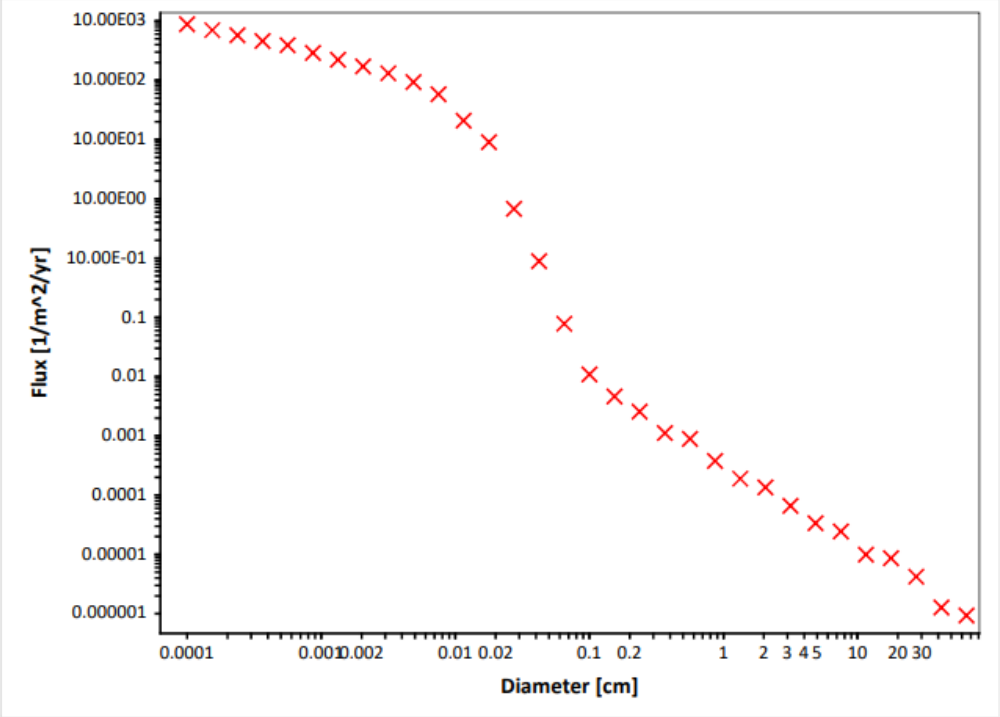

Fig. A79: Average flux (averaged over all faces) vs. diameter for a 3U CubeSat in the orbit described in Chapter 6.

Average flux vs. diameter for a 6U CubeSat:

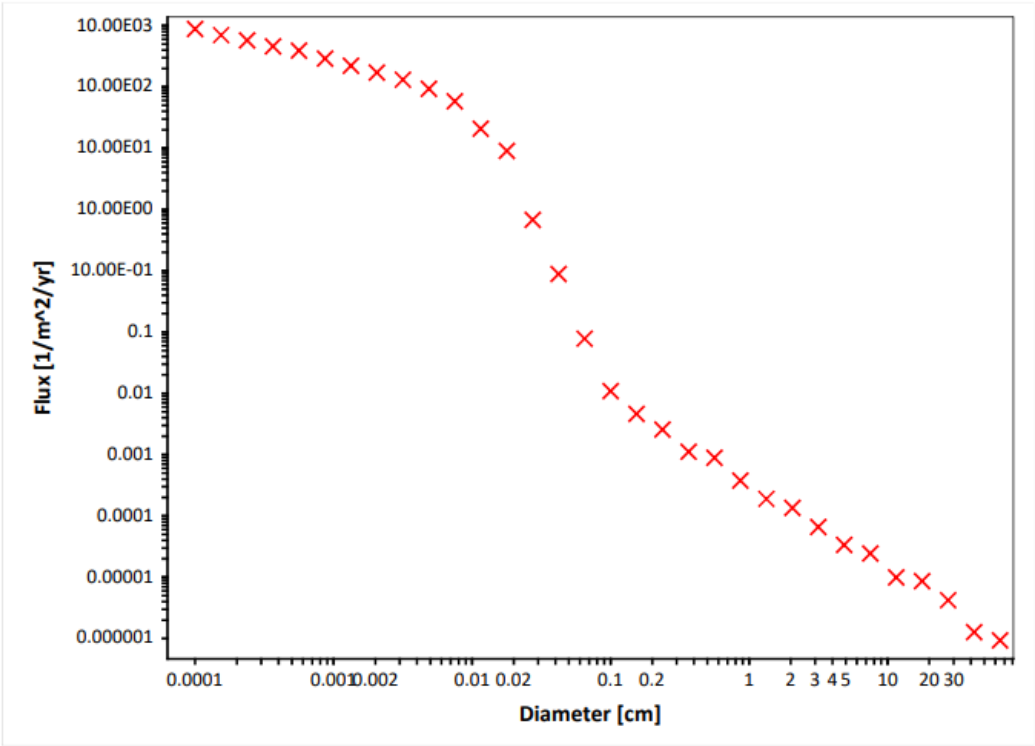

Fig. A80: Average flux (averaged over all faces) vs. diameter for a 6U CubeSat in the orbit described in Chapter 6.